

# Electronic and Magnetic Properties of the Fe/GaAs(110) Interface

Dissertation

zur Erlangung des mathematisch-naturwissenschaftlichen Doktorgrades  
"Doctor rerum naturalium"  
der Georg-August-Universität Göttingen

im Promotionsprogramm ProPhys  
der Georg-August-University School of Science (GAUSS)

vorgelegt von  
**Tim Iffländer**  
aus Wolfsburg

Göttingen 2015

## **Betreuungsausschuss**

Prof. Dr. Rainer G. Ulbrich,  
IV. Physikalisches Institut, Georg-August-Universität Göttingen

Prof. Dr. Markus Münzenberg,  
Institut für Physik, Ernst-Moritz-Arndt Universität Greifswald

Dr. Martin Wenderoth,  
IV. Physikalisches Institut, Georg-August-Universität Göttingen

## **Mitglieder der Prüfungskommission**

Referent: Prof. Dr. Rainer G. Ulbrich,  
IV. Physikalisches Institut, Georg-August-Universität Göttingen

Korreferent: Prof. Dr. Hans Christian Hofsäss,  
II. Physikalisches Institut, Georg-August-Universität Göttingen

## **Weitere Mitglieder der Prüfungskommission**

Prof. Dr. Hans-Ulrich Krebs,  
Institut für Materialphysik, Georg-August-Universität Göttingen

Prof. Dr. Vasily Moshnyaga,  
I. Physikalisches Institut, Georg-August-Universität Göttingen

Prof. Dr. Michael Seibt,  
IV. Physikalisches Institut, Georg-August-Universität Göttingen

Prof. Dr. Cynthia A. Volkert,  
Institut für Materialphysik, Georg-August-Universität Göttingen

Tag der mündlichen Prüfung: 30.10.2015





## Introduction

The ever decreasing size of modern semiconductor devices as predicted by Gordon Moore back in 1965 [1] is approaching inconceivably small dimensions. The “International Technology Roadmap for Semiconductors 2013” [2] states that, at the time of writing this thesis, silicon fins in the cutting-edge three-dimensional *fin field effect transistor* (FinFET) architecture have reached a width of less than 8 nm. However, due to fundamental physical and practical limits of that miniaturization, the rate of device shrinking is likely to be curtailed in the foreseeable future and novel approaches have to be explored for future device functionality [3].

One idea is a spin-based electronics or *spintronics* where the spin of the electron is used as a new degree of freedom in electronic devices [4, 5]. In 1990, Datta and Das were the first to propose the concept of a semiconductor based spintronics device [6]. This *spin field effect transistor* (spin-FET) consists of two separate ferromagnetic contacts on a semiconductor. One of the contacts serves as a source to inject spin-polarized carriers into the non-magnetic semiconductor. The other ferromagnetic contact detects the spin-polarization of the carriers that can be manipulated by a gate electrode utilizing the effect of *spin orbit coupling*.

One possibility to realize a spin-FET architecture is to use a ferromagnetic metal such as iron (Fe) for the source and drain contacts. In contrast to ferromagnetic semiconductors, ferromagnetic metals have the advantage of lower coercive fields, high Curie temperatures, and a highly developed thin film technology [3]. However, theoretical work suggests that due to the large difference in conductivity between the metal and the semiconductor in contact an efficient spin injection is not possible [7]. It was proposed that this *conductivity mismatch* problem is resolved by introducing an additional tunnel barrier between the semiconductor and the ferromagnet which naturally comes along with a Schottky contact and can serve as a spin-filter [7, 8]. In 2001, Zhu *et al.* [9] could indeed demonstrate spin injection from a ferromagnetic metal into a semiconductor for the first time. They observed spin injection from Fe into GaAs at room-temperature with an efficiency of 2%. Later, Hanbicki et al. [10] found spin injection efficiencies as large as 32%

for injecting electrons from Fe into GaAs across a Fe/AlGaAs interface. They achieved this by tailoring the doping profile in such a way that the Schottky contact had a narrow depletion width serving as a triangular shaped tunnel barrier and by growing the Fe film with a substrate temperature of 10—15 °C to minimize intermixing at the interface [10]. A recent study combining transmission electron microscopy measurements with *ab initio* calculations by Fleet *et al.* [11] supports the idea that the spin transport across the Fe/GaAs(001) interface strongly depends on the interface structure. This should not be of any surprise because altering the physical structure of the interface also gives rise to a change of the electronic structure at the interface. The knowledge of both the atomic and electronic structure at the interface is the key for understanding and optimizing spin injection across metal-semiconductor interfaces [3]. In this context, a central aspect is the understanding of the microscopic process of Schottky barrier formation at metal-semiconductor interfaces as it determines the band bending inside the semiconductor as well as the electronic structure of the interface.

Since the discovery of the rectifying behavior of metal-semiconductor interfaces by Ferdinand Braun back in 1874 [12], the investigation of this type of interfaces has been an active research field. In 1938, Schottky and Mott [13-15] explained the rectifying behavior by the formation of a space charge region inside the semiconductor due to a difference between the metal work function and the semiconductor electron affinity. However, the subsequent experimental observation of a weak dependence of the Schottky barrier on the metal work function (also known as *Fermi level pinning*) indicated the presence of an additional microscopic (extending one to several atomic layers) electric dipole at the interface [16]. Several mechanisms have been proposed to describe the Schottky barrier formation on this microscopic scale [16-26]. However, up to the present day, it remains controversial which of these mechanisms is dominant. In order to answer this question, one would need an “ideal” sample system combined with an experimental technique that is able to simultaneously probe the atomic and electronic structure of the interface in real space in a sufficiently large energy range.

However, even after the advent of ultrahigh vacuum technology it has proven difficult to produce “ideal” metal-semiconductor interfaces. Thus far, only a handful of studies have claimed the investigation of atomically controlled epitaxial interfaces [27-31]. All of them observed a strong dependence of the Schottky barrier height on the atomic structure and orientation of the ordered metal-semiconductor interface. Nevertheless, since the Schottky barrier heights in these studies were obtained by macroscopic capacitance-voltage and current-voltage methods, the influence of the local atomic structure on the local Schottky barrier could not be determined by these measurements.

Only after the introduction of ballistic electron emission microscopy (BEEM) [32], a spatially resolved detection of the Schottky barrier height was possible for the first time. Several BEEM studies revealed lateral inhomogeneities of the Schottky barrier on the nanometer-scale [32-38]. However, due to the topview geometry of the experimental geometry no direct information on the local atomic structure can be obtained by the

---

BEEM technique. In order to probe structural and electronic properties simultaneously, scanning tunneling microscopy (STM) and spectroscopy (STS) measurements were performed on top of metal clusters deposited on GaAs(110)<sup>1</sup> [39-42]. Nevertheless, the planar geometry did not allow a direct probing of the metal-semiconductor interface. Therefore, using a double cleavage technique, Reusch *et al.* [43-45] performed STM and STS measurements in cross-sectional geometry which allowed them to scan the STM tip across an Au/GaAs(110) interface. However, due to sample preparation, they did not succeed to directly access the immediate interface with the STM tip.

A more promising approach with regard to the sample preparation has been undertaken by Winking *et al.* [46, 47]. They chose to grow Fe on *n*-type GaAs(110) as the sample system Fe/GaAs is well-known for its very small lattice mismatch allowing the growth of epitaxial interfaces [48]. The growth of Fe, with the GaAs substrate held at room-temperature, yields abrupt interfaces that show only partial intermixing [11, 49, 50], making this sample system an interesting candidate for potential spintronics devices. In order to further suppress intermixing at the interface, Winking *et al.* [46, 47] developed a low-temperature growth process yielding epitaxial layer-by-layer grown films. Using STM in cross-sectional geometry, Winking was able to directly access the low-temperature grown interface with the STM tip and found very abrupt interfaces without any sign of intermixing [47]. This makes the low-temperature grown Fe/GaAs(110) interface an “ideal” sample system to study the relevance of different theoretical models for Schottky barrier formation. Performing STS measurements in cross-sectional geometry, Winking [47] simultaneously investigated the atomic and electronic structure of the interface. He explored the potential landscape of the space charge region and extracted the Schottky barrier height of the system by means of a three-dimensional finite element simulation of the electrostatic potential of the space charge region. High resolution spectra of the immediate interface region revealed a continuum of states inside the band gap of the semiconductor [47]. However, up to now a “complete” energetic and spatial map of the local density of states that also covers the valence and conduction bands at the interface was still missing. Nevertheless, such a map is essential for checking the validity of any proposed model and for a deeper understanding of the microscopic process of Schottky barrier formation. Moreover, not only the understanding of the atomic and electronic structure of the ferromagnet/semiconductor interface is of crucial importance for potential spintronics applications but also the knowledge of the magnetic anisotropy of the thin ferromagnetic film grown on the semiconductor is a central aspect for spintronics device design. In particular, for optical spin detection with light generally propagating normal to the surface plane, quantum selection rules require a saturation of the magnetic spin source normal to the surface plane as well [3, 9, 51]. Typically, ferromagnetic films with thicknesses of several tens of nanometers are used as spin injectors. However, due to the shape anisotropy, they

---

<sup>1</sup> Since the GaAs(110) surface does not exhibit any surface states inside the fundamental band gap [123], metal/GaAs(110) interfaces seem to be good candidates for the “undisturbed” investigation of possibly interface-induced gap states.

are in-plane magnetized. This requires the application of magnetic fields of several Tesla normal to the surface plane. For an optical spin detection in the low-field regime, one also might consider the use of films magnetized perpendicularly to the surface plane [51]. Therefore, this thesis focuses on both the investigation of the atomic-scale electronic properties and the magnetic anisotropies of the low-temperature grown “ideal” Fe/GaAs(110) interface. The electronic properties are investigated by means of STM and STS measurements in cross-sectional geometry. The magnetic properties of ultrathin Fe films on GaAs(110) are studied by *in situ* magneto-optic Kerr effect (MOKE) measurements.

This thesis is organized as follows: Chapter 1 gives an introduction to the theoretical concepts of Schottky barrier formation and an overview of the cutting-edge knowledge of Fe/GaAs Schottky contacts. In chapter 2, the theoretical background of the experimental techniques used in this thesis, namely STM and MOKE, are presented together with a brief description of the experimental setups and the sample preparation process.

In chapter 3, low-temperature grown “ideal” *p*-type Fe/GaAs(110) interfaces are investigated by means of low-temperature STM and STS in cross-sectional geometry for the first time. The data is discussed and compared with the findings obtained by Winking [47] for the *n*-type junction.

In chapter 4, the STS current-voltage spectra taken along the space charge region of the “ideal” *p*-type interface are analyzed quantitatively by adapting a three-dimensional finite element model originally developed by Winking [47] that allows the extraction of the Schottky barrier height of the system. Furthermore, a new analysis tool is presented that reveals variations of the local density of states inside the valence and conduction bands. In combination with density functional calculations conducted by Ali Al-Zubi and Stefan Blügel presented in chapter 5 this leads to a deeper understanding of the process of Schottky barrier formation on the atomic scale. Moreover, a model is developed that qualitatively explains the dependence of the local *p*-type Schottky barrier height on the interface charge distribution taking into consideration the electronic states inside the band gap and the valence band.

A model system like the low-temperature grown Fe/GaAs(110) interface now also allows to investigate the influence of atomic disorder in the interface layer on the Schottky barrier. This is done in chapter 6 by studying the structural and electronic properties of room-temperature submonolayer pre-grown *p*-type interfaces. Furthermore, the influence of the Fe film thickness on the electronic structure of the interface is investigated.

In chapter 7, the magnetic anisotropy of low-temperature grown ultrathin (2–3 monolayers) Fe films on GaAs(110) is discussed. Based on previous results from an *in situ* MOKE study in longitudinal geometry by Iffländer [52] the measurements are extended to transverse and polar geometries. This yields a more advanced picture of the magnetic properties of the Fe/GaAs(110) interface and provides information for a more detailed discussion of potential models that might be able to explain the experimental

---

findings. Chapter 8 presents a photon energy-dependent MOKE study that aims to determine which electronic states dominate the magnetic properties of the low-temperature grown (2–3 ML Fe)/GaAs(110) interface.

Chapter 9 concludes this thesis with a summary of the main results obtained.

In the section “Darstellung der wissenschaftlichen Zusammenarbeit” on page 145 I state how the results of this thesis have been obtained and which parts of this thesis have already been published.



# Table of Contents

Introduction	i
Table of Contents	vii
Abbreviations and Definitions	xi
1 Metal-Semiconductor Contacts	1
1.1 Schottky-Mott Model	2
1.2 Gap States and Fermi Level Pinning	4
1.3 Metal-Induced Gap States Model	6
1.4 Defect Model	7
1.5 Bond Polarization Model	8
1.6 Review of Fe/GaAs Interfaces	9
2 Experimental Techniques	17
2.1 Scanning Tunneling Microscopy	17
2.1.1 The Tunnel Current	18
2.1.2 Measuring Modes	19
2.1.3 Experimental Setup and Tip Preparation	20
2.2 Magneto-Optic Kerr Effect	21
2.2.1 Theoretical Background	21
2.2.2 Experimental Setup	26

---

## Table of Contents

2.3	Low Temperature Sample Preparation Process	29
<b>3</b>	<b>Structural and Electronic Properties of the Ideal Fe/GaAs(110) Interface</b>	<b>31</b>
3.1	Structural Characterization of the Interface	32
3.1.1	STM on the Free GaAs(110) Surface	32
3.1.2	Investigation of the Immediate Interface Region	34
3.1.3	STM Tip Preparation for Interface Characterization	37
3.2	Electronic Characterization of the Interface	38
3.2.1	Tip-Induced Band Bending	38
3.2.2	Space Charge Region Analysis	39
3.2.3	High-spectral resolution characterization of the interface	44
<b>4</b>	<b>Quantitative Analysis of the Ideal Interface</b>	<b>49</b>
4.1	3D Simulation of the Electrostatic Potential of Metal-Semiconductor Interfaces	49
4.1.1	3D Model and Boundary Conditions	50
4.1.2	The Charge Density in GaAs	54
4.1.3	Electrostatic Potential Energy and Space Charge Density	55
4.1.4	Comparability between 3D FEM Simulation and Experimental <i>I-V</i> Spectra	56
4.2	Extracting the Schottky Barrier Height from the Data	60
4.3	The Local Density of States at the Interface	63
<b>5</b>	<b>LDOS Model of the Interface</b>	<b>67</b>
5.1	DFT Calculations	67
5.2	A Combined MIGS-and-BP-Model	71
<b>6</b>	<b>LDOS for Differently Grown Interfaces</b>	<b>75</b>
6.1	Room Temperature Grown Interface	75
6.2	Influence of Fe Film Thickness	78
6.3	Discussion of the Different <i>p</i> -type Interfaces	79
<b>7</b>	<b>Magnetic Properties of the Fe/GaAs(110) Interface</b>	<b>85</b>
7.1	Magnetic Anisotropy of Ultrathin Fe Films on GaAs(110)	87
7.2	Kerr Signal Dependence on Surface Orientation	91

---

7.3	In-Plane Uniaxial Anisotropy	93
7.4	No Dependence on Type of Doping	97
7.5	Thickness Dependence of the Kerr Signal	98
7.6	Discussion	102
7.6.1	Canted Fe Film Magnetization	102
7.6.2	Influence of the Interface Quality	111
7.6.3	Interface Magnetism	114
8	Combined Electronic and Magnetic Discussion of the Interface	123
9	Summary	127
A	Appendix	131
A.1	Topographic Analysis of the Space Charge Region	131
	Bibliography	135
	Darstellung der wissenschaftlichen Zusammenarbeit	145
	Danksagung	149
	Lebenslauf	151



## Abbreviations and Definitions

As	arsenic
$e$	elementary charge
$dI/dV$	differential conductivity
$E$	energy
$E_C$	conduction band minimum
$E_F$	Fermi energy
$E_F^M$	Fermi energy of the metal
$E_F^{sc}$	Fermi energy of the semiconductor
$E_F^t$	Fermi energy of the tip
$E_g$	energetic width of the band gap
$E_V$	valence band maximum
Fe	iron
Ga	gallium
GaAs	gallium arsenide
(hkl)	Miller indices notation: specific plane
{hkl}	Miller indices notation: group of planes
[hkl]	Miller indices notation: specific direction
$\langle hkl \rangle$	Miller indices notation: group of directions
$I_T$	tunnel current
$m^*$	effective mass
$m_0$	electron mass
$V$	voltage
$V_s$	sample bias voltage

$w_{SCR}$	width of the space charge region
$\Phi_{abh}$	apparent barrier height
$\Phi_{SB}^{n,p}$	Schottky barrier height for <i>n</i> - and <i>p</i> -type Schottky barriers
$\rho$	charge density

bcc	body centered cubic
DFT	density functional theory
DOS	density of states
EA	easy axis
fcc	face centered cubic
HA	hard axis
HR	high resolution
IPMA	in-plane magnetic anisotropy
LDOS	local density of states
LEED	low energy electron diffraction
LT	low-temperature
MBE	molecular beam epitaxy
MOKE	magneto-optical Kerr effect
PMA	perpendicular magnetic anisotropy
RT	room-temperature
SB	Schottky barrier
SMOKE	surface magneto-optical Kerr effect
SRT	spin-reorientation transition
STM	scanning tunnelling microscopy
TEM	transmission electron microscopy
TIBB	tip-induced band bending
UHV	ultrahigh vacuum

# 1 Metal-Semiconductor Contacts

Back in 1874, Ferdinand Braun was the first to discover the rectifying behavior of metal-semiconductor contacts [12] and simultaneously marked the beginning of the field of interface science and semiconductor device physics. About 30 years later, in the beginning of the 20th century, the first metal-semiconductor point contacts were used as solid-state rectifiers in the emerging field of radio and telecommunication [53]. In 1938, Walter Schottky [13, 14] and Nevill Mott [15] independently explained the rectifying behavior of metal-semiconductor contacts by using a microscopic band structure model. In the framework of this model they identified the barrier height at metal-semiconductor contacts as the difference between the metal work function and the electron affinity of the semiconductor in contact. However, in the following years it became apparent that the Schottky-Mott model was not able to explain the vast amount of experimental data that was produced thereafter. In the last 70 years numerous theories have been proposed in order to explain the discrepancies between the Schottky-Mott model and the experimental data. In these theories different microscopical mechanisms have been suggested for a better understanding of Schottky barrier formation. Nevertheless, up to the present day the question which of these mechanisms dominates the physics of metal-semiconductor interfaces could not unambiguously be answered yet. A comprehensive overview on the field of metal-semiconductor interfaces is given in Refs. [53-56].

In subsections 1.1 to 1.5 of this chapter, microscopic models and concepts of Schottky barrier formation are presented. In subsection 1.6 we introduce the geometry of the sample system Fe/GaAs(110) investigated in this thesis and give a brief overview of the relevant cutting-edge knowledge of Fe/GaAs Schottky contacts.

## 1.1 Schottky-Mott Model

In 1938, Schottky was the first to suggest that the rectifying behavior of metal-semiconductor interfaces is due to a *space charge region* inside the semiconductor [13]. He proposed that inside the semiconductor the donor concentration  $N_D$  for the *n*-type case as well as the acceptor concentration  $N_A$  for the *p*-type case are homogeneous. Therefore, the ionized doping atoms give rise to a uniform space charge density  $\rho(\vec{r})$  in the space charge region described by the step function (for  $T = 0$  K):

$$\rho(x) = \begin{cases} eN_D, & 0 < x < w_{SCR} \quad (n\text{-type}) \\ -eN_A, & 0 < x < w_{SCR} \quad (p\text{-type}) \\ 0, & x > w_{SCR} \quad (\text{both types}) \end{cases} \quad (1.1)$$

where  $x$  is the spatial coordinate perpendicular to the interface and  $w_{SCR}$  is the width of the space charge region. The corresponding electrostatic potential  $V(\vec{r})$  in the space charge region is given by the Poisson equation:

$$\nabla^2 V(\vec{r}) = -\frac{\rho(\vec{r})}{\epsilon_r \epsilon_0}. \quad (1.2)$$

where  $\epsilon_0$  is the permittivity of the vacuum and  $\epsilon_r$  is the relative permittivity of the semiconductor. The assumed uniform charge density results in a parabolic shape of the barrier and the width of the space charge region for the *n*-type and the *p*-type case can be expressed as [56]:

$$w_{SCR}^n = \sqrt{\frac{2\epsilon_r \epsilon_0}{e^2 N_D} (\Phi_{SB}^n - (E_C - E_F))} \quad (1.3)$$

$$w_{SCR}^p = \sqrt{\frac{2\epsilon_r \epsilon_0}{e^2 N_A} (\Phi_{SB}^p - (E_F - E_V))} \quad (1.4)$$

with  $e$  the elementary charge,  $\Phi_{SB}^{n,p}$  the Schottky barrier height for *n*- and *p*-type contacts,  $E_F$  the Fermi energy,  $E_C$  the conduction band minimum, and  $E_V$  the valence band maximum (see also Figure 1.1 for definition).

An expression for the Schottky barrier height can be obtained in the framework of the band structure model developed by Schottky and Mott [14, 15]. In the following Gedankenexperiment [47, 53, 55] we assume that finite metal and semiconductor surfaces are planar and face each other. Initially, the surfaces are very far apart from each other but electrically contacted on their back side as shown in Figure 1.1(a). This aligns the Fermi energies of the semiconductor  $E_F^{SC}$  and the metal  $E_F^M$ . The energy needed to bring an electron from the Fermi energy to the vacuum level<sup>2</sup>  $E_{vac}$  immediately outside the surface of

---

<sup>2</sup> The vacuum level  $E_{vac}$  is defined as the energy of an electron at rest just outside the surface (typical of the order of  $10^{-6}$  m away from the surface). Since here we assume that the surface dipole layers have a finite lateral extension the vacuum level just outside the surface  $E_{vac}$  is not equivalent to the vacuum level infinite-

the solid is defined as the work function. A difference in the work function of the metal  $\Phi_M$  and the work function of the semiconductor  $\Phi_{SC}$  yields a contact potential difference  $\Delta = (\Phi_{SC} - \Phi_M)/e$ . For the *p*-type junction<sup>3</sup> considered here we assume  $\Phi_{SC} > \Phi_M$ . The work function of the semiconductor for the *p*-type case can also be written as  $\Phi_{SC} = \chi_{SC} + E_g - (E_F^{SC} - E_V)$ , where  $\chi_{SC}$  is the electron affinity of the semiconductor,  $E_g$  denotes the energetic width of the band gap, and  $E_V$  is the valence band maximum.

Now, the two surfaces are brought into close proximity with a distance  $d$  between them as shown in Figure 1.1(b). The Schottky-Mott model does not consider any charges on the surface of the semiconductor that could effectively screen the electric field from the metal. Therefore, a space charge region with a parabolic shape of the electron energy bands is formed by ionized acceptors in the *p*-type case. As can be seen in Figure 1.1(b), a part of the difference in electron potential energy<sup>4</sup> between metal and semiconductor now drops along the width of the space charge region  $w_{SCR}$ .

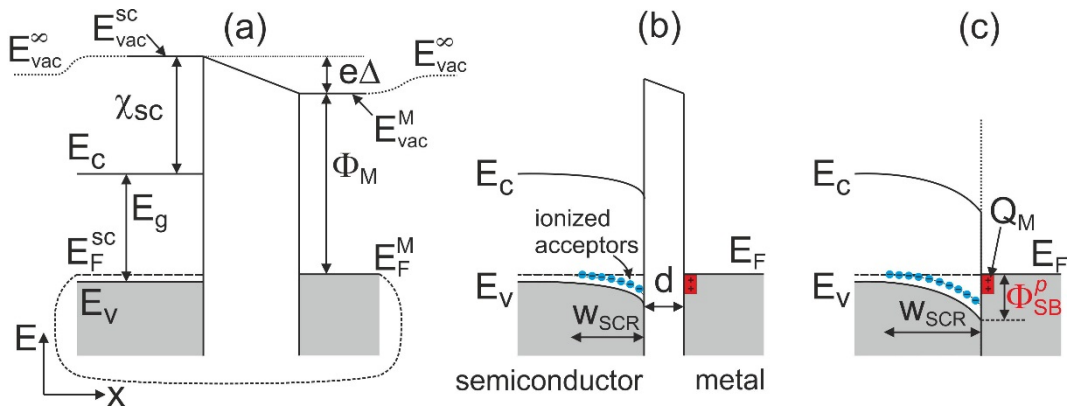


Figure 1.1: Formation of a space charge region in dependence of the distance  $d$  between semiconductor and metal. The Schottky-Mott relation for the *p*-type junction can be derived from this band structure model. For more details see continuous text.

If the distance between the semiconductor and the metal is further decreased, the width of the space charge region further increases. When metal and semiconductor are in direct contact, the entire difference in electron potential energy drops along the space charge region inside the semiconductor as depicted in Figure 1.1(c). The charge of the ionized acceptors in the space charge region of the semiconductor  $Q_{SC}$  is compensated by an equal charge  $Q_M$  of opposite sign on the side of the metal (overall charge neutrality):

$$Q_{SC} + Q_M = 0. \quad (1.5)$$

---

ly far away from the surface  $E_{vac}^\infty$  (see also Figure 1.1(a)). This is due to the fact that for larger distances of the electron from the finite surface the surface dipole can be regarded as a point dipole whose potential is proportional to  $1/x^2$  [155].

<sup>3</sup> The same considerations can also be applied to the *n*-type case, see, e.g., Refs. [47, 53, 55].

<sup>4</sup> The relation between the electron potential energy  $E(x)$  and the electrostatic potential  $V$  and its impact on the energy bands is discussed in greater detail in chapter 4 on page 50.

In the framework of the Schottky-Mott model the Schottky barrier heights for the *n*-type and *p*-type junction without externally applied voltage<sup>5</sup> can then be expressed as:

$$\Phi_{SB}^n = \Phi_M - \chi_{SC} \quad (1.6)$$

$$\Phi_{SB}^p = \chi_{SC} + E_g - \Phi_M. \quad (1.7)$$

Here it is assumed that the quantities  $\Phi_M$  and  $\chi_{SC}$ , which are defined for free surfaces, stay constant when metal and semiconductor are brought into contact. Equations (1.6) and (1.7) are also known as the Schottky-Mott rule. However, after Schottky and Mott predicted this strong dependence of the Schottky barrier height on the metal work function subsequent experiments revealed a much weaker dependence [56].

## 1.2 Gap States and Fermi Level Pinning

In 1947, John Bardeen proposed a model [16] in order to explain the experimentally observed much weaker dependence of the Schottky barrier height on the metal work function than the Schottky-Mott model predicts. He introduced the concept of surface states inside the fundamental band gap of the semiconductor as shown in the right panel of Figure 1.2. When a metal is brought into contact with the semiconductor, the charge  $Q_{GS}$  is transferred into these gap states. The overall charge of the system has to be neutral so that we can rewrite equation (1.5) to:

$$Q_{SC} + Q_M + Q_{GS} = 0. \quad (1.8)$$

The gap states charge  $Q_{GS}$  is assumed to be located at a fixed distance  $\delta$  (usually several angstrom) from the metal surface in order to form an additional interface dipole together with its image charge on the metal. As can be seen in Figure 1.2, this interface dipole partially compensates the effect of the difference between the work function of the semiconductor and the work function of the metal on the Schottky barrier height. Therefore, by including the gap states the Schottky-Mott rule can be extended to:

$$\Phi_{SB}^n = \Phi_M - \chi_{SC} - e\Delta_{GS} \quad (1.9)$$

$$\Phi_{SB}^p = \chi_{SC} + E_g - \Phi_M - e\Delta_{GS} \quad (1.10)$$

---

<sup>5</sup> Throughout this thesis only metal-semiconductor contacts without externally applied voltage are investigated. Therefore, the electrochemical potential  $\mu_{ec}$  is constant across the interface as depicted, e.g., in Figure 1.1 and Figure 1.2.

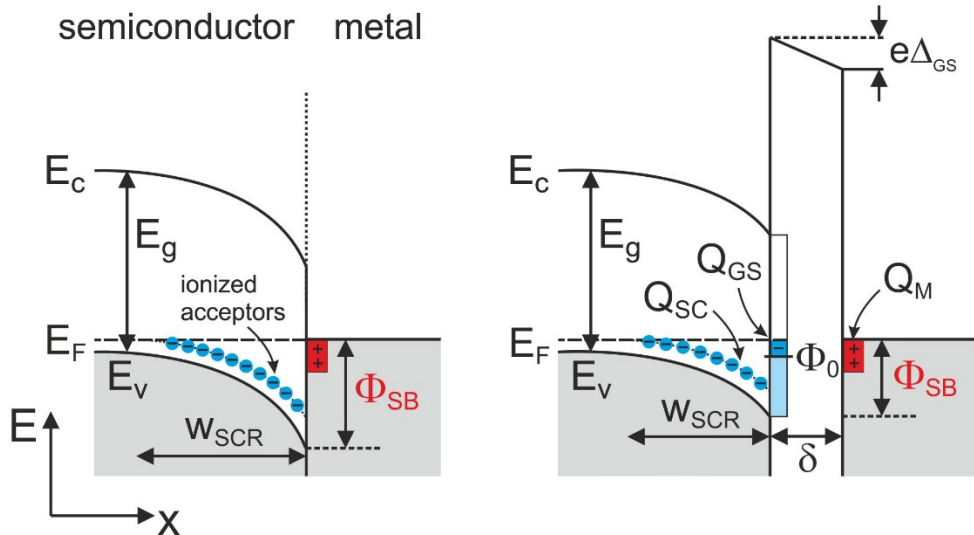


Figure 1.2: (left) Band structure scheme of a metal-semiconductor interface without gap states after Schottky and Mott. (right) Metal-semiconductor interface with gap states at the semiconductor surface separated by the distance  $\delta$  (several angstrom) from the metal surface. The gap states charge  $Q_{GS}$  comes along with an additional potential drop  $\Delta_{GS}$  at the interface.

Bardeen could show that a sufficiently high density of band gap states ( $> \sim 10^{12} \text{ cm}^{-2}$ ) tends to make the Schottky barrier height virtually independent of the metal work function [16]. This can be explained by the concept of *Fermi level pinning* (FLP) that will be briefly discussed by looking at the right panel of Figure 1.2. In the context of FLP the charge neutrality level (CNL)  $\Phi_0$  is introduced. If the Fermi level is aligned with the CNL, the gap states charge is neutral and there is no additional interface dipole. If the Fermi level lies below the CNL, the donor-like gap states will exhibit a positive net charge. The case depicted in Figure 1.2 shows the Fermi level above the CNL yielding acceptor-like gap states with a negative net charge. This additional charge creates an interface dipole counteracting to any change in  $\Phi_M$  and therefore reducing the change in the Schottky barrier height  $\Phi_{SB}$ : if we assume an increase in  $\Phi_{SB}$ , a rigid shift of the bands together with  $\Phi_0$  would lead to an increase of the negative charge of the gap states  $Q_{GS}$ . This in turn would decrease the space charge  $Q_{SC}$  together with  $w_{SCR}$ . This pushes  $\Phi_0$  back towards the Fermi energy  $E_F$ . One could also say that the Fermi energy is *pinned* to the characteristic energy  $\Phi_0$  and ‘stabilizes’  $\Phi_{SB}$ . The same line of arguments holds also for the case where the Fermi level is below the CNL.

As we will see in the following sections, the concept of FLP is central in many theoretical models that were developed after Bardeen’s contribution to describe the Schottky barrier formation.

## 1.3 Metal-Induced Gap States Model

At a free metal surface the electron wave functions decay exponentially into the vacuum. If the metal is in contact with a semiconductor, the wave functions tail into the semiconductor. Volker Heine showed that this leads to a continuum of states within the energy range of the fundamental band gap [17]. These states are also called *metal-induced gap states* (MIGS). Heine calculated a metal-induced density of states of  $> 3.5 \times 10^{14} \text{ eV}^{-1}\text{cm}^{-2}$  on the semiconductor side of the interface that can explain the observed FLP for metal-semiconductor interfaces. Due to the continuum of metal-induced gap states the immediate semiconductor interface region can electronically be thought of as a metal.

The MIGS are an intrinsic property of the semiconductor and are derived from the complex semiconductor band structure giving rise to virtual gap states (ViGS) [17-19]. This is illustrated in the left panel of Figure 1.3. The valence and conduction band continue into the complex  $k$  space and are joined by a complex band. In the energy range of the band gap the states are described by complex wave vectors yielding exponentially decaying wave functions. The imaginary part of the wave vector is largest in the center of the band gap and decreases towards the band edges. Therefore, in the center of the band gap the decay length of the MIGS is the smallest and increases towards the band edges (see right panel in Figure 1.3). Tersoff calculated the midgap decay length for the ViGS in the case of a GaAs(110) substrate to  $\lambda = 3 \text{ \AA}$  [19]. This is in good agreement with first-principle numerical calculations on the density of states at metal/GaAs(110) interfaces that found a MIGS penetration depth of a few atomic layers [20, 57]. In a scanning tunneling microscopy study of Fe clusters on GaAs(110) First *et al.* observed a minimum decay length of  $\lambda = 3.4 \text{ \AA}$  at midgap and the divergence of the gap states at the band edges [42].

The band structure of the semiconductor also determines the character of the ViGS. Depending on their energetic position inside the band gap the spectral composition of these states is dominated either by the valence or the conduction band. The energy at which the ViGS cross over from predominantly valence band to conduction band character is called the branch point energy and can be calculated using the complex bulk band structure. Tersoff calculated the branch point energy of GaAs to be  $E_B = E_V + 0.5 \text{ eV}$  with  $E_V$  as valence band maximum [58]. Essentially, the branch point energy can be thought of as the charge neutrality level (CNL) that was already introduced in section 1.2.

Several first-principle calculations of metal-semiconductor interfaces revealed a large continuous density of states in the fundamental band gap of the semiconductor [20, 57, 59, 60]. However, the influence of these gap states on the FLP was controversial: the calculation of the electronic structure of 7 ideal metal/GaAs interfaces by van Schilfgaarde and Newman did not yield a universal pinning position [57]. They concluded that metal  $d$  states significantly alter the electronic structure of the interface and that models invoking intrinsic interface states to explain FLP cannot consistently explain the experimental observations. Furthermore, a study on the influence of different interface structures of the Al/GaAs(001) interface on the Schottky barrier height showed that the

MIGS alone do not result in barrier heights independent of interfacial chemical composition [60]. These shortcomings of the MIGS model are addressed by the bond polarization model that is presented in section 1.5.

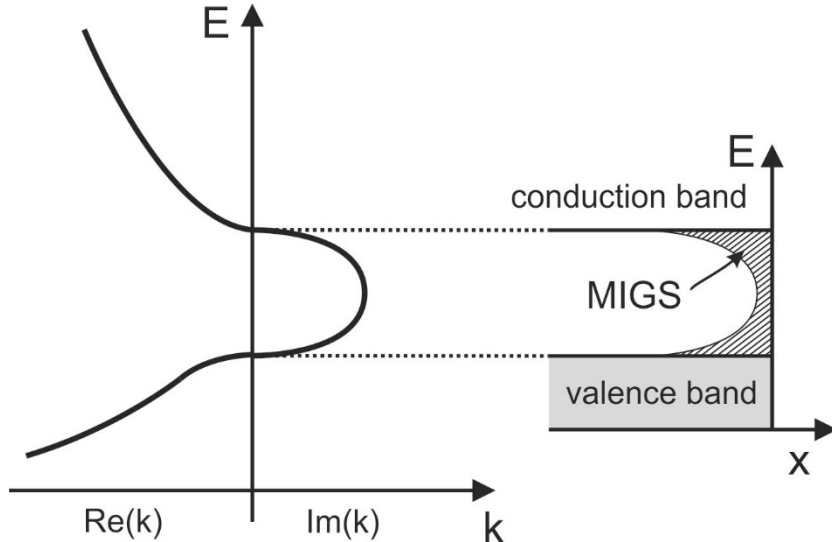


Figure 1.3: (left) Schematic of the complex band structure of a semiconductor whose valence and conduction band are connected by a complex band with an imaginary wave vector. (right) Schematic of the energy-dependent decay length of the MIGS (striped pattern). The penetration depth of the MIGS is the smallest at midgap and increases towards the band edges.

Moreover, Winfried Mönch investigated the dependency of the FLP on the metal film and proposed that the difference between the electronegativities of the metal and semiconductor determines how much charge is transferred into the gap states [61]. Depending on if the electronegativity of the semiconductor is larger, equal, or smaller than the one of the metal, the energy where the Fermi level pinning takes place lies systematically below, directly at, or above the charge neutrality level. Indeed, this MIGS-and-electronegativity model is able to explain a vast amount of experimental data [53].

## 1.4 Defect Model

Another approach to explain the FLP at metal-semiconductor interfaces is to consider defect-induced states in the fundamental band gap of the semiconductor [21-24]. The development of the *Unified Defect Model* (UDM) by Spicer *et al.* [21, 22] was motivated by photoemission spectroscopy (PES) measurements showing that the final pinning energy is already obtained at a low submonolayer coverage and virtually independent of the type of adatoms. This led Spicer *et al.* to the assumption that the growth process of the metal generates extrinsic defects at or near the interface of the semiconductor giving rise

to states at characteristic energies inside the fundamental band gap of the semiconductor. If the density of these defect states is sufficiently large, the Fermi level is pinned at the energetic positions of these defect levels in the band gap. Therefore, a crucial difference between the UDM and the MIGS model is that in the defect model the density of states inside the band gap is not a uniform continuum but has distinct peaks at characteristic energies at which the Fermi level can be pinned.

In the framework of the UDM, for *n*-doped GaAs(110) it is assumed that the spontaneous generation of As vacancies during cleavage gives rise to defect states at an energy of  $E_V + 0.75\text{eV}$  with acceptor-like character [21]. For *p*-type interfaces missing Ga is considered to be responsible for donor-like defect states at  $E_V + 0.5\text{ eV}$  [22]. However, x-ray photoemission spectroscopy experiments suggested that FLP for *n*- and *p*-type metal/GaAs interfaces due to two different kind of defects was unlikely and that FLP could be more consistently explained by a single kind of defect instead [62].

By means of electron paramagnetic resonance measurements Weber *et al.* found that the  $\text{As}_{\text{Ga}}$  antisite (substitutional As atom on Ga lattice side) could be a possible candidate for such a single defect. They determined the two energy levels of this double donor to be located at  $E_V + 0.52\text{ eV}$  and  $E_C - 0.77\text{ eV}$  [63]. However, for *n*-GaAs this double donor alone cannot explain the FLP consistently. In the *Advanced Unified Defect Model* (AUDM) (a further refinement of the UDM) Spicer *et al.* proposed that a combination of the  $\text{As}_{\text{Ga}}$  antisite and an additional  $\text{Ga}_{\text{As}}$  antisite (substitutional Ga atom on As lattice side) giving rise to a minority compensating acceptor might explain the FLP [24].

## 1.5 Bond Polarization Model

Thus far, only a handful of atomically controlled epitaxial metal-semiconductor interfaces have been grown and investigated [27-31]. The effect on the Schottky barrier height of two different epitaxial arrangements of the same metal-semiconductor pair were experimentally investigated for  $\text{NiSi}_2$  on Si(111) by Tung [28], for the Pb/Si(111) interfaces by Heslinga *et al.* [29], and for  $\text{Fe}_3\text{Si}$  on Ge(100) and Ge(111) by Yamane *et al.* [30] and Kasahara *et al.* [31]. All of these studies found that the Schottky barrier height significantly depends on the atomic structure of the interface. Furthermore, several ballistic electron emission microscopy (BEEM) studies reported lateral imhomogeneities of the Schottky barrier height on the nanometer-scale [32-38]. The MIGS model (as described in section 1.3) cannot explain these observations because it does not consider the detailed local atomic structure of the interface but is rather based on the complex band structure of the semiconductor which is an intrinsic property of the semiconductor.

In the year 2000, Tung [25, 26] presented a model where he stresses the importance of interface bonding for the formation of the interface dipole: If a semiconductor and a metal are brought into immediate contact, chemical bonds are formed at the interface. The

charge rearrangement at the interface is determined by the chemical character of these bonds. The bond polarization gives rise to a dipole at the interface as illustrated in Figure 1.4.

In his *bond polarization model* (BPM) Tung considers the entire interface region as a giant molecule whose dipole moment can be estimated by applying the *electrochemical potential equalization* (ECPE) method [26]. Tung approximates the molecular energy by a second order Taylor expansion around the state for neutral atoms. Subsequently, he minimizes the energy under the boundary condition of a net zero charge.

However, one drawback of the BPM is that it does not offer any concrete predictions for Schottky barrier heights. Moreover, the BPM only considers the immediate interface layers of the metal and the semiconductor. Here the BPM might be better understood as a next step to understand the influence of the atomic structure of the interface on the process of Schottky barrier formation. For a more realistic approach also the adjacent atomic layers should be included in the considerations which requires extensive numerical efforts. Nevertheless, this might be the most promising way to further advance the understanding of the microscopic process of Schottky barrier formation.

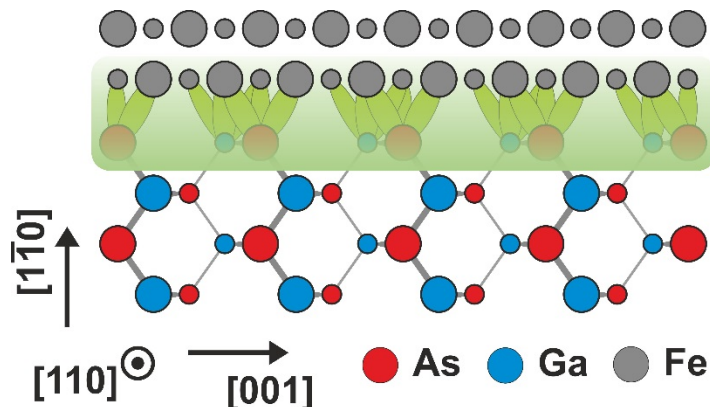


Figure 1.4: Schematic of the bond polarization model for the example of an Fe/GaAs(110) interface. This simplified illustration of the chemical bonds between metal and semiconductor also indicates the polarization by a higher density of electron charge on the semiconductor side (green color gradient).

## 1.6 Review of Fe/GaAs Interfaces

So far, in this chapter, the physics of metal-semiconductor interfaces has been discussed in general. However, in this thesis the electronic and magnetic properties of Fe/GaAs{110} interfaces will be investigated. Therefore, in this subsection, we will briefly discuss the geometry of the investigated sample system and review the cutting-edge knowledge of Fe/GaAs interfaces (see also Ref. [47], Ch. 5).

The semiconductor *gallium arsenide* (GaAs) belongs to the group of cubic III-V compound semiconductors. The GaAs bulk crystal consists of a face-centered cubic (fcc) Ga sublattice and a fcc As sublattice that are offset with respect to each other by  $a_{\text{GaAs}}/4 \cdot (1,1,1)$  along the diagonal of the fcc cube as indicated by the black arrow in the GaAs unit cell on the left side in Figure 1.5. Here  $a_{\text{GaAs}}$  is the lattice constant of GaAs that amounts to  $a_{\text{GaAs}} = 5.65 \text{ \AA}$  at room temperature [64]. This kind of structure is also called *zinc blende crystal*. As can be seen in Figure 1.5, in this crystal one As atom is tetrahedrally surrounded by 4 Ga atoms and vice versa. The gray shaded area in the GaAs crystal indicates the (110) plane. The family of {110} planes constitute the group of natural cleavage planes for the GaAs crystal [64]. On the right-hand side of Figure 1.5 a projection of the atoms on a plane parallel to a (110) surface is shown. There, the gray shaded area indicates the surface unit cell that coincides with  $a_{\text{GaAs}}$  along the [001] direction and measures 4.00  $\text{\AA}$  along the [1̄10] direction.

In 1981, Prinz and Krebs showed that iron (Fe) grows epitaxially in body-centered cubic (bcc) structure on the GaAs(110) surface [48]. In the lower left part of Figure 1.5, the bcc unit cell of Fe is illustrated. The gray shaded area indicates the (110) plane. On the lower right-hand side of Figure 1.5 only the atoms projected on a plane parallel to a (110) surface are shown together with the surface unit cell (gray shaded area). The lattice constant of Fe amounts to  $a_{\text{Fe}} = 2.866 \text{ \AA}$  [48]. Therefore, the lattice constant of Fe is very close to be half of the lattice constant of GaAs. This yields a lattice mismatch of less than  $\sim 1.4\%$  [48] which is an excellent condition for epitaxial growth.

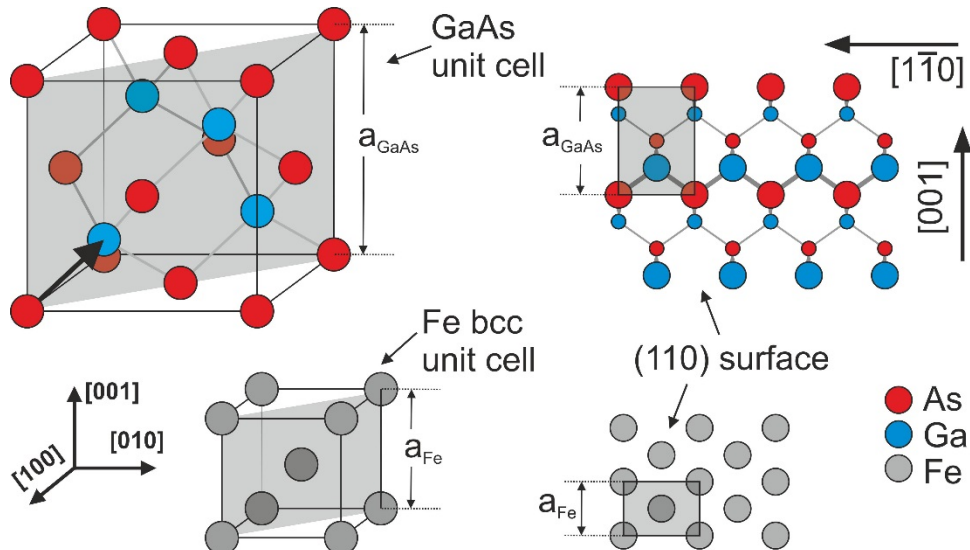


Figure 1.5: (upper left) The GaAs unit cell with a zinc blende structure and a lattice constant of  $a_{\text{GaAs}}$ . (upper right) (110) surface of GaAs with surface unit cell (gray shaded area). (lower left) bcc Fe unit cell with a lattice constant of  $a_{\text{Fe}}$ . (lower right) (110) surface of bcc Fe with surface unit cell (gray shaded area).

The small lattice mismatch between Fe and GaAs allowed the observation of epitaxial growth of Fe on GaAs(110) for substrate temperatures between room temperature (RT)

and  $\sim 450$  °C [48, 65]. By means of reflection high-energy electron diffraction (RHEED) the optimum growth (best crystal quality) was found at substrate temperatures between 175 and 225 °C [48].

In several studies it has been shown that the growth of Fe on GaAs(110) at RT or higher temperatures starts with the formation of three-dimensional (3D) Fe nuclei [42, 48, 65]. For RT grown Fe films, Höllinger *et al.* [65] observe the appearance of RHEED patterns characteristic of the Fe bcc structure at a film thickness of 4 ML which they explain by the coalescence of the Fe islands at this film thickness. Furthermore, by means of RT magneto-optic Kerr effect (MOKE) measurements they observe the onset of a ferromagnetic order at the same film thickness [65]. These thin films exhibit a uniaxial magnetic anisotropy with an in-plane easy axis (EA) parallel to the <110> direction [65]. Depending on the growth temperature, a reorientation of the in-plane magnetic anisotropy occurs between 24—50 ML with a subsequent EA parallel to the <001> direction [65]. RT growth of Fe on GaAs(001)-4×6 shows similar behavior: low energy electron diffraction (LEED) patterns appear at a film thickness of 5 ML, and MOKE measurements indicate the onset of the ferromagnetic phase at about the same film thickness [66].

Photoemission studies of Fe films grown on GaAs(110) and GaAs(001) at RT and at 175 °C show that the GaAs substrate is disrupted by the Fe and an intermixed interfacial region arises [67-69]. In this interfacial region the formation of  $\text{Fe}_2\text{As}$  and  $\text{Fe}_3\text{Ga}_{2-x}\text{As}_x$  phases is observed [67, 70-74]. The formation of these compounds is supported by higher growth temperatures (175—200 °C) where the intermixed interface region can have an extension of 6—10 nm [71, 74]. Furthermore, RT grown Fe/GaAs interfaces exhibit almost ohmic  $I$ - $V$  characteristics [75].

Several high-resolution transmission electron microscopy (HR-TEM) studies of Fe/GaAs interfaces have been carried out [11, 49, 50, 76]. Figure 1.6(a) shows a HR-TEM image of RT grown Fe/*p*-GaAs(110) interface taken along [001] by Kim and Yoon [49]. The interface between the Fe film and the GaAs(110) substrate can be clearly identified and seems to be quite abrupt. However, they observe a slightly “sawtoothed”-shaped structure along the interface that they attribute to intermixing during the initial growth stage of the Fe film. HR-TEM studies of Fe/GaAs(001) interfaces for Fe film growth temperatures  $\leq 50$  °C [76] and at RT [11, 50] reveal partial intermixing at the interface. Figure 1.6(b) shows HR-TEM images of a RT grown As-terminated Fe/GaAs(001) interface taken along the [110] direction by Fleet *et al.* [11]. The interface appears to be very abrupt and uniform. However, the higher magnification in Figure 1.6(c) shows two distinct structures at the interface: an abrupt structure (structure I) that is observed for the majority of the interface, and a structure where Fe partially intermixes with the As-terminated layer (structure II). Furthermore, Fleet *et al.* [11] find that these partially intermixed regions enhance the minority carrier injection. This emphasizes the importance of the interfacial structure and composition with respect to the efficiency of injecting spins from a ferromagnet into a semiconductor. In this context, the suppression of interdiffusion at the interface seems to be of crucial importance. A decrease of the substrate temperature during

the Fe growth to below 5 °C improves spin injection efficiencies [77]. Furthermore, a study with several Fe/GaAs interfaces, all grown at different temperatures, showed the largest majority spin injection for the lowest growth temperature at –5 °C [78]. Moreover, from DFT calculations of differently terminated Fe/GaAs(001) interfaces it has been concluded that a significant atomic reordering of the interface occurs if temperatures are sufficiently high [79].

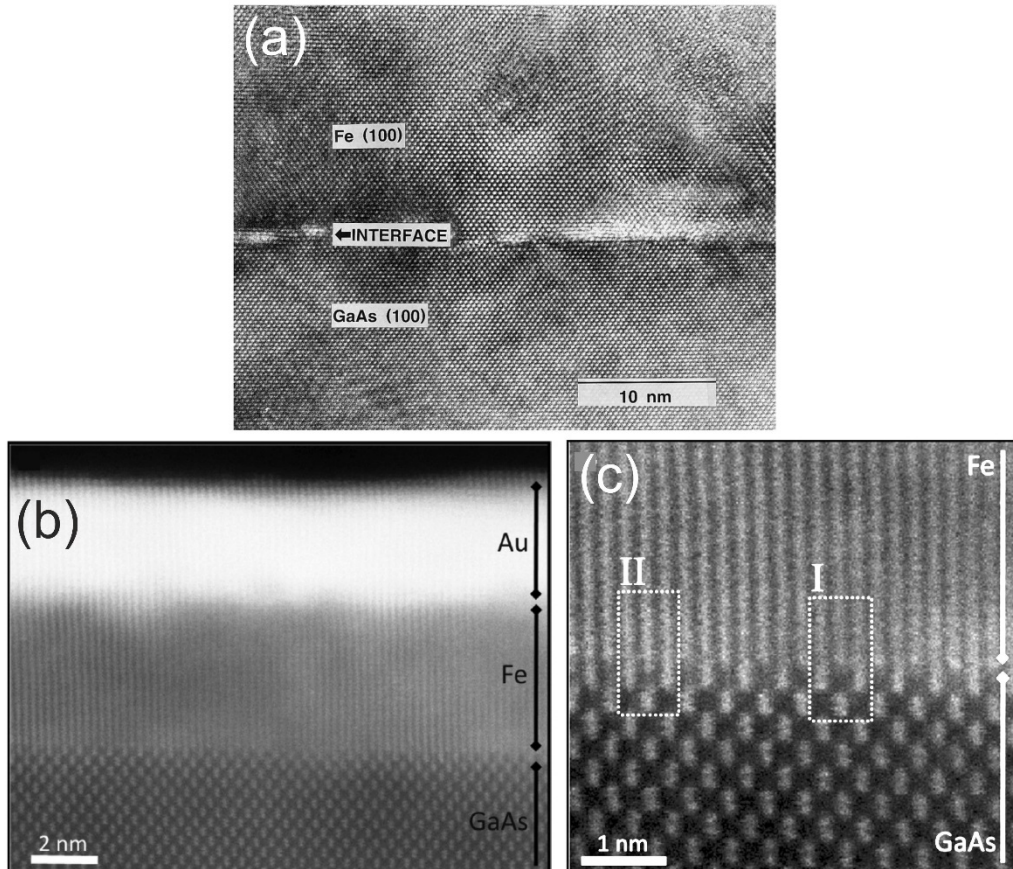


Figure 1.6: (a) High-resolution transmission electron microscopy (HR-TEM) image of a RT grown Fe/GaAs(110) interface [49]. (b)+(c) High-resolution TEM images of a RT grown As-terminated Fe/GaAs(001) interface taken along [110]. Most of the interface is grown abrupt (structure I). Some regions along the interface exhibit a partially intermixed structure (structure II) [11].

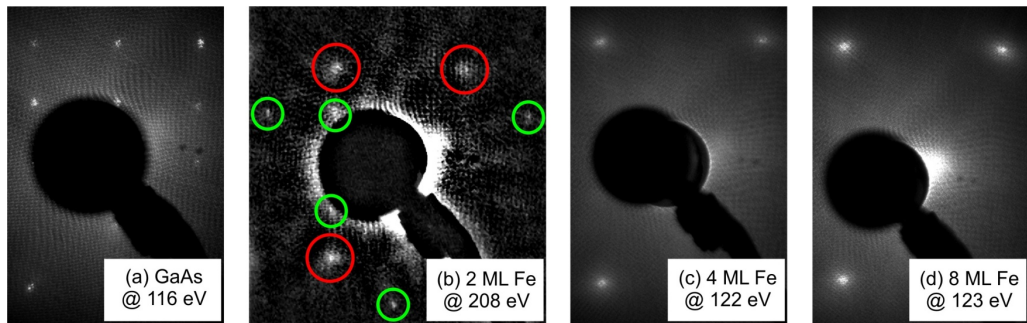


Figure 1.7: (a) LEED pattern of the GaAs(110) substrate. (b–d) LEED pattern for LT grown Fe films with a thickness of (b) 2 ML, (c) 4 ML, and (d) 8 ML. For 2 ML thick Fe films LEED patterns characteristic of GaAs(110) (green circles) and Fe bcc (red circles) are observed simultaneously [46, 47].

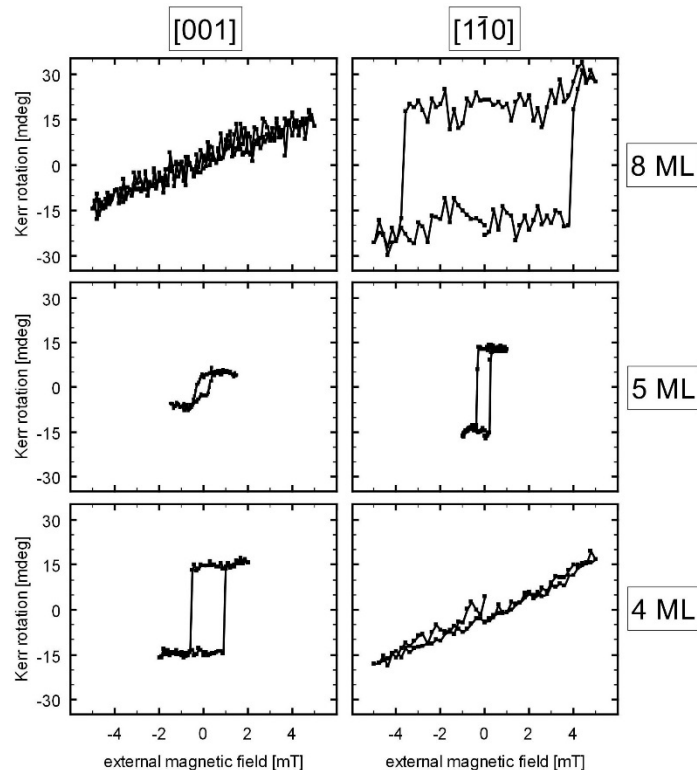


Figure 1.8: *In situ* MOKE measurements of the thickness dependent in-plane spin reorientation transition at an Fe film thickness of 4–5 ML [52].

In order to further reduce intermixing at the Fe/n-GaAs(110) interface, Winking *et al.* [46, 47] introduced a two-step low-temperature (LT) preparation process where the Fe film is grown at a substrate temperature of  $\sim 130$  K followed by an annealing to RT. This LT preparation technique is also applied in this thesis and described in detail in section 2.3. Figure 1.7 shows LEED measurements of LT grown 2 ML Fe on GaAs(110) that simultaneously exhibit diffraction spots characteristic of the GaAs(110) surface and the bcc Fe lattice [46, 47]. This behavior has not been reported for RT grown films [65, 66].

Winking *et al.* attribute this observation to the epitaxial growth of two-dimensional (2D) thin films in combination with an abrupt nonreacted interface [46, 47]. The layer-by-layer film growth is confirmed by additional top-view STM topographies [46, 47]. The onset of ferromagnetism of these LT grown interfaces is observed at a Fe film thickness of  $\sim 2$  ML [52] (see also chapter 7). These thin films show an in-plane magnetic anisotropy with an easy axis parallel to the  $<001>$  direction [46, 47, 52]. Figure 1.8 shows that spin reorientation transition at a film thickness of 4—5 ML is observed with the easy axis turning into the in-plane  $<110>$  direction for thicker films [46, 47, 52].

Furthermore, Winking conducted a scanning tunneling microscopy and spectroscopy study of a LT grown Fe/*n*-GaAs(110) interface in cross-sectional geometry [47] where he did not find any sign of intermixing or compound formation at the interface.

The experimental findings of an abrupt, epitaxial, flat, and non-intermixed LT grown Fe/GaAs(110) interface are supported by density functional calculations by Grünebohm *et al.* [80]. They investigated the initial growth of Fe on GaAs(110) by simulating the effect of different Fe flux rates:

A high growth rate is simulated by 1 ML Fe as depicted in Figure 1.9(c). In this case the relaxation of the GaAs(110) surface (as observed for the free surface in Figure 1.9(a)) vanishes and no penetration of Fe atoms into the GaAs surface takes place. Adding a second layer of Fe yields a nearly flat interface with a bcc like Fe film structure as shown in Figure 1.9(d). Therefore, sufficiently high deposition rates and low substrate temperatures seem to suppress any intermixing at the interface. Furthermore, the DFT calculations for the flat interface do not indicate any quenching or significant decrease of the magnetic moments of the Fe [80]. The calculated magnetic moments for the ideal interface amount to  $2.4 \mu_B$  [80].

Grünebohm *et al.* also simulated a moderate flux rate by “depositing” single Fe atoms on the surface which they assume to be the case for a Fe film coverage of 1/4 ML. Figure 1.9(b) shows that for low coverages a penetration of the Fe atoms into the GaAs surface lowers the energy of the Fe/GaAs(110) system [80]. This is in accordance with the finding by Ruckman *et al.* [68] that free Fe atoms at the GaAs surface promote the disruption of the substrate. Grünebohm *et al.* explain this behavior with the large hybridization between Fe *d*- and As *p*-orbitals which gives rise to a much stronger As-Fe bond compared to the Ga-Fe bond. Therefore, breaking the topmost Ga-As bond and replacing the Ga atom by a Fe atom lowers the energy of the system leading to a Ga adatom bonded to the surface [80] (see Figure 1.9(b)).

In conclusion, the DFT calculations suggest the growth of abrupt and non-intermixed interfaces at higher flux rates whereas an increased amount of intermixing is expected for lower flux rates.

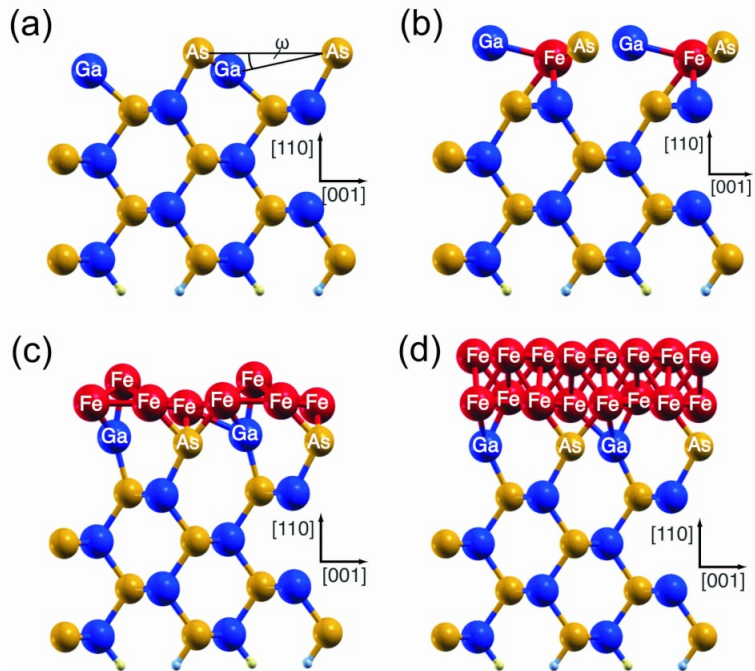


Figure 1.9: Density functional calculations of the Fe/GaAs(110) interface. (a) Side view of the relaxed free GaAs(110) surface. (b–d) Side view of the relaxed interface for Fe film coverages of (b) 1/4 ML, (c) 1 ML, and (d) 2 ML [80].



## 2 Experimental Techniques

This chapter gives a brief overview of the experimental techniques applied in this thesis. Section 2.1 briefly discusses the theoretical background of the scanning tunneling microscope and the experimental setup used in this thesis. Section 2.2 introduces the reader to the theory of the magneto-optic Kerr effect (MOKE) and the *in situ* MOKE setup. Finally, section 2.3 gives a short description of the low-temperature preparation process used in this thesis.

### 2.1 Scanning Tunneling Microscopy

The experimental technique of scanning tunneling microscopy (STM) belongs to an entire family of scanning probe techniques that all underly the same concept originally developed by Gerd Binnig and Heinrich Rohrer in 1981 [81]. In order to investigate a surface, a sharp probe is approached to this surface until a local and strongly distance-dependent interaction is obtained. This interaction is measured and used to control the distance between the probe and the sample surface. The probe is scanned across the surface and by means of a control loop the interaction between probe and sample surface is kept at a constant value. The relative height  $z$  of the probe is recorded (together with other quantities) as a function of the lateral coordinates  $x, y$ .

In the case of the STM a bias voltage is applied between a sharp metal tip and a conductive sample. If tip and sample are brought into close proximity, the wave functions of tip and sample will overlap and a tunnel current  $I_T$  will flow through the vacuum barrier between tip and sample surface. This tunnel current then serves as the distance-dependent interaction. To obtain tunnel currents of 10 to several 100 pA the tip-sample distance is typically set to 7–9 Å [82, 83]. The exponential decrease of the local density of states into the vacuum barrier is the reason why also the tunnel current depends exponentially on the distance between tip and sample. This exponential dependence together with the

small lateral extension of the wave functions allows a very high spatial resolution (for some tip-sample systems even an atomic resolution).

In the following subsections a very brief introduction to the concept of the tunnel current, the different measuring modes applied in this thesis, and the experimental technique of cross-sectional scanning tunneling microscopy (STM) will be given. For a more detailed description of theoretical and experimental aspects in STM the reader is referred to Refs. [84-86].

### 2.1.1 The Tunnel Current

The model of tunneling transport in STM is based on the theoretical description of a macroscopic planar tunneling contact which was developed by Bardeen in 1961 [87]. In 1983, this model was extended by Tersoff and Hamann in order to take into account the geometry of the probe tip in STM experiments [88, 89]. They assumed that the tip can be approximated as a spherically symmetric s wave function. Furthermore, they only considered small sample bias voltages  $V_s \leq 10$  mV at low temperatures so that only states near the Fermi energy of the sample  $E_F^S$  can contribute to the tunneling process. Like that they obtained the following expression for the tunnel current:

$$I_T \propto eV_s D_t(E_F^t) \cdot LDOS(\vec{r}_t, E_F^S) \quad (2.1)$$

Here  $D_t(E)$  represents the density of states of the probe tip at the energy  $E$  and  $E_F^t$  is the Fermi energy of the probe tip.  $LDOS(\vec{r}_t, E_F^S)$  is the *local density of states* (LDOS) of the sample at the Fermi energy and at the tip position  $\vec{r}_t = (x, y, z = d)$ . Here  $\vec{r}_t$  is given by the center of the s wave function at the lateral position  $(x, y)$  and the vertical position  $z$  given by the tunnel distance  $d$ . The LDOS is defined as the sum over the square moduli of the sample wave functions for a given energy  $E$ :

$$LDOS(\vec{r}, E) := \sum_v |\psi_v(\vec{r})|^2 \delta(E_v - E) \quad (2.2)$$

It is important to note that expression (2.1) exhibits a direct proportionality between tunnel current and the LDOS of the sample.

The assumption of small bias voltages ( $V_s \leq 10$  mV) within the Tersoff-Hamann model is normally fulfilled for STM studies on metals. However, if other sample systems such as semiconductors are investigated, bias voltages in the range of  $|V_s| \approx 1 \dots 3$  V are applied between tip and sample. The dependence of the tunnel probability on the energetic position of different states in such a high bias voltage range cannot be neglected anymore. Therefore, Hamers *et al.* have extended the Tersoff-Hamann model by introducing an energy-dependent transmission coefficient  $T(E, eV_s, d)$  [90]:

$$I_T \propto \int_{E_F}^{E_F + eV_s} D_t(E - eV_s) \cdot LDOS(r_t, z = 0, E) \cdot T(E, eV_s, d) dE \quad (2.3)$$

Here  $r_t$  describes the lateral position ( $x, y$ ) of the tip at the sample surface located at  $z = 0$ . The transmission coefficient is obtained by a Wentzel-Kramers-Brillouin approximation:

$$T(E, eV_s, d) = \exp\left(-\frac{2d}{\hbar} \sqrt{2m_0 \left(\frac{\Phi_T + \Phi_S}{2}\right) + \frac{eV_s}{2} - E}\right) \quad (2.4)$$

where  $d$  again is the distance between tip and sample,  $\hbar$  is the reduced Planck constant,  $m_0$  is the electron mass,  $\Phi_T$  and  $\Phi_S$  are the work functions of tip and sample, respectively, and  $E$  is the energy of the electron. The transmission coefficient also takes into consideration the voltage-dependent barrier shape. Furthermore, it can be seen in equation (2.4) that due to the transmission coefficient, in the Hamers model, states at higher energies contribute stronger to the tunnel current.

## 2.1.2 Measuring Modes

### 2.1.2.1 Constant Current Topography

The constant current mode is the most widely applied measuring mode in STM (see, e.g., Ref. [84]). Between tip and sample a bias voltage is applied. In the STM experiments conducted throughout this thesis the potential of the tip is defined as  $V_T = 0$  V. The bias voltage  $V_s$  is applied to the sample. For small tip-sample distances a tunnel current flows between tip and sample. Via an electronic control circuit the  $z$  position of the tip, which is attached to a piezoelectric crystal, is adjusted to a constant tunnel current  $I_T$ . In this way the tip scans the sample in a line-by-line fashion: first the tip scans along a line in positive  $x$  direction (also called “trace”) and then back along the same line in negative  $x$  direction (also called “retrace”). Subsequently, the tip is adjusted to the next  $y$  value and scans along the next line in  $x$  direction. During the scan motion the  $z$  signal of the control circuit is read out at discrete  $(x, y)$  points (pixels) and plotted color-coded against the lateral position. In the following, the obtained  $z(x, y)$  maps will be referred to as “topographies”. If one looks at expression (2.3), it becomes clear that for  $I_T = \text{const.}$  a topography does not correspond to the actual structure of the surface. Rather, a topography maps the surface of constant integral density of states between  $E_F$  and  $E_F + eV_s$  being a superposition of the surface structure and the electronic contrast of the sample surface.

In general, the electronic contrast depends on the sample bias voltage. A comparison of topographies taken at different sample bias voltages  $V_s$  can yield information on the energy dependence of the integral LDOS. To ensure a comparability between topographies taken at different bias voltages and to avoid lateral thermal drift the topographies are tak-

en quasi-simultaneously. This can be achieved by mapping the same scan line in  $x$  direction (trace and retrace), first, at the bias voltage  $V_{s,1}$ , then at the bias voltage  $V_{s,2}$ , and so on, before moving to the next  $y$  value. Like that the temporal delay between the different topographies is given by the time that is necessary to map one scan line in  $x$  direction (trace and retrace). This also minimizes the thermal drift between the different topographies. This measuring mode is also called “multi-bias” mode.

### 2.1.2.2 Scanning Tunneling Spectroscopy

The measuring mode of scanning tunneling spectroscopy (STS) yields locally and energetically resolved information on the LDOS of the sample. In general, it can be said that the tunnel current  $I_T(x, y, z, V_s)$  depends on the space coordinates  $(x, y, z)$  and the sample bias voltage  $V_s$ . In analogy to the constant current mode, in the STS mode the distance between tip and sample  $z = d$  at the lateral position  $(x, y)$  is adjusted by defining a set-point bias voltage  $V_{s,1}$  and a setpoint tunnel current  $I_{sp}$ . Subsequently, the feedback loop is switched off and the  $z$  position of the tip is kept constant like that. At this constant tip-sample distance the tunnel current is measured in dependence of the sample bias voltage  $V_s$  inside a given voltage range  $V_{s,1} \dots V_{s,2}$ . This results in a data set  $I_T(x, y, V_s)$  with a measured value for the tunnel current  $I_T$  at each topographic pixel  $(x, y)$  and each discrete voltage value between  $V_{s,1} \dots V_{s,2}$ . More details on scanning tunneling spectroscopy can be found, e.g., in Ref. [84].

### 2.1.2.3 Apparent Barrier Height

For a meaningful analysis of the STS data, the spectroscopic data needs to be normalized to a constant tip-sample distance. This so-called *topography normalization* is necessary because the tip-sample distance for a STS measurement is defined by the setpoint values and therefore locally varies corresponding to the electronic contrast at the surface (for more details see also section 3.2.2.1). The local apparent barrier height  $\Phi_{abh}(x, y)$  is an important quantity regarding the normalization.  $\Phi_{abh}(x, y)$  is obtained by measuring the tunnel current while the tip-sample distance is modulated (see, e.g., Ref. [84]). From the resulting data  $\Phi_{abh}(x, y)$  can be calculated according to the following expression:

$$\Phi_{abh}(x, y)|_{V_s=\text{const}} = \frac{\hbar^2}{8m_0} \left( \frac{d \ln(I_T(x, y, z))}{dz} \right)^2 \quad (2.5)$$

## 2.1.3 Experimental Setup and Tip Preparation

For all STM measurements presented in this thesis, home-built STMs are used. One STM operates at room temperature (RT) only. The other STM is coupled to a liquid helium

bath cryostat so that it can operate at a temperature of  $\sim 6$  K. The scanning unit is based on the *beetle*-type design by Besocke [91] and was adapted to the experimental requirements as described in Ref. [92]. More details on the experimental setup can be found in Refs. [92-95].

The STM tips are prepared using a polycrystalline tungsten wire which is, first, electro-chemically etched in KOH base, and subsequently, cleaned in demineralized water and ethanol. The further tip preparation takes place under ultrahigh vacuum (UHV) conditions, where the tips are annealed by resistive heating in order to remove oxide and dirt layers from the surface. Subsequently, the tips are sputtered with Argon ions. Finally, the tips are characterized by bringing them in front of a metal plate and recording a field-emission current-voltage curve. More details on the tip preparation can be found in [96, 97].

## 2.2 Magneto-Optic Kerr Effect

### 2.2.1 Theoretical Background

The magneto-optic Kerr effect (MOKE) describes the rotation of the polarization plane of an electromagnetic wave when reflected off a ferromagnetic sample. The rotation angle is proportional to the magnetization of the sample. This effect was discovered and empirically described for the first time by John Kerr in 1877.

Microscopically, the MOKE in ferromagnets can be explained by the concurrence of the exchange interaction and the spin-orbit interaction. For a detailed description of the quantummechanical approach to explain magneto-optic effects the reader is referred to Refs. [98-100].

A qualitative explanation can also be given by Lorentz' model of electrons elastically coupled to the atomic cores (see also Ref. [101]). Here the electric field of an incident light wave  $\vec{E}_i$  stimulates a harmonic oscillation of the electron. Let us consider the specific case of the polar Kerr geometry as shown in Figure 2.1(a). Here the magnetization of the sample is oriented perpendicular to the surface and the impinging light is parallelly (p) polarized inside the plane-of-incidence. This linearly polarized light induces an oscillation of the electrons in the same direction of polarization. Without magnetization the light would be reflected with the same polarization indicated by the light blue arrow and denoted by  $\vec{E}_r$ . However, an additional magnetization comes along with the Lorentz force that induces a small oscillating component perpendicular to the primary motion given by the electric field of the incident light and perpendicular to the direction of magnetization. Therefore, the oscillating motion is proportional to  $\vec{v}_L \propto \vec{E}_i \times \vec{M}$  (right-hand rule, see green arrow). According to Huygen's principle (see, e.g., Ref. [102]) this secondary motion is starting point of the Kerr amplitude  $\vec{E}_K$  (little red arrow). The superposition of the primary and secondary motion yields magnetization-dependent polarization rotations.

The same line of argument can be applied to the longitudinal MOKE geometry shown in Figure 2.1(b) for p polarized light. Here the magnetization is oriented parallel to the sample surface and parallel to the plane of incidence. The direction of polarization rotation follows from the right-hand rule again.

Figure 2.1(c) shows the case of the transverse MOKE geometry. Here the right-hand rule yields a Lorentz force pointing along the direction of light propagation for p polarized light. Therefore, no Kerr rotation is observed in the transverse geometry. For p polarized light a change in intensity of the reflected wave is observed.

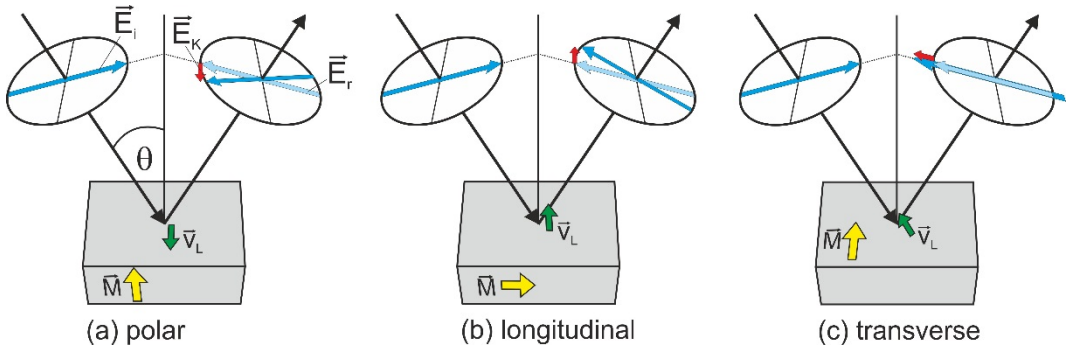


Figure 2.1: The different experimental magneto-optic geometries illustrating the effect of polarization and magnetization direction on the Kerr rotation. Figure inspired by Ref. [101].

### 2.2.1.1 Phenomenological Approach

The following considerations presented in this subsection are based on Refs. [103-105]. The dielectric tensor  $\underline{\epsilon}$  of an optically isotropic non-magnetic material has diagonal elements with the value of the dielectric permeability  $\epsilon$  of the material whereas the non-diagonal elements are zero. In contrast, the dielectric tensor of a magnetic material is not symmetric and in the case of a ferromagnetic material the Onsager relation  $\epsilon_{ij}(-\vec{M}) = \epsilon_{ji}(\vec{M})$  applies. In this case the dielectric tensor can be written as:

$$\underline{\epsilon} = \epsilon \begin{pmatrix} 1 & iQm_z & -iQm_y \\ -iQm_z & 1 & iQm_x \\ iQm_y & -iQm_x & 1 \end{pmatrix} \quad (2.6)$$

Here  $m_{x,y,z}$  denote the components of the unit vector  $\vec{m}$  in the direction of magnetization and  $Q$  is the complex Voigt constant. Here we consider only first-order magneto-optic coefficients. The relation between the electric displacement field  $\vec{D}$  and the electric field  $\vec{E}$  is then given as

$$\vec{D} = \underline{\epsilon} \vec{E} = \epsilon \vec{E} + i\epsilon Q \vec{E} \times \vec{m} \quad (2.7)$$

For a simplistic illustration, in the following derivation we consider solely the polar geometry with the magnetization oriented in  $z$  direction. Furthermore, we assume that the electromagnetic wave impinges perpendicularly to the surface so that the wave vector  $\vec{k}$  is parallel to the  $z$  direction. (A more general approach facilitating the calculation of the Kerr rotation for any arbitrary geometry is presented in the next subsection 2.2.1.2.) Using expression (2.7) for the described polar geometry together with the Maxwell equations yields the eigenvalue problem

$$\varepsilon \begin{pmatrix} 1 & iQ & 0 \\ -iQ & 1 & 0 \\ 0 & 0 & 0 \end{pmatrix} \begin{pmatrix} E_x \\ E_y \\ 0 \end{pmatrix} = N^2 \begin{pmatrix} E_x \\ E_y \\ 0 \end{pmatrix} \quad (2.8)$$

where  $N$  denotes the complex refractive index and is defined by

$$\vec{k} = \frac{\omega}{c} N \vec{e}_k \quad (2.9)$$

Here  $\omega$ ,  $c$ , and  $\vec{e}_k$  are the angular frequency, the speed of light, and the unit vector in the direction of the wave vector  $\vec{k}$ , respectively.

The eigenvalues of expression (2.8) are the roots of the characteristic polynomial:

$$(N^2 - \varepsilon)^2 + (i\varepsilon Q)^2 = 0 \quad \Rightarrow \quad N_{\pm}^2 = \varepsilon(1 \pm Q). \quad (2.10)$$

The corresponding eigenvectors can be expressed as

$$\vec{E}_{\pm} = E_0 \vec{e}_{\mp} e^{i(\frac{\omega}{c} N_{\pm} z - \omega t)} \quad \text{with} \quad \vec{e}_{\pm} = \frac{1}{\sqrt{2}} \begin{pmatrix} 1 \\ \pm i \\ 0 \end{pmatrix}, \quad (2.11)$$

where  $\vec{e}_{+,-}$  and  $N_{+,-}$  represent the unit vectors and complex refractive indices of left and right circularly polarized light waves. The superposition of a left and right circularly polarized light wave with the same amplitude results in a linearly polarized light wave. The left and right circularly polarized waves pass through a magnetized material with slightly different velocities given by the different refractive indices. After transmitting a distance  $l$  through the magnetized material (Faraday effect) the two waves have a phase difference of  $\Delta\varphi$  and therefore the linearly polarization exhibits a Faraday rotation of

$$\Phi_F = \frac{1}{2} \Delta\varphi = \frac{\omega l}{2c} (N_+ - N_-) \approx \frac{\omega l}{2c} \sqrt{\varepsilon} Q \quad (2.12)$$

The expression on the right side of the “approximate equal” sign is obtained by using expression (2.10). The complex Faraday rotation  $\Phi_F$  has a real part and a imaginary part stemming from the real part and the imaginary part of the complex refractive indices  $N_{+,-}$ . The real part of  $\Phi_F$  describes the rotation of the polarization plane whereas the imaginary part represents the ellipticity of the transmitted wave.

In the case of reflection (Kerr effect) the relation between complex refractive indices and the complex Kerr rotation angle is obtained by using the Fresnel equations. These equations yield the reflection coefficients  $r$  describing the ratio of the amplitudes of the reflected and the incident waves (see, e.g., [102]). If we assume that the light propagates perpendicularly to the surface, the reflection coefficients of the two circularly polarized waves are given by

$$r_{\pm} = \frac{N_{\pm} - 1}{N_{\pm} + 1} \quad (2.13)$$

If we assume that the incident wave is linearly polarized parallel to the  $x$  direction,  $\vec{E}_i = (E_x, 0, 0)$ , the reflected wave will have a component in  $x$  direction and an additional component in  $y$  direction due to the magnetization:  $\vec{E}_r = (r_x E_x, r_y E_x, 0)$ . The quantities  $r_x$  and  $r_y$  are the reflection coefficients in  $x$  and  $y$  direction. Using the Jones calculus [106, 107] they can be expressed by the reflectivities in the circularly polarized basis:  $r_x = (r_+ + r_-)/\sqrt{2}$  and  $r_y = (-ir_+ + ir_-)/\sqrt{2}$ . The complex Kerr rotation is defined as

$$\Phi_K = \varphi_K + i\eta_K \stackrel{\text{def}}{=} -\frac{r_x E_x}{r_y E_x} \quad (2.14)$$

From that it follows

$$\Phi_K = i \frac{r_+ - r_-}{r_+ + r_-} = i \frac{N_+ - N_-}{N_+ N_- - 1} \approx i \frac{\sqrt{\varepsilon} Q}{\varepsilon - 1}. \quad (2.15)$$

The approximate equality is obtained by using expression (2.10). Second order terms in  $Q$  are neglected because  $|Q| \ll 1$ . A quantum-mechanical treatment shows that the non-diagonal elements of the conductivity tensor  $\underline{\underline{\sigma}}$ , which is directly proportional to the dielectrical material tensor  $\underline{\underline{\epsilon}}$ , are proportional to the spin polarization and therefore also to the magnetization [108]. Looking at expression (2.15), this means that the Kerr rotation is also proportional to the magnetization.

### 2.2.1.2 General Approach to Magneto-Optics

In this subsection a formalism is presented that enables the calculation of the Kerr rotation for magnetic single layer or multilayer systems with arbitrary orientation of the magnetization in each layer. This formalism is based on Fresnel's equations and was developed in its entirety by Zak *et al.* [109-111]. In the following, a brief summary of this formalism will be given.

Let us assume a boundary between two media in the  $x$ - $y$  plane. The tangential components of the electric  $E_x$ ,  $E_y$  and the magnetic  $H_x$ ,  $H_y$  fields of an electromagnetic wave travelling from medium 1 into medium 2 are conserved. By defining the magneto-optic coefficients these fields can also be expressed using a set of the electric fields of the incident (i) and reflected (r) waves for s and p polarization:  $E_s^{(i)}$ ,  $E_p^{(i)}$ ,  $E_s^{(r)}$ , and  $E_p^{(r)}$ . Here s

and  $p$  denote the perpendicular and the parallel components of the electric field with respect to the plane of incidence. One can define a matrix  $\underline{\underline{A}}$  connecting the two different sets of fields

$$\vec{F} = \begin{pmatrix} E_x \\ E_y \\ H_x \\ H_y \end{pmatrix} = \underline{\underline{A}} \vec{P} = \underline{\underline{A}} \begin{pmatrix} E_s^{(i)} \\ E_p^{(i)} \\ E_s^{(r)} \\ E_p^{(r)} \end{pmatrix} \quad (2.16)$$

$\underline{\underline{A}}$  is also denoted as the *medium boundary matrix*. The elements of this  $4 \times 4$  matrix are composed of the complex refractive index  $N$  and the complex Voigt constant  $Q$  describing the electromagnetic properties of the medium and also contain geometrical angles describing the orientation of the magnetization of the sample. The exact form of the matrix is given in Refs. [109-111]. The boundary between two media can be matched by the condition

$$\underline{\underline{A}}_1 \vec{P}_1 = \underline{\underline{A}}_2 \vec{P}_2. \quad (2.17)$$

In the case of more than two media – which is generally the case for a thin film system (vacuum, magnetic film, substrate) – the wave propagates through the medium between two boundaries. The *medium propagation matrix*  $\underline{\underline{D}}$  describes the wave propagation inside the  $n$ th medium at the depth  $z$  from the boundary and is defined by the following condition

$$\underline{\underline{D}}_n \vec{P}_n(z) = \vec{P}_n(z=0) \quad (2.18)$$

Applying the propagation matrix to the field matrix  $\vec{P}_n(z)$  at the position  $z$  inside the  $n$ th medium yields the field  $\vec{P}_n(z=0)$  at position zero (at the boundary between the two media) of the  $n$ th medium. Considering the general case of a multilayer system one can write

$$\underline{\underline{A}}_i \vec{P}_i = \prod_{n=1}^m \left( \underline{\underline{A}}_n \underline{\underline{D}}_n \underline{\underline{A}}_n^{-1} \right) \underline{\underline{A}}_f \vec{P}_f, \quad (2.19)$$

where  $i$  and  $f$  denote the initial and final medium, respectively. Equation (2.19) can also be written as

$$\vec{P}_i = \underline{\underline{M}} \vec{P}_f, \quad (2.20)$$

with the matrix

$$\underline{\underline{M}} = \underline{\underline{A}}_i^{-1} \prod_{n=1}^m \left( \underline{\underline{A}}_n \underline{\underline{D}}_n \underline{\underline{A}}_n^{-1} \right) \underline{\underline{A}}_f = \begin{pmatrix} \underline{\underline{G}} & \underline{\underline{H}} \\ \underline{\underline{I}} & \underline{\underline{J}} \end{pmatrix}. \quad (2.21)$$

The Fresnel transmission and reflection coefficients are obtained from the  $2 \times 2$  matrices in the following way:

$$\underline{\underline{G}}^{-1} = \begin{pmatrix} t_{ss} & t_{sp} \\ t_{ps} & t_{pp} \end{pmatrix} \quad \wedge \quad \underline{\underline{IG}}^{-1} = \begin{pmatrix} r_{ss} & r_{sp} \\ r_{ps} & r_{pp} \end{pmatrix}. \quad (2.22)$$

The complex Kerr rotations for s and p polarized light are then given by

$$\Phi_{K,s} = \varphi_{K,s} + i\eta_{K,s} = \frac{r_{ps}}{r_{ss}} \quad \wedge \quad \Phi_{K,p} = \varphi_{K,p} + i\eta_{K,p} = \frac{r_{sp}}{r_{pp}}. \quad (2.23)$$

The formalism presented here is applied in chapter 7 to analyze MOKE data. In all calculations conducted the complex refractive indices  $N$  for a laser wavelength of  $\lambda = 632.8$  nm and the complex Voigt constant  $Q$  for Fe from Refs. [109, 112] are used:

$$\text{GaAs:} \quad N = 3.856 + i \cdot 0.196$$

$$\text{Fe:} \quad N = 2.87 + i \cdot 3.36 \quad Q = 0.0376 + i \cdot 0.0066$$

## 2.2.2 Experimental Setup

For the *in situ* MOKE investigation of ultrathin Fe films on GaAs{110} a homebuilt polarization-modulated ellipsometer (PME) is used in this thesis. The ellipsometer is combined with a homebuilt ultrahigh vacuum chamber that contains the investigated sample and 4 coiled magnetic poles for external field application (see Figure 2.2). This *in situ* 4-magnetic-pole setup based on a similar setup presented by Qiu *et al.* [113] was developed in the Master's thesis of A. Grimsel [114]. The 4 magnetic pole shoes, which are arranged in a plane parallel to the sample surface, consist of soft iron and are each coiled with a separate copper wire so that each pole can be addressed separately. This allows the application of an external magnetic field to the sample in any arbitrary direction. Due to the implementation of high-current power supplies in the framework of S. Weikert's Bachelor's thesis [115] in-plane fields of up to 130 mT and out-of-plane fields (all 4 magnetic poles have the same sign) of about 18 mT can be achieved with this setup. More details on the *in situ* 4-magnetic-pole setup can be found in Refs. [114, 115].

The setup allows an in-plane rotation of the sample by  $360^\circ$ . The arrangement of the windows of the UHV chamber permits the two angles of incidence of  $\theta = 15^\circ$  and  $\theta = 67^\circ$  for the optical path (for definition see also Figure 7.2 in chapter 7).

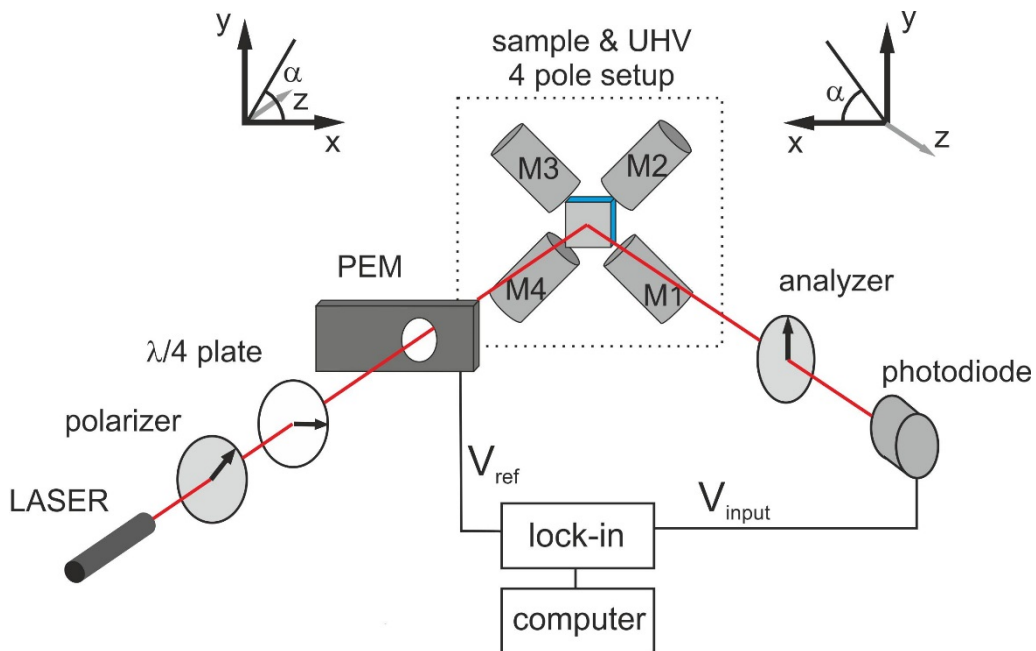


Figure 2.2: The MOKE setup consisting of the optical path of the polarization-modulated ellipsometer with a photoelastic modulator (PEM) and the *in situ* 4-magnetic-pole setup (encircled by the dotted black line) with the 4 magnetic poles M1—M4. Adapted from Ref. [116].

The working principle of the polarization-modulated ellipsometer used in this experimental setup is described in the textbook by Azzam [106] and was introduced by Jasperson *et al.* [117, 118]. The optical path of the setup is illustrated in Figure 2.2 and starts with the laser. Most of the measurements in this thesis are conducted with a linearly polarized HeNe laser with a wavelength of  $\lambda_{\text{HeNe}} = 632.8 \text{ nm}$ .<sup>6</sup> The laser light then passes through a linear polarizer (extinction ratio better than 1:  $10^4$ ) set to an angle of  $\alpha_p = 45^\circ$  (angles along the optical path are specified with respect to the horizontal  $x$  axis as defined in Figure 2.2). Subsequently, the linearly polarized light propagates through a  $\lambda/4$  compensator (waveplate) set to an angle of  $\alpha_{\lambda/4} = 0^\circ$  so that the laser light is transformed into a circularly polarized wave. Afterwards, this wave propagates through the photoelastic modulator (PEM) [117] shifting the  $x$  component alternating by  $\pm\pi/2$  with respect to the  $y$  component of the wave at a modulation frequency of  $\omega_M = 2\pi/T = 50 \text{ kHz}$ . This means that at  $t = 0$  and at  $t = T/2$  the circularly wave passed through the PEM unaltered and at  $t = T/4$  and at  $t = 3T/4$  the light leaves the PEM with a linear polarization at an angle of  $\alpha = 45^\circ$  and  $\alpha = 135^\circ$ , respectively. This modulated light wave then impinges onto the sample and is reflected off its surface. Subsequently, the wave reaches the analyzer (extinction ratio better than 1:  $10^4$ ) that solely lets pass the wave component in  $y$  direction perpendicular to the plane of incidence. If the sample is

<sup>6</sup> Also other laser wavelengths can be chosen. In that case the polarizers and compensators have to be selected accordingly.

magnetized, the linearly polarized waves will be rotated by the Kerr angle  $\varphi_K$ . This yields two slightly different amplitudes  $\sin(45^\circ + \varphi_K)$  and  $\sin(135^\circ + \varphi_K)$  passing through the analyzer for the two orthogonal linearly polarized light waves separated by  $t = T/2$ . Eventually, this leads to a 50 kHz modulation of the light intensity that is detected by the photodiode and fed into the lock-in amplifier where it is multiplied by the reference signal of  $\omega_M = 50$  kHz from the PEM. The time-dependent product is integrated over a defined time which yields the output signal that is directly proportional to the Kerr rotation  $\varphi_K$ . A detailed derivation of the detected intensity  $I_D$  is given in [52, 116] and yields the proportionality

$$I_D \propto (\alpha_A - \varphi_K) J_1(\delta_{max}) \sin(\omega_M t) + \eta_K J_2(\delta_{max}) \cos(2\omega_M t). \quad (2.24)$$

Here  $\delta_{max}$  is the maximum phase shift the PEM is adjusted to,  $\alpha_A$  presents the angle the analyzer is set to, and  $J_1(x)$  and  $J_2(x)$  represent the first and second Bessel function [119], respectively. Expression (2.24) shows that if the reference frequency from the PEM, which is fed into the lock-in, is set to the first harmonic of  $\omega_M$ , the output of the lock-in is proportional to the Kerr rotation. In this case one should choose  $\delta_{max} = \pi/2$  because there the first Bessel function has a global maximum. Setting the reference frequency to the second harmonic of  $\omega_M$  leads to a proportionality of the lock-in output signal to the Kerr ellipticity  $\eta_K$ . If one wants to measure the Kerr ellipticity the maximum phase shift of the PEM should be set to  $\delta_{max} = \pi$  because there the second Bessel function has a global maximum.

It can be shown [52] that for the experimental arrangement used in this thesis (analyzer solely lets pass the wave component perpendicular to the plane of incidence) the 50 kHz modulation of the light intensity at the detector  $\Delta I_D$  is given by

$$\Delta I_D \propto E_s E_p \varphi_p, \quad (2.25)$$

where  $E_s$  and  $E_p$  are the amplitudes of the electric fields of the s and p polarized light and  $\varphi_p$  is the Kerr rotation of the p polarized light. This means that the MOKE setup described in Figure 2.2 and used in this thesis is primarily sensitive to the Kerr rotation of the p polarized light  $\varphi_p$ . This information is of particular importance for the analysis of the experimental data in chapter 7 by means of the formalism presented in section 2.2.1.2. In chapter 7, the experimental values for the Kerr rotation are given in units of mdeg. These values are obtained by calibrating the lock-in in the following way: the analyzer is rotated around the zero position by  $\pm 2.5^\circ$  in both directions. Then the calibration factor is obtained by dividing  $5^\circ$  by the corresponding detected voltage difference between the two positions of the analyzer.

## 2.3 Low Temperature Sample Preparation Process

The Fe films are grown in a low temperature (LT) two-step growth process introduced by Winking et al. [46, 47]. With this preparation technique samples are prepared in a top view layer system [see inset in Figure 2.3(a)] for MOKE measurements as well as in a cross-sectional geometry [see inset in Figure 2.3(b)] to investigate the interface by scanning tunneling microscopy and spectroscopy. All samples are prepared and measured at a base pressure of  $p < 5 \times 10^{-11}$  mbar without breaking the ultrahigh vacuum (UHV) at any time. In the following, the LT growth process is briefly described.

First of all, the GaAs sample is cooled down to  $\sim 130$  K and then cleaved along one of the natural  $\{110\}$  cleavage planes yielding a well defined substrate<sup>7</sup> [see Figure 2.3]. Subsequently, iron (Fe) is grown epitaxially on the cleaved cold surface using an electron beam evaporator at a growth rate of  $\sim 1$  ML/min. In a next step the sample is annealed to room temperature. For the top view samples the preparation process ends here and the sample can be transferred into the MOKE UHV chamber. The samples for the cross-sectional STM studies require another preparation step: a second cleavage is conducted along the  $\{1\bar{1}0\}$  natural cleavage plane perpendicular to the first one producing a cross-section of the Fe/GaAs(110) interface. Afterwards the sample is transferred into the custom built STM and is investigated<sup>8</sup> at 6K or at room temperature in cross-sectional geometry as depicted in the inset in Figure 2.3(b).

---

<sup>7</sup> In order to obtain well defined GaAs $\{110\}$  cleavage planes, which are essential for the STM measurements in cross-sectional geometry, the thickness of the GaAs samples should not exceed 100  $\mu\text{m}$  [47, 83, 95].

<sup>8</sup> To ensure that electric current to or from the sample can flow during the STM experiment, ohmic contacts between the GaAs sample and the sample holder are necessary. For details see, e.g., Ref. [47, 83, 95].

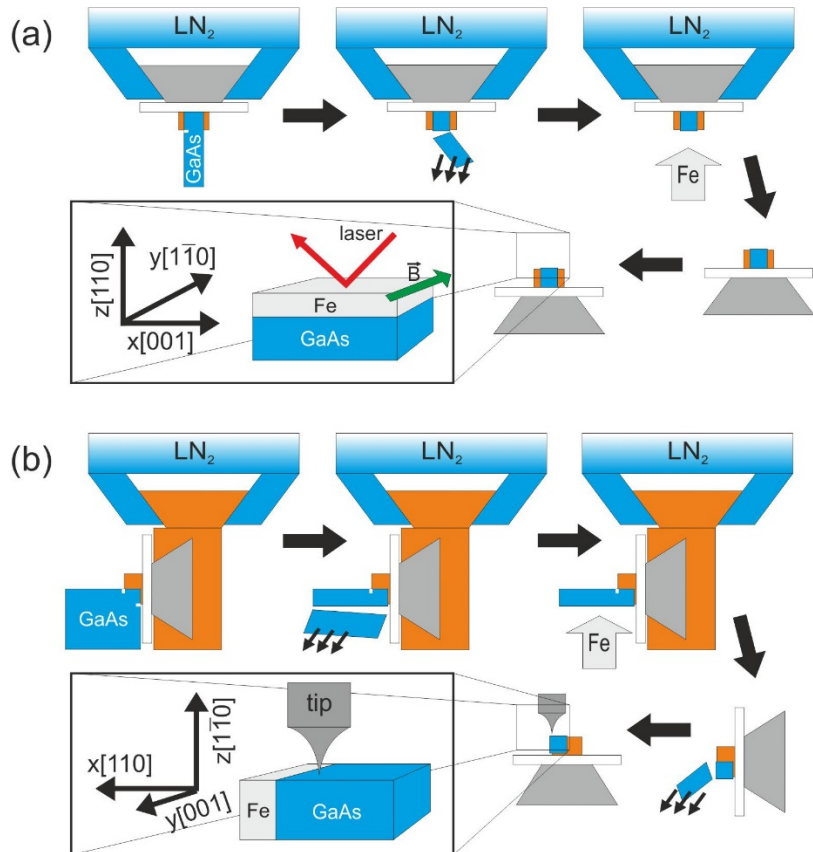


Figure 2.3: Low temperature (LT) growth process for (a) top view samples and (b) for cross-sectional samples [120]. A more detailed description can be found in the continuous text.

### 3 Structural and Electronic Properties of the Ideal Fe/GaAs(110) Interface

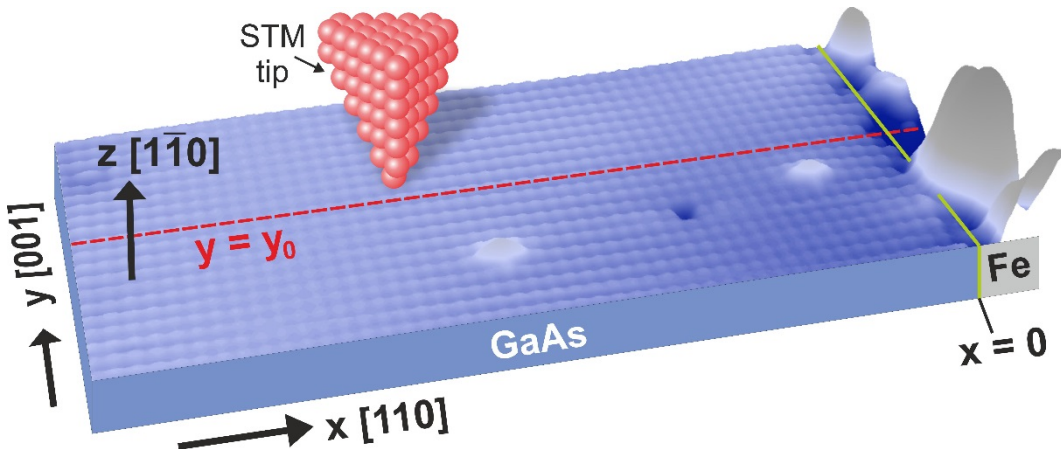


Figure 3.1:  $20 \times 10 \text{ nm}^2$  constant current topography ( $V_{bias} = +2 \text{ V}$ ,  $I_T = 100 \text{ pA}$ ) of an  $n$ -type Fe/GaAs(110) interface in cross-sectional geometry [47, 121]. Data was taken at room temperature. The interface is located at  $x = 0$  indicated by the green solid line.

After preparing the sample as described in section 2.3, the Fe/GaAs(110) interface is investigated by STM and STS in cross-sectional geometry. Figure 3.1 shows a cross-sectional STM image of a low temperature grown Fe/GaAs(110) interface including the coordinate system that will be used throughout this and the next chapters. The solid green line indicates the position of the interface at  $x = 0$ . The GaAs is located on the left hand side of the interface whereas on the right hand side the Fe film can be found. The elevations of the Fe film of a few angstrom in height are due to the ductility of the Fe film during the second cleavage process at room temperature. Furthermore, Figure 3.1 indicates that the second cleavage yields regions along the interface where Fe film and GaAs exhibit a constant apparent height in  $z$  direction. These regions allow direct access to the

atomically flat interface with the STM tip as indicated by the red dashed line at  $y = y_0$ . This allows a detailed structural and electronic investigation of the Fe/GaAs(110) interface.

Winking [47] was the first to investigate a low temperature grown Fe/GaAs(1̄10) interface by means of STM and STS in cross-sectional geometry. He studied the *n*-type Fe/GaAs(1̄10) interface at room temperature. In the following sections this study will be extended to a structural and electronic investigation of the ideal *p*-type Fe/GaAs(110) interface by means of low temperature STM and STS. Parts of section 3.2 have been published in Refs. [120, 121].

## 3.1 Structural Characterization of the Interface

### 3.1.1 STM on the Free GaAs(110) Surface

Before the STM data of the ideal Fe/GaAs(110) interface is discussed in greater detail, the atomic and electronic structure of the free GaAs(110) surface, which serves as a reference in the STM experiments, is described in this subsection. The family of {110} surfaces represents the natural cleavage planes of the GaAs crystal as was already pointed out in section 1.6. The cleavage along the {110} planes yields 2 broken bonds per surface unit cell which are called *dangling bonds* (db). The ideal bulk-like atomic arrangement at the {110} planes is energetically not favorable at the surface. Therefore, the bonding angles in the surface layer are tilted and the surface atoms relax [122]. Figure 3.2 shows the outwards relaxation of the As anions and the inwards relaxation of the Ga cations in the surface layer with respect to the position in bulk (dashed line). This so-called *buckling* is associated with a charge rearrangement where the db states at the As atoms are occupied and the db states at the Ga sites remain unoccupied.

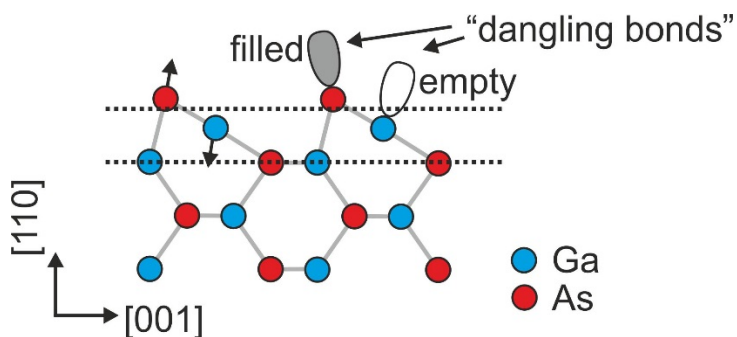


Figure 3.2: Sideview of the GaAs(110) surface with relaxed surface layer. The “dangling bonds” (db) at the As atoms are occupied whereas the db at the Ga atoms are unoccupied. The As atoms relax outwards the surface whereas the Ga atoms relax into the opposite direction.

Chelikowsky and Cohen determined the local density of states (LDOS) at the relaxed GaAs(110) surface by means of a self-consistent pseudopotential calculation [123]. According to the prevailing spatial localization of the surface resonances at either the As anions or the Ga cations they are denoted as A<sub>4</sub>, A<sub>5</sub>, A<sub>6</sub> and C<sub>3</sub>, C<sub>4</sub>, respectively. Figure 3.3(a) depicts the calculated energy dependence of the LDOS at the surface layer (solid line) and for bulk (dashed line). Obviously, the band gap at the GaAs(110) surface does not significantly differ from the corresponding bulk band gap. It is important to note that unlike for the unrelaxed surface where one would expect db states inside the fundamental band gap, the db states of the relaxed surface are energetically shifted and are therefore outside the band gap. The occupied db states at As anions and the empty db states at Ga cations are located inside the valence band and conduction band, respectively.

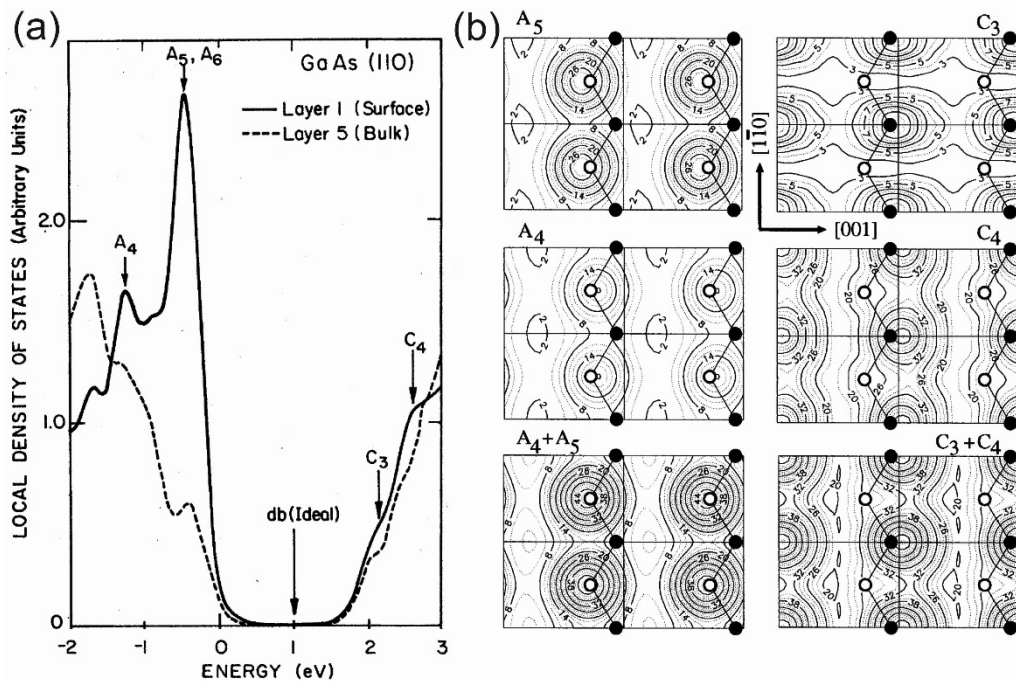


Figure 3.3: (a) Calculated local density of states at the relaxed (110) surface and in bulk for the band gap region of GaAs [123]. A<sub>4</sub>, A<sub>5</sub>, and A<sub>6</sub> denote surface resonances localized at anions whereas C<sub>3</sub> and C<sub>4</sub> denote surface resonances localized at cations. The unrelaxed surface would have dangling-bond (db) surface states located at the position marked by the arrow. (b) Calculated lateral distribution of the integral LDOS at a distance of  $z_0 = 0.36$  nm from the InP(110) surface [124]: The panels show integrals over different energy ranges characteristic for the different states: A<sub>5</sub>: -0.95 to 0 eV, A<sub>4</sub>: -1.77 to -0.95 eV, A<sub>4</sub> + A<sub>5</sub>: -1.77 to 0 eV, C<sub>3</sub>: 0 to 2.27 eV, C<sub>4</sub>: 2.27 to 2.81 eV, C<sub>3</sub> + C<sub>4</sub>: 0 to 2.81 eV. Black and white filled circles represent cations and anions, respectively.

By means of density functional theory (DFT) Ebert *et al.* calculated the spatial distribution of the anionic and cationic resonances for the (110) surface of the III-V semiconductor indium phosphide (InP) [124]. Figure 3.3(b) depicts the integral LDOS at a distance of  $z_0 = 0.36$  nm from the InP(110) surface for different energy ranges. Ebert *et al.* conduct-

ed multi-bias STM measurements on several III-V semiconductor (110) surfaces which exhibited a very good agreement with the calculated lateral distribution of the energy integrated LDOS [124]. According to equation (2.3) the tunnel current between STM tip and sample is proportional to the integral LDOS at the sample surface. Therefore, depending on the applied bias voltage, STM addresses different states at the (110) surface and selectively maps the cation or anion sublattice. Figure 3.3(b) indicates that the atomic corrugation differs for the different surface resonances. In particular, the  $C_3$  resonance exhibits a pronounced corrugation in  $[1\bar{1}0]$  direction whereas the other states exhibit a more pronounced corrugation along the  $[001]$  direction. Vice versa, in an STM constant current topography at a certain bias voltage the observed corrugation can give a first clue about the dominant tunneling channel.

### 3.1.2 Investigation of the Immediate Interface Region

The atomic structure of the interface has a significant impact on the electronic structure and the SB height across the interface as has been already discussed in section 1.5. In this context it is of particular interest to find out more about the homogeneity of the interface, the amount and type of defects at the interface, and how abrupt the interface actually is. A suitable tool to investigate these questions is highly resolved STM in cross-sectional geometry (XSTM) across the immediate interface region [47]. Figure 3.4 shows  $10 \times 10 \text{ nm}^2$  constant current topographies of the immediate interface region of a LT grown *p*-type Fe/GaAs(110) interface taken in the multi-bias mode for positive and negative sample bias voltage.

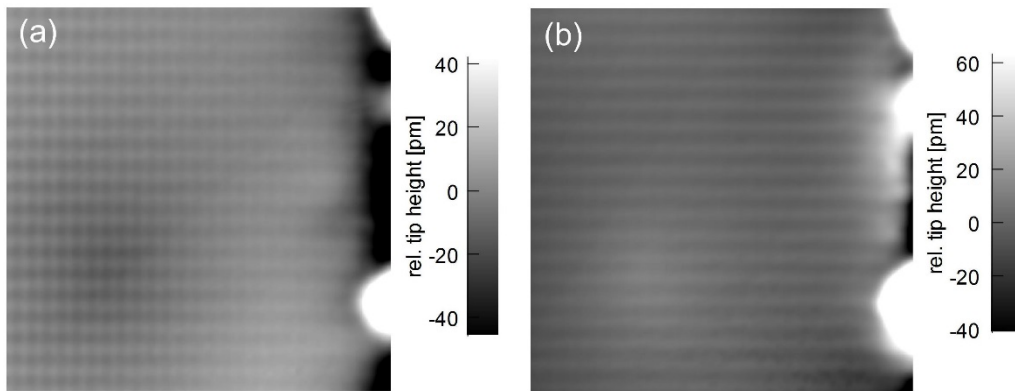


Figure 3.4:  $10 \times 10 \text{ nm}^2$  constant current topographies of the immediate interface region of a low temperature grown *p*-type Fe/GaAs(110) interface (7 ML Fe) for setpoint values of (a)  $V_s = +2.2 \text{ V}$  and  $I_T = 10 \text{ pA}$  and (b)  $V_s = -1.5 \text{ V}$  and  $I_T = 60 \text{ pA}$ .

The topography in Figure 3.4(a) was taken at a sample bias voltage of  $V_s = +2.2 \text{ V}$  and exhibits an atomic corrugation along the  $[110]$  direction (perpendicular to the interface) as well as along the  $[001]$  direction (parallel to the interface). This indicates that electrons

tunnel from the tip into the unoccupied C<sub>3</sub> and C<sub>4</sub> resonances located at the Ga sites (see section 3.1.1). Closer to the interface the atomic corrugation along the [001] direction (parallel to the interface) dominates because the part of the tunnel current into the C<sub>4</sub> resonances increases due to the bending of the energy bands along the space charge region (for more details see appendix A.1). The topography in Figure 3.4(b) was taken at a sample bias voltage of  $V_s = -1.5$  V indicating tunneling from the occupied A<sub>4</sub> and A<sub>5</sub> resonances located at the As sites (see section 3.1.1) into the STM tip. Near the lower left corner of Figure 3.4 (a) and (b) the contrast of a Zn acceptor can be observed as decrease (increase) of relative tip height at positive (negative) sample bias voltage. The sharp elevations at the interface are due to Fe film protrusions caused by the ductility of the Fe film during the second cleavage process at room temperature as has already been mentioned in the beginning of this chapter. It is important to note that in the areas completely free of Fe film protrusions extending up to 5 surface lattice constants in [001] direction (parallel to the interface) the topographies show that both the Ga and the As sublattice build up an atomically flat and abrupt interface. This indicates that the first cleavage process successfully created an ideally planar substrate surface for growing the Fe/GaAs(110) interface. Furthermore, along the interface no signs of interdiffusion or intermixing can be observed. The same was found by Winking [47] who performed room temperature XSTM measurements across the LT grown *n*-type Fe/GaAs(110) interface.

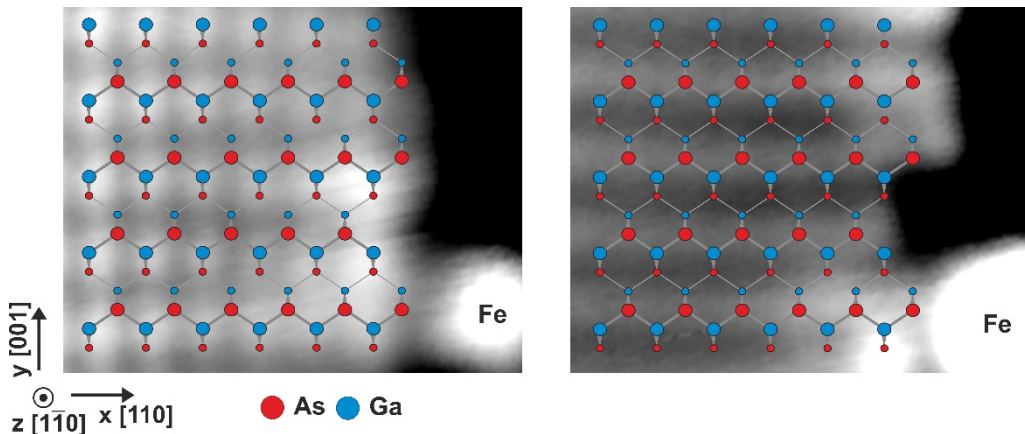


Figure 3.5: Constant current topographies of the LT grown *p*-type Fe/GaAs(110) interface (7 ML Fe) at (left)  $V_s = +1.75$  V,  $I_T = 75$  pA and (right)  $V_s = -1.5$  V,  $I_T = 150$  pA [125]. The superimposed atomic scheme indicates the position of the atoms and the As vacancy at the interface.

However, occasionally As vacancies can be found along the interface as can be seen in the topography on the right hand side of Figure 3.5. Winking [47] already discussed the origin of these sporadic As vacancies at the interface and assumed that the rearrangement of Fe atoms during the second cleavage process due to the ductility of the Fe film at room temperature might generate the formation of defects at the interface. In particular, the strong Fe-As bond [80, 126] would explain why usually As vacancies are the only kind of vacancies observed along the interface. Nevertheless, Siewers [127] studied an *n*-type

GaAs(110)-(1̄10) edge without Fe film and also found sporadic As vacancies along the edge. This implies that the creation of As vacancies at the interface might be caused by other energy-minimizing processes during the second cleavage process itself. Furthermore, it implies that the structural variations along the cross-section of the interface, such as sporadic As vacancies or Fe film protrusions, can be attributed directly or indirectly to the second cleavage process itself and are therefore a direct product of the cross-sectional approach [47].

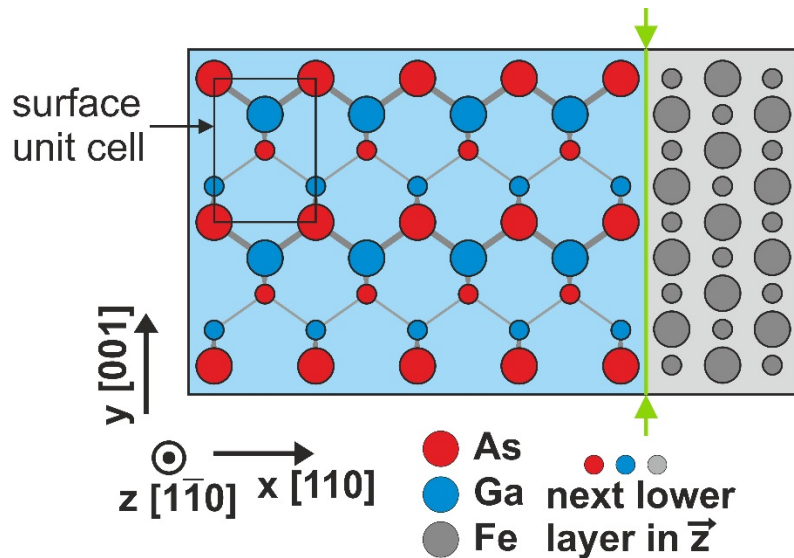


Figure 3.6: Scheme of the atomic structure of the ideal interface with coordinate system. The large filled circles represent the atoms in the (1̄10) surface layer. The smaller filled circles are located one layer below. The surface unit cell of  $4 \text{ \AA} \times 5.65 \text{ \AA}$  is shown. The green solid vertical line indicates the position of the interface.

In conclusion, the STM measurements across the *p*-type Fe/GaAs(110) interface confirm the finding of Winking [47] for the *n*-type junction that the LT growth process yields an abrupt and atomically flat Fe/GaAs(110) interface. This is in excellent agreement with DFT calculations by Grünebohm *et al.* [80] that also predict an atomically flat interface for Fe films of at least 1 monolayer thickness (see Figure 1.9 in section 1.6). A simplified scheme of this result is presented in Figure 3.6. It schematically shows the arrangement of Ga, As, and Fe atoms of the first (larger filled circles) and second (smaller filled circles) surface layer along the [1̄10] direction at an ideal Fe/GaAs(110) interface. The abrupt interface is indicated by the green solid vertical line.

### 3.1.3 STM Tip Preparation for Interface Characterization

To investigate the immediate interface region on the atomic scale by means of cross-sectional STM, very sharp tips with small radii of curvature are required. The cross-sectional sample of the Fe/GaAs(110) interface allows to directly determine the tip radius of curvature by scanning across the elevated Fe film [47] as shown in the left panels in Figure 3.7. The tip radius is obtained by plotting the topographic section with the same scale in  $x$  and  $z$  direction and finding the circle that best fits the course of the Fe film elevation (not shown here). All tungsten tips used in this thesis exhibit a radius of curvature of at least several tenths of nm. For the particular tip used in the left panels of Figure 3.7 the radius of curvature amounts to  $r_T = 40$  nm. Since the tip is comparatively large with regard to the sharp Fe film protrusions, the convolution of the tip in the topography can be seen. Furthermore, the tip is too large to reach the immediate interface region before tunneling into the Fe film and therefore cannot resolve the interface.

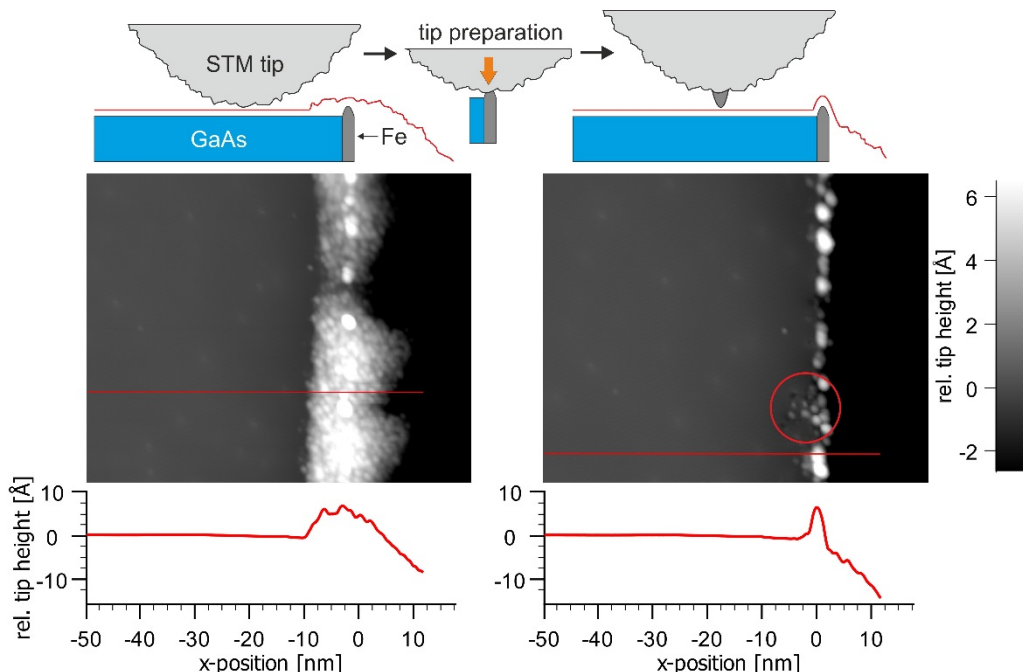


Figure 3.7: (upper panels) Schematic of the tip preparation process. (center panels)  $70 \times 55 \text{ nm}^2$  topography taken at  $V_s = -1.5 \text{ V}$  and  $I_T = 50 \text{ pA}$  (left) before and (right) after preparation. The area where the tip has been dipped into the Fe film is marked by a red solid circle. (lower panels) Topography sections showing the relative tip height taken along the red solid lines above. The tip preparation decreased the tip radius of curvature from  $r_T = 40 \text{ nm}$  to  $r_T = 2 \text{ nm}$ .

By applying an advanced preparation technique this issue can be overcome [125]. The tip is prepared by dipping it into the Fe film (see upper panels in Figure 3.7). This is achieved by positioning the center of the tip above the center of the Fe film and approaching the tip around 10 to 20 Å towards the Fe film. To check the geometry of the new tip, it is scanned across the interface again (see right panels in Figure 3.7). In this way stable

Fe-on-tungsten-tips with a radius of curvature of  $r_T = 2 \text{ nm}$  and smaller can be obtained which allow highly resolved STM and STS measurements of the immediate Fe/GaAs(110) interface.

## 3.2 Electronic Characterization of the Interface

Parts of this section have been published in Refs. [120, 121].

### 3.2.1 Tip-Induced Band Bending<sup>9</sup>

As described in section 3.1.1 the observed atomic corrugations for different bias voltages between tip and sample in an STM topography can be explained by anionic and cationic surface resonances that are found at characteristic energies in the conduction and valence band. However, the bias voltage range in which a particular state is observed usually differs from the energy range one would expect from *ab initio* electronic structure calculations [124, 128]. This is due to the fact that the STM tip itself together with the doping of the semiconductor have an impact on the measurement. Since the GaAs(110) surface does not exhibit any occupied states localized at the surface (see section 3.1.1) that could screen the electric field from the STM tip, a space charge builds up inside the semiconductor. This gives rise to a relative shift of the energy bands at the semiconductor surface with respect to the bulk [82] as illustrated in Figure 3.8. The amount of this shift is also called tip-induced band bending (TIBB) [82].

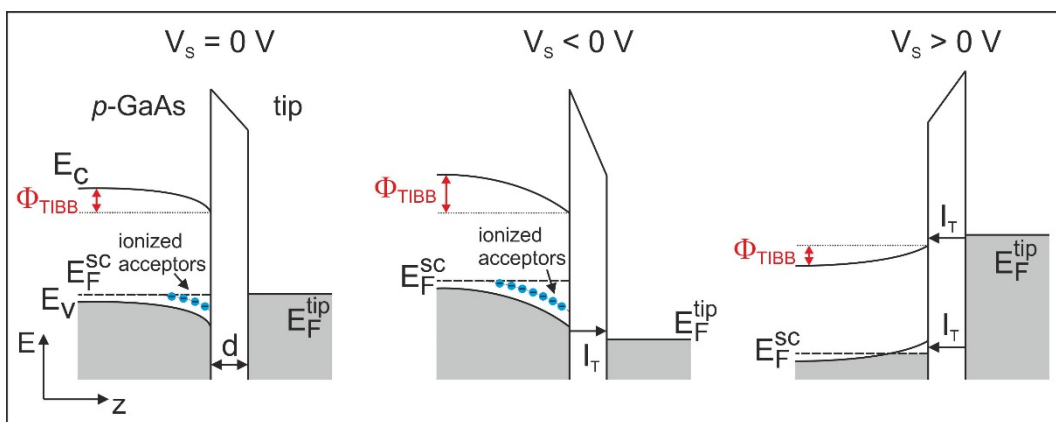


Figure 3.8: 1D band scheme of the tunnel experiment for *p*-type GaAs. The tip-induced band bending  $\Phi_{TIBB}$  is sketched for different sample bias voltages  $V_s$ . For more details see continuous text.

<sup>9</sup> Compare this subsection to Ref. [47] (ch. 3.3.1) for the case of *n*-doped GaAs(110).

In Figure 3.8 the case of *p*-type GaAs with the work function of the tip being smaller than the work function of the semiconductor ( $\Phi_T < \Phi_S$ ) is illustrated. If the tip is brought into tunnel contact with the unbiased sample (shown in the left panel of Figure 3.8), charge carriers are interchanged until the Fermi levels of the tip and the semiconductor are aligned in accordance with the Gedankenexperiment from section 1.1. For the considered *p*-type semiconductor the space charge region consists of negatively charged acceptors with a corresponding downward shift of the energy bands (see left panel in Figure 3.8).

The TIBB depends on the distance between tip and sample (see Figure 1.1) as well as on the bias voltage  $V_s$  between tip and sample (see Figure 3.8). It can be seen in Figure 3.8 that due to the build-up of a space charge inside the semiconductor only a part of the difference in electron potential energy between tip and sample  $|eV_s + \Phi_T - \Phi_S|$  drops along the vacuum gap between tip and semiconductor. Therefore, from solely knowing the applied bias voltage one cannot draw any conclusions on which states in a specific energy range are actually addressed.

The case of *p*-type GaAs at negative sample bias voltages  $V_s$  is shown in the center panel in Figure 3.8. Obviously, for electrons to tunnel from the valence band into the tip it takes a certain bias voltage to overcome the TIBB and to lift the valence band edge  $E_V$  at the surface above the Fermi energy of the tip. Above a certain positive bias voltage (flatband voltage) the energy bands are bent upwards. The case for higher positive bias voltages is shown in the right panel of Figure 3.8. The valence band edge and the acceptor band at the interface lie above the Fermi level and can be addressed by electrons tunneling from the tip into the semiconductor. If the bias voltage is high enough, this opens up another tunneling channel and electrons can tunnel from the tip into the conduction band. Therefore, the proportion that each channel contributes to the tunnel current changes also with the bias voltage.

As the discussion in this section shows, a detailed knowledge of the TIBB is of essential importance for a correct analysis of the scanning tunneling microscopy and spectroscopy data. A one-dimensional approximation is not appropriate for realistic tip geometries [129]. Therefore, based on the work by Winking [47] a 3-dimensional finite element method approach is presented in section 4.1 that takes into consideration the 3-dimensional geometry of the STM tip and yields realistic values for the TIBB and the electrostatic potential inside the semiconductor.

### 3.2.2 Space Charge Region Analysis

For a deeper understanding of the electronic properties of the ideal Fe/GaAs(110) interface the space charge region is investigated by scanning tunneling spectroscopy in cross-sectional geometry (XSTS). In the spectroscopy mode as described in section 2.1.2.2, one *I-V* spectrum is taken at each topographic pixel after the relative tip height is adjusted in accordance with the set point values of tunnel current and sample bias voltage and the feedback loop is switched off. In the lower panels of Figure 3.9 XSTS spectra of a low-temperature grown (a) *n*-type and (b) *p*-type interface are shown. The spectra are taken

along the corresponding red solid lines perpendicular to the interface shown in the upper panels. The spectra are topography-normalized to a constant tip-sample distance (see section 3.2.2.1). In order to obtain the course of the valence and conduction band along the entire space charge region, the voltage range and spatial range are chosen accordingly. The logarithm of the tunnel current is plotted color-coded. Due to the band gap of the semiconductor there is a voltage range in which the tunnel current drops below the background noise of less than 1 pA. If sufficiently high positive or negative bias voltages are applied, tunneling into or from the band-like states of GaAs becomes possible. The bias voltage where a well-defined tunnel current is measurable (starting at  $\sim 3$  pA) is called *onset voltage*. Due to the tip-induced band bending (TIBB) (see also section 3.2.1) this onset voltage does not exactly coincide with the band edges (conduction band minimum or valence band maximum) of GaAs but can serve as a first indicator showing the qualitative course of the band edges and the entire energy bands along the space charge region.

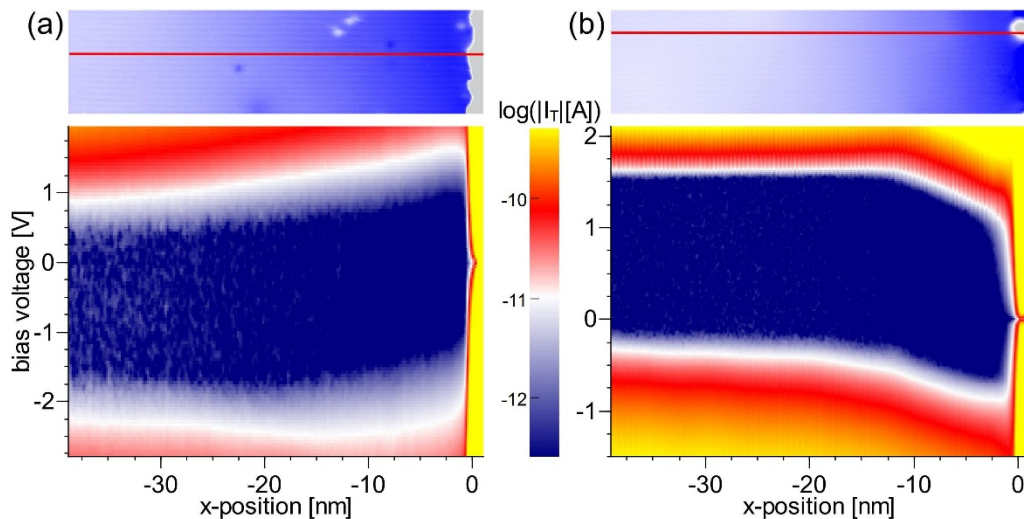


Figure 3.9: (upper panels)  $40 \times 13 \text{ nm}^2$  XSTM topographies across a low-temperature grown (7 ML Fe) (a) *n*-type [47] and (b) *p*-type Fe/GaAs(110) interface. The set point values for the *n*-type and the *p*-type case are  $V_s^n = +2 \text{ V}$ ,  $I_T^n = 100 \text{ pA}$  and  $V_s^p = -1.5 \text{ V}$ ,  $I_T^p = 150 \text{ pA}$ , respectively. (lower panels) 250 topography-normalized *I*-*V* spectra of the low-temperature grown (a) *n*-type [47] and (b) *p*-type Fe/GaAs(110) interface taken along the corresponding red solid lines from the upper panels. The logarithm of the absolute value of the tunnel current  $I_T$  is plotted color-coded as a function of the distance to the interface and the bias voltage. The interface is located at  $x = 0 \text{ nm}$ . Each *I*-*V* curve is averaged over three spectra in *y* direction (parallel to the interface). The data was taken at (*n*-type) room temperature (RT) and (*p*-type) at  $T = 6 \text{ K}$ . Spectra have been published in Ref. [121].

Figure 3.9 shows that the energetic position of the band edges with regard to the Fermi energy depends on the distance to the interface in *x* direction. Towards the interface the conduction (at positive sample bias voltages) and the valence band (at negative sample

bias voltages) clearly exhibit an upward and downward bending for the *n*-type and *p*-type Fe/GaAs(110) interface, respectively. By means of the spectra the width of the space charge region can be estimated: The distance from the interface where the energy bands flatten out and therefore any influence of the space charge region or the interface vanishes is a measure for the width of the space charge region  $w_{SCR}$ . For the *n*-type interface Figure 3.9(a) exhibits a space charge region width of  $w_{SCR}^n \approx 40$  nm. Taking the donor (Si atoms) concentration of  $N_D = 0.8 \times 10^{18} \text{ cm}^{-3}$  as specified by the manufacturer and assuming a SB height of  $\Phi_{SB}^n = 0.8 \text{ eV}$  as found in the literature [130, 131], equation (1.3) yields a space charge region width of  $w_{SCR}^n \approx 38$  nm which is in very good agreement with the experimentally obtained value. For the *p*-type interface the spectra in Figure 3.9(b) show a space charge region width of  $w_{SCR}^p \approx 25$  nm. According to the manufacturer, the *p*-type sample is doped with Zn atoms with an acceptor concentration of  $N_A = 2.75 \times 10^{18} \text{ cm}^{-3}$ . This value is in excellent agreement with the carrier density obtained from room temperature Hall measurements.<sup>10</sup> If one assumes a *p*-type SB height of  $\Phi_{SB}^p = 0.6 \text{ eV}$  as found in the literature for Fe/GaAs(001) interfaces [130, 131] and takes the acceptor concentration to be  $N_A = 2.75 \times 10^{18} \text{ cm}^{-3}$ , equation (1.4) from section 1.1 yields  $w_{SCR}^p \approx 19$  nm. This is around 25 % smaller than the experimentally indicated value.<sup>11</sup> The spectra of another *p*-type Fe/GaAs(110) interface with an acceptor concentration of  $N_A = 4.7 \times 10^{18} \text{ cm}^{-3}$  shown in Figure 3.10 exhibit a space charge region with a width of  $w_{SCR}^p \approx 20$  nm. This is in good agreement with a decreasing width of the space charge region with increasing acceptor concentration as suggested by equation (1.4).

A closer look to the immediate interface region shows that the energetic position of conduction band edge for the *n*-type interface does not increase monotonously all the way towards the interface. Around 2 nm off the interface the onset voltage reaches a maximum and then decreases. The valence band edge for the *p*-type interface does not decrease monotonously all the way towards the interface but exhibits a minimum around 2 nm off the interface. As it was already pointed out by Winking [47] this feature can only be explained by considering the three-dimensional superposition of the band bending of the space charge region  $\Phi_{SCR}(x)$  and the tip-induced band bending. This will be discussed in greater detail in chapter 4.

Furthermore, the spectra in Figure 3.9 show the closing of the band gap and a very high tunnel current at the interface. The tunnel spectra show metallic behavior and can be explained by tunnel processes into or out of the Fe film protrusions at the interface. However, a closer look to the immediate interface region, in particular for the *p*-type interface, reveals a small tunnel current inside the band gap starting around 1 nm off the interface. That this additional tunnel current inside the band gap is detected on the side of the semi-

---

<sup>10</sup> At room temperature virtually all shallow acceptors are ionized and therefore the obtained carrier density is equal to the doping concentration of the sample.

<sup>11</sup> As it will turn out later on in chapter 4, the discrepancy between experimental and theoretically expected value can be partly explained by the fact that the actual SB height of the investigated Fe/GaAs(110) interface significantly differs from the literature value for Fe/GaAs(001) interfaces.

conductor and not on a Fe film protrusion can be concluded from the atomic modulation of the conduction band edge. This can be seen even better in the spectra across another *p*-type Fe/GaAs(110) interface shown in Figure 3.10 where the spectra are not taken across an Fe film protrusion but only close to it (see red solid line in the upper panel). This strongly indicates the possibility of states inside the band gap of the GaAs. This question will be addressed in greater detail in section 3.2.3 where the immediate interface region of a *p*-type Fe/GaAs(110) interface is investigated by means of highly resolved low-temperature XSTS.

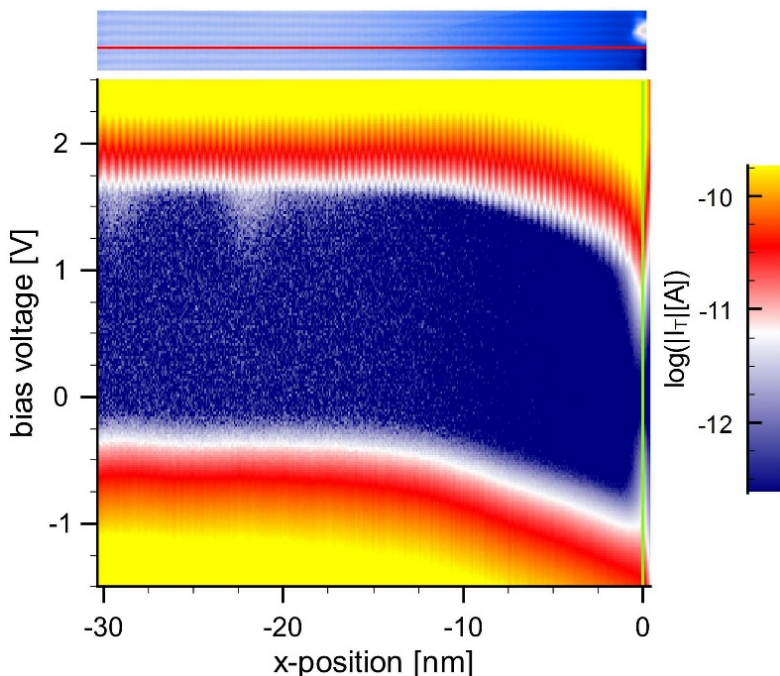


Figure 3.10: *I-V* spectra taken along the space charge region (red solid line from the upper panel) of a low-temperature grown (2 ML Fe) *p*-type Fe/GaAs(110) interface with an acceptor concentration of  $N_A = 4.7 \times 10^{18} \text{ cm}^{-3}$ . The interface is located at  $x = 0 \text{ nm}$  indicated by the green solid vertical line. The two bumps in the tunnel current at the conduction band edge far away from the interface can be attributed to Zn acceptors in proximity. The data was taken at  $T = 6 \text{ K}$  and set point values of  $V_s^p = -1.5 \text{ V}$ ,  $I_T^p = 150 \text{ pA}$ .

### 3.2.2.1 Projection of STS Data to the Same Relative Tip Height

Current-voltage (*I-V*) spectra are taken at each topographic pixel by interrupting the feedback loop after the relative tip height is adjusted to the corresponding set point values (tunnel current  $I_T$  and sample bias voltage  $V_s$ ) that are kept constant throughout data acquisition (see also section 2.1.2.2). On the left hand side in Figure 3.11 the raw *I-V* spectra of a *p*-type junction are plotted. In the original data the downward band bending of the conduction band towards the interface is clearly visible. Also the energetically upper part

of the valence band is bent downwards towards the interface. Since the relative tip height at each point is adjusted to the constant set point values of  $V_s = -1.5$  V and  $I_T = 150$  pA, this band bending is not observed deep inside the valence band (see tunnel current isolines depicted by the black solid lines). This is accompanied by a change of the relative tip height along the space charge region which is shown in the upper part in Figure 3.11.

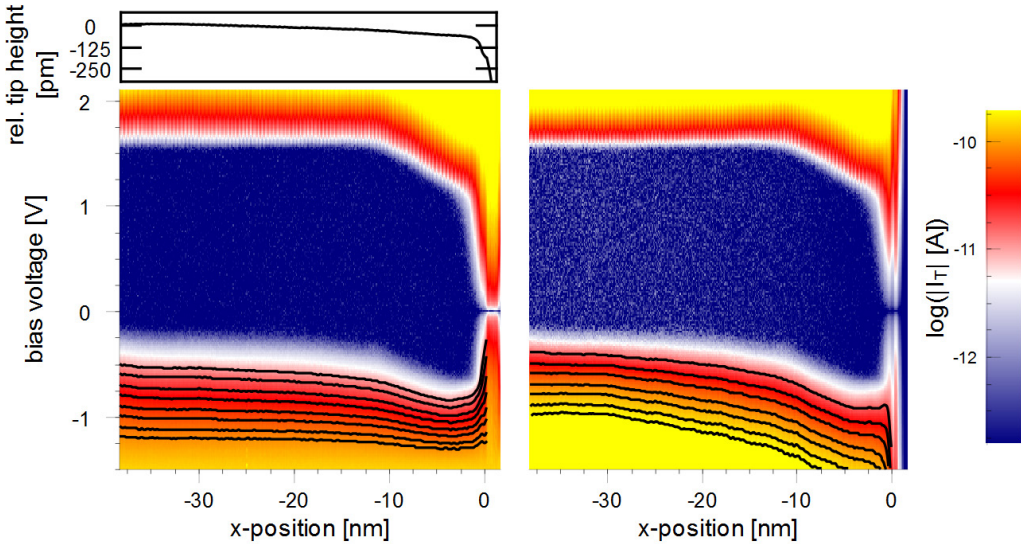


Figure 3.11: (upper panel) The relative tip height taken at  $I_T = 150$  pA and  $V_s = -1.5$  V perpendicular to a *p*-type interface. (lower panels) 230 color-coded  $\log(|I_T|)(x, V)$  spectra taken along the same line as the topography section from the upper panel [120, 125]. The interface is located at  $x = 0$  nm. The left spectra show the original data whereas the right spectra are topography-normalized. The black solid lines inside the valence band depict tunnel current isolines.

To make all the  $I$ - $V$  spectra taken along the space charge region comparable among each other, they are projected to the same relative tip height. Following Ref. [132], this *topography-normalization* is done by taking into consideration the exponential dependence of the tunnel current on the relative tip height  $\Delta z(x, y)$  and the local apparent barrier height  $\Phi_{\text{abh}}(x, y)$  which is also acquired at each measurement point. The normalized tunnel current  $\tilde{I}(V, \vec{r})$  is obtained by

$$\tilde{I}(V, \vec{r}) = I(V, \vec{r}) \exp \left( \Delta z(x, y) \frac{2\sqrt{2m_0 \Phi_{\text{abh}}(x, y)}}{\hbar} \right) \quad (3.1)$$

where  $I(V, \vec{r})$  represents the non-normalized tunnel current raw data,  $m_0$  is the electron mass, and  $\hbar$  is the Planck constant divided by  $2\pi$ .  $\Phi_{\text{abh}}(V, x, y)$  is determined by measuring the tunnel current in dependence of the tip height. Subsequently,  $\Phi_{\text{abh}}(x, y)$  can be extracted from the data in accordance with expression (2.5) from subsection 2.1.2.3.

On the right hand side of Figure 3.11 the topography-normalized spectra are plotted. In the normalized data also the band bending deep inside the valence band can be observed

as indicated by the tunnel current isolines (black solid lines). The normalized spectra are also used for the quantitative analysis of the space charge region in chapter 4.

Apparently, the tunnel current in the normalized data set vanishes around 1.5 nm on the right hand side from the interface even though tunneling into the Fe film takes place at this position. This is caused by the sharp decrease of the relative tip height beyond the edge of the sample. Therefore, the exponential dependence of the normalized tunnel current on the relative tip height from equation (3.1) leads to this artifact. For the quantitative analysis of the space charge region in chapter 4 this is of no relevance because the analyzed space charge region ends at the interface.

### 3.2.3 High-spectral resolution characterization of the interface

It was already pointed out in section 3.2.1 that the spectra across the ideal Fe/GaAs(110) interface indicate states inside the energy band gap of the semiconductor in the immediate interface region. With respect to the microscopic origin of the Fermi level pinning mechanism these states are of particular interest as has already been discussed in chapter 1. Therefore, in this section the immediate interface region is investigated by means of highly resolved XSTS measurements.

The lower panel in Figure 3.12 shows atomically resolved XSTS data taken across a low-temperature (LT) grown *p*-doped Fe/GaAs(110) interface. The differential conductance calculated from *I-V* spectra is plotted color-coded and serves as a measure for the local density of states (LDOS). For positive sample bias voltages the surface resonance C<sub>3</sub> localized on the surface cations (see also section 3.1.1) is addressed and therefore reveals the Ga sites as maxima at the conduction band edge. The same atomic modulation is observed in the corresponding topography in the upper panel of Figure 3.12 which was taken at a positive sample bias voltage. The atomic corrugation continues up to the interface which is located at  $x = 0$  nm and indicated by the green solid vertical line. In contrast to the atomic corrugation that is clearly visible in the conduction band, the  $dI/dV$  spectra exhibit a spatial and energetic continuum of states inside the band gap in the first few atomic layers of the GaAs at the interface. Most strikingly, there is no sign of any localized states neither in energy nor in real space inside the band gap. Therefore, there is no evidence of defect-induced gap states as suggested by the defect model described in section 1.4. This further corroborates that the LT grown interface is free of defects [47].

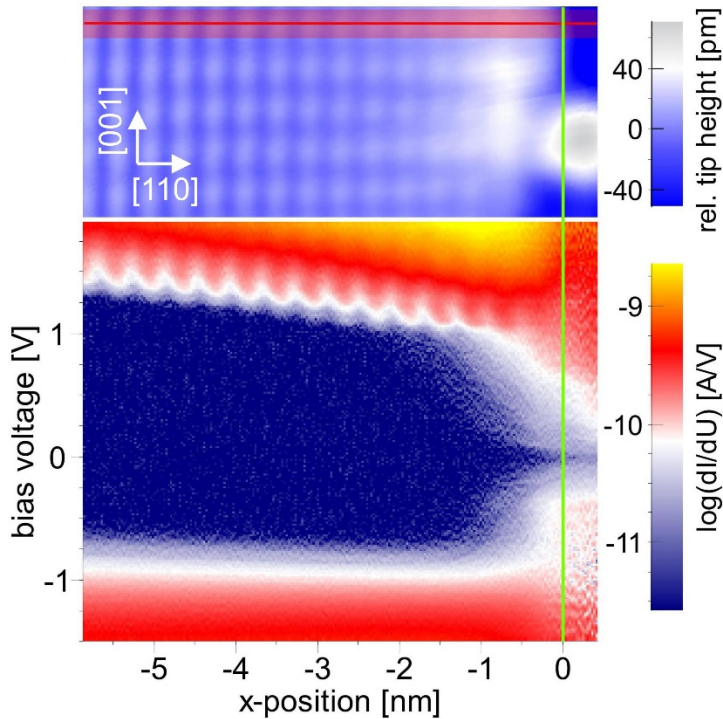


Figure 3.12: Highly resolved XSTS spectra across the immediate interface region of an ideal *p*-type Fe/GaAs(110) interface (7 ML Fe) [121, 125]. The interface is located at  $x = 0$  nm (indicated by the green solid vertical line). The color-coded differential conductance  $dI/dV$  is obtained from 230  $I$ - $V$  spectra (with setpoint values of  $V_s = -1.5$  V,  $I_T = 150$  pA) taken along the red solid line as depicted in the constant current topography above ( $V_s = +1.75$  V,  $I_T = 75$  pA). The data is averaged over 10 spectra in  $y$  direction (transparent red area in the topography).

As can be seen in the  $dI/dV$  spectra from Figure 3.12 the decay length of the gap states into the semiconductor is the largest at the band edges and decreases towards midgap. This kind of behavior one would expect in the framework of the metal-induced gap states (MIGS) model which was presented in section 1.3. Furthermore, exponential fits at midgap yield a decay length of  $\lambda \approx 4$  Å [125]. This is in good agreement with other experimental findings of  $\lambda \approx 3.4$  Å measured in topview geometry at Fe clusters on GaAs(110) [42]. Calculations that take the complex band structure of GaAs into consideration yield a midgap decay length of  $\lambda \approx 3$  Å [19]. Therefore, the gap states observed by XSTS measurements exhibit essentially the same features that the MIGS model predicts.

In section 3.1.2 it has been shown that due to the second cleavage process structural variations, such as sporadic As vacancies or Fe film protrusions, occur along the LT grown interface. In the following, the qualitative influence of these variations on the continuum of MIGS is investigated in greater detail. The lower panels of Figure 3.13 show five highly resolved spectroscopy sections of differential conductance spectra taken along the five corresponding solid red lines in  $x$  direction across the interface (see upper panels).

The uppermost line and spectroscopy section represent the undisturbed case that was already discussed before in this section (see Figure 3.12). Along the second section an As vacancy can be found at the interface. This type of defect seems not to have any significant impact on the continuum of MIGS. Moreover, along the third and fourth spectroscopy sections a prominent Fe film protrusion is located at the interface. Close to the protruding Fe film small energetic variations inside the band gap for negative voltages can be observed in the fourth section. Along the third section at positive voltages a small additional bump in  $x$  direction can be seen close to the interface. Furthermore, in the fifth section an As vacancy is located together with a Ga vacancy in the 2nd atomic layer from the interface. Weak local variations of the LDOS are observed at the Ga vacancy for positive voltages.

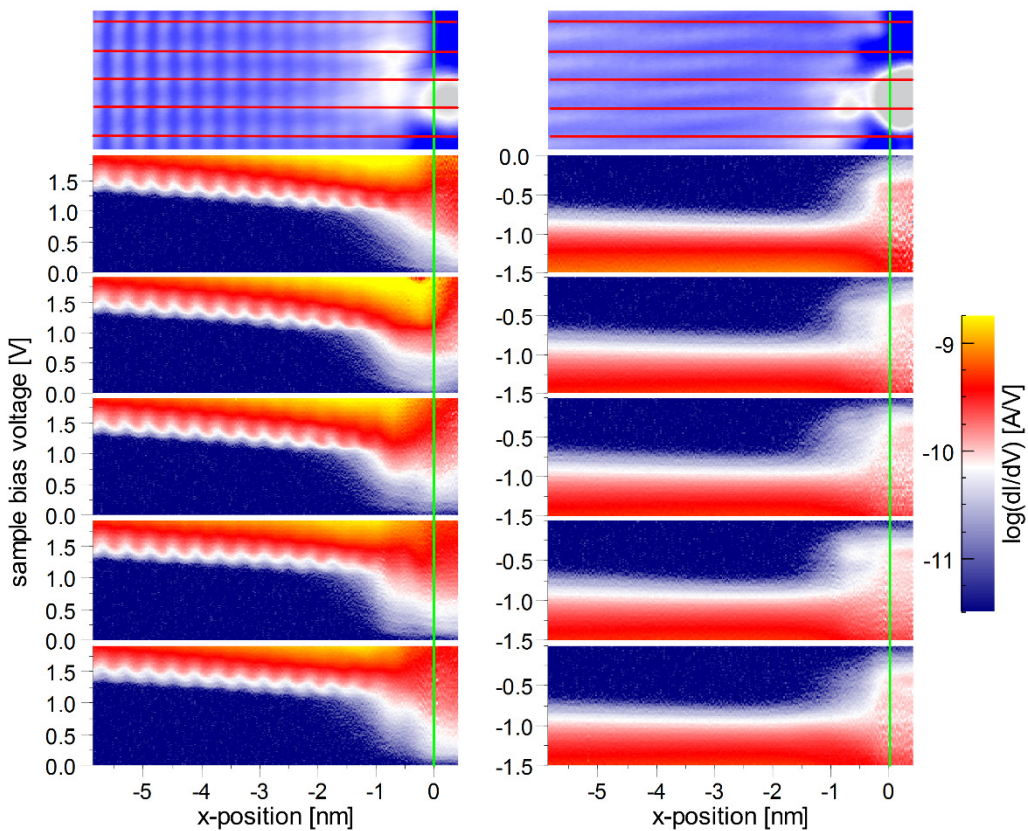


Figure 3.13: (upper panels)  $6.3 \times 2.8 \text{ nm}^2$  constant current topographies of the interface region at (left)  $V_s = +1.75 \text{ V}$ ,  $I_T = 75 \text{ pA}$  and (right)  $V_s = -1.5 \text{ V}$ ,  $I_T = 150 \text{ pA}$ . (lower panels) Logarithmically plotted differential conductance  $dI/dV$  (LDOS) calculated from 230  $I$ - $V$  curves (with setpoint values of  $V_s = -1.5 \text{ V}$ ,  $I_T = 150 \text{ pA}$ ) taken along the 5 solid red lines in the topography perpendicular to the Fe/GaAs(110) interface [120, 125]. The 5 corresponding sections are each separated by one unit cell in the topography. The spectra are plotted for (left) positive voltages and for (right) negative voltages. The spectra are averaged over 10 pixel parallel to the interface (in  $y$ -direction). The green solid vertical line at  $x = 0 \text{ nm}$  indicates the position of the interface plane.

A spatial and energetic continuum of metal-induced gap states along all five sections in Figure 3.13 is observed. It is important to note that the continuum of metal-induced gap states is independent of local variations (e.g., Fe film protrusions or vacancies) at the interface and remains virtually unchanged along the interface. This demonstrates that the metal-induced gap states are delocalized along the entire interface and dominate the LDOS inside the band gap of the semiconductor. The slight variations in LDOS at vacancies or Fe film protrusions should not be of any surprise: Generally, a change in the local atomic structure comes along with a change in the LDOS. In fact, these small variations in LDOS demonstrate the high sensitivity of the XSTS measurements and at the same time show that they play only a minor role in the process of Fermi level pinning at the ideal Fe/GaAs(110) interface.

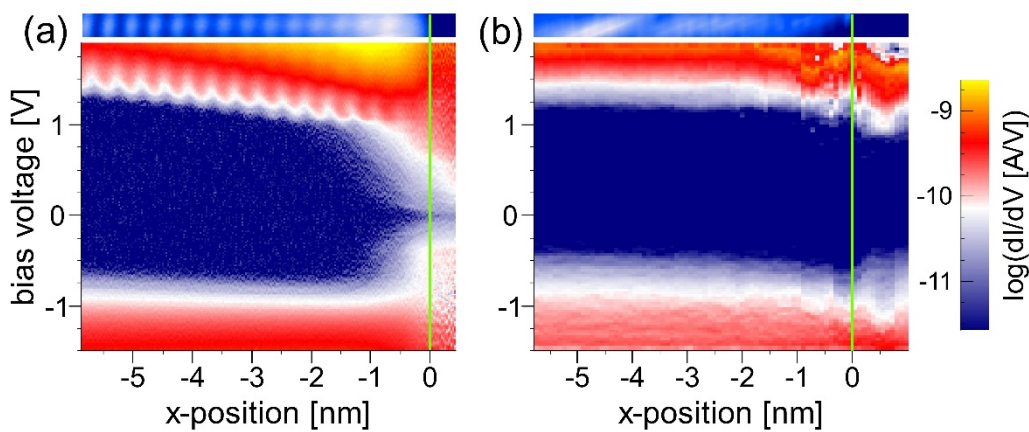


Figure 3.14: Differential conductance spectra showing the direct comparison between the LDOS of (a) the Fe/GaAs(110) interface from Figure 3.12 and (b) the GaAs(110)-(1̄10) edge without Fe film (with setpoint values of  $V_s = -2 \text{ V}$ ,  $I_T = 150 \text{ pA}$ ) [121]. The spectra are taken along the topography section from above. The interface and the edge are indicated by the green solid vertical line.

The question if the observed continuum of gap states is actually induced by the metal, is addressed in a control experiment across a *p*-type GaAs(110)-(1̄10) edge without the Fe film shown in Figure 3.14(b). In contrast to the  $dI/dV$  spectra of the LT grown Fe/GaAs(110) interface in Figure 3.14(a) the GaAs(110)-(1̄10) edge without Fe film does not show any signs of states inside the band gap. Therefore, the experiment reveals a purely metal-induced continuum of gap states for the ideal Fe/GaAs(110) interface.

In conclusion, in this section the technique of highly resolved XSTS spectra at the immediate LT grown Fe/GaAs(110) interface has been extended from *n*-type [47] to *p*-type junctions. The continuum of gap states with larger decay lengths at the band edges and the smallest decay length at midgap suggests that the gap states are induced by the metal [47]. This is supported by an additional control experiment across the GaAs(110)-(1̄10) edge without Fe film that does not exhibit any gap states at all. The homogeneity of the continuum of gap states along the entire interface underlines that defects play only a minor role in the microscopic process of Fermi level pinning.



## 4 Quantitative Analysis of the Ideal Interface

In section 3.2.2 it has been shown that XSTS is a suitable tool to investigate the electronic properties of the *n*-type [47] and *p*-type Fe/GaAs(110) interfaces along the entire space charge region. In this chapter this experimental technique is combined with 3-dimensional finite element simulations of the semiconductor's space charge region. This approach gives access to more quantitative information such as the Schottky barrier height of the system and the charge distribution at the interface. The finite element model presented in section 4.1 was developed by Winking [47] using the commercially available software package COMSOL multiphysics. Winking extracted the Schottky barrier height from XSTS data of a *n*-type junction [47]. In the Master's thesis of Rolf-Pissarczyk [125] the calculations have been extended to analyze *p*-type Schottky contacts with special tip geometries. In section 4.2 it is shown how the Schottky barrier heights can be extracted from the data. In section 4.3 a new tool to extract information on the local density of states at the interface is developed. A large part of this chapter has been published in Ref. [120].

### 4.1 3D Simulation of the Electrostatic Potential of Metal-Semiconductor Interfaces

In chapter 3 we saw that the tip-induced band bending (TIBB) [82] plays a significant role in STM and STS measurements on the GaAs(110) surface (see also appendix A.1 for effect of TIBB on multibias topographies). Therefore, for a realistic and quantitative investigation of the electronic properties of the Fe/GaAs(110) interface based on local *I*-*V* spectra the knowledge of the TIBB is of essential importance. A calculation of the TIBB has to take into consideration the three-dimensional (3D) shape of the STM tip [129] as well as the influence of the space charge region (SCR) of the metal-semiconductor interface on the TIBB itself [47].

In general, the electrostatic potential inside the GaAs  $V(\vec{r})$  is described by the Poisson equation (1.2) as discussed in section 1.1. The Poisson equation can only be solved analytically for simple cases. However, the geometry of the experiment (STM tip and sample surface) is rather complex. Therefore, we apply a three-dimensional (3D) finite element method (FEM) approach to solve the Poisson equation numerically for the tip-sample system [47]. In the simulation the discrete distribution of the doping atoms is neglected and a homogeneous space charge density in the semiconductor is assumed.

To include the effect of a nonzero electrostatic potential on the semiconductor charge density  $\rho(\vec{r})$ , a semiclassical approximation is applied in which the electron energy bands are shifted rigidly by an energy  $\Phi(\vec{r}) = -eV(\vec{r})$  due to the electrostatic potential  $V(\vec{r})$  [129]: The energies associated with the band structure of the semiconductor such as the conduction band minimum  $E_C$ , the valence band maximum  $E_V$ , the donor and acceptor energy levels  $E_D$  and  $E_A$ , as well as the Fermi energy  $E_F$  are given with respect to a fixed point in the energy bands. It is well known that the charge density inside a semiconductor depends on the Fermi level position relative to the energy bands (see also section 4.1.2). Shifting the energy bands by  $\Phi$  at a given spatial position and keeping  $E_F$  constant throughout the semiconductor results in the new Fermi level position  $E_F - \Phi$  relative to the energy bands with the corresponding charge density  $\rho(E_F - \Phi)$  [129]. Since the charge density  $\rho(\vec{r})$  also depends on the rigid band shift  $\Phi(\vec{r}) = -eV(\vec{r})$ , the charge density  $\rho(\vec{r})$  and the electrostatic potential  $V(\vec{r})$  have to be calculated iteratively and selfconsistently in compliance with the boundary conditions [47].

In the following sections and chapters the data will be analyzed and discussed in the framework of single electron band energy diagrams. Therefore, the electrostatic potential  $V(\vec{r})$  obtained from the 3D FEM simulation and the corresponding boundary conditions will be expressed also in terms of the electrostatic potential energy  $\Phi(\vec{r}) = -eV(\vec{r})$  of a single electron.

### 4.1.1 3D Model and Boundary Conditions

FEM simulations allow a detailed adjustment of the simulated system to the actual experimental 3D geometry. The 3D geometry that is used for the FEM simulation is plotted in Figure 4.1. The simulation volume is divided into different domains: STM tip (blue volume), GaAs sample (small box), and vacuum (remaining volume inside the big box). In order to avoid artifacts due to boundary conditions at the outer boundaries a sufficiently large simulated volume of  $400 \times 400 \times 300$  nm<sup>3</sup> is chosen. Furthermore, the mirror symmetry perpendicular to the  $x$ - $z$  plane is utilized which cuts down the simulated volume to half at  $y = 0$  (see Figure 4.1) and reduces computing time.

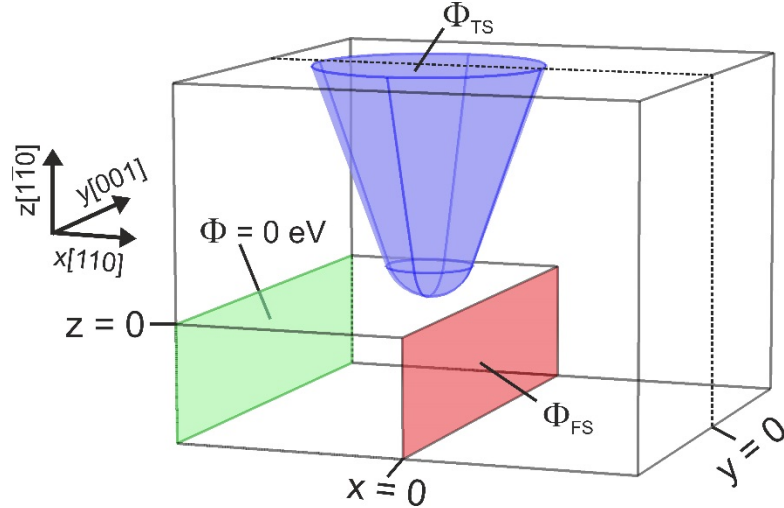


Figure 4.1: 3D finite element model of the experimental setup. The big box represents the simulated volume of  $400 \times 400 \times 300 \text{ nm}^3$ . The small box inside represents the GaAs sample. The GaAs(1̄10) surface is located at  $z = 0$ . The back part of the GaAs located at  $x = -200 \text{ nm}$  (transparent green area) is grounded ( $\Phi = 0 \text{ eV}$ ). The front part at  $x = 0$  (transparent red area) on which the Fe film is grown in the experiment is set to the fixed electrostatic potential energy  $\Phi_{FS}$  in the simulation. The surface of the tip (transparent blue area) is set to the fixed electrostatic potential energy  $\Phi_{TS}$ .

In FEM simulations the simulated volume can be divided into any arbitrary number of finite elements. In this study the 3D mesh divides the simulated volume into approximately  $6.5 \times 10^5$  tetrahedral elements. The mesh width at the tunneling contact and at the space charge region is decreased because there the largest potential gradients exist. This minimizes artifacts that are caused by the discretization of the mesh.

The electronic parameters and boundary conditions that are used for the FEM simulation are summarized here:

- The normal components of the electric displacement field  $\vec{D}$  at the interfaces of two different media 1 and 2 that are located inside the simulated volume, e.g., between semiconductor and vacuum, is assumed to be continuous:

$$\vec{n} \cdot (\vec{D}_1 - \vec{D}_2) = 0 \quad (4.1)$$

- At the outer boundaries of the finite simulated volume the normal component of the electric displacement field is set to zero ( $\vec{n} \cdot \vec{D} = 0$ ). This of course is an approximation because in general one would expect a nonzero component of the electric displacement field perpendicular to the outer boundaries. However, if the outer boundaries are sufficiently far away from the region of interest at  $y = z = 0$  and  $x = -50 \dots 0 \text{ nm}$  (see Figure 4.1), the influence of this approximation on the calculated electrostatic potential energy in the same region can be neglected. Therefore, the actual simulated volume (here  $V = 400 \times 400 \times 300 \text{ nm}^3$ ) was chosen in such a manner that even when cutting it down to 1/8 ( $V = 200 \times$

$200 \times 150 \text{ nm}^3$ ) the change of the simulated electrostatic potential energy in the region of interest is less than 1 meV.

- The relative permittivity of GaAs is taken as  $\epsilon_{\text{GaAs}} = 13.1$  [133].
- The charge density  $\rho(\vec{r})$  inside each finite element of the semiconductor has to be defined (for details see section 4.1.2).
- In all simulations the tip-sample distance is taken to be  $d = 8 \text{ \AA}$ .
- The tip radius of curvature  $r_T$  is set to the corresponding experimental value which is obtained as described in chapter 3.1.3. Tips prepared by dipping them into the Fe film exhibit a small Fe protrusion in front. This shape is also implemented as realistic as possible in the 3D FEM simulation [125].
- The electrostatic potential energy of the tip with regard to the semiconductor bulk is set to the value  $\Phi_{\text{TS}}$ . It is defined as the difference between the vacuum level at the tip and the vacuum level of the semiconductor bulk.  $\Phi_{\text{TS}}$  can also be written as

$$\Phi_{\text{TS}} = eV_s + \Phi_T - \Phi_S \quad (4.2)$$

where  $V_s$  is the experimental sample bias voltage and  $\Phi_T$  and  $\Phi_S$  are the work functions of the tip and sample, respectively.

- The interface areas between GaAs and the back contact (Figure 4.1, green) and between GaAs and Fe at  $x = 0$  (Figure 4.1, red) are taken as Dirichlet boundary conditions for self-consistent solutions of the Poisson equation (see eq. (1.2) and remarks on p.50, line 19-21). They are set to *constant* values  $\Phi = 0 \text{ eV}$  and

$$\Phi_{\text{FS}}^n = \Phi_{\text{SB}}^n - (E_C - E_F) \quad \text{and} \quad \Phi_{\text{FS}}^p = -\Phi_{\text{SB}}^p + (E_F - E_V) \quad (4.3)$$

for *n*-type and *p*-type Schottky contacts, respectively.  $E_F$  is the Fermi energy,  $E_C$  is the conduction band minimum,  $E_V$  is the valence band maximum, and  $\Phi_{\text{SB}}^n$  and  $\Phi_{\text{SB}}^p$  are the Schottky barrier heights for the *n*-type and *p*-type case, respectively. Since here we consider the electrostatic potential energy of a single electron,  $\Phi_{\text{FS}}^n$  and  $\Phi_{\text{FS}}^p$  have positive and negative sign, respectively. However, in the literature  $\Phi_{\text{SB}}^n$  and  $\Phi_{\text{SB}}^p$  are both defined with a positive sign [53] as also done in equations (1.6) and (1.7) which leads to the negative sign in front of  $\Phi_{\text{SB}}^p$  in equation (4.3). These Dirichlet boundary conditions guarantee that the COMSOL-simulated 3D charge distributions  $\rho(\vec{r})$  and their electrostatic potentials  $V(\vec{r})$  are representations of a finite “Schottky-Mott” metal-semiconductor model system in 3D with fixed parameter  $\Phi_{\text{SB}}$ .

The 2D charge distributions  $\sigma(y, z)$  at the interface area  $x = 0$  are inhomogeneous and show the usual “edge” and “corner” effects. This does not affect the validity of the simulated Schottky-Mott model system but it might affect the densi-

ty-dependent formation of MIGS, defects and bond polarizations (see sections 1.3–1.5) in a real system. A further influence may come from finite-size effects in the thin Fe-film like, e.g., 2D quantized LDOS resonances. In the simulation such effects are not taken into account.

By setting the contact between GaAs and Fe at  $x = 0$  to a fixed electrostatic potential energy  $\Phi_{FS}$  in the electrostatic 3D FEM simulation we assume that a tunnel current between tip and metal film in the experiment does not charge the metal film additionally. In other words we assume a constant electrochemical potential across the interface ( $\mu_{ec}^{\text{Fe}} = \mu_{ec}^{\text{GaAs}}$ ). This assumption is justified by the following considerations:

- (i) The tunnel probability between tip and film is roughly given by [85]

$$P_{STM} = \exp\left(-\frac{2d}{\hbar}\sqrt{2m_0\Phi_{Fe}}\right) \quad (4.4)$$

where  $d$  is the tunnel distance between tip and metal film,  $m_0$  is the electron mass, and  $\Phi_{Fe}$  is the work function of the Fe film and the iron-on-tungsten tip. If we assume an iron work function of  $\Phi_{Fe} \approx 4.5$  eV [134] and a typical tunnel distance of  $d = 8$  Å, we obtain  $P_{STM} \approx 3 \times 10^{-8}$ .

- (ii) At low temperatures (the STM/STS data for the *p*-type junction was taken at  $T = 6$  K) the current transport across the metal-semiconductor contact is dominated by tunneling through the barrier. The probability of a hole tunneling across the *p*-type Schottky barrier (SB) with an energy  $\Delta E$  less than the height of the barrier can be expressed as [55]

$$P_{SB} = \exp\left[-\frac{2(\Delta E)^{3/2}}{3E_{00}\Phi_{bb}^{1/2}}\right] \quad \text{with} \quad E_{00} = \frac{e\hbar}{2}\sqrt{\frac{N_A}{m_h^*\epsilon_{GaAs}\epsilon_0}} \quad (4.5)$$

where  $\Phi_{bb}$  is the bending of the energy bands along the space charge region and  $m_h^*$  is the hole effective mass. There are two energetically degenerate tunnel channels for light and heavy holes. In the following we will consider the light holes with an effective mass of  $m_{lh}^* = 0.082m_0$  [133]. We assume an acceptor concentration of  $N_A = 2.75 \times 10^{24}$  m<sup>-3</sup>,  $\Phi_{bb} = 0.8$  eV (roughly the SB height of the *p*-type sample, see section 4.2), and we assume  $\Delta E = 0.8$  eV corresponding to a hole at the valence band maximum just outside the space charge region. This yields the light hole tunnel probability  $P_{SB} \approx 1.7 \times 10^{-8}$ .

- (iii) We find that  $P_{SB}$  amounts to about half of  $P_{STM}$ . Here one has to keep in mind that both tunnel probabilities are referenced to the same unit area. However, tunneling between tip and film is confined to an area of about  $A_{STM} = 10 \times 10$  Å<sup>2</sup>. The applied LT growth process yields a continuous thin 2D Fe film [46, 47] and the sheet resistance of Fe films in the thickness regime investigated here is found to be in the range of several hundreds of Ω/□ [135]. Therefore, tunneling through the Schottky barrier can take place

across the entire interface area which in our case amounts to  $A_{SB} = 100 \times 2500 \mu\text{m}^2$ . Thus, the tunnel current through the Schottky barrier could be up to  $I_{SB}/I_{STM} = P_{SB}A_{SB}/P_{STM}A_{STM} \approx 2 \times 10^{11}$  larger than the tunnel current between tip and metal film. For heavy holes with an effective mass of  $m_{hh}^* = 0.45m_0$  [133] the ratio is reduced to  $I_{SB}/I_{STM} \approx 5$  but still larger than 1.

The above considerations are supported by experimental observation: Current-voltage spectra taken directly above the Fe film in cross-sectional geometry (see example in Figure 4.2) clearly show metallic behavior. The corresponding  $dI/dV$  spectra exhibit positive differential conductance for the entire bias voltage range. In particular, around zero bias voltage the differential conductance is positive. Therefore, a Coulomb blockade caused by additional charge in the Fe film can be excluded.

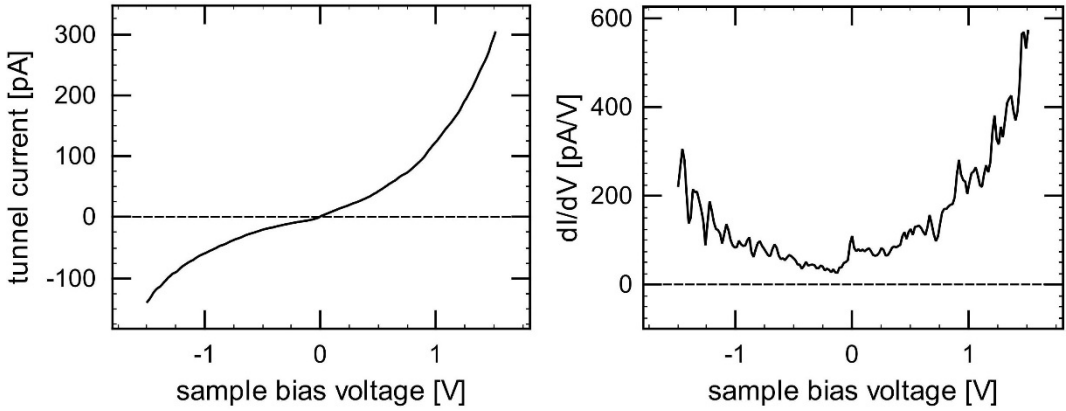


Figure 4.2: (left) Current-voltage spectrum taken above the 7 ML Fe film in cross-sectional geometry. (right) Corresponding  $dI/dV$  curve calculated from the  $I$ - $V$  spectrum on the left.

### 4.1.2 The Charge Density in GaAs

The charge density is obtained from equations that result from an effective mass approximation, see, e.g., Ref. [136]. In the following the most important equations of this approximation are summarized. For the electron density in the conduction band and the hole density in the valence band one finds

$$n = N_C \frac{2}{\sqrt{\pi}} F_{1/2} \left( \frac{E_F - E_C}{kT} \right) \quad \text{with} \quad N_C = 2(2\pi m_{d,e}^* kT/h^2)^{3/2} \quad (4.6)$$

$$p = N_V \frac{2}{\sqrt{\pi}} F_{1/2} \left( \frac{E_V - E_F}{kT} \right) \quad \text{with} \quad N_V = 2(2\pi m_{d,h}^* kT/h^2)^{3/2} \quad (4.7)$$

where  $E_F$  is the Fermi energy,  $E_C$  is the conduction band minimum,  $E_V$  is the valence band maximum,  $T$  is the temperature,  $k$  is the Boltzmann constant,  $F_{1/2}$  is the Fermi-Dirac integral of order 1/2,  $h$  is the Planck constant,  $m_{d,e}^*$  and  $m_{d,h}^*$  is the density of states effective mass for electrons and holes, respectively. The factor 2 before the bracket

ets in the expression for  $N_C$  and  $N_V$  accounts for the spin degeneracy. In the case of nondegenerate doping, the density of ionized donors  $N_D^+$  and the density of ionized acceptors  $N_A^-$  can be written as

$$N_D^+ = \frac{N_D}{1 + 2\exp(E_F - E_D/kT)} \quad (4.8)$$

$$N_A^- = \frac{N_A}{1 + 4\exp(E_A - E_F/kT)} \quad (4.9)$$

where  $N_D$  is the concentration of donors,  $N_A$  is the concentration of acceptors,  $E_D$  is the donor energy level, and  $E_A$  is the acceptor energy level. The factor 2 in front of the exponential term in equation (4.8) arises from spin degeneracy. The factor 4 in equation (4.9) originates from total degeneracy, considering both spin and heavy and light hole bands [136].

The Fermi energy is defined inside the semiconductor by  $\rho(E_F) \stackrel{!}{=} 0$  [129] with

$$\rho(E_F) = e[p(E_F) + N_D^+(E_F) - n(E_F) - N_A^-(E_F)] \quad (4.10)$$

where  $e = +1.602 \times 10^{-19}$  C is the elementary charge.

In the 3D FEM model, surface states are not considered because tunneling spectra are not very sensitive to the exact shape of the density of states at the surface as already pointed out by Reusch [45]. This is supported by simulations of tunnel spectra on GaAs(110) by Feenstra and Stroscio [82]: Neglecting surface states in their simulations, they find a good agreement between simulation and experiment. They reason that the surface resonances in the valence and conduction bands of the clean GaAs(110) surface (see also section 3.1.1) do not play a significant role in determining the observed tunnel current [82].

### 4.1.3 Electrostatic Potential Energy and Space Charge Density

When solving the Poisson equation iteratively and selfconsistently in compliance with the boundary conditions as described above, one obtains the spatial dependence of the electrostatic potential energy  $\Phi(\vec{r})$  as depicted in the color-coded cross-section in Figure 4.3(a). In this example the electrostatic potential energy is plotted for a tip-sample distance of  $d = 8$  Å (being within a typical range of tip-sample distances in STM experiments) and a lateral tip position of  $x = -50$  nm. The electrostatic potential energy of the semiconductor bulk is set to zero whereas the electrostatic potential energy of the STM tip is set to  $\Phi_{TS} = -2$  eV and the interface area at  $x = 0$  is set to  $\Phi_{FS} = -0.8$  eV. Figure 4.3 reveals the space charge region extending from  $x = 0$  into the semiconductor. Furthermore, the tip-induced space charge region at the semiconductor surface right below the tip can be observed. For  $x > 0$  (i.e. beyond the Fe-film)  $\Phi(\vec{r})$  decays slowly, on the axis of the dipolar far-field it is proportional to  $1/x^2$ .

The width of the space charge region extending from  $x = 0$  into the GaAs can be easily identified as  $w_{SCR}^p \approx 20$  nm when plotting the space charge density inside the GaAs as

done in Figure 4.3(b). This is in excellent agreement with equation (1.4) as one would expect. Multiplying the space charge density inside the space charge region by the volume of the space charge region in the simulation  $V_{SCR} \approx 20 \times 400 \times 100 \text{ nm}^3$  yields a space charge of  $Q_{SC} \approx -2200e$ . The  $y$ - $z$  plane of the GaAs at  $x = 0$  exhibits an average surface charge density of  $\sigma \approx +8.86 \times 10^{-3} \text{ C/m}^2$  corresponding to about the same charge  $Q_{SC}$  but with opposite sign.

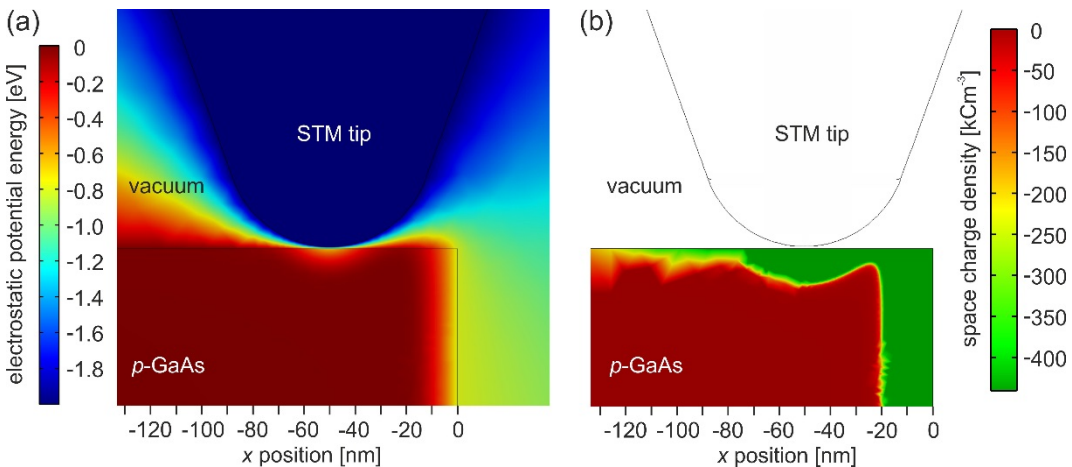


Figure 4.3: (a) The simulated electrostatic potential energy<sup>12</sup> plotted as a  $x$ - $z$  section at  $y = 0$  (see Figure 4.1) across a  $p$ -type GaAs edge ( $x = 0$ ) assuming a homogeneous acceptor concentration of  $N_A = 2.75 \times 10^{18} \text{ cm}^{-3}$  inside the GaAs. The electrostatic potential energies of the STM tip and the GaAs  $y$ - $z$  plane at  $x = 0$  are set to  $\Phi_{TS} = -2 \text{ eV}$  and  $\Phi_{FS} = -0.8 \text{ eV}$ , respectively, with regard to the GaAs bulk. In this example the tip radius of curvature is  $r_T = 40 \text{ nm}$ . (b) Space charge density inside the GaAs across the same section as in (a).

#### 4.1.4 Comparability between 3D FEM Simulation and Experimental I-V Spectra

In order to extract the Schottky barrier height from the spectroscopic data (see section 4.2), one needs to obtain isolines from the 3D FEM simulation that are directly comparable with tunnel current isolines from the  $I$ - $V$  spectra taken along the space charge region. As it will turn out in this subsection, one can extract a quantity from the simulation that can be thought of as a measure for the tunnel current. In the following, this quantity is denoted as  $\Phi_{VT}$  and represents the energy range in which electrons tunnel solely through the vacuum barrier between tip and sample and not through the additional tip-induced space charge barrier as indicated in Figure 4.4. According to the 1D band model, for the case of a  $p$ -type junction  $\Phi_{VT}$  can be written as

<sup>12</sup> Here the reader is reminded that the local electrostatic potential energy  $\Phi = -eV$  differs from the electrochemical potential  $\mu_{ec}$  which is given by  $\mu_{ec} = \mu_c + \Phi$  where  $\mu_c$  represents the chemical potential.

$$\Phi_{VT} = eV_s - \Phi_{TIBB} - \Phi_{SCR} - (E_F^{SC} - E_V) \quad (4.11)$$

where  $V_s$  is the applied voltage between tip and sample,  $\Phi_{TIBB}$  is the tip-induced band bending,  $\Phi_{SCR}$  is the band bending of the space charge region,  $E_F^{SC}$  is the Fermi energy in the semiconductor bulk and  $E_V$  is the valence band maximum.  $\Phi_{TIBB}$  can be extracted from the FEM simulation. For any position of the tip along the space charge region of the semiconductor

$$\Phi_{TIBB} = \Phi_{sbb} - \Phi_{SCR} \quad (4.12)$$

applies. Here  $\Phi_{sbb}$  is simply the band bending at the surface of the semiconductor right below the tip.  $\Phi_{sbb}$  and  $\Phi_{SCR}$  are simulated in dependence of the distance between tip and interface (see also upper panel in Figure 4.5). With relation (4.12) also  $\Phi_{TIBB}$  can be extracted from that. However, if one inserts expression (4.12) into equation (4.11) it becomes apparent that one only needs to read out the surface band bending  $\Phi_{sbb}$  below the tip to obtain  $\Phi_{VT}$ . The same considerations can be transferred to the case of an *n*-type junction, the only difference being that electrons tunnel from the tip into the conduction band of the semiconductor [47].

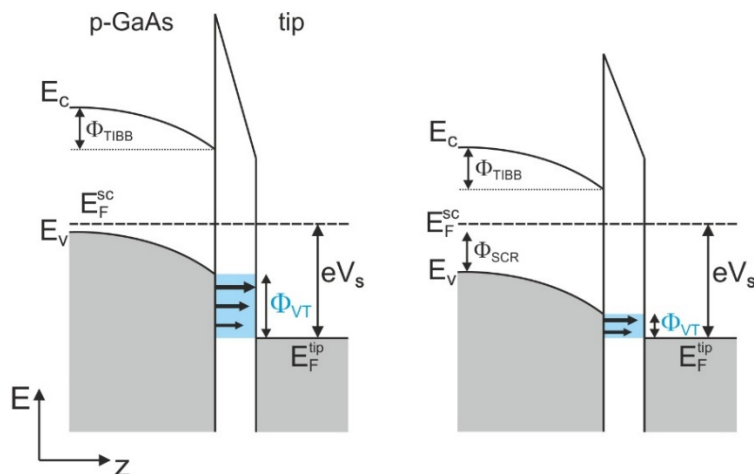


Figure 4.4: 1D energy band model to explain the derivation of the quantity  $\Phi_{VT}$ . The band schemes depict the case of a negative sample bias voltage  $V_s$  and (a) far away from the metal-semiconductor interface and (b) inside the space charge region (SCR) induced by the metal-semiconductor contact causing a rigid shift of the energy bands by  $\Phi_{SCR}$ . For more details see text.

Now it will be shown that the quantity  $\Phi_{VT}$  can be seen as a measure for the tunnel current  $I_T$  or in other words that there is a bijection between the energy interval  $\Phi_{VT}$  and the tunnel current  $I_T$ . This is only the case if one can exclude a significant tunnel current from any other energy interval than  $\Phi_{VT}$ . Another energy interval where tunneling can take place is the tip-induced space charge region inside the semiconductor  $\Phi_{TIBB}$  which

built up another finite barrier adjacent to the vacuum gap, see Figure 4.4. Feenstra and Stroscio [82] described the transmission through this tip-induced space charge region in an effective mass scenario and obtained the following expression for the corresponding transmission coefficient

$$T_{\text{TIBB}} = \exp\left(\frac{-w\sqrt{2m^*\Phi_{\text{TIBB}}}}{\hbar}\right) \quad \text{with} \quad w = \sqrt{\frac{2\varepsilon_r\varepsilon_0\Phi_{\text{TIBB}}}{Ne^2}} \quad (4.13)$$

where  $w$  is the width of the tip-induced space charge region,  $m^*$  is the effective mass of an electron or hole depending on the type of doping,  $\varepsilon_r$  is the relative permittivity of the semiconductor, and  $N$  is the doping concentration.

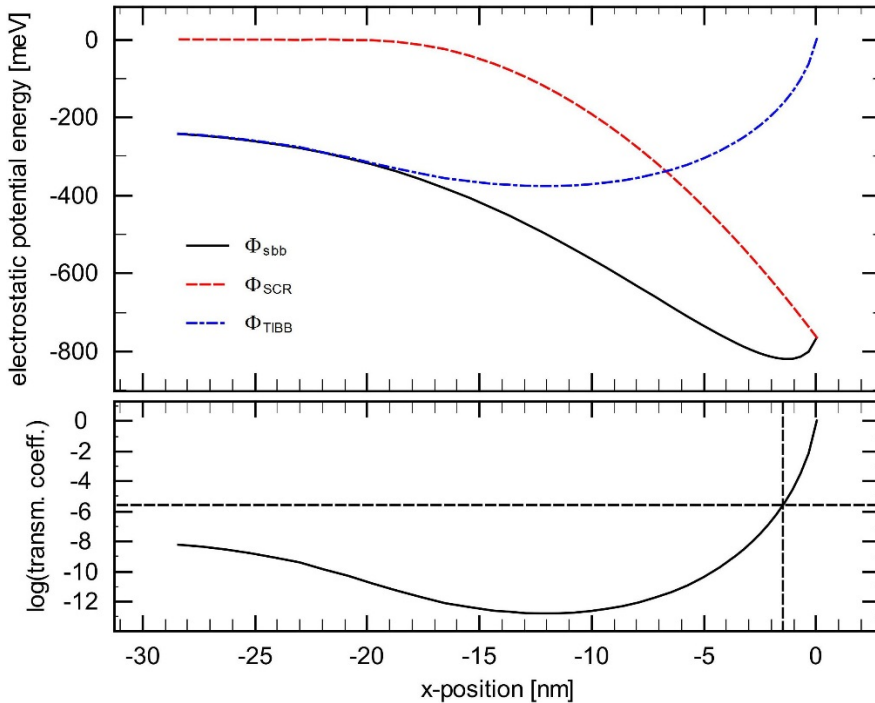


Figure 4.5: (upper panel) Plot of the surface band bending  $\Phi_{\text{sbb}}$ , the band bending of the space charge region  $\Phi_{\text{SCR}}$  in the semiconductor bulk, and the tip-induced band bending  $\Phi_{\text{TIBB}}$  along the space charge region of a *p*-type interface (interface is located at  $x = 0$  nm) [120]. For the simulation the acceptor concentration is taken to be  $N_A = 2.75 \times 10^{18}$  cm $^{-3}$  and  $\Phi_{FS} = -0.776$  eV ( $\Phi_{SB} = 0.78$  eV) is assumed. (lower panel) Logarithmic plot of the transmission coefficient along the space charge region calculated according to Ref. [82]. The dashed vertical line indicates up to which position the data was fitted (see also section 4.2).

In the lower panel of Figure 4.5  $T_{\text{TIBB}}$  is plotted logarithmically in dependence of the distance to the interface. The transmission coefficient is smaller than  $2 \times 10^{-6}$  for the relevant data (that are fitted up to 1.5 nm to the interface, see also chapter 4.2). If one assumes a maximal tunnel current in the order of 100 pA, the contribution from the tip-

induced space charge region to the tunnel current would be in the sub-fA range. This is well below the resolution limit of the experiment. Therefore, any contribution to the tunnel current from the tip-induced space charge region can be neglected in the analysis of the data. Thus, one finds a bijection between  $\Phi_{VT}$  and the tunnel current  $I_T$ : in general one can say that the larger  $\Phi_{VT}$  is, the larger also  $I_T$  will be. This relation applies at any distance of the tip to the interface. Hence, the bias voltages at which the same tunnel current  $I_{T,\text{ref}}$  was measured (a tunnel current isoline in the  $I$ - $V$  spectra along the space charge region) correspond to the bias voltages with a constant  $\Phi_{VT,\text{ref}}$  [47]:

$$V(x, I_{T,\text{ref}}) \cong V(x, \Phi_{VT,\text{ref}}) \quad (4.14)$$

This equivalence allows the direct comparison of the experimental and simulated data in a way that is described in more detail in chapter 4.2.

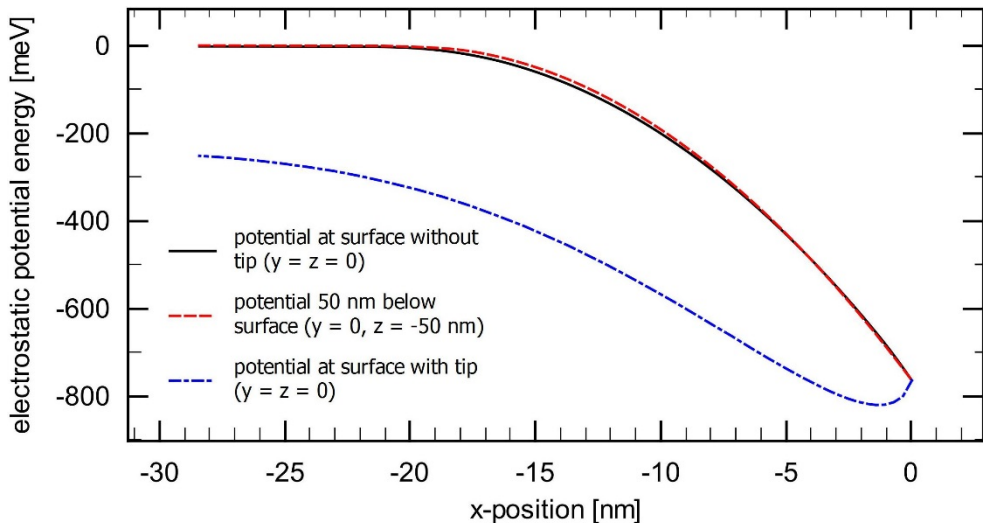


Figure 4.6: Electrostatic potential energy  $\Phi(x)$  along the space charge region of a *p*-type interface with  $N_A = 2.75 \times 10^{18} \text{ cm}^{-3}$  and  $\Phi_{FS} = -0.776 \text{ eV}$ . The black solid, the red dashed, and the blue dashed-dotted lines represent the potential energy at the surface without an STM tip, the potential energy 50 nm below the surface, and the potential energy at the surface with a scanning tip, respectively.

At the end of this section the significance of electrostatic effects due to the surface geometry of this approach is discussed. Therefore, the metal-semiconductor contact is simulated without the STM tip. The corresponding electrostatic potential energy  $\Phi(x)$  is plotted in Figure 4.6. The solid black and the red dashed lines represent the electrostatic potential energy  $\Phi(x)$  simulated without an STM tip at the surface and 50 nm below the surface, respectively. The two curves almost perfectly lie on top of each other. The blue dashed-dotted line demonstrates that the tip has a much stronger impact on the electrostatic potential at the surface (due to the tip-induced band bending) than the cross-sectional geometry itself. As a conclusion one can say that a purely electrostatic effect resulting from the

surface geometry is small and will not have a significant impact on the quantitative analysis of the Schottky contact.

## 4.2 Extracting the Schottky Barrier Height from the Data

The procedure described in this section was originally developed by Winking [47] for the extraction of the *n*-type Schottky barrier height. The experimental STS data are analyzed by using the simulated 3D FEM data, which is illustrated in Figure 4.7(a) for the case of a *p*-type junction. First of all, a constant current isoline is extracted from the topography-normalized STS data. The constant current isoline is taken deep inside the valence band to minimize any influence of charged dopant atoms nearby. In the illustrated case the  $I_T$  isoline is taken at a starting bias voltage of -0.75 V on the flat side of the isoline about 28 nm away from the interface. Since tunneling from the valence band of the free GaAs(110) surface into the tip starts at around  $V_{bias} = -0.1$  V the tunnel current isoline is taken at about 0.65 eV below the valence band edge.

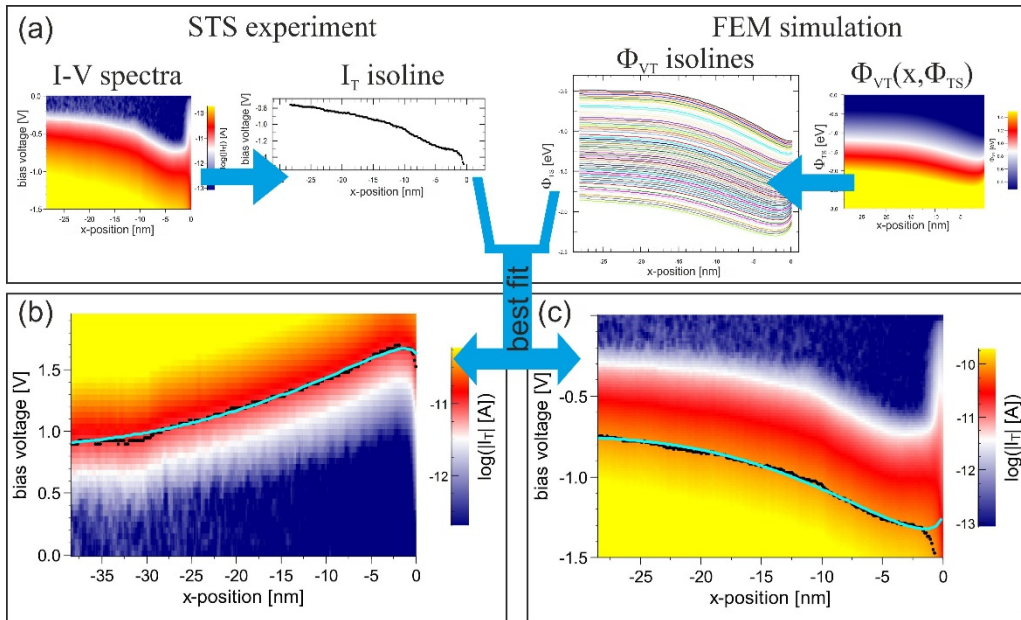


Figure 4.7: (a) Sketch illustrating how to find the best fit between experimental and simulated data [120]. More information can be found in the continuous text. In the lower panels the best fits between  $I_T$  and  $\Phi_{VT}$  isolines for the ideal (b) *n*-type [47] and (c) *p*-type Fe/GaAs(110) interface are shown.

In a next step,  $\Phi_{VT}$  isolines are extracted from a 3D FEM data set simulated for one particular Schottky barrier height in dependence of the tip-interface distance  $x$  and the electrostatic potential energy between tip and sample  $\Phi_{TS}$ . One has to keep in mind that the simulated data is plotted in dependence of the electrostatic energy between tip and sample

$\Phi_{TS}$  whereas the experimental data is plotted in dependence of the sample bias voltage  $V_s$ . Both quantities are linked by equation (4.2), i.e., the electrostatic potential energy is the sum of the bias voltage and the contact potential difference  $eV_{CPD}$  which is defined as the difference between the work function of the sample and the work function of the tip:

$$eV_{CPD} = \Phi_S - \Phi_T \quad (4.15)$$

Subsequently, the  $\Phi_{VT}$  isoline with the smallest deviation from the constant current isoline is found. As a measure for the deviation  $\sigma$  the square root of the mean squared error is taken:

$$\sigma = \sqrt{\frac{1}{n-1} \sum_{i=1}^n [eV_{\text{exp}}(x_i, I_T = \text{const}) - eV_{\text{sim}}(x_i, \Phi_{SB}, \Phi_{VT} = \text{const})]^2} \quad (4.16)$$

where  $n$  is the number of data points along the  $x$  axis,  $\Phi_{SB}$  is the Schottky barrier height for the respective simulated data set, and  $V_{\text{sim}}$  is the bias voltage along the simulated  $\Phi_{VT}$  isoline. The  $\Phi_{VT}$  isoline starting at a certain value of  $\Phi_{TS}$  on the flat side of the isoline farthest away from the interface with the smallest deviation is the best fit for a particular Schottky barrier height. The deviation of the simulated curve from the experimental curve is obtained for data points up to 1.5 nm off the interface. Closer to the interface, simulation and experiment can strongly deviate due to interface effects as can be particularly seen in Figure 4.7(c) for the *p*-type case.

If one repeats the fitting procedure for simulated data sets of different Schottky barrier heights, one obtains the plots shown in Figure 4.8. For each simulated data set with a particular Schottky barrier height the smallest obtainable deviation is plotted. This yields Schottky barrier heights of  $\Phi_{SB}^n = 0.94(3)$  eV [47] and  $\Phi_{SB}^p = 0.78(2)$  eV for ideal *n*-type and *p*-type Fe/GaAs(110) interfaces, respectively. The error is obtained from fitting at different starting voltages inside the bands ( $\pm 0.1$  V) and from fitting at different suitable (weakly affected by defects) positions along the interface in  $y$  direction. The best fit  $\Phi_{VT}$  isolines together with the tunnel current isolines for the ideal *n*-type and the *p*-type junction are shown in Figure 4.7(b) and (c). The simulated isoline for the *n*-type case describes the experimentally observed space charge region very nicely [47]. Also for the *p*-type case experimental and simulated isolines are in very good agreement up to 1.5 nm off the interface. The strong deviation at the interface between experiment and simulation are discussed in greater detail in section 4.3.

In the example in Figure 4.7(c) of a *p*-type junction with an acceptor concentration of  $N_A = 2.75 \times 10^{18} \text{ cm}^{-3}$  the average distance between two acceptors is  $\sim 7$  nm. Therefore, most scan lines in  $x$  direction along the space charge region will exhibit acceptor related features. In the tunnel current isoline from Figure 4.7(c) one also finds a weak signature of a Zn acceptor located in proximity to the scan line which is indicated by a small “bump” at  $x \approx -11$  nm. However, the extracted Schottky barrier height does not change

significantly for fits at different positions along the interface (in  $y$  direction) as long as the respective signatures of dopant atoms are weak.

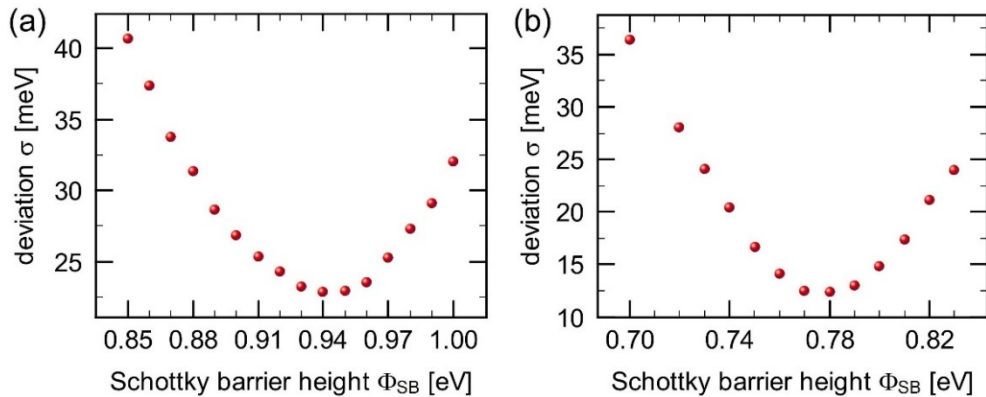


Figure 4.8: Deviation  $\sigma$  between experimental and simulated isolines for different Schottky barrier heights  $\Phi_{SB}$  [120] for the ideal (a)  $n$ -doped [47] and (b)  $p$ -doped [125] interface.

For the  $n$ -type Schottky barrier height the MIGS-and-electronegativity model predicts  $\Phi_{SB}^n = 0.96$  eV [137] which is in excellent agreement with the experimentally obtained value. However, the  $p$ -type Schottky barrier height extracted from the XSTS  $I$ - $V$  spectra cannot be explained in the framework of the MIGS-and-electronegativity model which predicts a value of  $\Phi_{SB}^p = 0.46$  eV [137] at room temperature. This deviation between experiment and MIGS-and-electronegativity model for the  $p$ -type junction will be discussed in greater detail in chapters 5 and 6.

By finding the simulated  $\Phi_{VT}$  isoline that has the smallest deviation from the experimental constant tunnel current isoline in the way described above, one not only obtains the Schottky barrier height of the system but also the simulated electrostatic energy between tip and sample  $\Phi_{TS}$  that corresponds to the bias voltage in the experiment. Therefore, by using equations (4.2) and (4.15) one can also extract the contact potential difference  $V_{CPD}$  between tip and sample [47]. For the  $n$ -type contact the best fit yields a contact potential difference of  $V_{CPD}^n = 0.0$  V. This is in good agreement with STM barrier height measurements on  $n$ -doped GaAs(110) by Teichmann [83]. For the  $p$ -type junction a contact potential difference of  $V_{CPD}^p = +0.62$  V is obtained. This is in the same range found in recent Kelvin probe force spectroscopy measurements on  $p$ -doped GaAs(110) [138]. Therefore, the contact potential differences that follow from the best fits are consistent with other most recent measurements.

In an overall perspective the fitting algorithm based on 3D FEM simulations of the electrostatic energy along the entire space charge region yields reasonable values for the contact potential difference between tip and sample and can therefore be regarded as a reliable tool to extract information on the electronic properties of Schottky contacts.

## 4.3 The Local Density of States at the Interface

As was already stated earlier in the introductory part of this thesis, up to the present day no experiment has been reported that yields a “complete” energetic and spatial map of the local density of states (LDOS) covering both the band gap region and the valence and conduction band at the interface. However, solely such a complete energetic and spatial LDOS map allows to check the validity of any proposed model. In chapter 3.2.3 highly resolved cross-sectional scanning tunneling spectroscopy (XSTS) at the ideal Fe/*p*-GaAs(110) interface has been applied to observe the continuum of interface-induced states in the band gap of the semiconductor. In this section it will be shown for the first time that XSTS in combination with 3D FEM simulations also allows to investigate the variation of the LDOS inside the valence and conduction band at the interface.

The experimental *I-V* spectra can be thought of as a superposition of an electrostatic part and an interface specific part. The electrostatic part contains both the band bending along the space charge region of the Schottky contact and the tip-induced band bending (TIBB). Both are described by essentially the same physics and are included in electrostatic 3D FEM simulations described in section 4.1. However, the second component of the experimental *I-V* spectra, namely the interface specific contribution, is due to charge rearrangements at the interface. These charge rearrangements are either due to MIGS (see section 3.2.3) or due to chemical bond effects energetically localized inside the valence band (see chapter 5). These interface specific contributions are not considered by the 3D FEM simulations. In the following it will be shown how the 3D FEM data is used to remove the electrostatic contribution from the experimental *I-V* spectra revealing the charge rearrangement at the interface.

As a first example the experimental *I-V* spectra along the *n*-doped sample from Figure 4.7(b) is taken. In the upper panel in Figure 4.9 the same data set is shown. In a first step the best fit between the tunnel current isoline deep inside the conduction band (black dots starting at a bias voltage of  $V_{bias} = +0.9$  V) and the  $\Phi_{VT}$  isoline (solid light blue line) from the 3D FEM simulation is found in the same way as described in section 4.2. The best fit is obtained for a Schottky barrier height of  $\Phi_{SB}^n = 0.94(3)$  eV and a contact potential difference of  $V_{CPD}^n = 0.0$  V. For a first visualization of deviations between experiment and simulation, several isolines at different starting voltages are plotted as depicted in the upper panel in Figure 4.9. The starting energy of  $\Phi_{TS}$  for the simulated  $\Phi_{VT}$  isolines is shifted by the same amount as the starting voltage of the corresponding tunnel current isolines is shifted. In this example the first  $I_T$  isoline starts at a sample bias voltage of  $V_s = +0.9$  V whereas the second  $I_T$  isoline starts at  $V_s = +0.8$  V. Therefore, the starting value of  $\Phi_{TS}$  for the second corresponding  $\Phi_{VT}$  isoline is also decreased by 0.1 eV. The same applies to all other isolines as well. In this way an explicit energetic relation between the experimental data and the simulated data is established. The solid yellow  $\Phi_{VT}$  isoline represents the conduction band edge in the electrostatic rigid band model. Anything below this band edge isoline is located inside the band gap. The voltage where the tunnel current from the tip into the conduction band sets in is measured on the

free GaAs(110) surface far away from the interface. In this case the onset voltage is at  $V_s = +0.25$  V and therefore the band edge isoline starts also at this voltage.

By plotting several  $\Phi_{VT}$  isolines over the corresponding tunnel current isolines one can get a first impression on deviations between experiment and simulation on a broader energetic range. The overall progression of the experimentally observed space charge region is reproduced quite nicely by the simulated isolines. However, a rather large deviation between experiment and simulation is found at  $x \approx -32$  nm. This deviation is due to an STM tip modification and therefore of no further relevance. Furthermore, smaller deviations between experimental and simulated isolines can be observed directly at the interface with the tendency that the tunnel current isolines lay energetically below the  $\Phi_{VT}$  isolines. Also important to note is that at the interface a small additional tunnel current inside the band gap (below the yellow band edge isoline) is observed. At the band edge this additional tunnel current extends about 2 nm from the interface.

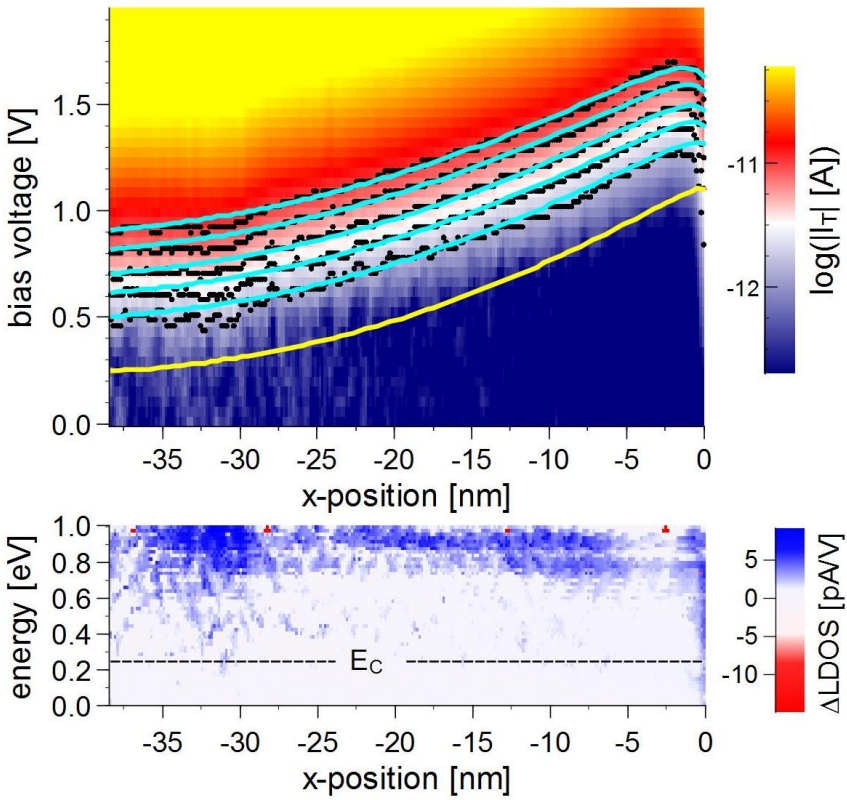


Figure 4.9: (upper panel) Color-coded plot of  $\log(|I_T|)$  for positive voltages of 250 topography-normalized  $I$ - $V$  spectra taken along the  $x$  direction across an ideal  $n$ -type Fe/GaAs(110) interface at set-point values of  $I_T = 100$  pA and  $V_s = +2$  V [121]. The interface is located at  $x = 0$  nm. Data was taken at room temperature [47]. The black dots represent isolines of constant tunnel current. The solid light blue and yellow lines are  $\Phi_{VT}$  isolines from 3D finite element simulations. The yellow isoline represents the conduction band edge in the rigid band model. (lower panel) Variation of the LDOS inside the conduction band for the  $n$ -type junction extracted from the STS data set above. The dashed black line indicates the conduction band minimum  $E_C$ .

So far solely tunnel current isolines and  $\Phi_{VT}$  isolines have been compared. In a next step the variation of the LDOS will be discussed. To obtain the LDOS variation the following algorithm is applied to the  $I$ - $V$  spectra:

- First of all,  $\Phi_{VT}$  isolines as in the upper panel of Figure 4.9 are extracted from the 3D FEM simulation. However, this time a larger amount of isolines ( $\sim 100$ ) is extracted for starting voltage values between  $V_s = 0.0$  V and  $V_s = +1.0$  V.
- In a next step the experimental tunnel current data is read out along these  $\Phi_{VT}$  isolines. In this way electrostatic effects (band bending of the space charge region and TIBB) are removed from the  $I$ - $V$  data.
- Subsequently, the read out tunnel current data is differentiated along the energy axis ( $dI/dV$ ) yielding a measure for the LDOS.
- Finally, the average LDOS offset far away from the interface (on the free surface) is subtracted from the data yielding the LDOS variation  $\Delta$ LDOS at the interface with respect to the free surface.

By applying this algorithm to the STS data, one obtains the lower panel of Figure 4.9. One finds the same tendencies as in the upper panel. A rather slight increase of LDOS is observed inside the conduction band directly at the interface with respect to the free surface. There is also a slight increase in LDOS deep inside the conduction band between  $x \approx -25$  nm and  $x \approx -5$  nm. A more pronounced increase of LDOS in the order of several pA/V is observed at  $x \approx -32$  nm which is due to the measurement artefact mentioned above.

The data for the ideal *p*-type Fe/GaAs(110) interface is shown in Figure 4.10. In the upper panel, the bump on the tunnel current isolines at  $x \approx -11$  nm can be attributed to a charged acceptor in proximity. Clearly, the *p*-type junction exhibits stronger deviations between the experimental tunnel current isolines and the simulated  $\Phi_{VT}$  isolines than the *n*-type junction. The largest deviation between simulated and experimental isolines is found directly at the interface. The spectra clearly show an additional tunnel current inside the band gap. At the band edge (solid yellow isoline) this additional tunnel current extends around 5 nm into the band gap, nicely showing the diverging character of the gap states at the band edge as described by the MIGS model (see section 1.3).

The lower panel in Figure 4.10 shows the corresponding LDOS variation with respect to the free surface for the *p*-type junction. The map exhibits two very prominent features: first of all, there is a very sharp decrease in LDOS deep inside the valence band directly at the interface (red color). This LDOS decrease with respect to the free surface is in the order of several hundred pA/V. The sharp decrease in LDOS sets in at  $\sim 0.35$  eV below the valence band maximum  $E_V$ . The second prominent feature is the increase in LDOS at the valence band edge. This LDOS increase with respect to the free surface is rather smeared out and extends around 5 nm from the interface into the semiconductor. The slight LDOS increase further inside the semiconductor can be attributed to the charged

acceptor at  $x \approx -11$  nm. It should be pointed out here that while the very small LDOS variation of only a few pA/V in the *n*-type case can be attributed to noise, for the *p*-type case a clear signal of the LDOS variation is observed being about 100 times stronger than for the *n*-type case.

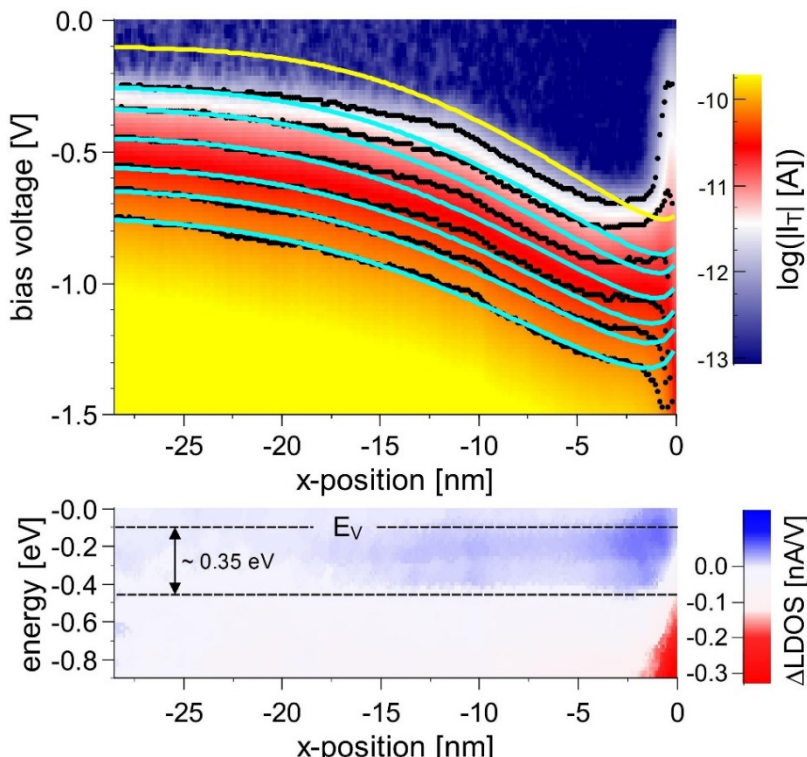


Figure 4.10: (upper panel) Color-coded plot of  $\log(|I_T|)$  for positive voltages of 250 topography-normalized  $I$ - $V$  spectra taken along the  $x$  direction across an ideal *p*-type Fe/GaAs(110) interface at set-point values of  $I_T = 150$  pA and  $V_s = -1.5$  V [121, 125]. The interface is located at  $x = 0$  nm. Data was taken at  $T = 6$  K. The black dots represent isolines of constant tunnel current. The solid light blue and yellow lines are  $\Phi_{VT}$  isolines from 3D finite element simulations. The yellow isoline represents the valence band edge in the rigid band model. (lower panel) Variation of the LDOS inside the valence band for the *p*-type junction extracted from the STS data set above. The upper dashed black line indicates the valence band edge  $E_V$ . The lower dashed black line indicates the energetic position where a sharp decrease of the LDOS at the interface sets in [121].

In conclusion, in this section a new approach to analyze  $I$ - $V$  spectra along the space charge region of a metal-semiconductor interface is presented. This approach based on 3D FEM simulation data allows to visualize the LDOS variation with respect to the free surface inside the conduction and valence band for *n*-type and *p*-type junctions, respectively. For the *n*-type interface a rather slight increase in conduction band LDOS is observed directly at the interface whereas the *p*-type case exhibits a strong decrease of LDOS deep inside the valence band. How this relates to the experimentally obtained Schottky barrier height will be discussed in chapter 5 after a short presentation of density functional calculations of the ideal Fe/GaAs(110) interface.

## 5 LDOS Model of the Interface

For a deeper understanding of the STS data that show the electronic properties of the ideal Fe/GaAs(110) interface presented in chapter 4, complementary density functional calculations have been performed. In the framework of this thesis a collaboration with the Peter-Grünberg-Institut of the Forschungszentrum Jülich has been initiated in which Dr. Ali Al-Zubi and Prof. Stefan Blügel conducted all density functional calculations presented in section 5.1. In this section the calculations are also compared to the experimental findings. In part, section 5.1 has been published literally in Refs. [120, 121]. In section 5.2, a model is developed that aims to qualitatively explain the relation between the interface charge distribution and the Schottky barrier height. The main idea of this model has been presented in Ref. [121].

### 5.1 DFT Calculations

The density functional theory (DFT) calculations presented in the following rely on the full-potential linearized augmented plane-wave method (FLAPW) as utilized in the FLEUR code [139]. In order to simulate the Fe/GaAs(110) interface, a slab of 9 ML GaAs(110) covered with 2 ML Fe on one side [see Figure 5.1] and 1 ML of hydrogen for passivation on the other side of the GaAs (not shown in Figure 5.1) has been taken as structural model [120].

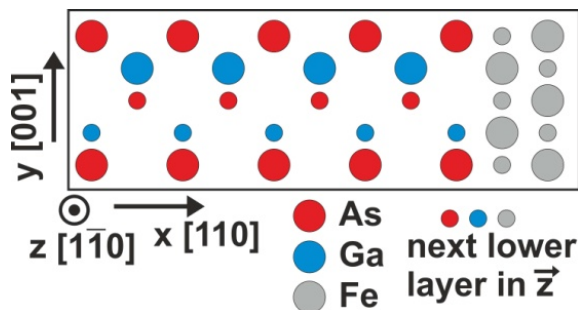


Figure 5.1: Slab of 9 layers GaAs and 2 layers Fe used for the DFT calculations. The passivating hydrogen layer on the left side of the GaAs film is not shown.

The resulting LDOS for the first 7 GaAs layers at the interface is shown in the upper panels in Figure 5.2(b). The plots show the sum of spin-up and spin-down density of states of the  $n$ th GaAs layer off the interface. The 4th, 5th, and 6th GaAs layers off the interface clearly exhibit a band gap with zero LDOS. The Fermi energy is located at the valence band edge. Approaching the interface, states in the band gap arise starting in the 3rd layer off the interface. These gap states become more and more prominent in the layers closer to the interface and reach a maximum LDOS in the interface layer. Furthermore, the asymmetric behavior of the gap states' decay lengths, with slightly larger lengths on the conduction band side, is in good agreement with the high-resolution  $dI/dV$  spectra of the MIGS shown in Figure 3.12 from section 3.2.3.

In section 4.3, the variation of the interface LDOS with respect to the free surface has been investigated. Similarly, from the DFT data an LDOS variation at the interface can be extracted by subtracting the LDOS of the reference “bulk” layer ( $n = 6$ ) from the LDOS of the  $n$ th layer. The result for each GaAs layer is plotted in the lower panels in Figure 5.2(b). In the first few GaAs layers at the interface the DFT data exhibit a sharp decrease in LDOS (transparent red area) with respect to the “bulk” at an energy of 0.35 eV below the valence band edge which is indicated by the horizontal dashed black line. The strongest drop in LDOS is observed in the interface layer. The drop in LDOS decreases with each layer further away from the interface. The data from STS measurements across the  $p$ -type interface presented in section 4.3 exhibit essentially the same behavior: at the interface the LDOS also decreases abruptly with respect to the free surface at 0.35 eV below the valence band edge [see Figure 5.2(a)]. Thus, the DFT calculations are in good agreement with both the experimental observation of MIGS and the surplus positive charge deep inside the valence band for the  $p$ -type interface.

Here it should be mentioned that the DFT calculations describe a bulk interface whereas in the STS experiment the interface is investigated in a cross-sectional surface geometry.<sup>13</sup> However, the cross-sectional STS approach yields an LDOS variation map that is stunningly similar to DFT predictions (see Figure 5.2). Therefore, the combination of

<sup>13</sup> At the end of section 4.1.4 it has been shown that the electrostatic effect resulting from the surface geometry is small.

cross-sectional STS and complementary DFT calculations offers an excellent probe to explore the microscopic origin of the metal-semiconductor interface dipole.

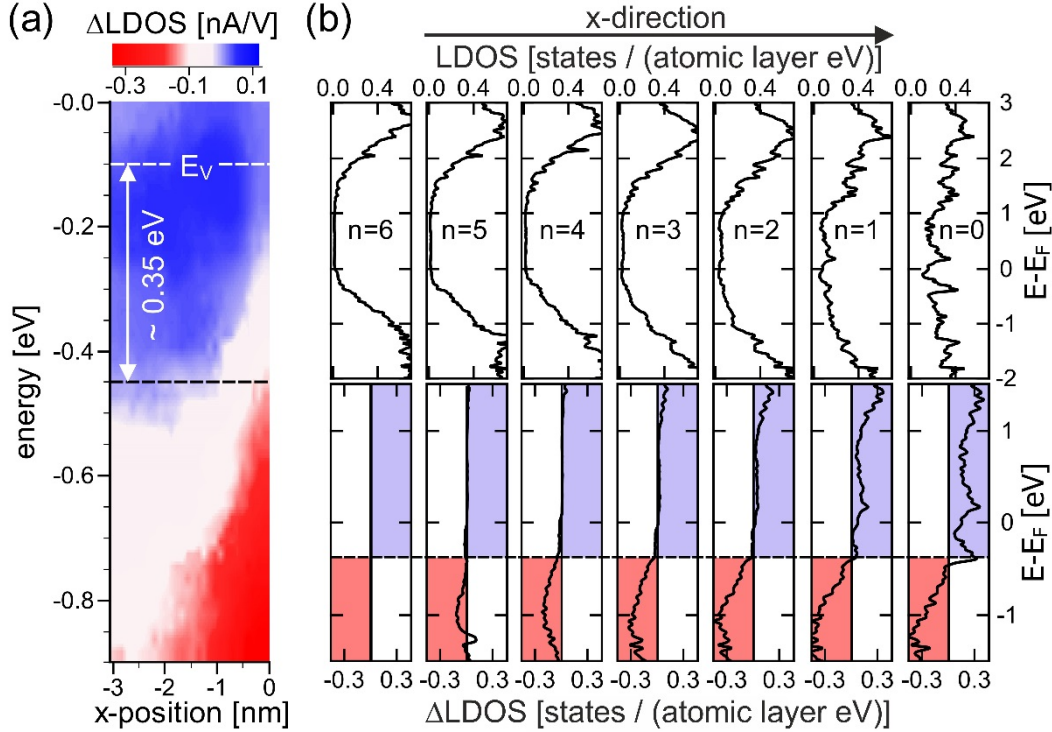


Figure 5.2: (a) Variation of the LDOS inside the valence band obtained from the STS data set for the *p*-type interface from Figure 4.10 (interface is located at  $x = 0$  nm). The white dashed line indicates the valence band maximum  $E_V$  [121]. (b) Density functional calculations for the ideal Fe/GaAs(110) interface: (upper panels) The total (sum of spin-up and -down) density of states of the  $n$ th GaAs layer off the interface. The Fermi energy is located at the valence band edge. (lower panels) Variation of the LDOS in the  $n$ th GaAs layer with respect to the 6th layer. At 0.35 eV below the valence band edge (horizontal dashed line) the DFT calculations show a sharp drop in  $\Delta$ LDOS (transparent red area) [121].

In order to obtain a better understanding of the origin of the surplus positive charge deep inside the valence band observed for the *p*-type interface, the DFT data are analyzed with respect to the LDOS at individual atomic sites. This analysis yields the plots in Figure 5.3. They show the (left) majority and (right) minority LDOS for the Fe interface layer and for the As atomic sites in the first 4 layers at the interface. The DFT data exhibit a strong hybridization between the majority states of Fe and As at the immediate interface (see left panels in Figure 5.3). The hybridization between Fe and As takes place over a broad energy range and extends also into the valence band. The sharp drop in LDOS with respect to the bulk layers is observed in the same energy range and can therefore be regarded as a direct consequence of the Fe-As hybridization. Here it also should be pointed out that from the strong hybridization between solely the majority states of Fe and As a spin-polarization in the GaAs interface layer is expected.

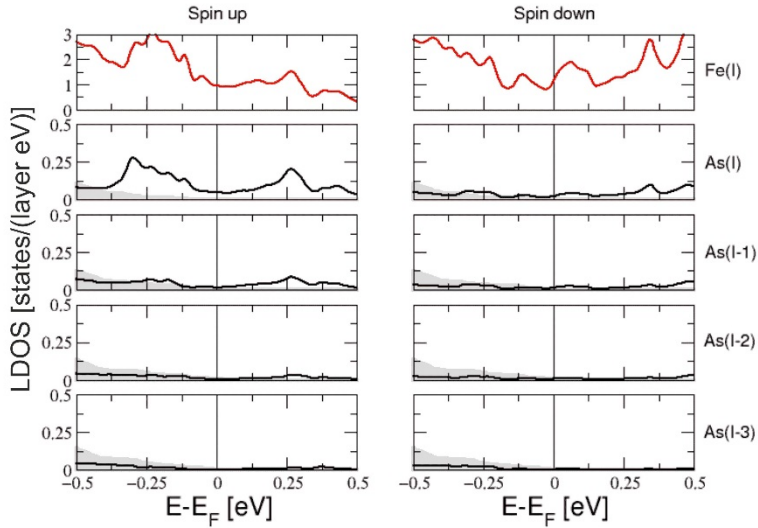


Figure 5.3: Calculated LDOS for Fe (upper panel, red solid line) and As for four different interface layers I to I-3 (black solid lines) for the majority states (left panels) and minority states (right panels). Gray shaded areas are the As local densities of states without Fe on-top of GaAs [120].

Moreover, one can also extract the Schottky barrier (SB) height from the DFT data. This is done by aligning the Fermi energies of the pure Fe monolayer and the clean uncovered GaAs(110) surface and adding the surface-dipole term. For the *p*-type Fe/GaAs(110) interface the DFT calculations yield a SB height of  $\Phi_{SB}^p = 0.69$  eV. The SB height obtained from XSTS measurements across an ideal *p*-type interface is  $\Phi_{SB}^p = 0.78(2)$  eV (see section 4.2) which deviates only by around 12 % from the value predicted by DFT calculations. The MIGS-and-electronegativity model (see section 1.3) predicts a SB height of  $\Phi_{SB}^p = 0.46$  eV and therefore cannot explain the experimental value.

Thus, only a detailed atomic description of the interface in the sense of the bond polarization model (see section 1.5), which is realized by DFT calculations, can explain the experimental *p*-type SB height and the variation of the LDOS inside the valence band. Furthermore, the DFT calculations also yield a realistic picture of the metal-induced states inside the semiconductor's band gap.

Therefore, cross-sectional STS measurements and DFT calculations show that the Fe/*p*-GaAs(110) interface dipole essentially comprises of two different contributions: the first part is represented by metal-induced gap states and the second part originates from bond polarization. The influence of each part on the SB height will be discussed in section 5.2. The overall interface dipole, i.e., the effective charge distribution at the interface, will also be of particular interest in the following section. Therefore, the effective charge across the interface is extracted from the DFT data.<sup>14</sup> This is accomplished by obtaining

<sup>14</sup> Since the DFT calculation does not take into consideration doping inside the semiconductor, the calculated effective charge does not include space charges from the space charge region.

the charge of each atom (sum of electrons and nucleus) and subsequently adding the charge of all atoms in the slab for each layer. The resulting effective charge for each layer is indicated by the black filled circles in Figure 5.4. It can be seen that the DFT calculations predict an overall negative surplus charge located inside the first two interface layers of the GaAs whereas an overall positive surplus charge is found inside the Fe.

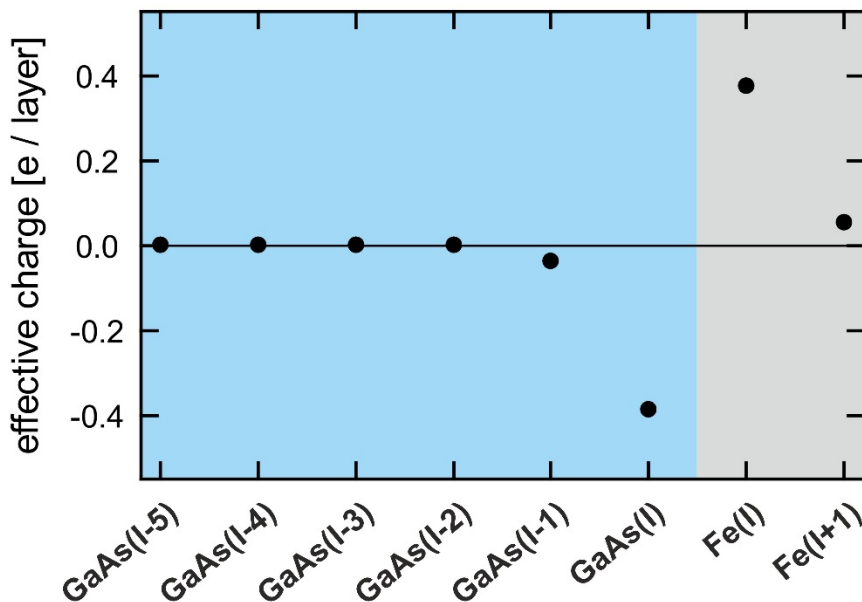


Figure 5.4: Effective charge density across the ideal Fe/GaAs(110) interface extracted from DFT calculations. The resulting effective charge for each layer is indicated by the black filled circles in units of elementary charge  $e$ . Data by courtesy of Dr. Ali Al-Zubi.

## 5.2 A Combined MIGS-and-BP-Model

In sections 4.2 and 4.3 cross-sectional STS measurements in combination with 3D FEM simulations yield the Schottky barrier height and information on the variation of the LDOS across the ideal Fe/GaAs(110) interface. In section 5.1, DFT calculations on the same interface have been presented that show a very good agreement with experiment. In this section a model is developed that qualitatively explains the relation between the charge distribution at the ideal interface and the Schottky barrier height.

Starting point for the following discussion is the upper sketch (case I) in Figure 5.5. Case I shows the Schottky-Mott model which does not consider any kind of interface states. According to equation (1.7) the Schottky-Mott relation yields a Schottky barrier (SB) height for the  $p$ -type Fe/GaAs interface of  $\Phi_{SB}^p \approx 1.1$  eV assuming an electron affinity of  $\chi_{GaAs} = 4.07$  eV [64], a band gap energy of  $E_g = 1.52$  eV [140], and an iron work function of  $\Phi_{Fe} \approx 4.5$  eV [134].

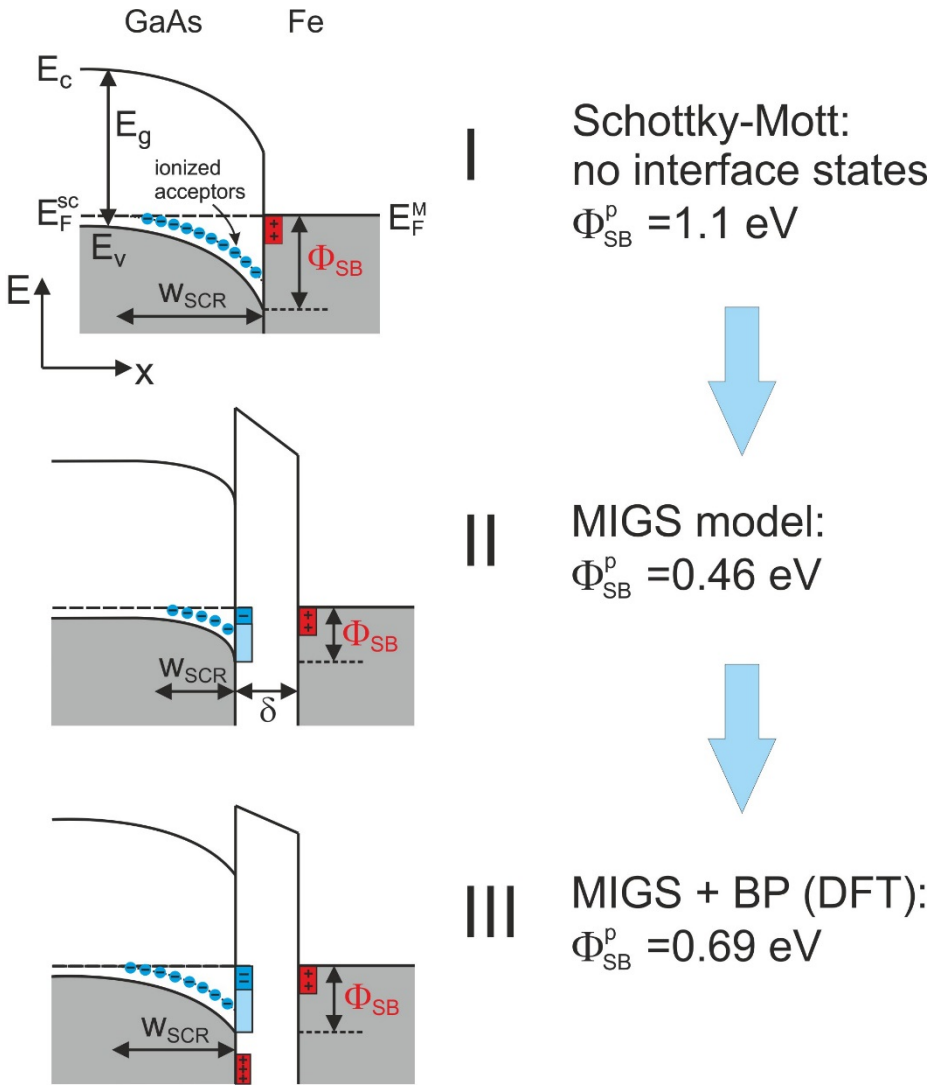


Figure 5.5: Sketch to explain the relation of Schottky barrier height (SBH) and interface dipole for a *p*-type Fe/GaAs(110) interface. Case I represents the case without interface states (Schottky-Mott). The width of the space charge region  $w_{SCR}$  and the SBH are large. Case II represents the MIGS model. Additional electron states in the band gap of the semiconductor screen the electric field which decreases the width of the space charge region inside the semiconductor and therefore also the SBH. Case III also takes bond polarization (BP) into consideration. Due to the additional positive charge on the semiconductor side the space charge region increases together with the SBH with respect to case II.

In a next step, interface states are taken into consideration. As described in section 1.2 these additional interface states on the semiconductor side and the metal side are separated by the distance  $\delta$  and constitute the so-called interface dipole. Case II in Figure 5.5 shows the interface dipole in the case of the MIGS model. Inside the band gap, states are induced by the metal and therefore add an additional negative charge on the GaAs side at the immediate interface. This additional negative charge screens the electric field from

the positive charge of the metal and therefore decreases the width of the space charge region inside the semiconductor which also yields a smaller SB height compared to case I which now is  $\Phi_{SB}^p = 0.46$  eV [137].

The cross-sectional scanning tunneling spectroscopy data from section 4.3 and the density functional calculations in section 5.1 clearly demonstrate an additional positive charge at the immediate interface on the *p*-type GaAs side inside the valence band. This situation is sketched by case III in Figure 5.5. The additional positive charge on the GaAs side due to bond polarization (BP) partially compensates the MIGS charge which is of opposite sign. The resulting charge distribution is the sum of the MIGS and the BP charges. Both parts are automatically included in the DFT calculations which yield an overall interface charge distribution that is positive on the metal side and negative on the semiconductor side of the interface as can also be seen in Figure 5.4 in section 5.1. Therefore, the combined MIGS-and-BP overall negative charge on the semiconductor (case III) still screens the electric field from the metal film but not as strong as the MIGS charge alone (case II). Thus, the space charge region extends deeper into the semiconductor and the SB height is increased compared to case II (DFT calculations yield a SB height of  $\Phi_{SB}^p = 0.69$  eV). Moreover, the SB height of the combined MIGS-and-BP charge distribution (case III) is still smaller than the SB height one would expect according to Schottky and Mott (case I). This somewhat simple model of a combined MIGS-and-BP-dipole qualitatively explains the experimentally obtained SB height of  $\Phi_{SB}^p \approx 0.78(2)$  eV which lies in between the predicted values by the MIGS model and the Schottky-Mott rule and is very close to the value predicted by the DFT calculations. In short, the combined MIGS-and-BP-model can be expressed as a rule: For the *p*-type Fe/GaAs(110) interface the negative MIGS charge decreases the predicted SB height and the positively charged states inside the valence band increase the predicted SB height.

For the sake of completeness it should be mentioned here that also the fact that the experimentally obtained *n*-type SB height of  $\Phi_{SB}^n = 0.94(3)$  eV is significantly larger than the value of  $\Phi_{SB}^n \approx 0.4$  eV that one would expect within the Schottky-Mott model. This can be explained by the negative MIGS charge on the GaAs side. For the *n*-type junction this additional negative charge decreases the screening of the electric field from the metal film which yields a larger space charge region and therefore also a larger SB height. As already mentioned in section 4.2, the experimentally obtained SB height for the *n*-type junction is in excellent agreement with the prediction by the MIGS-and-electronegativity model. From that it can be concluded that the SB formation at *n*-type Fe/GaAs{110} interfaces can be explained in the framework of the MIGS-and-electronegativity model [47].

Moreover, from the experimentally obtained SB heights for the *n*-type and *p*-type junction one can extract the relative energetic position of the valence band maximum  $E_V$  at the interface with respect to the Fermi level. For the *p*-type interface  $E_V$  is  $\sim 0.3$  eV further downward shifted than for the *n*-type case. Apparently, the larger energetic shift between the GaAs and Fe band structures in the *p*-type case significantly increases the im-

pact of the hybridization between the Fe and As atoms on the formation of the interface dipole.

## 6 LDOS for Differently Grown Interfaces

In this chapter the influence of different growth conditions on the electronic properties of the Fe/GaAs(110) interface and the Schottky barrier height is investigated. One interface is grown at room temperature and another interface is grown with an only 2 ML thin Fe film. The combined MIGS-and-BP-model from section 5.2 is used to analyze the effect of the observed charge distribution at the interface on the SB height of the system.

### 6.1 Room Temperature Grown Interface

In chapter 3, 4, and 5 the structure and the electronic properties of the ideal Fe/GaAs(110) interface have been investigated and the importance of metal-induced gap states and bond polarization models has been discussed. The ideal Fe/GaAs(110) interface is grown at low temperature (LT) as described in section 2.3. In order to understand the relevance of the ideality of the interface with regard to the influence on the Schottky barrier (SB) height and the charge distribution at the interface, it would be of great interest to investigate the same interface with a higher degree of disorder. As discussed in section 1.6 a higher degree of intermixing is achieved at higher growth temperatures. Furthermore, density functional calculations for a low (sub-monolayer) Fe coverage on GaAs(110) predict a penetration of the Fe atoms into the semiconductor surface [80]. Therefore, in this section a Fe/GaAs(110) interface is prepared by growing about 0.4 ML Fe at room temperature (RT) on top of a clean GaAs(110) surface right after the first cleavage at a base pressure of  $p < 5 \cdot 10^{-11}$  mbar. After waiting for about 1 hour, additional 6.6 ML Fe are grown at RT on top of the surface so that the overall thickness of the Fe film amounts to 7 ML. After the second cleavage perpendicular to the first one, the sample is investigated by means of cross-sectional STM.

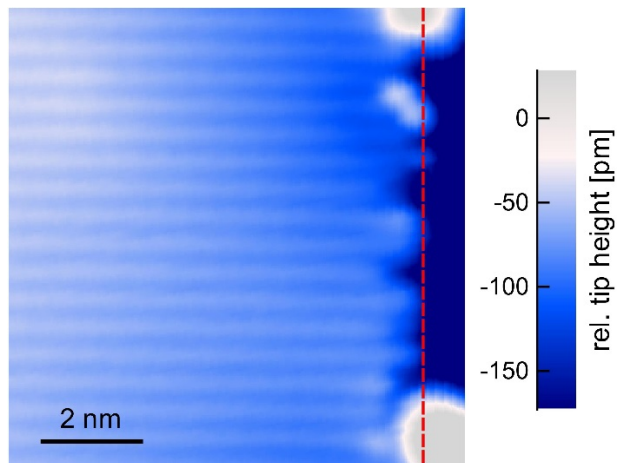


Figure 6.1:  $9 \times 9 \text{ nm}^2$  constant current topography along a RT grown Fe/GaAs(110) interface. The setpoint values are  $V_s = -1.5 \text{ V}$  and  $I_T = 50 \text{ pA}$ . The red dashed line indicates the position of the interface.

Figure 6.1 shows a constant current topography of the RT grown Fe/GaAs(110) interface taken at a negative bias voltage. In comparison to the LT grown interface in Figure 3.4, the RT grown interface is not as abrupt but rather frayed and significantly more As vacancies along the entire interface are found. As already mentioned in section 3.1.2, Winking [47] suggested that the occurrence of As vacancies might be explained by the strong Fe-As bonds and the ductile cleavage behavior of the Fe film during the second cleavage process. However, Siewers [127] conducted cross-sectional STM studies at the  $n\text{-GaAs}(110)\text{-(}\bar{1}\bar{1}0)$  edge without Fe film and also found sporadic As vacancies along the edge suggesting the second cleavage process itself being the reason for the As vacancies. Nevertheless, the representative STM topography in Figure 6.1 shows that the concentration of As vacancies at the interface is significantly larger for the RT grown interface than for the LT grown interface or the GaAs(110)-( $\bar{1}\bar{1}0$ ) edge without Fe film. Therefore, the Fe growth at RT seems to have changed the atomic structure at the interface with respect to the ideal interface. One possible explanation could be of similar quality as the one suggested by Winking [47] considering the strong Fe-As bonds: In the case of submonolayer RT growth one expects the penetration of Fe atoms into the GaAs(110) surface as predicted in DFT calculations by Grünebohm *et al.* [80] which are illustrated in Figure 1.9 in section 1.6. This creates a strong bond between the penetrating Fe atom and an As atom and cracks the bond between the Ga and the As atom in the surface layer. The subsequent Fe overgrowth might then bind the As atom in the interface layer very strongly to the Fe film which would increase the probability that the As atom is removed together with the ductile Fe film during the second cleavage process. Here a more advanced DFT study with a mixture of penetrating Fe atoms and a Fe film overgrowth might yield more clarity concerning this question.

In order to learn more about the SB height and the charge distribution at the RT grown interface, the interface is investigated by means of cross-sectional STS. The corresponding STS spectra along the space charge region for negative bias voltages are shown in the upper panel in Figure 6.2 and are plotted in the same convention as in sections 4.2 and 4.3. The black dots and the colored solid lines represent experimental constant current isolines and 3D FEM simulated constant  $\Phi_{VT}$  isolines, respectively.

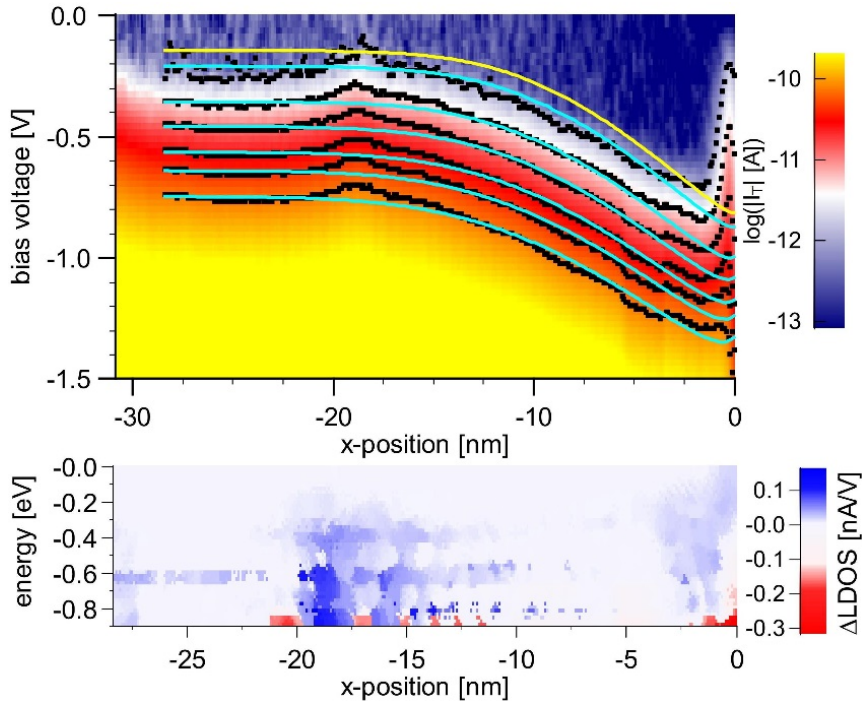


Figure 6.2: (upper panel) STS spectra across a RT grown *p*-type Fe/GaAs(110) interface for negative voltages taken at  $T = 6$  K with set-point values of  $I_T = 150$  pA and  $V_s = -1.5$  V. Interface is located at  $x = 0$  nm. The best fit between the experimental and simulated isolines deepest inside the valence band is obtained for a SB height of  $\Phi_{SB}^p = 0.74$  eV and a contact potential difference of  $V_{CPD} = -0.31$  V. The solid yellow isoline represents the valence band maximum. (lower panel) Corresponding LDOS variation map.

At around  $x \approx -19$  nm the experimental constant current isolines exhibit a “hump” with respect to the simulated isolines which is due to a Zn acceptor in proximity. At  $x \approx -4$  nm the experimental isolines show a small dip which is due to a tip modification. To obtain the SB height the simulated isolines are fitted to the constant current isoline deepest inside the valence band (starting at a sample bias voltage of  $V_s = -0.75$  V) as described in section 4.2. The best fit is obtained for a SB height of  $\Phi_{SB}^p = 0.74$  eV and a contact potential difference of  $V_{CPD} = -0.31$  V. Furthermore, inside the band gap (the solid yellow line indicates the valence band edge) an additional tunnel current is observed as it has been observed for the ideal interface in Figure 4.10 in section 4.3 as well.

The LDOS variation map is obtained in the same way as described in section 4.3. The LDOS variation map for the RT grown interface is shown in the lower panel in Figure 6.2. One noticeable feature is the increase of LDOS inside the valence band with respect to the free surface at around  $x \approx -19$  nm which is due to the charged acceptor in proximity. Even more striking is the fact that at the RT grown interface there is no sharp decrease of LDOS observed inside the valence band. Taking into consideration the LDOS model from Figure 5.5 in section 5.2, this observation can qualitatively explain the slight decrease of the SB height observed for the RT grown interface ( $\Phi_{SB}^p = 0.74$  eV) with respect to the LT grown interface ( $\Phi_{SB}^p = 0.78$  eV). A more detailed discussion in this regard follows in section 6.3. Similar LDOS variation maps are found along the entire RT grown interface so that the map in Figure 6.2 has a representative character. In contrast, the LT grown ideal Fe/GaAs(110) interface exhibits a sharp drop of LDOS starting about 0.35 eV below the valence band edge (see Figure 5.2) which is explained by a strong Fe-As hybridization at the interface as suggested by DFT calculations (see section 5.1). From that it can be concluded that the growth temperature has a significant impact on both the atomic structure of the Fe/GaAs(110) interface and the hybridization between Fe and As atoms at the interface. For the RT grown interface the degree of intermixing is increased and the impact of Fe-As hybridization on SB formation seems to be decreased with respect to the LT grown interface.

## 6.2 Influence of Fe Film Thickness

By means of the LT preparation technique presented in section 2.3 it is possible to grow Fe films of different thicknesses which enables the experimentator to investigate if the Fe film thickness has any influence on the electronic properties and the SB height of the Fe/GaAs(110) interface. The ideal Fe/GaAs(110) interface that has been investigated in chapters 3 and 4 was grown with 7 ML of Fe. In this section an interface is grown with only 2 ML of Fe and investigated by means of cross-sectional STS.

The upper panels of Figure 6.3 compare the STS *I-V* spectra of the (left) 7 ML Fe/GaAs(110) interface with the (right) 2 ML Fe/GaAs(110) interface. The extracted SB height for the case of 2 ML Fe amounts to  $\Phi_{SB}^p = 0.92$  eV which is 0.14 eV larger than for the case of the 7 ML Fe film. Furthermore, the additional tunnel current inside the band gap seems to be smaller for the 2 ML Fe/GaAs(110) interface which can be even better seen in the lower panels of Figure 6.3 that show an enlargement of the spectra at the immediate interface. Moreover, the LDOS variation maps show that the additional positive charge at the interface starting at  $\sim 0.35$  eV below the valence band edge is also present for the 2 ML case albeit not as pronounced as for the 7 ML case. Furthermore, the additional negative charge at the valence band edge for the 2 ML interface also seems to be significantly decreased with regard to the 7 ML interface.

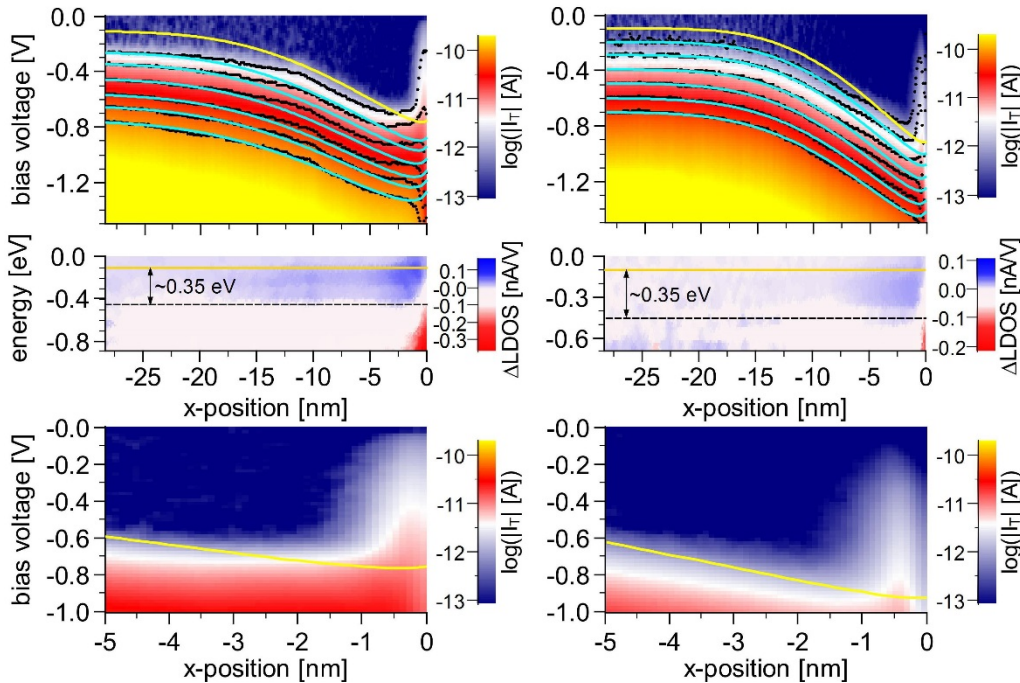


Figure 6.3: Comparison of LT grown ideal *p*-type Fe/GaAs(110) interfaces with a film thickness of (left) 7 ML Fe, an acceptor concentration of  $N_A = 2.75 \times 10^{18} \text{ cm}^{-3}$  [121, 125], and an extracted Schottky barrier height (SBH) of  $\Phi_{SB}^p = 0.78 \text{ eV}$  and (right) 2 ML Fe,  $N_A = 4.7 \times 10^{18} \text{ cm}^{-3}$ , and an extracted SBH of  $\Phi_{SB}^p = 0.92 \text{ eV}$ . The upper panels show the *I*-*V* spectra with isolines along the space charge region. Set-point values for both interfaces are  $I_T = 150 \text{ pA}$  and  $V_s = -1.5 \text{ V}$ . The center panels show the corresponding variation maps of the LDOS. And the lower panels show an enlargement of the *I*-*V* spectra at the immediate interface region. The solid yellow isoline represents the valence band maximum.

## 6.3 Discussion of the Different *p*-type Interfaces

In this thesis, in total three *p*-type Fe/GaAs(110) interfaces have been investigated. An overview of these three samples is provided in Table 6.1.

The two interfaces with 7 ML Fe, one of which was grown at LT and the other at RT, exhibit different Schottky barrier (SB) heights. The SB height for the RT grown interface of  $\Phi_{SB}^p = 0.74 \text{ eV}$  is a little smaller than the SB height for the LT grown interface of  $\Phi_{SB}^p = 0.78 \text{ eV}$ . This can be qualitatively discussed in the framework of the combined MIGS-and-BP-model that was developed in section 5.2. For the *p*-type Fe/GaAs(110) interface the screening of the electric field from the metal film by the interface-induced states behaves as follows: the more interface-induced states with an overall negative charge are present on the semiconductor surface, the more effectively they can screen the

electric field from the metal. As a consequence, the width of the space charge region of the semiconductor and the SB height decrease. In comparison to the ideal LT grown interface the RT grown interface does not exhibit the additional positive charge inside the valence band (VB). From that one can draw the conclusion that the overall charge on the semiconductor side at the immediate interface is more negative for the RT grown interface which is consistent with the observed smaller SB height. In the literature, SB heights obtained by electrical current-voltage measurements for *p*-type Fe/GaAs(001) interfaces grown at RT yield  $\Phi_{SB}^p = 0.6$  eV [130, 131]. This value for the SB height is even smaller than the value obtained for the partially intermixed RT grown interface from this thesis. However, the SB height from literature has only a limited informative value because due to the different atomic structures of the Fe/GaAs(001) and the Fe/GaAs(110) interface a comparison seems to be rather difficult.

Fe film	growth	$N_A = 2.75 \times 10^{18} \text{ cm}^{-3}$	$N_A = 4.7 \times 10^{18} \text{ cm}^{-3}$
7 ML	LT	$\Phi_{SB}^p = 0.78$ eV positive charge in VB	X
	RT	X	$\Phi_{SB}^p = 0.74$ eV <u>no</u> positive charge in VB
2 ML	LT	X	$\Phi_{SB}^p = 0.92$ eV positive charge in VB

Table 6.1: Comparison of experimental findings for *p*-type Fe/GaAs(110) interfaces. “VB” stands for “valence band”.

As shown in section 6.2 and summarized in Table 6.1, a smaller Fe film thickness increases the SB height. In the framework of the combined MIGS-and-BP-model from section 5.2, this could be attributed to a relative decrease of negatively charged interface-induced states in the semiconductor for the 2 ML Fe/GaAs(110) interface with respect to the 7 ML Fe/GaAs(110). This could be achieved by either increasing the positive charge inside the valence band or by reducing the negative charge inside the band gap due to the MIGS. An increase of the positive charge inside the valence band is not found in the LDOS variation map in Figure 6.3. The positive charge seems rather decreased compared to the interface with the thicker Fe film which would tend to decrease the SB height. However, the intensity of the tunnel current inside the band gap, which is also a measure of the addressable MIGS, appears to be decreased in the *I-V* spectra for the 2 ML Fe/GaAs(110) interface (right panels in Figure 6.3). A decrease in negative charge of the

MIGS should increase the SB height of the system as proposed by the combined MIGS-and-BP-model.

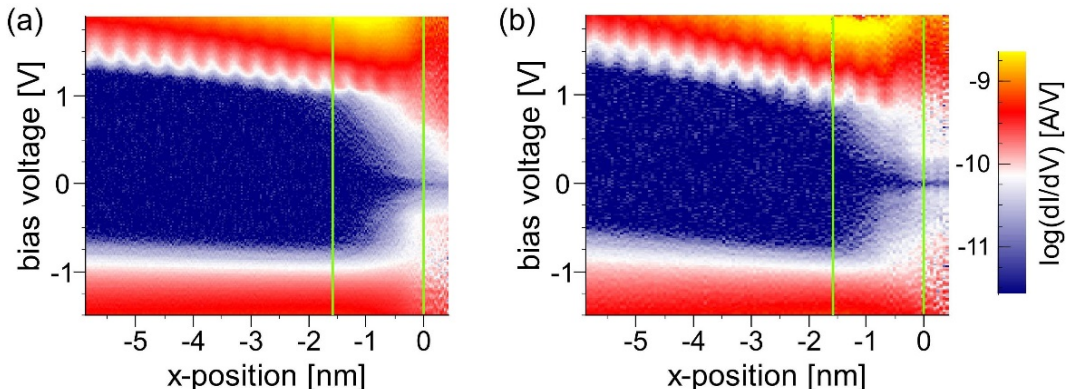


Figure 6.4: High-resolution  $dI/dV$  spectra with setpoint values of  $V_s = -1.5$  V and  $I_T = 150$  pA across a  $p$ -type Fe/GaAs(110) interface with an Fe film thickness of (a) 7 ML [121, 125] and (b) 2 ML. The vertical green solid lines indicate the position of the interface at  $x = 0$  nm and the extension of the metal-induced gap states around the band edges into the semiconductor.

The influence of the Fe film thickness on the MIGS is investigated by means of high resolution  $dI/dV$  spectra of the immediate interface for the 7 ML and the 2 ML case shown in Figure 6.4 (a) and (b), respectively. A comparison of the two spectra does not show a significant difference neither in the extension of the MIGS into the semiconductor nor in the intensity of the MIGS. However, a straightforward comparison between the spectra of the two different interfaces is difficult because the tip geometry for the two data sets is not exactly the same and might alter the measurement as well.

Furthermore, the work function of metallic thin films can be strongly influenced by quantum size effects [141, 142]. A self-consistent density functional calculation of freestanding ultrathin metal films using a jellium model revealed oscillations in the work function as a function of film thickness [141]. At certain film thicknesses new eigenfunctions along the confined direction of the film start contributing to the electron density [141]. This leads to oscillating electron densities at and outside the surface as a function of film thickness. The associated oscillation in the strength of the surface dipole directly translates into an oscillation in the work function. In this model, oscillations in the work function of about 1 eV in the monolayer thickness regime were found [141]. Therefore, for the ultrathin Fe films on the GaAs(110) investigated in this thesis this quantum size effect could also have an influence on the work function of the Fe films. According to equation (1.10) a relative decrease of the metal work function would increase the Schottky barrier. Therefore, in the framework of the quantum size effect model the large Schottky barrier for the Fe/GaAs(110) interface with 2 ML Fe ( $\Phi_{SB}^p = 0.92$  eV) might be explained by a decreased Fe film work function with respect to the 7 ML Fe ( $\Phi_{SB}^p = 0.78$  eV) film. To verify if an actual oscillatory behavior of the Fe film work function as a function of film thickness is on hand, more measurements for samples with different Fe film thicknesses

would be necessary. Here it should also be mentioned that MOKE measurements show a spin reorientation transition at a Fe film thickness of 4–5 ML with the easy axis turning from the in-plane <110> direction into the in-plane <001> direction for thinner films [46, 47, 52]. For 2–3 ML Fe films an out-of-plane magnetization is observed as well [52] (see also chapter 7). This difference in magnetization orientation might also have an effect on the Schottky barrier.

In the following we will discuss the question if the different acceptor concentrations of the samples (see Table 6.1) might have an influence on the SB height. The effect of the doping concentration on the SB height of Pb/Si(111) interfaces is discussed by Slomski *et al.* [143]. Here their model is transferred to the case of the Fe/GaAs(110) interface and sketched in Figure 6.5. According to their model the interface dipole is placed inside a parallel plate capacitor that consists of the space charge as one “plate” and the charge in the metal as the other “plate” (see lower panels in Figure 6.5). The electric field of this plate capacitor (PC) is derived, e.g., in Ref. [55] and can be written as

$$|\overrightarrow{E_{PC}}| = \sqrt{\frac{2eN_A(\Phi_{SB} - E_F^{SC} + E_V)}{\varepsilon_r \varepsilon_0}} \quad (6.1)$$

where  $e$  is the elementary charge,  $N_A$  is the acceptor concentration,  $\varepsilon_r$  is the relative permittivity of the semiconductor,  $\varepsilon_0$  is the vacuum permittivity, and the quantities  $\Phi_{SB}$ ,  $E_F^{SC}$ , and  $E_V$  are depicted in the upper panels of Figure 6.5. It is important to note that the electric field of the plate capacitor increases with increasing acceptor concentration. For Fe in contact with *p*-type GaAs the negative “plate” of the capacitor is on the semiconductor side consisting of the charged acceptors in the space charge region, while an equally large positive charge is located on the Fe side. The overall charge distribution for the Fe/GaAs(110) interface was obtained from DFT calculations in section 5.1 and an overall negative charge on the GaAs side and a positive charge on the Fe side. Therefore, the electric field of the interface dipole and the electric field of the capacitor are directed parallel to each other for the discussed *p*-type interface. Now, an increase in acceptor concentration yields a larger electric field in the capacitor (see lower right panel in Figure 6.5) and therefore also increases the overall interface dipole voltage drop  $V_{int}$  (see upper right panel in Figure 6.5). As a consequence, the energy bands at the space charge region of the GaAs are shifted upwards and the SB height is decreased.

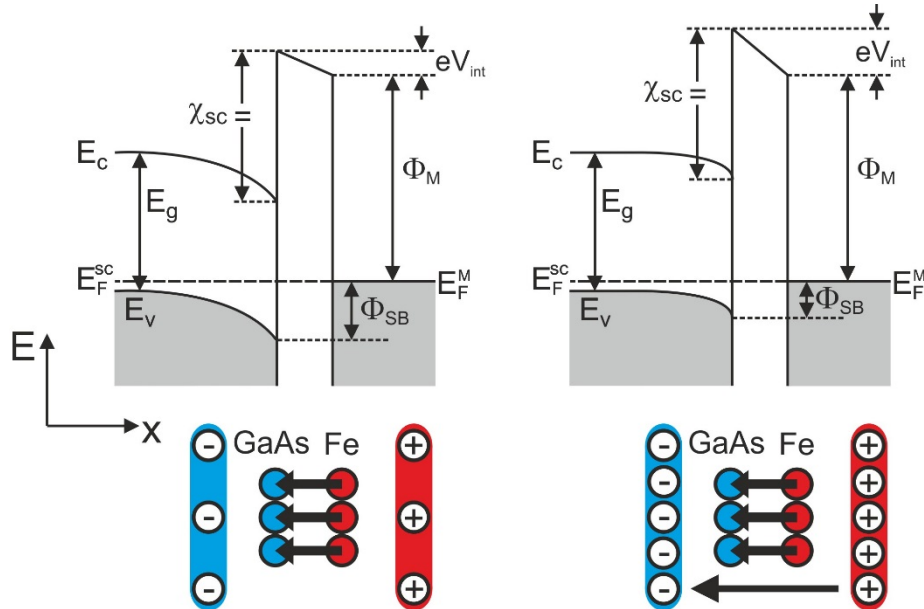


Figure 6.5: Model of SBH dependence on acceptor concentration. The idea is adopted from Ref. [143] and adapted to the *p*-type Fe/GaAs interface. The band sketch is shown for (a) a lightly and (b) a heavily doped semiconductor.

Thus, according to the model a higher acceptor concentration yields a smaller SB height. The decrease in SB height can be estimated using the equation [55]

$$\Delta\Phi_{SB} = -\frac{\delta\varepsilon_{GaAs}\varepsilon_0}{\varepsilon_{int}\varepsilon_0 + e\delta D_{int}} |\overrightarrow{E_{PC}}| \quad (6.2)$$

where  $\delta$  is the separation of the positive and negative side of the interfacial dipole,  $\varepsilon_{int}$  is the relative permittivity of the interfacial layer, and  $D_{int}$  is the density of interface states. If we assume  $\delta \approx 2 \text{ \AA}$  (see Figure 5.4), an upper limit of  $D_{int} \approx 0.4/(4 \times 5.65 \text{ \AA}^2 \text{ eV}) \approx 1.8 \times 10^{18} \text{ eV}^{-1} \text{ m}^{-2}$  (see Figure 5.4),  $\varepsilon_{int} \approx \varepsilon_{GaAs}$ , and  $\Phi_{SB} - E_F^S + E_V = 0.8 \text{ eV}$ , the Schottky barrier decreases by  $\Delta\Phi_{SB} \approx -10 \text{ meV}$  and  $\Delta\Phi_{SB} \approx -13 \text{ meV}$  for acceptor concentrations of  $N_A = 2.75 \times 10^{18} \text{ cm}^{-3}$  and  $N_A = 4.7 \times 10^{18} \text{ cm}^{-3}$ , respectively. Therefore, when increasing the acceptor concentration from  $N_A = 2.75 \times 10^{18} \text{ cm}^{-3}$  to  $N_A = 4.7 \times 10^{18} \text{ cm}^{-3}$  for the Fe/GaAs(110) samples, one would expect a decrease of the Schottky barrier by less than 10 meV.

However, the LT grown Fe/GaAs(110) with only 2 ML of Fe and an acceptor concentration higher than for the sample grown with 7 ML Fe shows a SB height which is larger compared to the one of the more heavily doped sample with 7 ML Fe. Therefore, in this case the difference in Fe film thickness seems to have a much stronger impact on the SB height than the difference in acceptor concentration does. Additional studies where the doping concentration is varied but all other parameters are kept constant could contribute to a better understanding.

In conclusion, in this chapter the influence of different growth conditions on the SB height and the charge distribution at the interface has been investigated. The RT growth

seems to have a significant impact on the atomic and electronic structure of the interface. Future studies at even higher growth temperatures and complementary DFT calculations with different interface structures might yield more information in this regard. Furthermore, the measurements show that the Fe film thickness significantly alters the SB height which might be related to modifications of the metal-induced gap states or quantum size effects. Further systematic experimental studies and corresponding DFT calculations with different film thicknesses could shed more light on the physics. The dependence of the electronic structure on the Fe film thickness might also be related to the film thickness dependence of the magnetic properties of the ideal Fe/GaAs(110) interface that are investigated and discussed in chapters 7 and 8.

## 7 Magnetic Properties of the Fe/GaAs(110) Interface

Starting point of this chapter is the discovery of unique magnetic properties of ultrathin (2–3 ML thin) low-temperature (LT) grown Fe films on GaAs{110} that have been presented in the diploma thesis of Iffländer [52]. He conducted *in situ* magneto-optic Kerr effect (MOKE) measurements in longitudinal geometry and found easy axis behavior along the in-plane [001] direction. More strikingly, he discovered a reversal of the sense of the hysteresis curve after turning the sample by 180° into the [00 $\bar{1}$ ] direction (leaving the external magnetic field and the light vectors unchanged) as shown in Figure 7.1. This can be explained by a superposition of an in-plane and an out-of-plane magnetization component [52, 144, 145].

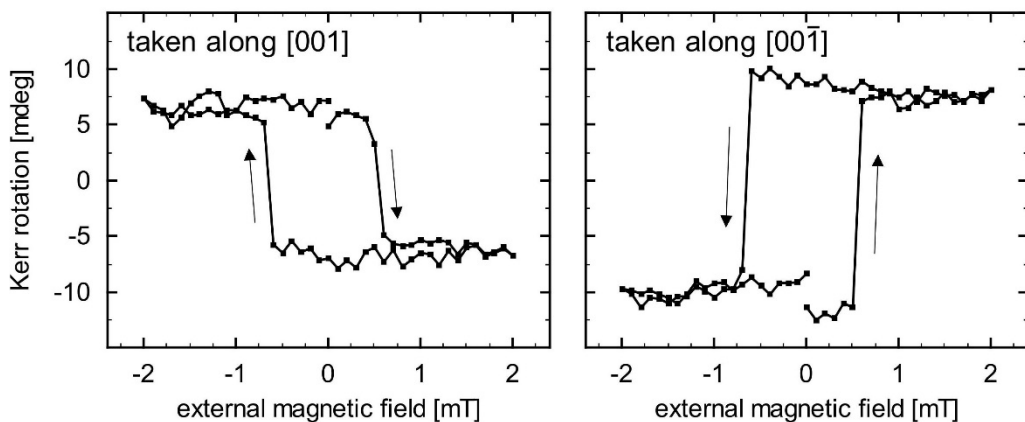


Figure 7.1: *In situ* Kerr rotation signal measured in longitudinal geometry along (left) [001] and (right) [00 $\bar{1}$ ] direction for a LT grown 2.5 ML thick Fe film on GaAs(1̄10). A reversal of the sense of the hysteresis curves is observed for the two different geometries [52].

In this thesis the magnetic properties of the ultrathin LT grown Fe films on GaAs{110} are investigated in greater detail by means of additional *in situ* MOKE measurements

followed by a more in-depth discussion of the experimental data. In order to give the reader a thorough overview, all findings – including the ones from Iffländer's diploma thesis [52] – are presented here.

In section 7.1, the observed reversal of the sense of the hysteresis curves is discussed in detail, and it is explained how this relates to a superposition of an in-plane and out-of-plane magnetization [52]. Subsequently, the dependence of the Kerr signal on the orientation of the surface is presented in section 7.2 and we will see that the out-of-plane magnetization originates from the interplay between the direction of the Fe film magnetization and the space inversion asymmetry of the GaAs{110} [52]. In section 7.3, additional MOKE measurements with the rotatable in-plane magnetic field will be presented. These measurements give more insight into the easy and hard axis behavior of the sample and show that only by applying a minimum magnetic field along the <001> in-plane direction the magnetization can be switched. Similar data has been presented in the Bachelor's theses of Rolf-Pissarczyk [146] and Weikert [115] which were supervised by the author of this PhD thesis. In section 7.4, it is shown that the type of doping does not have any influence on the observed magnetic anisotropy of the LT grown Fe/GaAs{110} interfaces [52]. In section 7.5, the evolution of the Kerr signal and the magnetic anisotropy in dependence on the Fe film thickness is presented [52]. This quantitative information is particularly important for the discussion in section 7.6: In subsection 7.6.1, a qualitative and quantitative discussion shows that a simple canted film magnetization cannot explain the experimental data [52]. The investigation of room temperature (RT) submonolayer pre-grown samples with an intermixed interface in subsection 7.6.2 shows that the interface quality is crucial for the observation of the out-of-plane magnetization component [52]. This leads directly to subsection 7.6.3 where a possible interface magnetization is discussed. In this context, additional measurements with out-of-plane applied magnetic fields are presented that confirm a unidirectional magnetic anisotropy. Similar data has been presented in the Bachelor's theses of Rolf-Pissarczyk [146] and Weikert [115]. Furthermore, in subsection 7.6.3, an extended canted magnetization model with a magnetic interface layer is presented that also cannot explain the experimental data. The subsection closes with the outlook on a possible interpretation of the data involving the Dzyaloshinskii-Moriya interaction [147, 148].

The geometric arrangement of the MOKE measurements in this chapter differs from the cross-sectional geometry from chapters 3 to 6. The MOKE measurements are conducted in top-view geometry with the Fe film grown in  $z$  direction and therefore the coordinate system shown in Figure 7.2 is used in the following. As already described in section 2.2.2, the MOKE setup allows the free rotation of the plane of incidence of the laser beam as well as the free orientation of the external magnetic field with respect to the sample. The coordinate system for all four possible sample orientations in  $z$  direction is defined in Table 7.1.

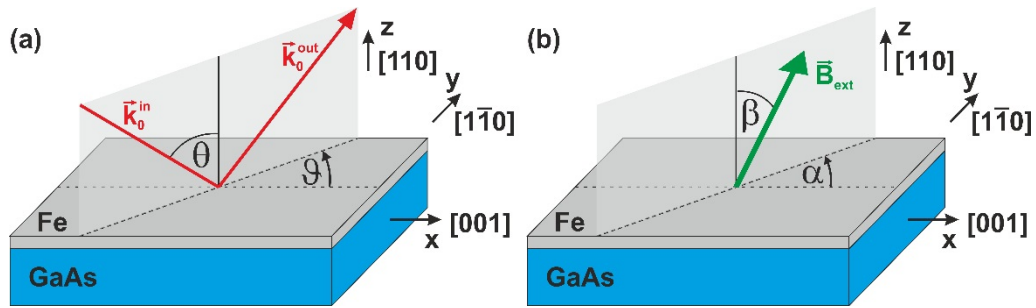


Figure 7.2: Coordinate system for the MOKE measurements. (a) The angle of incidence  $\theta$  of the incoming laser beam is adjustable. The plane of incidence can be rotated by any arbitrary angle  $\vartheta$  with respect to the [001] direction. (b) The direction of the external magnetic field  $\vec{B}_{\text{ext}}$  can be adjusted to any arbitrary in-plane angle  $\alpha$  and out-of-plane angle  $\beta$ .

sample orientation in z direction	in-plane magnetic field and plane-of-incidence direction			
	$\alpha = \vartheta = 0^\circ$	$\alpha = \vartheta = 90^\circ$	$\alpha = \vartheta = 180^\circ$	$\alpha = \vartheta = 270^\circ$
[110]	[001]	[1̄10]	[00̄1]	[̄110]
[̄1̄10]	[001]	[̄110]	[00̄1]	[1̄10]
[̄110]	[001]	[110]	[00̄1]	[̄110]
[1̄10]	[001]	[̄110]	[00̄1]	[110]

Table 7.1: For the four possible sample orientations in z direction the rotation angles of the magnetic field and the laser plane of incidence are listed together with the corresponding sample orientation indices.

## 7.1 Magnetic Anisotropy of Ultrathin Fe Films on GaAs(110)

In this section the magnetic properties of low-temperature (LT) grown Fe/GaAs{110} interfaces are investigated by *in situ* MOKE measurements. The samples were prepared as described in section 2.3.

In Figure 1.8 of section 1.6 it has already been discussed that for ultrathin Fe films on GaAs{110} a spin reorientation transition takes place. At a film thickness of around 10 monolayers (ML) the Fe film has the magnetic easy axis (EA) in <110> direction. For Fe film thicknesses below 4 ML the EA shifts into the <001> direction [46, 47, 52]. Figure 7.3 shows an *in situ* longitudinal Kerr measurement of a 10 ML thick Fe film on the GaAs(1̄10) surface. At a rotation angle of the in-plane magnetic field and the plane of incidence of the laser beam of  $\alpha = \vartheta = 90^\circ$  a sharp square-shaped hysteresis curve is detected indicating the EA along the <1̄10> direction. Furthermore, if the plane of incidence and the magnetic field are rotated by  $180^\circ$  with respect to the sample to  $\alpha = \vartheta = 270^\circ$  (or the sample itself is rotated as actually done in the experiment), essentially

the same signal is detected. In both cases the Kerr rotation amounts to  $\sim 12$  mdeg and the sense of the hysteresis curve is counterclockwise. Exactly this behavior is expected for an in-plane EA in  $<\bar{1}10>$  direction.

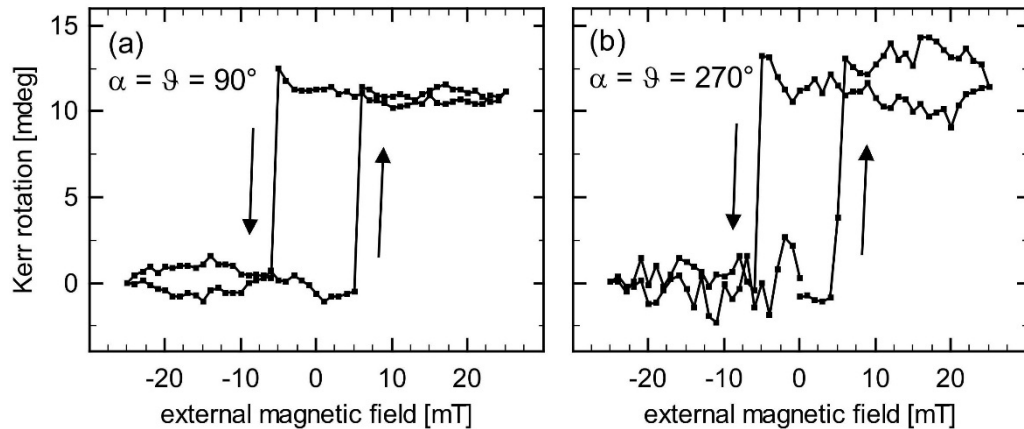


Figure 7.3: *In situ* longitudinal MOKE measurement for a 10 ML thick Fe film grown on *p*-type GaAs( $\bar{1}\bar{1}0$ ). The Kerr rotation is plotted against the applied magnetic field. Data was taken with an in-plane magnetic field ( $\beta = 90^\circ$ ) and at an angle of incidence of  $\theta = 15^\circ$  and a laser wavelength of  $\lambda \approx 632.8$  nm.

In contrast, samples with Fe films in the thickness range of 2—3 ML show a completely different behavior as has been shown for the first time in the diploma thesis of Iffländer [52]. The left panel of Figure 7.4(a) shows the Kerr rotation of a longitudinal (in-plane) MOKE measurement of a 2.5 ML thick Fe film on a GaAs( $\bar{1}\bar{1}0$ ) surface with  $\alpha = \vartheta = 0^\circ$ . The sharp square-shaped hysteresis curve with coercive fields of less than 1 mT indicates that the EA is parallel to the [001] direction (which corresponds to the rotation angles  $\alpha = \vartheta = 0^\circ$ ). The sense of the obtained hysteresis curve is clockwise as indicated by the arrows. If now the in-plane magnetic field and the plane of incidence are rotated by  $180^\circ$  to  $\alpha = \vartheta = 180^\circ$ , which corresponds to a rotation of the sample by  $180^\circ$  as actually done in the experiment, the hysteresis is still sharp and square-shaped but the sense of the hysteresis curve is reversed and thus counterclockwise [see right panel in Figure 7.4(a)]. Also the absolute values of the Kerr rotation in both cases differ from each other.

A first approach to understand this data is to assume that it can be described as a superposition of an in-plane and an out-of-plane magnetization component. It should be pointed out here that in section 7.6 it will become apparent that this approach cannot explain the magnetic behavior of the sample system in its entirety. Nevertheless, this first approach paves the way for a deeper understanding of the obtained data. The sketches in Figure 7.4(b) illustrate the idea of superimposed in-plane and out-of-plane magnetization components. Case A represents the situation where the external in-plane magnetic field and the plane of incidence are set up to  $\alpha = \vartheta = 0^\circ$  (parallel to the [001] direction). In the following, a whole hysteresis cycle for case A is discussed. The initial situation is denot-

ed by A1 where the in-plane magnetization points into [001] direction which is represented by the dashed blue arrow. The out-of-plane component points downwards and is indicated by the dotted magenta arrow. The corresponding longitudinal (in-plane) and polar (out-of-plane) Kerr signals are represented by A1L and A1P in the dashed blue hysteresis and the dotted magenta hysteresis curves below. The overall Kerr signal is illustrated by the solid black hysteresis curve.

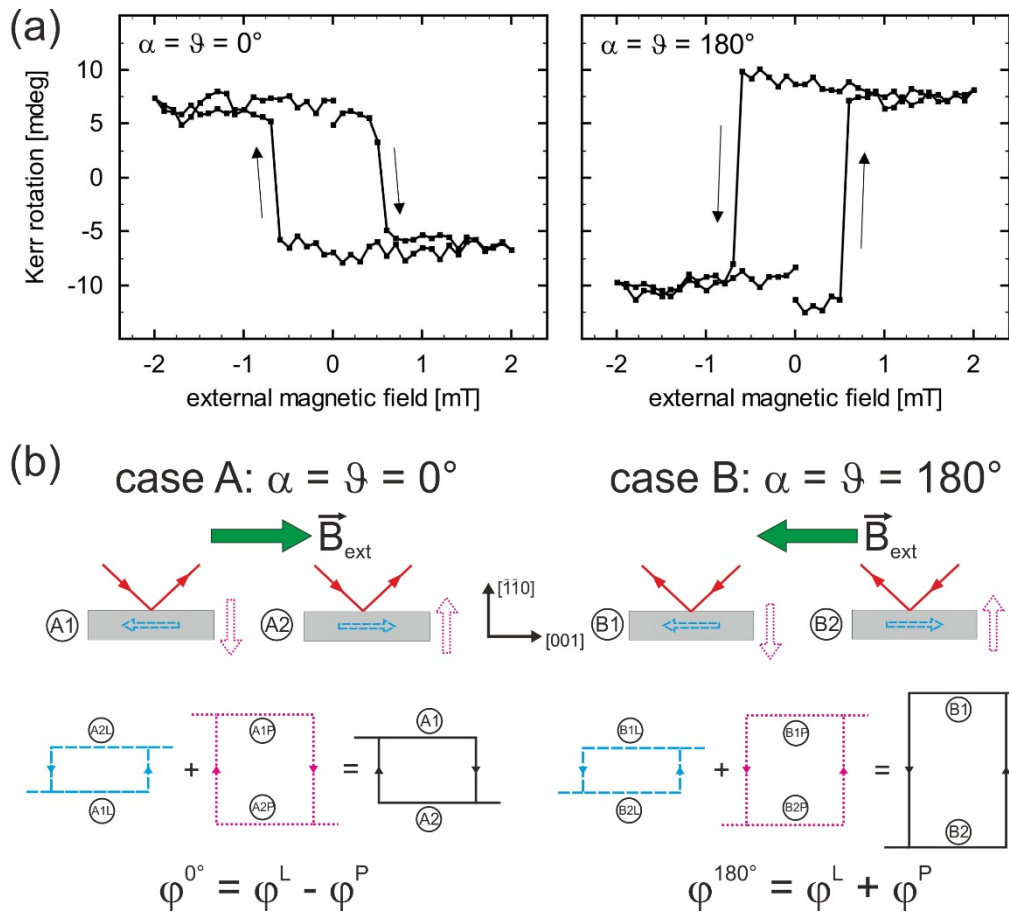


Figure 7.4: (a) *In situ* Kerr rotation signal measured in longitudinal geometry ( $\beta = 90^\circ$ ) for a 2.5 ML thick Fe film on GaAs(110) with an angle of incidence of  $\theta = 15^\circ$  and a laser wavelength of  $\lambda \approx 632.8$  nm. A reversal of the sense of the hysteresis curves is observed [52]. (b) Model of superimposed in-plane and out-of-plane magnetization which explains the reversal of the hysteresis curves [52]. The green arrows indicate the direction into which the external magnetic field is applied first in the hysteresis cycle. For more details see continuous text.

The cycle begins by applying the external magnetic field in [001] direction as indicated by the green arrow. As soon as the coercive field is reached, the in-plane magnetization switches into the [001] direction and the out-of-plane magnetization switches upwards. This is illustrated by the dashed blue arrow and dotted magenta arrow in case A2, respectively. The corresponding longitudinal (in-plane) Kerr signal jumps to the value A2L shown in the dashed blue hysteresis curve. In contrast, the polar (out-of-plane) Kerr sig-

nal falls to the value A2P as indicated by the dotted magenta hysteresis curve. Due to the relatively large polar Kerr signal the overall hysteresis curve, which is the sum of the longitudinal and polar Kerr signal, shows a downward jump to the baseline A2.

After the maximum magnetic field in [001] direction is applied and driven back to zero, the second half of the cycle starts by applying the magnetic field in [00 $\bar{1}$ ] direction. After reaching the coercive field, the in-plane magnetization switches back to the [00 $\bar{1}$ ] direction and the out-of-plane component switches downwards again (case A1). The longitudinal Kerr signal falls back to the A1L baseline. This yields a counterclockwise hysteresis curve for the longitudinal Kerr signal. The polar Kerr signal jumps back to the A1P value which yields a clockwise polar hysteresis curve. Due to the relatively large polar Kerr signal the sum of the longitudinal and polar hysteresis curve yields an overall clockwise hysteresis curve.

In a next step the plane of incidence and the applied external magnetic field are rotated by 180° with respect to the sample (case B). (In the experiment this geometry is achieved by turning the sample itself by 180°.) This is depicted by case B1 in Figure 7.4(b). Due to its mirror symmetry the out-of-plane magnetization component yields the same polar Kerr signal no matter if the laser light impinges from the left or right hand side. Therefore, the corresponding polar Kerr signal B1P is assigned to the upper baseline of the dotted magenta hysteresis curve in the same way as for A1P. In contrast, the orientation of the plane of incidence is now changed with respect to the in-plane magnetization and therefore yields a different longitudinal Kerr signal B1L if compared to A1L. Actually, the arrangement of in-plane magnetization and incident laser light in situation B1 corresponds to situation A2. Therefore, the longitudinal Kerr signal B1L is assigned to the upper baseline of the corresponding blue dashed hysteresis loop.

The hysteresis cycle begins by applying the external magnetic field now first along the [00 $\bar{1}$ ] direction corresponding to  $\alpha = 180^\circ$  as indicated by the green arrow. Since the in-plane magnetization already points into the [00 $\bar{1}$ ] direction no switching is observed. Subsequently, the applied magnetic field is decreased to zero and then directed into the [001] direction. As soon as the coercive field is reached, the in-plane magnetization switches into the [001] direction and the out-of-plane component switches upwards (case B2). This translates into a downward jump for both the longitudinal and polar hysteresis loops to the value B2L and B2P, respectively. By repeatedly directing the external magnetic field into the [00 $\bar{1}$ ] direction and reaching the coercive field, the in-plane magnetization switches back into the [00 $\bar{1}$ ] direction and the out-of-plane component switches downwards again (case B1). For both the longitudinal and the polar hysteresis loop this translates into an upward jump back to the values B1L and B1P, respectively. This also concludes an entire hysteresis cycle and reveals counterclockwise hysteresis curves for both the longitudinal and the polar Kerr signal. The sum of both signals yields the overall hysteresis curve which therefore also exhibits a counterclockwise sense.

In other words: one can say that the solid black hysteresis curves from Figure 7.4(b) and the measured Kerr signals from Figure 7.4(a) represent a superposition of a longitudinal

and a polar Kerr signal. In the case of  $\alpha_- = \vartheta_- = 0^\circ$  the polar Kerr rotation  $\varphi^P$  is subtracted from the longitudinal Kerr rotation  $\varphi^L$  and for  $\alpha_+ = \vartheta_+ = 180^\circ$  the polar signal is added to the longitudinal signal. Essentially, this is due to the different symmetry properties of the in-plane and out-of-plane magnetization components with respect to the orientation of the incident light as described above. Mathematically, the total Kerr rotation can be expressed as

$$\varphi^{\alpha_\pm/\vartheta_\pm} = \varphi^L \pm \varphi^P \quad (7.1)$$

By conducting two measurements with a reverse geometry to each other, i.e., at  $\alpha_- = \vartheta_- = 0^\circ$  and  $\alpha_+ = \vartheta_+ = 180^\circ$ , equation (7.1) yields the longitudinal and polar Kerr rotation:

$$\varphi^L = \frac{1}{2} (\varphi^{\alpha_+/\vartheta_+} + \varphi^{\alpha_-/\vartheta_-}) \quad (7.2)$$

$$\varphi^P = \frac{1}{2} (\varphi^{\alpha_+/\vartheta_+} - \varphi^{\alpha_-/\vartheta_-}) \quad (7.3)$$

Ding *et al.* [144, 145] were the first to use the different symmetry properties of the longitudinal and polar Kerr ellipticity signal to disentangle the mixed Kerr signal found in a general geometry (neither completely polar nor completely longitudinal but canted) for the case of Co/Au(111) films.

For the example of the LT grown 2.5 ML Fe film on GaAs(1̄10) from Figure 7.4(a) one obtains  $\varphi^{\alpha_+/\vartheta_+} = \varphi^+ \approx +17.6$  mdeg and  $\varphi^{\alpha_-/\vartheta_-} = \varphi^- \approx -12.2$  mdeg. The positive and negative signs indicated a counterclockwise and clockwise sense of the hysteresis curves, respectively. By filling these values into equations (7.2) and (7.3) one obtains  $\varphi^L \approx +2.7$  mdeg and  $\varphi^P \approx 14.9$  mdeg. Ding *et al.* [144, 145] attribute the obtained polar and longitudinal Kerr rotations to an in-plane and out-of-plane magnetization component of a canted film magnetization, respectively. However, in section 7.6 we will see that these Kerr rotation values are not compatible with a canted film magnetization and have therefore to be treated with care.

## 7.2 Kerr Signal Dependence on Surface Orientation

The GaAs crystal has two non-equivalent sets of natural cleavage planes (see Figure 7.5). One set of cleavage planes consists of the (110) and (1̄10) surfaces, the other set represents the (1̄10) and (110) surfaces. The (001) plane serves as a mirror plane for the two sets of cleavage planes with respect to each other. In other words: the GaAs{110} surface lacks a space inversion symmetry along the <001> direction.

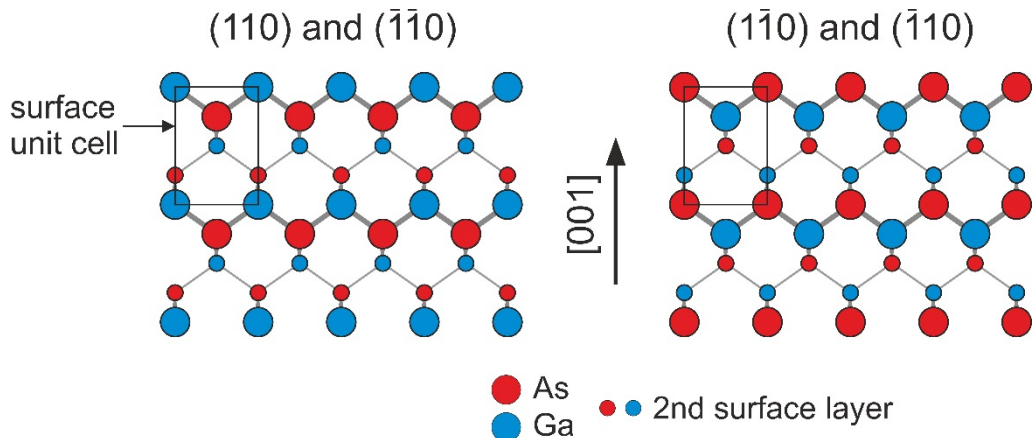


Figure 7.5: Ball-and-stick model of the GaAs{110} surface. Two non-equivalent cleavage planes of the GaAs crystal exist: on the left-hand side the set of (110) and ( $\bar{1}\bar{1}0$ ) surface is shown whereas on the right-hand side the set of ( $\bar{1}\bar{1}0$ ) and ( $\bar{1}10$ ) is depicted. In the crystal the two sets are oriented perpendicularly to each other.

In section 7.1, *in situ* longitudinal Kerr signals along the <001> easy axis of a 2.5 ML thick Fe film on GaAs( $\bar{1}\bar{1}0$ ) are presented in Figure 7.4(a). In this section, the same measurements are performed on the non-equivalent GaAs( $\bar{1}10$ ) surface. In order to do so, a GaAs sample was cut out of the wafer perpendicularly with respect to the sample discussed in section 7.1. Apart from that, both samples were prepared in the same manner. The obtained Kerr signal from the Fe/GaAs( $\bar{1}10$ ) interface is shown in Figure 7.6.

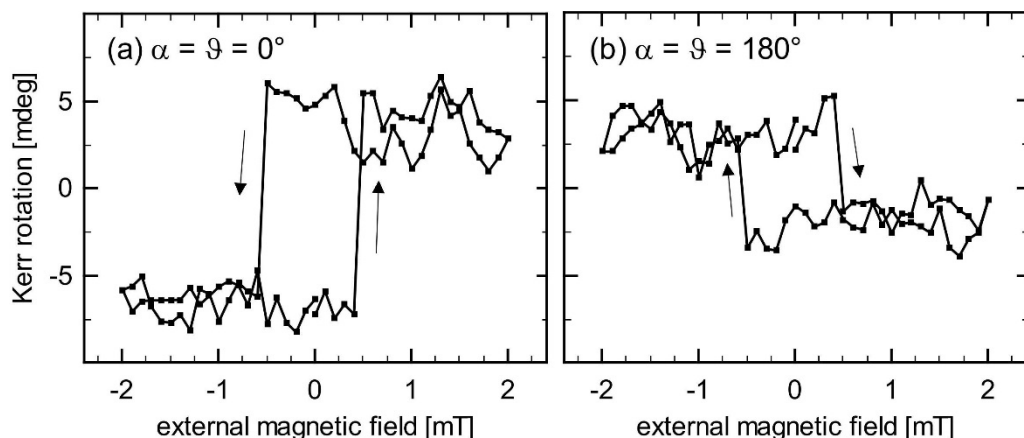


Figure 7.6: *In situ* Kerr rotation signal measured in longitudinal geometry ( $\beta = 90^\circ$ ) for a 2.7 ML thick Fe film on *p*-type GaAs( $\bar{1}10$ ) with an angle of incidence of  $\theta = 15^\circ$  and a laser wavelength of  $\lambda \approx 632.8$  nm [52].

A comparison between the Kerr signal from the two non-equivalent Fe/GaAs{110} interfaces reveals interchanged clockwise and counterclockwise hysteresis curves for the two different measurement geometries at  $\alpha = \vartheta = 0^\circ$  and  $\alpha = \vartheta = 180^\circ$ . This clearly indicates that the detected polar Kerr signal from the out-of-plane magnetization originates

from the interplay between the direction of the Fe film magnetization and the space inversion asymmetry of the GaAs{110} surface. Moreover, a connection of the polar Kerr signal to an externally induced preferential magnetization direction caused by the preparation technique, the sample holder, or the MOKE setup can be excluded by this experiment. The differences in the absolute value of the Kerr signal between the two non-equivalent GaAs{110} surfaces can be attributed to minimal differences in the thickness of the Fe film and will be addressed in section 7.5.

### 7.3 In-Plane Uniaxial Anisotropy

In this subsection, the in-plane magnetic properties of ultrathin Fe films on GaAs{110} are investigated in greater detail. In order to learn more about the in-plane magnetic anisotropy of the metal-semiconductor interfaces, the samples are investigated by means of the in-plane rotatable magnetic field of the MOKE setup (see also section 2.2.2). Similar measurements were already presented in the two Bachelor's theses of Rolf-Pissarczyk and Weikert [115, 146] which were supervised by the author of this PhD thesis.

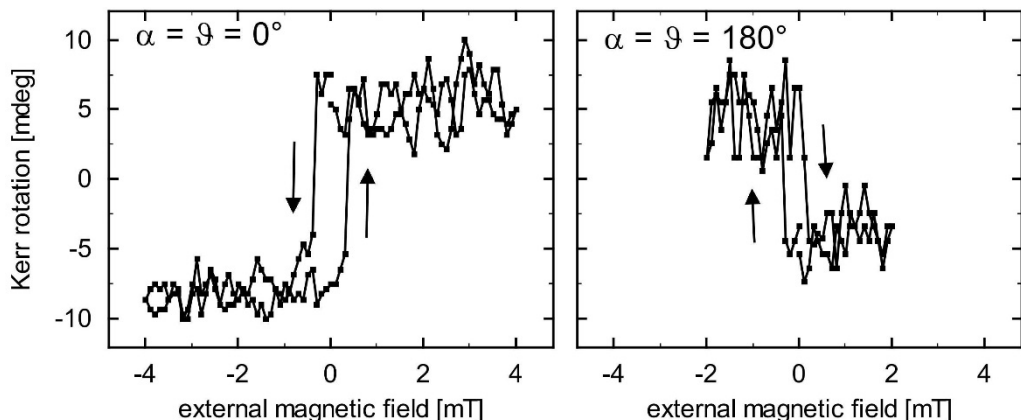


Figure 7.7: *In situ* Kerr rotation signal measured in longitudinal geometry ( $\beta = 90^\circ$ ) for a 3.2 ML thick Fe film on *p*-type GaAs(1̄10) with an angle of incidence of  $\theta = 15^\circ$ . The measurements have been conducted at a laser wavelength of  $\lambda \approx 785$  nm.

Here a Fe film of 3.2 ML nominal thickness on *p*-type GaAs(1̄10) is investigated. In a first step, longitudinal MOKE measurements are conducted with the laser plane-of-incidence and external magnetic field oriented parallel to the <001> easy axis of the sample. The corresponding Kerr signals are shown in Figure 7.7. At  $\alpha_+ = \vartheta_+ = 0^\circ$  one finds a counterclockwise hysteresis curve with a Kerr signal of  $\varphi^+ \approx 12$  mdeg. For angles of  $\alpha_- = \vartheta_- = 180^\circ$  one obtains a clockwise hysteresis curve with a Kerr signal of  $\varphi^- \approx -7.5$  mdeg. From these values the longitudinal and polar Kerr component are calculated to  $\varphi^L \approx 2.25$  mdeg and  $\varphi^P \approx 9.75$  mdeg in accordance with equations (7.2) and (7.3). As already mentioned above, these Kerr rotation values have to be treated with care be-

cause they assume a canted film magnetization. However, this assumption is not justified for the ultrathin Fe films as will be discussed in section 7.6.

In a next step, the sample is investigated by applying the external magnetic field into different in-plane directions. The laser plane-of-incidence is set to a fixed in-plane angle of  $\vartheta = 90^\circ$  corresponding to the  $[\bar{1}\bar{1}0]$  direction (perpendicular to the  $<001>$  easy axis). Initially, the external magnetic field is set to  $\alpha = 0^\circ$  which corresponds to the  $[001]$  direction, now perpendicular to the laser plane-of-incidence. This particular setup is also known as the transverse MOKE geometry as has been illustrated in Figure 2.1 in section 2.2.1. A Kerr rotation from any magnetization component perpendicular (transverse) to the plane-of-incidence cannot be detected in the transverse MOKE setup. In other words: this particular experimental arrangement should filter out the Kerr signal from the in-plane magnetization along the  $<001>$  easy axis. The measured Kerr rotation for this configuration is shown in the upper left panel in Figure 7.8. Indeed, a Kerr rotation of  $\varphi \approx 9.5$  mdeg is detected. This value is in very good agreement with the polar Kerr component of  $\varphi^P \approx 9.75$  mdeg obtained from the longitudinal measurement in Figure 7.7. Furthermore, the counterclockwise sense of the transverse MOKE measurement matches the proposed sense of the polar component in the corresponding hysteresis curve from Figure 7.7. Therefore, one can say that the transverse MOKE measurement solely detects the polar Kerr rotation component from the sample. Rotating the in-plane angle of the magnetic field to  $\alpha = 180^\circ$  (corresponding to the  $[00\bar{1}]$  direction) and keeping the laser plane-of-incidence at  $\vartheta = 90^\circ$  yields a hysteresis curve of the same height but with a reversed (now clockwise) sense (see right upper panel in Figure 7.8). This is the behavior one would expect because a rotation of  $\alpha$  by  $180^\circ$  means that positive and negative  $\vec{B}_{\text{ext}}$  are simply interchanged.

As was described in section 2.2.2, the MOKE setup allows to rotate the in-plane magnetic field into any arbitrary direction. In the following, this feature is used to detect the Kerr signal for angles between  $\alpha = 0^\circ$  and  $\alpha = 180^\circ$ . The corresponding data are shown in Figure 7.8. The data show hysteresis loops with abrupt jumps for all measured directions. Furthermore, the hysteresis widths (coercive fields) increase when approaching the  $[\bar{1}\bar{1}0]$  direction. At  $\alpha \approx 91^\circ$  one does not observe any hysteresis at all but an even function of the polar Kerr component which will be discussed later in this section.

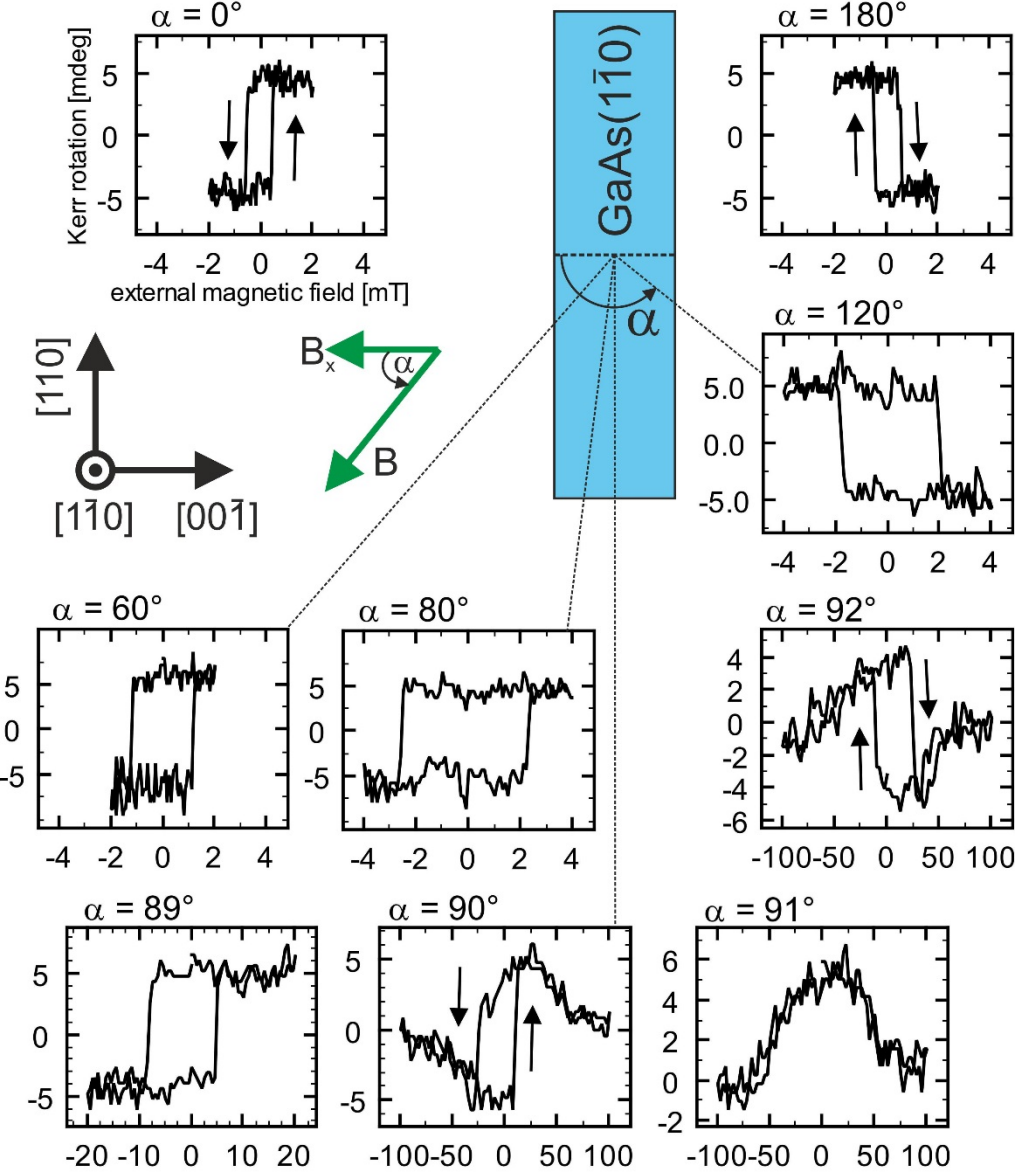


Figure 7.8: Measured Kerr signal for a 3.2 ML thick Fe film on  $p$ -GaAs(1̄10) at a fixed rotation angle of the laser plane-of-incidence of  $\vartheta = 90^\circ$  and for different in-plane magnetic field directions with rotation angles  $\alpha$ . The angle of incidence is set to  $\theta = 15^\circ$ . The measurements were conducted at a laser wavelength of  $\lambda \approx 785$  nm. For more details see continuous text.

Furthermore, another set of measurements is performed for the laser plane-of-incidence set to an in-plane angle of  $\vartheta = 270^\circ$ . The resulting coercive fields (half hysteresis widths) for both geometries ( $\vartheta = 90^\circ$  and  $\vartheta = 270^\circ$ ) are plotted against the  $\vec{B}_{\text{ext}}$  field rotation angle  $\alpha$  in Figure 7.9. In the experiment the accuracy in adjusting the angles  $\alpha$  and  $\vartheta$  is in the range of  $\sim 1$  deg. Therefore, the angles for which no switching (hysteresis) occurs can be identified as  $\alpha = 90^\circ$  and  $\alpha = 270^\circ$  corresponding to the  $\langle 110 \rangle$  in-plane direction. Moreover, the data suggest a  $1/\cos(\alpha)$  dependence of the coercive field [115, 146] which is indicated by the black dashed lines in Figure 7.9. As illustrated in Figure 7.8, the pro-

jection of the external magnetic field in the  $x$  direction (parallel to the  $<001>$  direction) is given by  $B_x = |\vec{B}_{\text{ext}}| \cdot \cos \alpha$ . Measurements where  $\vec{B}_{\text{ext}}$  is applied along the  $<001>$  direction ( $\alpha = 0^\circ$  and  $\alpha = 180^\circ$ ) exhibit a coercive field of  $B_x^{\text{cf}} \approx 0.45$  mT. If the direction of  $\vec{B}_{\text{ext}}$  is tilted out of the  $<001>$  direction, the measured coercive field grows by the factor of  $1/\cos \alpha$ . Therefore, solely the component of the external magnetic field projected on the  $<001>$  in-plane easy axis ( $x$  direction) determines the switching behavior of the sample. In other words:  $B_x^{\text{cf}}$  is the externally applied field along the  $<001>$  direction that is necessary to switch the magnetization of the sample.

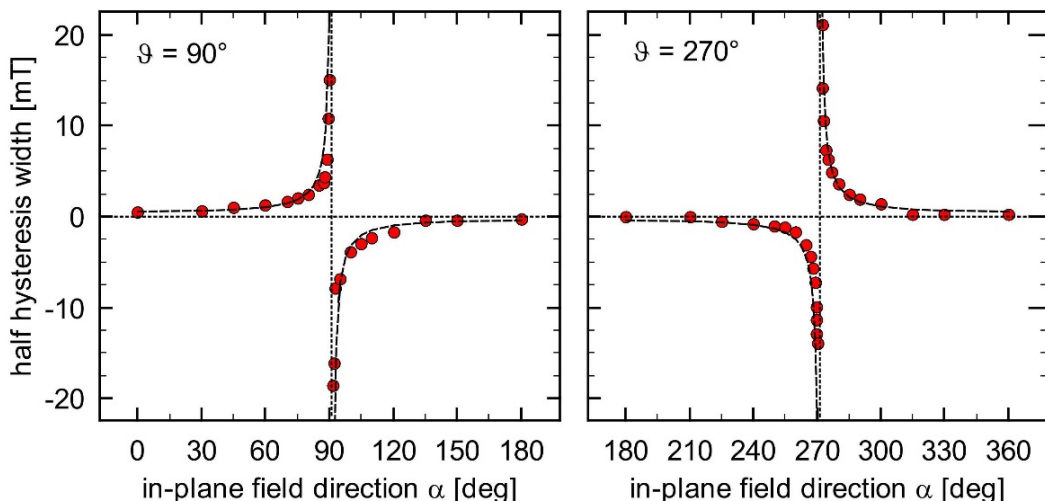


Figure 7.9: Half hysteresis widths (coercive fields) for a 3.2 ML thick Fe film on  $p$ -GaAs(1̄10) at a fixed rotation angle of the laser plane-of-incidence of (left)  $\vartheta = 90^\circ$  and (right)  $\vartheta = 270^\circ$  and for different in-plane magnetic field directions with a rotation angles  $\alpha$ . The angle of incidence is set to  $\theta = 15^\circ$ . The measurements are conducted at a laser wavelength of  $\lambda \approx 785$  nm. Positive and negative values denote counterclockwise and clockwise hysteresis curves, respectively. The data excellently describe a  $1/\cos(\alpha)$  dependence (black dashed lines).

The Kerr rotation measured for external magnetic fields parallel or almost parallel to the in-plane  $<110>$  direction (see the three lower right panels in Figure 7.8) can be explained in the framework of an out-of-plane magnetization component. If the external field is applied exactly into the  $<110>$  in-plane direction (case  $\alpha = 91^\circ$  in Figure 7.8) there is no field component along the  $x$  direction (or  $<001>$  direction) that is necessary to switch the in-plane magnetization component and the out-of-plane component coupled to it. Hence, no hysteresis is observed. The even function, which is observed instead, shows that the out-of-plane magnetization is continuously driven into the  $<110>$  direction. By applying an external field of sufficient strength of  $\sim 100$  mT the polar component is zero and the magnetization is completely aligned along the  $<110>$  direction. The Kerr signal of  $\sim 5$  mdeg of the even function accounts for half the polar component that is found for switching between two spin states (see upper panels in Figure 7.8). Furthermore, the difference in the Kerr signal for an applied field of  $+100$  mT and  $-100$  mT can be attribut-

ed to the parallel and antiparallel in-plane magnetized sample along  $\langle\bar{1}\bar{1}0\rangle$ , respectively. If the applied magnetic field is tilted a little away from the  $\langle110\rangle$  direction (see Figure 7.8 for  $\alpha = 90^\circ$  and  $\alpha = 92^\circ$ ), a part of the field is also applied along the  $\langle001\rangle$  direction and a switching of the polar component between two states is observed. After the switching, the out-of-plane magnetization is continuously driven into the  $\langle110\rangle$  direction until it is completely aligned along  $\langle110\rangle$  for fields of  $\sim 100$  mT.

Following the common jargon for canted thin film magnetism the  $\langle110\rangle$  direction could be denoted as “hard axis” [115, 146]. However, in section 7.6 it will become apparent that a completely different spin configuration might be present in this kind of samples.

## 7.4 No Dependence on Type of Doping

In this section it is investigated if the type of doping has any influence on the Kerr signal from the Fe/GaAs(110) interfaces with ultrathin Fe films [52]. Therefore, Fe films were low-temperature grown on GaAs(110) surfaces of *p*-type, *n*-type doped, and intrinsic GaAs samples. In the case of the *p*- and *n*-type doped samples the nominal Fe film thickness was around 2.7 ML. On the intrinsic sample a  $\sim 2.5$  ML thick Fe film was grown. The detected Kerr signal from these three samples is shown in Figure 7.10. The sense of the hysteresis curves for the two measurement geometries of  $\alpha = \vartheta = 0^\circ$  and  $\alpha = \vartheta = 180^\circ$  is clockwise and counterclockwise, respectively. It is important to note that the sense of the hysteresis curves is the same for all three types of doping which yields to the conclusion that the orientation of the out-of-plane magnetization does not depend on the type of doping. The slight differences of the absolute Kerr signal (height of the hysteresis curves) between the different samples can be attributed to small differences in the Fe film thickness (see also section 7.5).

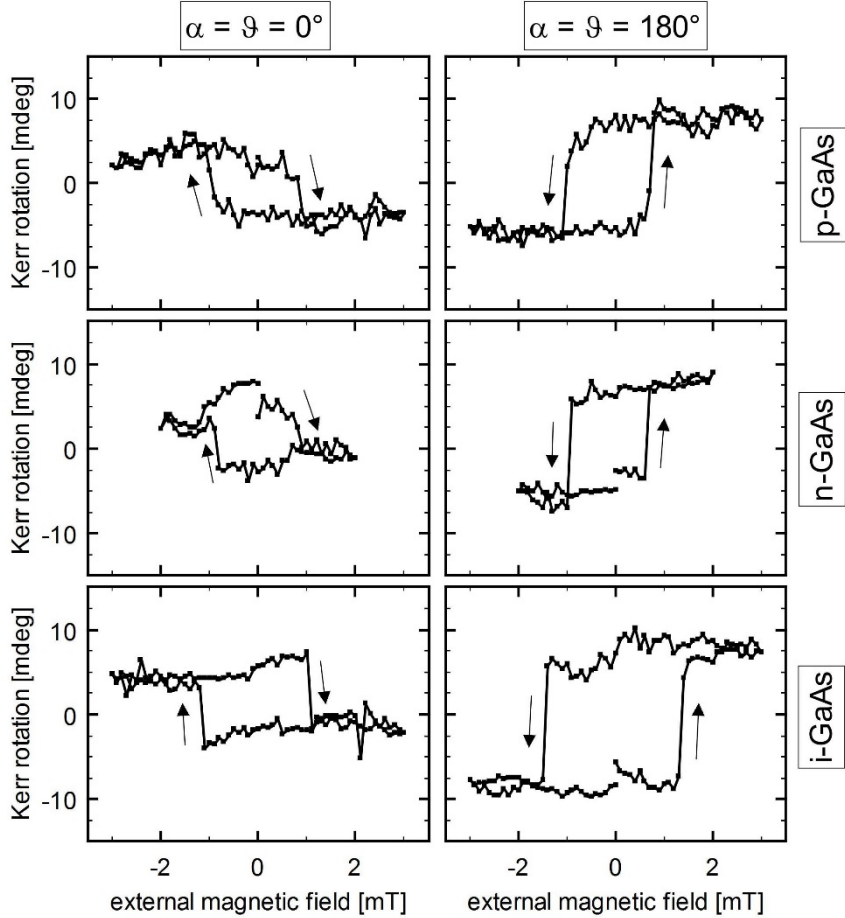


Figure 7.10: Kerr rotation for ultrathin (2.5 – 2.7 ML) low-temperature grown Fe films on GaAs(110) measured at an angle of incidence of  $\theta = 15^\circ$  and a laser wavelength of  $\lambda \approx 632.8$  nm for different types of doping. The sense of the hysteresis curve (indicated by the arrows) is equivalent for all types of doping [52].

## 7.5 Thickness Dependence of the Kerr Signal

In this subsection the dependence of the Kerr signal on the Fe film thickness is investigated. Fe films in the thickness range of 2–10 ML have been grown on the GaAs(1̄10) surface at low-temperature [52]. The obtained Kerr signals for an angle of incidence of  $\theta = 15^\circ$  are shown in Figure 7.11. The data sets for Fe films thinner or equal to 4 ML ( $\sim 8$  Å) were taken at measurement geometries with the plane of incidence of the laser beam and external magnetic field parallel to the easy axis along  $<001>$  direction. The blue filled triangles represent Kerr signals  $\varphi^+$  taken at  $\alpha_+ = \vartheta_+ = 0^\circ$  whereas the red filled circles represent Kerr signals  $\varphi^-$  taken at  $\alpha_- = \vartheta_- = 180^\circ$ . Kerr rotations with a positive (negative) sign exhibit counterclockwise (clockwise) hysteresis curves. As already pointed out in section 1.6 a spin reorientation transition takes place at a Fe film

thickness of around 4—5 ML [46, 47, 52]. Therefore, the Kerr signal for Fe films thicker than 4 ML was obtained from measurements along the  $\langle 110 \rangle$  easy axis. For these measurements, the blue filled triangles represent the Kerr signals measured at  $\alpha_+ = \vartheta_+ = 270^\circ$  (along the  $[110]$  direction) and the red filled circles show the Kerr signals measured at  $\alpha_- = \vartheta_- = 90^\circ$  (along the  $[\bar{1}\bar{1}0]$  direction). The green filled squared data points represent the longitudinal Kerr signal that was calculated according to equation (7.2).

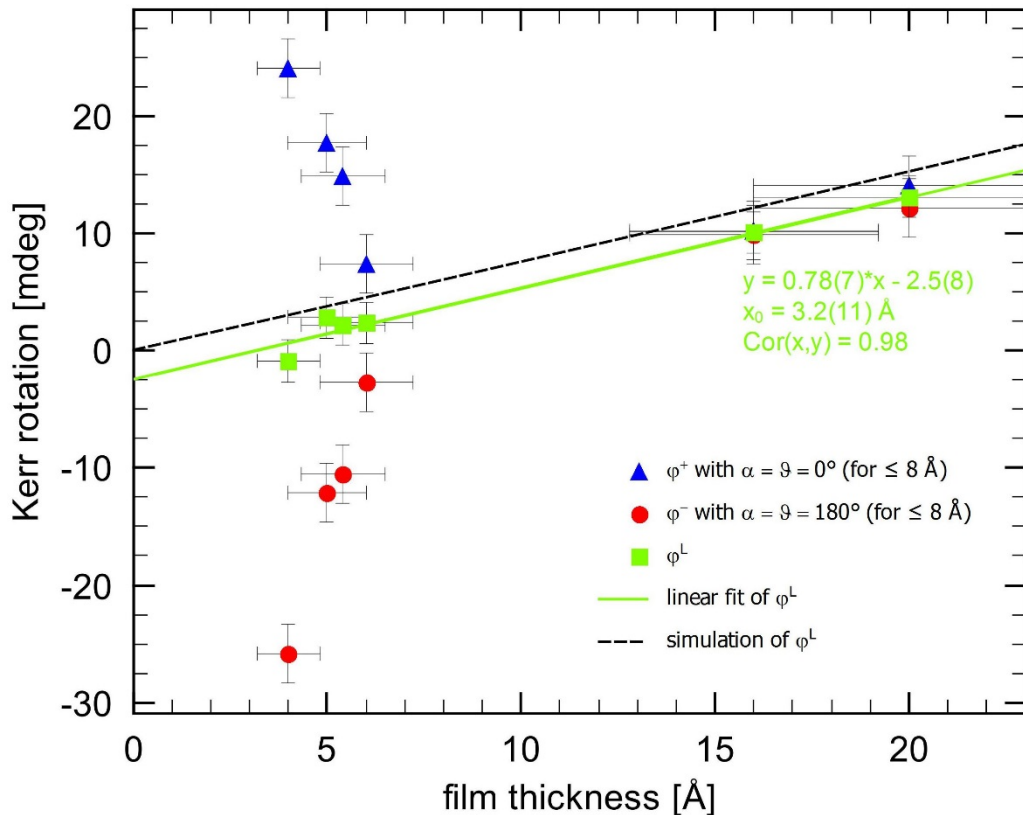


Figure 7.11: Dependency of the Kerr rotation on the Fe film thickness at an angle of incidence of  $\theta = 15^\circ$  [52]. The measurements were conducted at a laser wavelength of  $\lambda \approx 632.8$  nm. Fe films of different thicknesses were grown on  $p$ -doped GaAs(1̄10). Positive and negative signs for the Kerr rotation indicate counterclockwise and clockwise hysteresis curves, respectively.

The longitudinal Kerr signal  $\varphi^L$  exhibits a linear dependence on the Fe film thickness with an increasing Kerr signal for thicker Fe films. This behavior is also theoretically predicted and can be simulated by means of the formalism presented in subsection 2.2.1.2. For this simulation a purely in-plane magnetization of the Fe film is assumed. The primary sensitivity of the MOKE setup to the Kerr rotation of the p polarized  $\varphi_p$  light has already been discussed in section 2.2.2 and it was shown in expression (2.25) that the measured Kerr signal is proportional to  $\varphi_p$ . Hence, in the simulation solely the p polarized light needs to be considered. Longitudinal Kerr measurements of purely in-plane magnetized 50 ML thick Fe films on GaAs(1̄10) along the in-plane easy axis in  $\langle 110 \rangle$  direction at an angle of incidence of  $\theta = 15^\circ$  yield a longitudinal Kerr signal of

$\varphi^L \approx 49$  mdeg [52]. This reference value is used to properly adjust the simulation of the longitudinal Kerr component to the experiment.

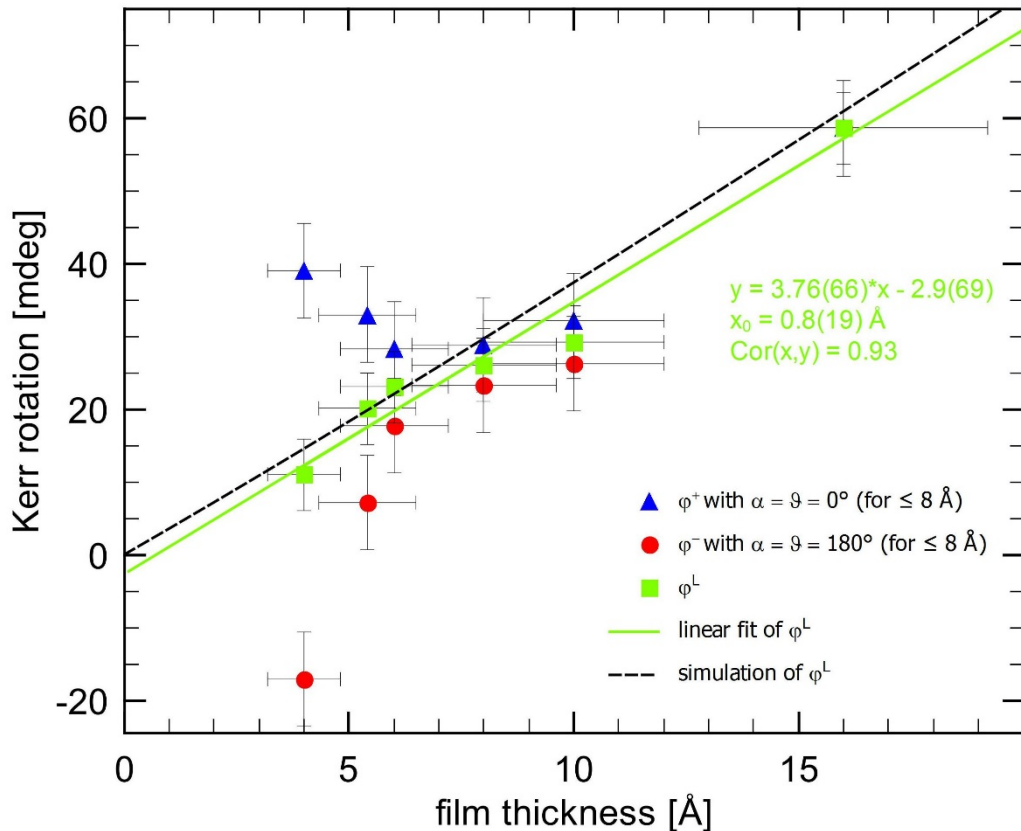


Figure 7.12: Dependency of the Kerr rotation on the Fe film thickness at an angle of incidence of  $\theta = 67^\circ$  [52]. The measurements were conducted at a laser wavelength of  $\lambda \approx 632.8$  nm. Fe films of different thicknesses were grown on *p*-doped GaAs(1̄10). Positive and negative signs for the Kerr rotation indicate counterclockwise and clockwise hysteresis curves, respectively.

In order to cross-check the consistency of the simulation and the experimentally obtained data, the film thickness dependency of the longitudinal Kerr rotation was measured at an angle of incidence of  $\theta = 67^\circ$  and also simulated for this value. The corresponding data are shown in Figure 7.12. Clearly, for an angle of incidence of  $\theta = 67^\circ$  the simulated values of the longitudinal Kerr rotation for a purely in-plane magnetized Fe film are in excellent agreement with the experimentally obtained values  $\varphi^L$  for the ultrathin Fe films. Therefore, the experimentally obtained  $\varphi^L$  values can indeed be interpreted as the longitudinal Kerr signal which stems from a pure in-plane magnetization of the Fe film. Furthermore, in the case of  $\theta = 67^\circ$ , the 50 ML in-plane magnetized Fe film yields a longitudinal Kerr signal of  $\varphi_K \approx 335$  mdeg [52] that excellently follows the linear fit from Figure 7.12 and therefore suggests that all plotted  $\varphi^L$  values represent the pure in-plane magnetization of Fe films of different thicknesses.

As can be seen in Figure 7.11 and Figure 7.12, the slope of the linear fit of the longitudinal Kerr signals  $\varphi^L$  in the case of the angle of incidence of  $\theta = 67^\circ$  is about 5 times larger than for the steeper angle of incidence of  $\theta = 15^\circ$ . This clearly shows that a larger angle of incidence allows a more sensitive detection of the in-plane magnetization of the Fe film. Qualitatively, this can be understood by looking at Figure 2.1(b) in section 2.2.1 depicting the case of an in-plane magnetized film and impinging p polarized light to which the MOKE setup is primarily sensitive (see also section 2.2.2). Applying the right-hand rule it becomes apparent that a large angle of incidence yields a large cross product of the electric and magnetic field vectors and therefore also a large Kerr rotation. Simulating the Kerr rotation of the p polarized light for an in-plane magnetized 2.5 ML thick Fe film on GaAs by means of the formalism presented in section 2.2.1.2 yields a 10-fold increase of the Kerr rotation at  $\theta = 67^\circ$  with respect to  $\theta = 15^\circ$ . In the experiment only a 5-fold increase of the Kerr rotation at  $\theta = 67^\circ$  with respect to  $\theta = 15^\circ$  is observed. Here one also has to keep in mind the prefactor  $E_s E_p$  from expression (2.25) which is about 2 times larger for an angle of  $\theta = 15^\circ$  than for an angle of  $\theta = 67^\circ$  in this thickness regime.<sup>15</sup> Therefore, the simulation excellently resembles the experimental data of the Kerr rotation from the in-plane magnetization component.

Most interestingly, Figure 7.11 and Figure 7.12 show that the Fe films in the thickness regime of 2–3 ML have the same linear dependence of the longitudinal Kerr signal as the thicker Fe films but exhibit a rapidly increasing polar Kerr component with decreasing film thickness. Furthermore, this polar component depends on the relative orientation of the in-plane magnetization component along the <001> easy axis which can be extracted from two different measurement geometries with  $\alpha = \vartheta = 0^\circ$  and  $\alpha = \vartheta = 180^\circ$  (see also sections 7.1 and 7.2). In this context, the sign of the Kerr rotation indicates the sense of the corresponding hysteresis curve. In section 7.6, possible approaches to explain this additional polar Kerr component found for 2–3 ML thick Fe films on GaAs{110} are discussed in detail.

Here it should be pointed out that the angle of incidence does not seem to have a significant influence on the detected polar Kerr signal for the 2–3 ML thick Fe films. This is indicated by the virtually unchanged distances between the  $\varphi^+$  and  $\varphi^-$  values for data points at constant film thickness but different angle of incidence of  $\theta = 15^\circ$  and  $\theta = 67^\circ$  (see Figure 7.11 and Figure 7.12). According to equation (7.3) half of the difference between the  $\varphi^+$  and  $\varphi^-$  values yields the polar Kerr component. In fact, simulating the Kerr rotation of an out-of-plane magnetized film by means of the formalism presented in section 2.2.1.2 yields a slight decrease of only 10% for the Kerr rotation of the p polarized light at an angle of incidence of  $\theta = 67^\circ$  with respect to the steeper angle of  $\theta = 15^\circ$  [52]. Therefore, the experimentally observed relatively weak dependence of the polar Kerr rotation on the angle of incidence is in very good agreement with the simulation.

---

<sup>15</sup> This is due to a strong dependence of the reflectivity on the angle of incidence. This dependence can also be extracted from the simulations.

The data presented in Figure 7.11 and Figure 7.12 indicate that Fe films of 4 or more ML of thickness do not exhibit an out-of-plane (polar) Kerr component. The small deviations between the  $\varphi^+$  and  $\varphi^-$  values for 4 and 5 ML thick Fe films in Figure 7.12 could easily be attributed to the noise of the MOKE setup. For thicker Fe films the  $\varphi^+$  and  $\varphi^-$  values cannot be discerned anymore.

## 7.6 Discussion

### 7.6.1 Canted Fe Film Magnetization

It is well-known from the literature that ultrathin Fe films exhibit a thickness-dependent spin-reorientation transition (SRT) on many different substrates [149]. This SRT usually describes the transition from a perpendicular magnetic anisotropy (PMA) to an in-plane magnetic anisotropy (IPMA) with increasing film thickness. An example of surface magneto-optical Kerr effect (SMOKE)<sup>16</sup> measurements of ultrathin Fe films on Ag(100) is shown in Figure 7.13(a). The measurements exhibit a SRT at a Fe film thickness of ~3 ML. At a thickness of 2 ML, polar Kerr measurements exhibit square-shaped hysteresis curves whereas the longitudinal measurements do not show any hysteresis indicating an out-of-plane easy axis (EA) and an in-plane hard axis (HA). In contrast, for 3 ML thick Fe films the longitudinal Kerr measurements exhibit a hysteresis and the polar measurements only show a very weak hysteresis which indicates interchanged EA and HA.

Figure 7.13(b) shows SMOKE and X-ray magnetic circular dichroism (XMCD) data for ultrathin low-temperature (LT) grown Fe films on GaAs(001). These studies also suggest a SRT in the 2–3 ML thickness regime. The 1.4 ML thick Fe films do not exhibit any ferromagnetic signal. For 2.1 ML thick Fe films the polar MOKE measurements show a square-shaped hysteresis with small coercive fields whereas the longitudinal MOKE measurements exhibit a hysteresis curve with poor squareness and larger coercive fields. From that it can be concluded that the 2.1 ML thick Fe film is ferromagnetic with a PMA [150]. For 2.8 ML thick Fe films the EA is found in-plane indicating that the SRT was completed at this thickness. The MOKE measurements are confirmed by the XMCD data that also exhibit a SRT. The delay of the SRT with respect to the MOKE measurements can be attributed to fluctuations of the deposition flux [150].

---

<sup>16</sup> The term *surface MOKE* (SMOKE) generally refers to *in situ* MOKE measurements of ultrathin films.

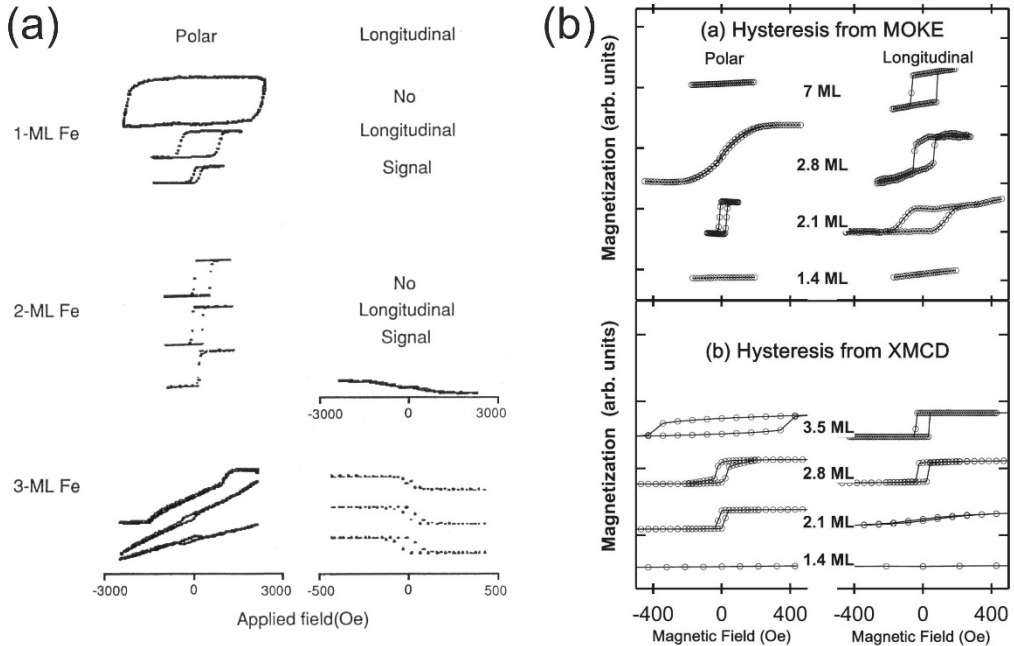


Figure 7.13: (a) SMOKE hysteresis loop behavior for  $p(1 \times 1)$  Fe thin films on Ag(100) showing the change in magnetic anisotropy from perpendicular (1 and 2 ML) to in-plane at 3 ML [149]. (b) Thickness-dependent SMOKE and XMCD hysteresis curves for Fe films on GaAs(001). The Fe films were grown and measured at  $\sim 80$  K. In the polar (longitudinal) geometry, the external magnetic field is directed along the [001] ([110]) direction [150].

In section 7.1 it was discussed that one possible way to look at the MOKE data for ultrathin (2–3 ML) Fe films on GaAs{110} is to think of them as a superposition of an in-plane (longitudinal) and an out-of-plane (polar) magnetization component. The SMOKE studies presented in Figure 7.13 show that there is a thickness range where a longitudinal as well as a polar Kerr signal are observed at the same time. In this thickness range a SRT takes place. Therefore, this might also be the case for the ultrathin Fe films on GaAs{110} investigated in this thesis. One could think of an ongoing SRT in the thickness range of 2–3 ML that manifests itself as a “canted” magnetization of the Fe film. The term “canted” expresses the idea of a film magnetization that is neither completely out-of-plane nor completely in-plane directed. An illustration of a canted Fe film magnetization is shown in Figure 7.14.

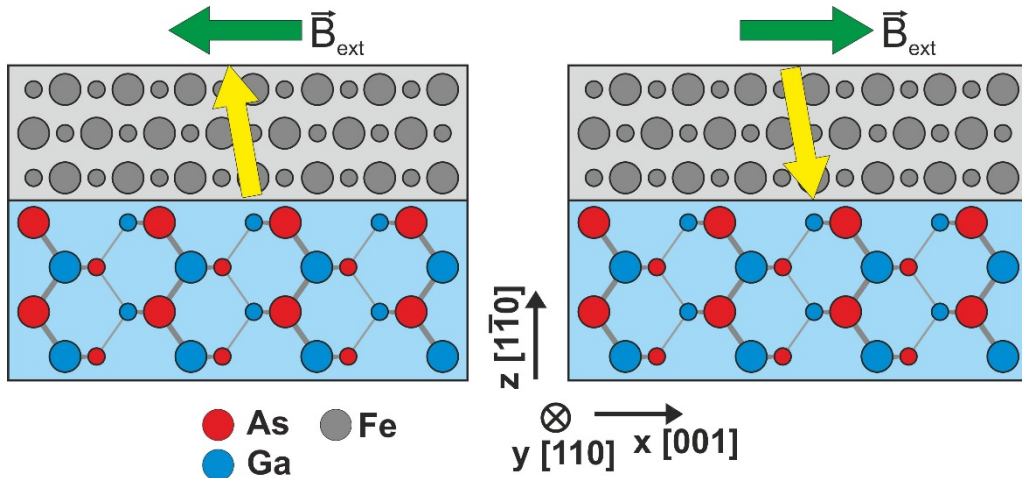


Figure 7.14: Model of canted Fe film magnetization. The external magnetic field (green arrows) switches the magnetization of the Fe film (yellow arrows) between two spin states.

In order to check if the Fe/GaAs{110} sample system exhibits a canted film magnetization, the samples are investigated in the polar geometry. As was pointed out in section 2.2.2, the 4-magnetic-pole geometry of the *in situ* MOKE setup allows to direct the magnetic field in any arbitrary direction. Therefore, the field can also be applied perpendicularly to the surface corresponding to the tilt angle  $\beta = 0^\circ$  (see Figure 7.2 for definition). The Kerr signals obtained by this polar MOKE setup on the same sample (3.2 ML Fe on *p*-GaAs(1̄10)), which was already discussed in section 7.3, are shown in Figure 7.15. In the left panel the Kerr signal for a plane-of-incidence rotation angle of  $\vartheta = 0^\circ$  (pointing into the [001] direction) is shown whereas in the right panel the angle is set to  $\vartheta = 180^\circ$  (pointing into the [00̄1] direction). The polar Kerr signal consists of hysteresis curves exhibiting the same perfect squareness as the corresponding longitudinal hysteresis curves shown in Figure 7.7 from section 7.3. However, the coercive fields are about 3 times (for  $\vartheta = 0^\circ$ ) to 5 times (for  $\vartheta = 180^\circ$ ) larger for the polar hysteresis loops compared to the longitudinal ones. Furthermore, the polar curve with  $\vartheta = 180^\circ$  exhibits asymmetric coercive fields for positive and negative applied fields. Similar asymmetric behavior has been observed for several samples with 2—3 ML Fe on GaAs{110} but was not reproducible. The measured Kerr rotation angle (height of the hysteresis curve) amounts to  $\varphi^+ \approx -13.2$  mdeg in the case of  $\vartheta = 0^\circ$  and  $\varphi^- \approx -7.3$  mdeg in the case of  $\vartheta = 180^\circ$ . The negative sign indicates the clockwise sense of both hysteresis curves. The hysteresis curves obtained in the polar geometry exhibit virtually the same height as the hysteresis curves in the longitudinal geometry from Figure 7.7. This indicates that for both measurement geometries, the polar geometry (magnetic field is applied in out-of-plane direction) and the longitudinal geometry (magnetic field in in-plane direction), the external magnetic field switches the magnetization between the same two spin states. The reversed sense of the polar hysteresis curve for  $\vartheta = 0^\circ$  with respect to the corresponding

longitudinal hysteresis curve can be explained by the reversed sequence in which the two states are addressed for the out-of-plane and in-plane directed fields.

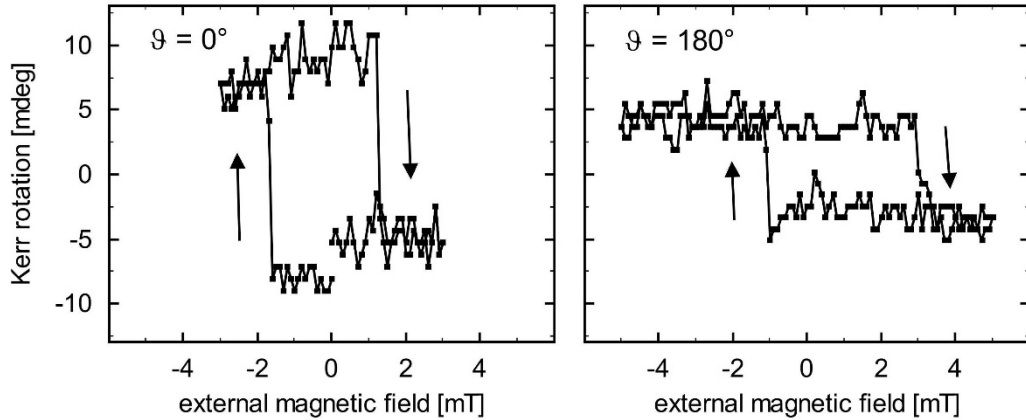


Figure 7.15: *In situ* Kerr rotation signal measured in polar geometry ( $\beta = 0^\circ$ ) for a 3.2 ML thick Fe film on *p*-type GaAs(110) with an angle of incidence of  $\theta = 15^\circ$ . The measurements are conducted at a laser wavelength of  $\lambda \approx 785$  nm.

At this point it becomes apparent that the magnetic properties of the ultrathin (2—3 ML) Fe films on GaAs{110} are difficult to describe in the common jargon used in the “thin magnetic films” community. Both the in-plane  $<001>$  direction and the out-of-plane direction exhibit magnetic switching behavior of an “easy axis”. In the literature usually one easy axis is found for a thin magnetic film and the other directions exhibit “hard axis” behavior without remanence, or “intermediate axis” behavior with rather smeared out hysteresis curves. Thin films where a spin reorientation transition (SRT) is present usually exhibit a smeared out hysteresis for the polar case and a square-shaped hysteresis for the longitudinal case or vice versa as shown in Figure 7.13. The author of this thesis did not encounter any study in the literature of thin magnetic films that exhibited a perfect squareness for polar and longitudinal Kerr measurements at the same time. In contrast, the ultrathin Fe films on GaAs{110} exhibit a perfect squareness for the entire 2—3 ML thickness regime which is also shown in Figure 7.16. In this thickness regime the perfect squareness of the hysteresis loops is found for the longitudinal as well as for the polar MOKE geometry. Despite the fact that these ultrathin films always show a superposition of an in-plane and an out-of-plane magnetization, the perfect squareness of the hysteresis curves does not suggest a SRT in the conventional sense as found in the literature for thin films with a canted magnetization.

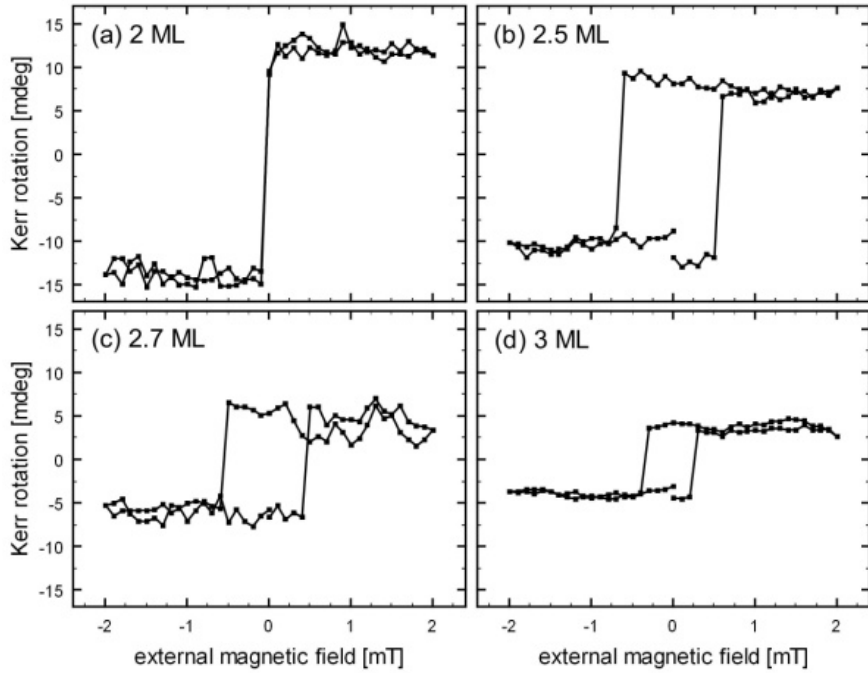


Figure 7.16: Detected Kerr rotation of LT grown Fe films in the thickness regime of 2–3 ML on GaAs(110) at  $\alpha = \vartheta = 0^\circ$  and an angle of incidence of  $\theta = 15^\circ$ . The perfect squareness of the longitudinal hysteresis curves indicate that the “easy axis” remains along the <001> in-plane direction throughout the entire 2–3 ML thickness regime [52].

In order to investigate the possibility of a canted film magnetization in a more quantitative manner, the formalism presented in section 2.2.1.2 is utilized. This formalism allows to calculate the Kerr rotation angle for ultrathin films with any arbitrary orientation  $\xi$  of the film magnetization. For orientations of  $\xi = 0^\circ$  and  $\xi = \pm 90^\circ$  the film is magnetized purely out-of-plane and in-plane, respectively. Figure 7.17 illustrates the approach of calculating the magneto-optic Kerr rotation for a unidirectional canted film magnetization. Here “unidirectional” means that the magnetic anisotropy energy is not an even function of  $\xi$ :

$$E(\vec{M}_{\parallel}, \vec{M}_{\perp}) \neq E(-\vec{M}_{\parallel}, \vec{M}_{\perp}) \quad (7.4)$$

where  $\vec{M}_{\parallel}$  and  $\vec{M}_{\perp}$  denote the in-plane (along the <001> direction) and out-of-plane magnetization component. This directionality is directly connected to the lack of inversion symmetry of the GaAs{110} surface along the <001> direction.

For the calculation, the Fe film thickness is kept at a constant value and the optical and magnetic constants from section 2.2.1.2 are used. Furthermore, the angle of incidence of the incoming laser light is kept constant which is illustrated by the red arrows in Figure 7.17. The space inversion asymmetry of the GaAs{110} surface (see section 7.2) cannot be taken into consideration within the framework of this calculation. Here the GaAs sub-

strate is assumed to be homogeneous and is defined solely by the optical constants given in section 2.2.1.2 Nevertheless, the possibility of a unidirectional canted film magnetization being induced by the anisotropy of the GaAs{110} surface can be simulated by appropriately adjusting the orientation  $\xi$  of the film magnetization for the two corresponding experimental setups with  $\alpha = \vartheta = 0^\circ$  and  $\alpha = \vartheta = 180^\circ$  as shown in the following (see Figure 7.17).

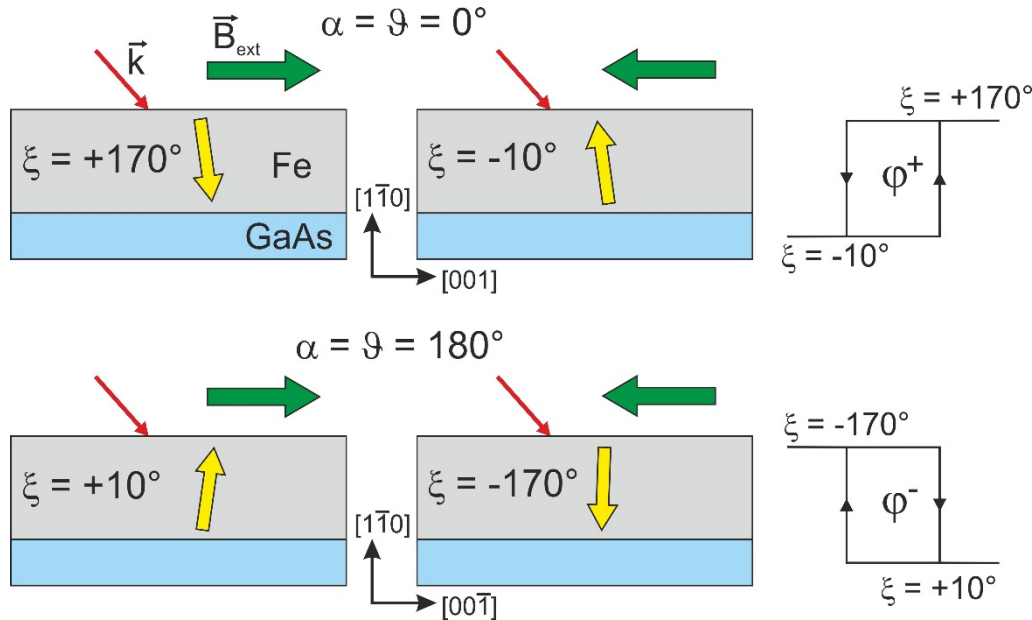


Figure 7.17: Scheme to explain the calculated Kerr rotation for different orientations  $\xi$  of the film magnetization (yellow arrows). For the calculations the angle of incidence of the laser light (red arrows) is kept constant. Depicted is the switching between two spin states for the two cases  $\alpha = \vartheta = 0^\circ$  and  $\alpha = \vartheta = 180^\circ$  [52].

In the upper part of Figure 7.17 the first case of  $\alpha = \vartheta = 0^\circ$  is shown. In this example it is assumed that the orientation of the Fe film magnetization is  $\xi = +170^\circ$ , hence  $10^\circ$  tilted away from a pure out-of-plane direction towards the  $[001]$  direction. This spin state is obtained after (imaginary) applying a sufficiently large external magnetic field  $\vec{B}_{ext}$  (green arrow) along the  $[001]$  direction (or also perpendicular to the surface into  $[\bar{1}\bar{1}0]$  direction in accordance with the results from Figure 7.15). The obtained Kerr rotation for this configuration would then correspond to the upper baseline of the experimentally obtained hysteresis curve. In a next step the external field  $\vec{B}_{ext}$  is (imaginary) reversed. This switches the film magnetization into another spin state. In this example it is assumed that the obtained spin state is antiparallel to the first spin state and therefore  $\xi = -10^\circ$  (see Figure 7.17). This assumption is not completely unjustified if one looks at the Kerr signal for  $\alpha = 91^\circ$  in Figure 7.8. There the polar component is found to be an even function of the magnetic field with a Kerr rotation of  $\sim 5$  mdeg for spin rotation from out-of-plane to completely saturated in-plane magnetization. This is about half of the total polar Kerr component of  $\varphi^P \approx 9.75$  mdeg determined for the same sample. This indicates that the

polar magnetization switches between an upward and a downward oriented spin state equal in magnitude. The obtained Kerr rotation for the  $\xi = -10^\circ$  configuration from the simulation would then correspond to the lower baseline of the experimentally obtained hysteresis curve. Therefore, the difference between the two calculated Kerr rotation values for  $\xi = +170^\circ$  and  $\xi = -10^\circ$  can be directly compared to the experimental Kerr rotation  $\varphi^+$  (height of the corresponding experimental hysteresis loop).

In order to simulate a unidirectional canted film magnetization for the experimental case of  $\alpha = \vartheta = 180^\circ$ , the angle of incidence is kept constant and the orientation  $\xi$  of the film magnetization is mirrored along the perpendicular axis (see lower panels in Figure 7.17). In other words: the sample is (imaginary) turned around by  $180^\circ$  with respect to the incoming laser light and the applied magnetic field which corresponds to a change of sign for the orientation angles  $\xi$ . By (imaginary) applying a sufficiently large magnetic field along the  $[00\bar{1}]$  direction (or also perpendicular to the surface into  $[1\bar{1}0]$  direction in accordance with the results from Figure 7.15) the orientation of the film magnetization is switched to  $\xi = +10^\circ$ . The calculated Kerr rotation for this spin state would correspond to the lower baseline of the experimentally obtained hysteresis curve. By (imaginary) reversing the applied field the magnetization is then switched into the antiparallel direction  $\xi = -170^\circ$ . The calculated Kerr rotation for this configuration would correspond to the upper baseline of the experimentally obtained hysteresis loop. Therefore, also the difference between the two calculated Kerr rotation values for  $\xi = +10^\circ$  and  $\xi = -170^\circ$  can be directly compared to the experimental Kerr rotation  $\varphi^-$  (height of the corresponding experimental hysteresis loop).

In Table 7.2 on the next page, the experimental Kerr rotation values  $\varphi^+$  and  $\varphi^-$  for ultrathin Fe films of different thicknesses  $d$  on GaAs(1̄10) are shown together with the calculated Kerr rotation values for different configurations of orientations  $\xi$  of the Fe film magnetization. E.g., the configuration consisting of  $\xi = -10^\circ$  and  $\xi = +10^\circ$  is the one illustrated in Figure 7.17. The experimental values are obtained from Figure 7.11 and Figure 7.12 from section 7.5. All Kerr rotation values are given in mdeg and positive and negative signs represent counterclockwise and clockwise hysteresis curves, respectively. Behind the calculated Kerr rotation values the deviation from the experimental values is given in units of standard deviation inside the brackets. For the angles of incidence  $\theta = 15^\circ$  and  $\theta = 67^\circ$  the standard deviation is given by  $\sigma = 2.5$  mdeg and  $\sigma = 6.5$  mdeg corresponding to the experimentally observed noise.

In the case of the 2 ML Fe on GaAs(1̄10) the experimental values cannot be described by the model of a unidirectional canted film magnetization within an uncertainty of  $1\sigma$ . The calculated Kerr rotation for a spin configuration with  $\xi = -10^\circ$  and  $\xi = +10^\circ$  comes closest to the experimental values with deviations between  $2\sigma$  and  $4\sigma$ . Table 7.2 also shows that a larger in-plane magnetization component in the calculations results in a much larger deviation from the experimental values for the 2 ML thick Fe film.

		calculated Kerr rotation [mdeg] (for p polarized light) for different orientations $\xi$ of the film magnetization $\vec{M}$												
$d$	$\theta$	exp. values	$\varphi^+$	$\varphi^-$	0°	90°	-10°	+10°	-45°	+45°	-55°	+55°	-80°	+80°
2 ML	15°	+24.0	-26.0	$\pm 20.1$	+3.0	+20.2 (2σ)	-19.2 (3σ)	+16.3 (4σ)	-12.1 (6σ)	+13.9 (5σ)	-9.0 (7σ)	+6.4 (8σ)	-0.5 (11σ)	
	67°	+39.0	-17.3	$\pm 12.0$	+14.6	+14.4 (4σ)	-9.3 (2σ)	+18.8 (4σ)	+1.8 (3σ)	+18.8 (4σ)	+5.1 (4σ)	+16.4 (4σ)	+12.3 (5σ)	
2.5 ML	15°	+17.6	-12.2	$\pm 24.3$	+3.7	+24.5 (3σ)	-23.2 (5σ)	+19.8 (1σ)	-14.5 (1σ)	+17.0 (1σ)	-10.9 (1σ)	+7.9 (4σ)	-0.5 (5σ)	
	67°	n/a	n/a	$\pm 13.5$	+18.3	+16.4	-10.1	+22.5	+3.4	+22.7	+7.3	+20.4	+15.7	
2.7 ML	15°	+14.8	-10.6	$\pm 25.9$	+4.0	+26.2 (5σ)	-24.8 (6σ)	+21.1 (3σ)	-15.4 (2σ)	+18.1 (2σ)	-11.5 (1σ)	+8.5 (3σ)	-0.5 (4σ)	
	67°	+32.9	+7.0	$\pm 13.9$	+19.8	+17.1 (3σ)	-10.2 (3σ)	+23.8 (2σ)	+4.2 (1σ)	+24.2 (2σ)	+8.3 (1σ)	+21.9 (2σ)	+17.1 (2σ)	
3 ML	15°	+7.3	-2.8	$\pm 28.2$	+4.5	+28.5 (9σ)	-27.0 (10σ)	+23.1 (7σ)	-16.8 (6σ)	+19.9 (5σ)	-12.5 (4σ)	+9.3 (1σ)	-0.5 (1σ)	
	67°	+28.2	+17.6	$\pm 14.4$	+22.1	+18.0 (2σ)	-10.3 (5σ)	+25.8 (1σ)	+5.5 (2σ)	+26.3 (1σ)	+9.9 (2σ)	+24.3 (1σ)	+19.3 (1σ)	

Table 7.2: Experimental and calculated values of the Kerr rotation of 2–3 ML thick Fe films on GaAs(1̄10) [52]. All values are given in mdeg.  $d$  and  $\theta$  denote the thickness of the Fe film and the angle of incidence, respectively. The orientations  $\xi = 0^\circ$  and  $\xi = 90^\circ$  describe a purely out-of-plane and a purely in-plane magnetized Fe film, respectively. For the canted magnetization configurations ( $\xi = \pm 10^\circ, \pm 45^\circ, \pm 55^\circ, \pm 80^\circ$ ) the deviation of the calculated values from the experimental values is given in units of the standard deviation in the brackets. For  $\theta = 15^\circ$  and  $\theta = 67^\circ$  the standard deviation is given by  $\sigma = 2.5$  mdeg and  $\sigma = 6.5$  mdeg, respectively, corresponding to the experimentally observed noise.

One could also consider possible deviations in the experimental Fe film thickness due to a deviating growth rate. In that case, one could compare the experimental Kerr rotation of the 2 ML Fe film to the calculated Kerr rotation for thicker Fe films. E.g., the calculated Kerr rotation for a 2.7 ML thick Fe film and an angle of incidence of  $\theta = 15^\circ$  are within a  $1\sigma$  uncertainty. However, the deviation between experiment and calculation is up to  $3\sigma$  for  $\theta = 67^\circ$ . Therefore, the experimentally obtained Kerr rotation values for the 2 ML thick Fe film on GaAs(1̄10) also cannot be explained by a possible deviation in the film thickness in the framework of a unidirectional canted film magnetization.

Table 7.2 also shows that for increasing film thickness the smallest deviation between experimental and calculated Kerr rotations shifts towards spin configurations with an increasing in-plane component. For the 2.7 ML thick Fe film, for instance, the smallest deviation of  $2\sigma$  is found for an orientation of the film magnetization with  $\xi = -55^\circ$  and  $\xi = +55^\circ$ . The calculated Kerr rotation for the 3 ML thick Fe film exhibits a deviation of less than  $1\sigma$  from the experimental values for the spin configuration with  $\xi = -80^\circ$  and  $\xi = +80^\circ$ . Therefore, the experimentally obtained Kerr rotation for the 3 ML thick Fe film is in good agreement with the magneto-optical calculations of a unidirectional canted film magnetization with a small out-of-plane component. However, the magnetic properties of films thinner than 3 ML cannot be explained quantitatively in the framework of a unidirectional canted film magnetization.

In the presented calculation the unidirectional canted film magnetization is described by two antiparallel spin states, e.g.,  $\xi = +10^\circ$  and  $\xi = -170^\circ$  as shown in Figure 7.17. This assumption appears to be quite random and one might suspect if this limitation to solely antiparallel configurations precludes a better agreement between experiment and calculation. It might be possible that the two spin states rather take another arbitrary orientation to each other which would be energetically more favorable. However, even though one considers any arbitrary orientation of the two spin states, the experimental Kerr rotation cannot be described by the simulated values. E.g., the maximum possible calculated Kerr rotation for the 2 ML thick Fe film at an angle of incidence of  $\theta = 67^\circ$  is  $\varphi^+ \approx +19$  mdeg. In contrast, the corresponding experimental value is  $\varphi^+ = +39$  mdeg [52]. Therefore, even if one allows any arbitrary orientations  $\xi$  of the two spin states, the calculated values disagree with the experiment.

In summary, in this subsection it was shown that a unidirectional canted film magnetization cannot explain the experimentally observed magnetic properties of the ultrathin (2—3 ML thick) Fe films on GaAs{110}. Qualitatively, the perfect squareness of both the longitudinal and the polar hysteresis curves does not suggest a SRT in the conventional sense as found in the literature for thin films with a canted magnetization. Quantitatively, the experimentally obtained Kerr rotation values cannot be reproduced by magneto-optical calculations of a unidirectional canted film magnetization. Both findings suggest that the magnetic properties of ultrathin (2—3 ML) Fe films on GaAs{110} are governed by another kind of physics.

### 7.6.2 Influence of the Interface Quality

As was discussed in detail in the previous subsection, the large experimental Kerr rotations for ultrathin ( $< 3\text{ML}$ ) Fe films cannot be explained in the framework of a canted film magnetization. In this context it is important to raise the question where the apparently large out-of-plane magnetization component of these thin films finds its origin. Thus far, in this chapter the magnetic properties of solely LT grown ideal Fe/GaAs{110} interfaces have been investigated. However, in chapter 6 we saw already that “slowly” RT grown interfaces exhibit signs of intermixing as predicted by DFT calculations [80] (see also section 1.6). From these findings it has been concluded that the growth of an initial submonolayer Fe film at RT has a significant impact on the atomic and electronic structure of the Fe/GaAs{110} interface. It therefore only seems logical to investigate the impact of the “slow” RT growth and the associated higher degree of intermixing on the magnetic properties of the ultrathin Fe films on GaAs{110}.

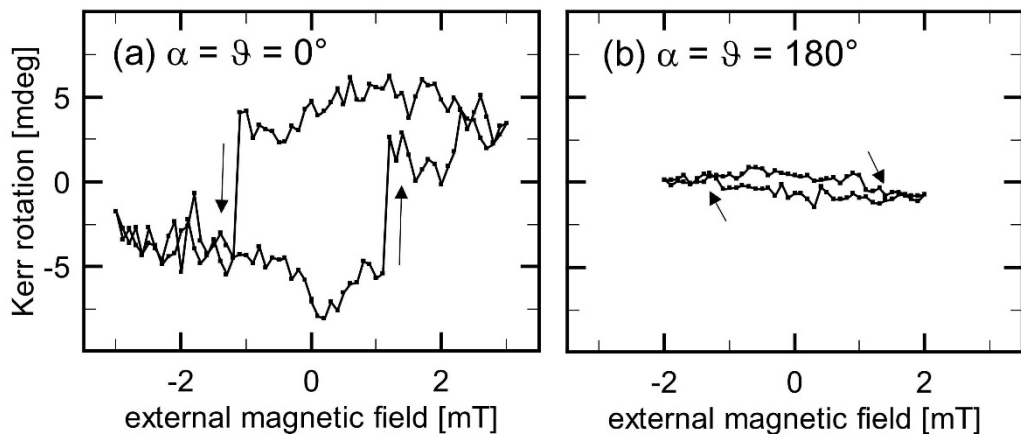


Figure 7.18: Experimentally obtained Kerr signal [52] for a sample that was prepared in the following way: First, 0.5 ML Fe were grown on a GaAs(1̄10) surface at RT. Then the sample was cooled down to  $\sim 130\text{ K}$  and additional 2 ML Fe were deposited on the surface. The MOKE measurements were conducted at  $\theta = 15^\circ$  and a laser wavelength of  $\lambda = 632.8\text{ nm}$ .

In a first attempt to do so, 0.5 ML Fe are grown on a GaAs(1̄10) surface at RT. This should cause intermixing of the Fe atoms with the topmost layer of the GaAs and therefore significantly reduce the quality of the GaAs(1̄10) surface. Subsequently, the sample is cooled down to  $\sim 130\text{ K}$  and additional 2 ML Fe are deposited on the surface so that the total Fe coverage adds up to 2.5 ML. After that the sample is annealed to RT and investigated by *in situ* MOKE. The obtained Kerr signals measured in the longitudinal ( $\beta = 90^\circ$ ) geometry for  $\alpha = \vartheta = 0^\circ$  and  $\alpha = \vartheta = 180^\circ$  are shown in Figure 7.18.

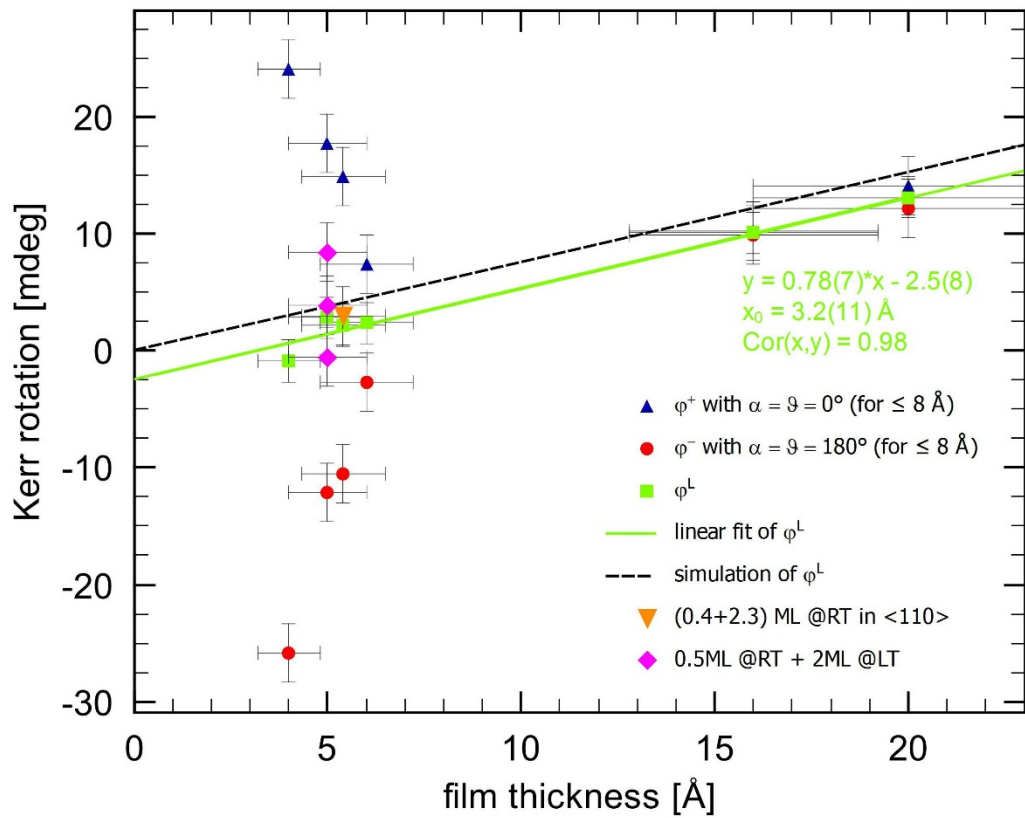


Figure 7.19: Dependency of the Kerr rotation on the Fe film thickness at an angle of incidence of  $\theta = 15^\circ$  as in Figure 7.11. In addition, here also the Kerr signals of the differently grown samples are plotted. The  $\varphi^+$ ,  $\varphi^L$ , and  $\varphi^-$  Kerr rotation values of the “0.5 ML Fe @RT + 2 ML Fe @LT” sample are represented by the upper, middle, and lower magenta diamonds, respectively. The Kerr rotation of the “0.4 ML @RT + 2.3 ML @RT” sample measured along the  $<110>$  easy axis is represented by the orange triangle [52].

The hysteresis curves can be directly compared to the data of the purely LT grown 2.5 ML Fe film in Figure 7.4(a) from section 7.1. The interchanged sense of the hysteresis curves can be attributed to the reversed anisotropy of the GaAs(110) and GaAs(1\bar{1}0) along the [001] direction (see section 7.2 for details). More interestingly, the absolute values of the Kerr signals (height of the hysteresis curves) are significantly reduced for the “0.5 ML @RT + 2 ML @LT” grown interface compared to the purely LT grown interface and amount to  $\varphi^+ \approx +8.3$  mdeg and  $\varphi^- \approx -0.7$  mdeg. This is nicely shown in Figure 7.19 where the corresponding values are plotted as magenta diamonds. The  $\varphi^+$ ,  $\varphi^L$ , and  $\varphi^-$  Kerr rotation values of the “0.5 ML Fe @RT + 2 ML Fe @LT” sample are represented by the upper, middle, and lower magenta diamonds, respectively. Apparently, the modification of the surface quality induced by intermixing has a significant impact on the detected magnetic momentum. The longitudinal component can be calculated according to equation (7.2) and amounts to  $\varphi^L \approx +3.8$  mdeg which is very close to the value of  $\varphi^L \approx +2.7$  mdeg for the purely LT grown sample. For the polar component, equation

(7.3) yields  $\varphi^P \approx 4.5$  mdeg which differs by more than 10 mdeg from the corresponding value of  $\varphi^P \approx 14.9$  mdeg for the purely LT grown sample. Therefore, one can say that the modification of the interface quality has a particularly strong impact on the detected polar Kerr component. However, one has to keep in mind that the specified film thicknesses have an uncertainty of  $\sim 20\%$  due to variations in the deposition flux and the calibration of the electron beam evaporator. As can be seen in Figure 7.19, the Kerr rotation values of the “0.5 ML Fe @RT + 2 ML Fe @LT” sample are very similar to the values for the purely LT grown 2.7 ML sample. Therefore, when interpreting the data one should exercise great caution.

To further investigate the impact of the interface quality on the magnetic properties of the sample, a second RT grown interface is prepared but this time all growth steps are carried out at RT. In a first step 0.4 ML Fe are deposited on a GaAs(1̄10) surface. About 3 hours later additional 2.3 ML Fe are grown on this pretreated surface again at RT. After each preparation step LEED measurements of the surface are conducted [52]. After the deposition of the 0.4 ML Fe the intensity of the LEED spots from the GaAs(1̄10) surface is decreased. This can be ascribed to the formation of disordered three-dimensional Fe nuclei [65]. After the deposition of additional 2.3 ML Fe, LEED patterns characteristic of bcc Fe are observed. Höllinger *et al.* [65] do not observe Fe LEED patterns for films thinner than 4 ML that they deposited at RT and at a rate of 0.5 ML/min. Seemingly, the submonolayer deposition and the subsequent 3 hours waiting time prior to further deposition altered the surface in such a manner that the additional 2.3 ML Fe was grown in a 2D-like mode.

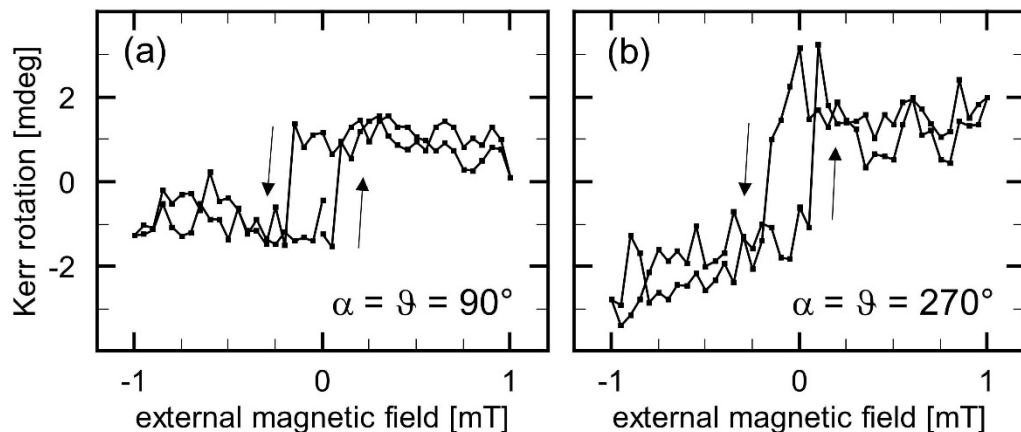


Figure 7.20: Experimentally obtained Kerr signal [52] for a sample that was prepared in the following way: First, 0.4 ML Fe were grown on a GaAs(1̄10) surface at RT. After some hours additional 2.3 ML Fe were deposited on the surface at RT. The easy axis is now directed along <110> (corresponding to  $\alpha = \vartheta = 90^\circ/270^\circ$ ) and no reversal of the hysteresis loops is observed (indicated by the arrows). The MOKE measurements were conducted at  $\theta = 15^\circ$  and a laser wavelength of  $\lambda = 632.8$  nm.

Moreover, the *in situ* MOKE measurements on the “0.4 ML Fe @RT + 2.3 ML Fe @RT” sample exhibit interesting magnetic properties. The square-shaped hysteresis curves with

small coercive fields taken at  $\alpha = \vartheta = 90^\circ$  and  $\alpha = \vartheta = 270^\circ$  show that for this sample the easy axis is now oriented along the in-plane  $<110>$  direction (see Figure 7.20). In contrast, the easy axis for the LT grown 2—3 ML Fe films on GaAs{110} appears to be oriented along the  $<001>$  in-plane direction as was discussed in the previous sections. Furthermore, the MOKE measurements at  $\alpha = \vartheta = 90^\circ$  and  $\alpha = \vartheta = 270^\circ$  on the “0.4 ML Fe @RT + 2.3 ML Fe @RT” sample do not exhibit a reversal of the sense of the two hysteresis curves as can be clearly seen in Figure 7.20. No sense reversal is observed in any arbitrary direction  $\vartheta$ . Furthermore, the Kerr rotation for the cases of  $\alpha = \vartheta = 90^\circ$  and  $\alpha = \vartheta = 270^\circ$  amount to  $\varphi^{90^\circ} \approx 2.1$  mdeg and  $\varphi^{270^\circ} \approx 2.3$  mdeg, respectively. This indicates that the “0.4 ML Fe @RT + 2.3 ML Fe @RT” sample is purely in-plane magnetized and no out-of-plane component is present.

In summary, a higher degree of intermixing at the interface, induced by RT deposition of a submonolayer Fe on the GaAs{110} surface, significantly decreases or even completely quenches the large polar Kerr component that has been observed for purely LT grown 2—3 ML Fe films. Apparently, the magnetic properties of the Fe/GaAs{110} interface are directly connected with the quality of the interface itself. Together with the finding from the previous subsection that a canted film magnetization cannot explain the experimental data this indicates that the polar Kerr component of the “LT grown 2—3 ML Fe on GaAs{110}” samples is somehow induced by the interface and the magnetic properties might be governed by interface magnetism.

### 7.6.3 Interface Magnetism

In subsection 7.6.1, we saw that the model of a canted film magnetization cannot explain the experimentally obtained Kerr signals from the ultrathin (2—3 ML thick) Fe films on GaAs{110}. In subsection 7.6.2, it was shown that the quality of the interface has a significant impact on the magnetic properties of the samples. These results suggest that the interface plays a crucial role with regard to the magnetic structure of the sample which we therefore want to investigate in greater detail in this subsection.

The polar MOKE measurements on the 3 ML thick Fe film on GaAs{110} from section 7.6.1 exhibited a perfect squareness of the corresponding hysteresis loops. This result taken alone would indicate an easy axis perpendicular to the GaAs{110} surface. However, as shown throughout this chapter, along the in-plane  $<001>$  direction we also find perfectly square-shaped hysteresis curves which indicate an in-plane easy axis along the  $<001>$  direction. In section 7.3, we saw that the coercive field exhibits a  $1/\cos(\alpha)$  dependency with  $\alpha$  being the in-plane angle between the  $<001>$  direction and the applied magnetic field. From that it was concluded that the component of the external magnetic field projected on the  $<001>$  in-plane easy axis determines the switching behavior of the sample. A comparison between the polar MOKE measurements from Figure 7.15 and the corresponding longitudinal MOKE measurements of the same sample from Figure 7.7 shows that the coercive fields are about 3 (for  $\vartheta = 0^\circ$ ) to 5 times (for  $\vartheta = 180^\circ$ ) larger for the polar hysteresis loops compared to the longitudinal ones. This suggests that a simi-

lar projection as has been observed for the in-plane field in section 7.3 might be on hand for the out-of-plane applied field. In order to further investigate this feature, the coercive field is measured in dependence of the out-of-plane magnetic field tilt angle  $\beta$  (see Figure 7.21 and Figure 7.2 for definition). The 4-magnetic-pole MOKE setup is used to tilt the magnetic field from the pure out-of-plane direction ( $\beta = 0^\circ$ ) towards the in-plane direction as described in section 2.2.2. Similar measurements have been presented in the Bachelor's theses of Rolf-Pissarczyk and Weikert [115, 146] which have been supervised by the author of this PhD thesis.

Figure 7.21 shows the measured Kerr signal in dependence of the magnetic field tilt angle  $\beta$ . For all tilt angles  $\beta$  that exhibit a hysteresis curve, the height of the hysteresis loop is  $\sim 13\text{--}14$  mdeg indicating that the magnetization is always switching between the same two spin states. For a tilt angle of  $\beta = -40^\circ$  (magnetic field tilted into the  $[00\bar{1}]$  direction) a square-shaped clockwise hysteresis loop with a coercive field of less than 1 mT is observed. For zero tilt of the magnetic field ( $\beta = 0^\circ$ ) the coercive field is increased while the perfect squareness and sense of the hysteresis loop remain the same. A positive tilt towards the  $[001]$  direction with  $\beta = +11.5^\circ$  further increases the apparent coercive field. A further increase of the tilt angle to values between  $\beta \approx +13^\circ$  and  $\beta \approx +14^\circ$  does not yield any observable hysteresis within the measurement range from -18 mT to +18 mT. At these tilt angles the Kerr signal solely exhibits a noisy horizontal line. A slight increase of the tilt angle to  $\beta = +15^\circ$  yields a square-shaped and now counter-clockwise hysteresis loop with relatively large coercive fields. A further increase of the tilt angle to  $\beta = +40^\circ$  leads to a decrease in the coercive field.

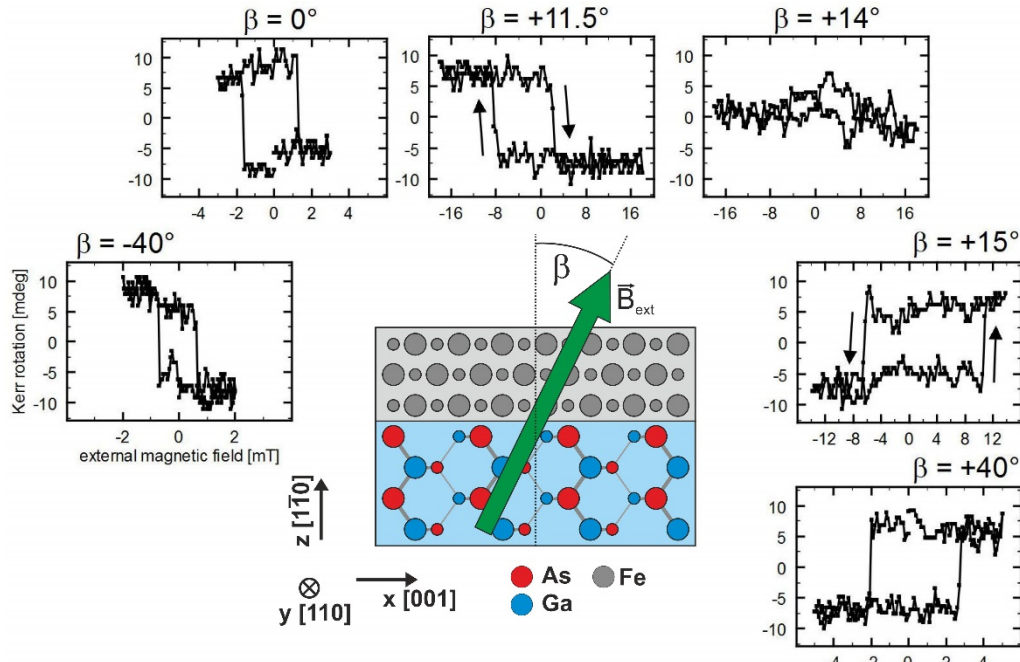


Figure 7.21: Experimentally obtained Kerr signal for different out-of-plane magnetic field tilt angles  $\beta$  together with a sketch of the coordinate system defining the tilt angle. The measurements are conducted at a laser wavelength of  $\lambda \approx 785$  nm.

The dependence of the coercive field on the magnetic field tilt angle  $\beta$  appears to be very similar to the observed dependence of the coercive field on the magnetic field in-plane angle  $\alpha$  as discussed in section 7.3. To investigate this in greater detail the half hysteresis widths (representing the coercive fields) are plotted against the tilt angle  $\beta$  for the two experimental geometries  $\alpha = \vartheta = 0^\circ$  and  $\alpha = \vartheta = 180^\circ$  as shown in Figure 7.22. Positive and negative values denote counterclockwise and clockwise hysteresis curves, respectively. For the two experimental geometries with  $\alpha = \vartheta = 0^\circ$  and  $\alpha = \vartheta = 180^\circ$  we observe a non-switching behavior (no hysteresis) at a tilt angle of  $\beta \approx +13^\circ$  and  $\beta \approx -7^\circ$ , respectively. The deviation of the two tilt angles from one another can be attributed to a slightly tilted sample holder and the limited accuracy in aligning the out-of-plane-field into the desired direction. Therefore, we identify the axis of non-switching behavior at tilt angles of  $\beta \approx +10^\circ$  (for  $\alpha = \vartheta = 0^\circ$ ) and  $\beta \approx -10^\circ$  (for  $\alpha = \vartheta = 180^\circ$ ) suggesting a hard axis along that tilt angle. In other words: to switch the magnetization of the sample, a minimum field has to be applied along the corresponding perpendicular directions described by  $\beta_\perp = -80^\circ$  or  $\beta_\perp = +80^\circ$ . Similar non-switching tilt angles  $\beta$  were also observed in the Bachelor's theses of Rolf-Pissarczyk and Weikert [115, 146].

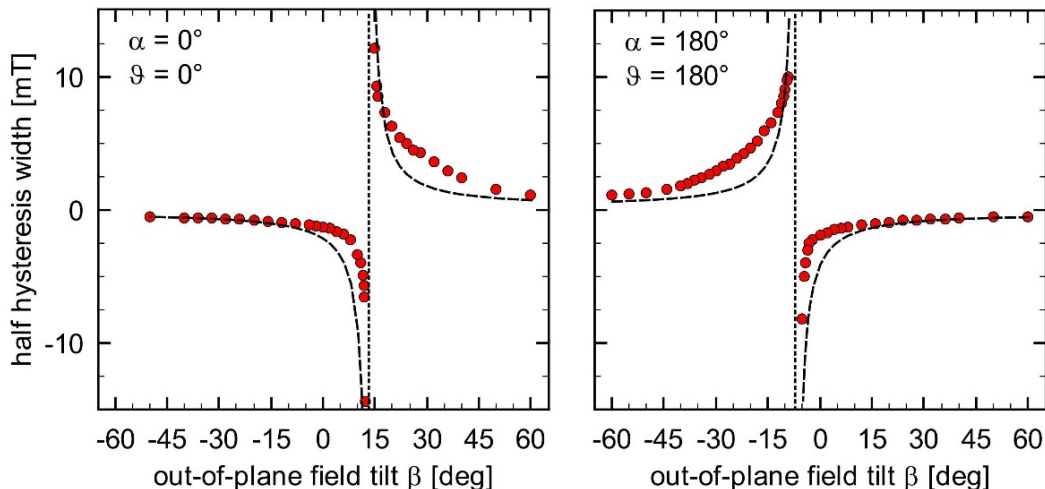


Figure 7.22: Half hysteresis widths (coercive fields) for a 3.2 ML thick Fe film on  $p$ -GaAs(110) at a fixed rotation angle of the laser plane-of-incidence and of the plane containing the external magnetic field vector of (left)  $\alpha = \vartheta = 0^\circ$  and (right)  $\alpha = \vartheta = 180^\circ$  plotted against the out-of-plane field tilt angle  $\beta$ . The black dashed lines describe a (left)  $1/\sin(\beta - 10^\circ)$  and (right)  $1/\sin(\beta + 10^\circ)$  dependence representing the necessary magnetic field applied along  $\beta$  to obtain the coercive field  $B_x^{cf} \approx 0.45$  mT perpendicular to the  $\beta = +10^\circ$  and  $\beta = -10^\circ$  direction, respectively. The angle of incidence is set to  $\theta = 15^\circ$ . The measurements are conducted at a laser wavelength of  $\lambda \approx 785$  nm. Positive and negative values denote counterclockwise and clockwise hysteresis curves, respectively.

Furthermore, the out-of-plane coercive fields do not follow a  $1 / \sin(\beta - 10^\circ)$  and  $1 / \sin(\beta + 10^\circ)$  dependence (black dashed lines). This dependence describes the necessary magnetic field applied along  $\beta$  to obtain the coercive field  $B_x^{cf} \approx 0.45$  mT (see also section 7.3) perpendicular to the  $\beta = +10^\circ$  and  $\beta = -10^\circ$  direction, respectively. In one tilt direction the magnetization switches at lower fields whereas in the other tilt direction larger fields have to be applied to switch the magnetization. This strongly supports the idea of a unidirectional anisotropy instead of a uniaxial anisotropy of the sample magnetization and a rather complex interplay between the in-plane and out-of-plane magnetization components.

In chapter 5.1 we already learned that the DFT data exhibit a strong hybridization between the majority states of Fe and As at the immediate Fe/GaAs{110} interface. Therefore, one would assume that the immediate GaAs interface layer takes on an effective spin-polarization and partially contributes to the total sample magnetization. In order to take this “interface magnetization” into consideration the simulation model of the canted Fe film magnetization from subsection 7.6.1 can be extended by an additional magnetic interface layer. Here this interface layer is assumed to be 1 ML thick and to have the refractive index of GaAs and the Voigt constant of Fe (see also section 2.2.1.2 for the values). On top of this “magnetic GaAs” we assume 2 ML Fe and below the interface layer we presume the GaAs substrate. Now we can test if the experimentally obtained Kerr rotation values for 2 ML thick Fe films on GaAs{110} from Table 7.2 in subsection 7.6.1 can be reproduced by this extended model. As a first idea to do so, one could choose a fixed orientation  $\xi_{Fe}$  for the Fe film magnetization, e.g., the orientations  $\xi_{Fe}$  from Table 7.2, and then try to optimize the simulated Kerr rotation values by varying the orientation  $\xi_{IF}$  of the magnetization of the magnetic interface layer. If we take the orientations  $\xi_{Fe} = +10^\circ$  and  $\xi_{Fe} = -10^\circ$  from Table 7.2, we see that the simulated values for the steep angle of incidence  $\theta = 15^\circ$  describe the experimental values better than the ones with the flatter angle of incidence  $\theta = 67^\circ$ . A setup with a flatter angle of incidence is more sensitive to an in-plane magnetization component than a setup with a steeper angle of incidence. Therefore, one could expect that an additional interface magnetization with a large in-plane component, which switches back and forth in the same way as the Fe film magnetization, could bring simulated and experimental values closer together. However, by keeping  $\xi_{Fe}$  fixed and finding certain  $\xi_{IF}$ , up to three simulated values (of the quadruple in Table 7.2) approach the corresponding experimental values but at least one simulated value deviates stronger from the experiment than the corresponding simulated value without additional interface magnetism.

The model with fixed  $\xi_{Fe}$  cannot reproduce the experimental data and therefore a more general approach is chosen in the following. Now,  $\xi_{Fe}$  is not kept constant any longer but is varied simultaneously with  $\xi_{IF}$ . This allows a lot more possibilities of relative orientations between film and interface magnetization. Here the same boundary condition of a switching between two spin states with polar components of equal magnitude but opposite sign is applied. As already discussed in subsection 7.6.1 this is justified by the obser-

vation from Figure 7.8 (panel for  $\alpha = 91^\circ$ ) that the polar magnetization switches between an upward and a downward oriented spin state equal in magnitude.

One finds two simulated spin configurations for each of the experimental values  $\varphi^+$  ( $\alpha = \vartheta = 0^\circ$ ) and  $\varphi^-$  ( $\alpha = \vartheta = 180^\circ$ ) from Table 7.2 that reproduce the experimental values for both angles of incidence. The two possible configurations that describe the experimental data for 2 ML Fe on GaAs are shown in Figure 7.23. For each of the two cases  $\alpha = \vartheta = 0^\circ$  and  $\alpha = \vartheta = 180^\circ$  the simulation yields an antiferromagnetic and a ferromagnetic configuration where the total magnetization of the Fe film and interface layer are aligned in a more antiparallel and parallel way, respectively. The sign convention for the simulated Kerr rotation is defined in the same way as in subsection 7.6.1. In that way an (imaginary) applied magnetic field  $\vec{B}_{ext}$  would yield an effective sample magnetization into the opposite direction for both possible configuration for the case  $\alpha = \vartheta = 0^\circ$ . For the case  $\alpha = \vartheta = 180^\circ$  only the second configuration would yield an effective magnetization into the same direction as the (imaginary) external field. This “antiparallel” alignment of external field and magnetization in the simulations are not coherent from a physical point of view. From that we can immediately conclude that also the extended canted magnetization model cannot describe the experimental findings consistently. One could assume that this lack of consistency might also be related to a change in the optical constants of the interface region possibly caused by metal-induced gap states in the semiconductor. However, additional simulations where the refractive index of Fe was taken for the 3—4 ML GaAs at the immediate interface could not reproduce the experimental data either [52]. In fact, by altering the refractive index of the interface region in that way, the deviation between experimental and simulated Kerr rotations increases.

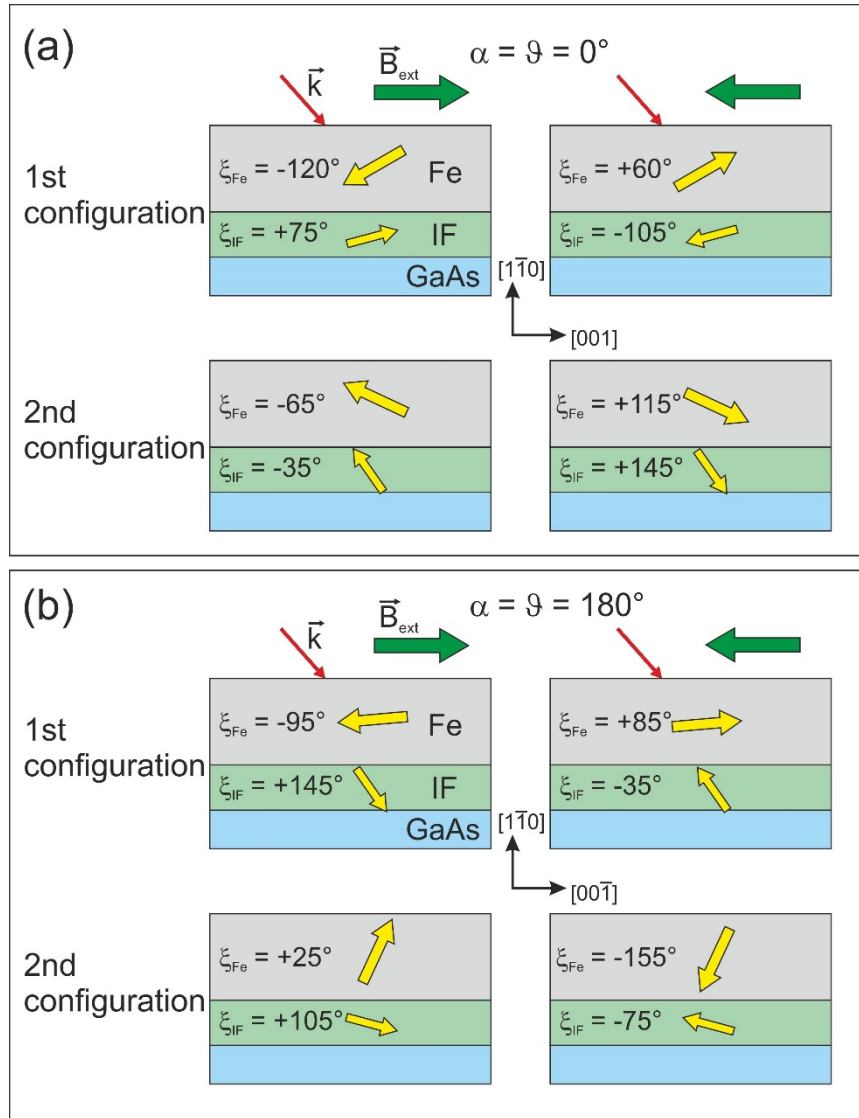


Figure 7.23: Extended canted magnetization model with a 2 ML Fe film and an additional magnetic interface (IF) layer. Shown are the two possible configurations of the magnetization (yellow arrows) for (a)  $\alpha = \vartheta = 0^\circ$  and (b)  $\alpha = \vartheta = 180^\circ$  that would reproduce the corresponding experimental Kerr rotations  $\varphi^+$  and  $\varphi^-$  from Table 7.2.

In this section we concluded that neither the canted film magnetization model nor the extended model of a canted interface magnetization can describe the experimental observations. This is leading us to search for other alternative models containing more complex spin structures. In order to do so let us reconsider the most important experimental findings for 2—3 ML Fe on GaAs(110) presented in this chapter:

- 1) Due to the squareness of the hysteresis curves obtained in polar and longitudinal geometry we expect a single domain structure.
- 2) The sample magnetization is perpendicular to the <110> in-plane hard axis ( $y$  direction).

- 3) The sample magnetization has an in-plane component along  $<001>$  ( $x$  direction) and an out-of-plane component along  $<1\bar{1}0>$  ( $z$  direction).
- 4) The direction of the out-of-plane component depends on the relative orientation between the in-plane magnetization and the sample surface along the  $<001>$  direction. This directionality [ $E(\vec{M}_{||}, \vec{M}_{\perp}) \neq E(-\vec{M}_{||}, \vec{M}_{\perp})$ ] is directly connected to the lack of inversion symmetry along the  $<001>$  direction.
- 5) The effect described in 3) breaks down with the magnetization completely oriented along the in-plane  $<110>$  direction if (i) the quality of the interface (RT growth) is significantly decreased, (ii) the LT grown Fe film is thicker than 5 ML, or (iii) by applying a sufficiently large magnetic field ( $\sim 100$  mT) along  $<110>$  ( $y$  direction).
- 6) With the experimental setup (maximum in-plane fields of  $\sim 130$  mT) it is not possible to align the magnetization of 2–3 ML thick Fe films completely along the in-plane  $<001>$  direction ( $x$  direction). It somehow seems as if two effects – the natural tendency of the Fe film to be magnetized along in-plane  $<110>$  and an effect yet to be determined – are competing against each other.

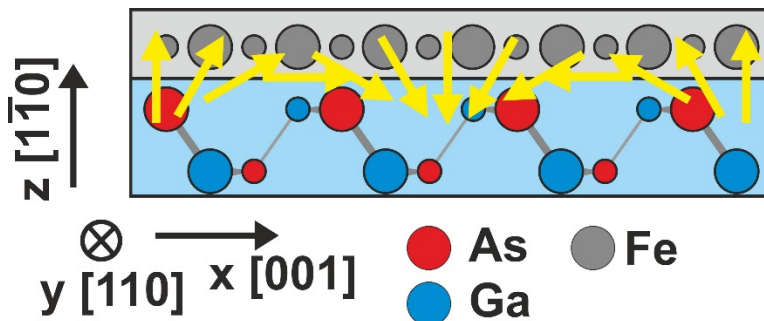


Figure 7.24: Symmetric spin spiral (yellow vectors) where the DMI vector  $\vec{D}_{ij}$  is parallel to the chirality vector ( $\vec{S}_i \times \vec{S}_j$ ) and the spin rotation path would be in the  $x$ - $z$  plane.

One model that might be able to explain the experimental results [151] would consider the Dzyaloshinskii-Moriya interaction (DMI) [147, 148]. This interaction is an intrinsic property of a magnetic system that lacks space inversion symmetry together with the presence of spin-orbit interaction (SOI). The *in situ* MOKE measurements of the Fe/GaAs{110} interface exhibit a unique magnetic anisotropy demonstrating a SOI that is particularly related to the ideal Fe/GaAs{110} system as a whole. The inversion asymmetry of this system is found along the in-plane  $<001>$  direction of the GaAs{110} surface as discussed in section 7.2. The energy contribution of the DMI can be expressed by  $E_{\text{DMI}} = \vec{D}_{ij} \cdot (\vec{S}_i \times \vec{S}_j)$ , where  $\vec{D}_{ij}$  is the DMI vector and  $\vec{S}_i$  and  $\vec{S}_j$  are magnetic spin moments located on adjacent atomic sites  $i$  and  $j$ . From the expression for  $E_{\text{DMI}}$  we see that magnetic spins on neighboring atomic sites are favored to be aligned orthogonally by the

DMI. The DMI and the exchange coupling compete energetically which will yield a non-collinear spin structure with a chirality. Applying the symmetry conditions given in Ref. [148] one obtains a DMI vector  $\vec{D}_{ij}$  lying in the film plane along the  $<110>$   $y$  direction. This would rotate the spin from the easy axis, which first DFT caluculations by Prof. S. Blügel and Dr. A. Al-Zubi indicate to be the  $z$  direction, into the  $x$  axis corresponding to  $<001>$ . However, if we consider a symmetric spin spiral as shown in Figure 7.24 where the DMI vector  $\vec{D}_{ij}$  is parallel to the chirality vector  $(\vec{S}_i \times \vec{S}_j)$  with spin rotation path in the  $x$ - $z$  plane, we would expect an effective magnetization of zero because the spins would average out over a single domain structure.

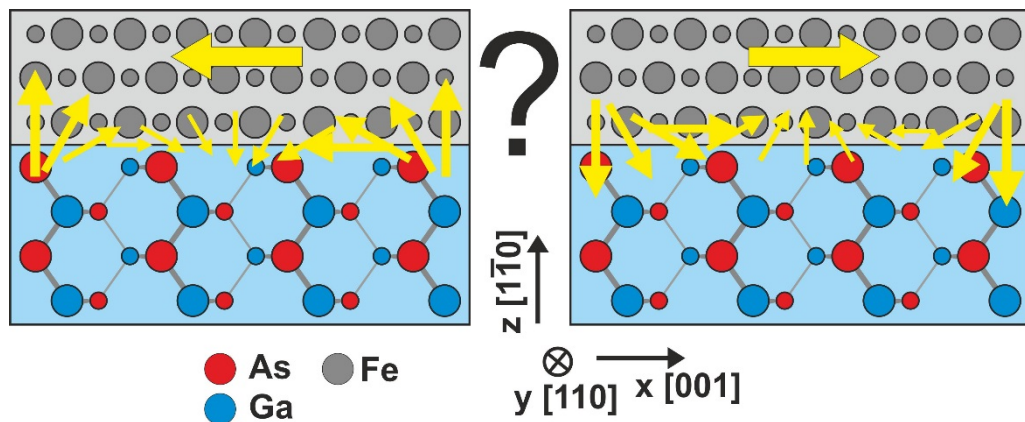


Figure 7.25: Model of an asymmetric spin spiral in an attempt to qualitatively explain the observed experimental data that do not suggest a simple canted film magnetization but exhibit a strong out-of-plane component that is unidirectionally coupled to an in-plane component.

In order to obtain a spin spiral single domain structure with an effective magnetization in  $x$  and  $z$  direction, one could consider an asymmetric spin spiral. With this in mind, Figure 7.25 illustrates the idea that the in-plane magnetization component is mainly contributed by the upper layer(s) of the Fe film as suggested by the thickness dependent MOKE measurements and an asymmetric spin spiral with a non-constant chirality contributes an effective out-of-plane magnetization. This is only a first attempt to qualitatively understand the experimental data. It should be mentioned here that at the time of writing this thesis, the DFT group of S. Blügel is making a great effort to solve this problem quantitatively. Therefore, at this point the attempt to qualitatively explain the experimental observation by an interplay of exchange coupling, spin-orbit interaction, and Dzyaloshinskii-Moriya interaction should be rather understood as an outlook.



## 8 Combined Electronic and Magnetic Discussion of the Interface

In chapter 7 *in situ* MOKE measurements revealed an out-of-plane magnetization component for ultrathin 2–3 ML thick Fe films on GaAs{110} that is unidirectionally coupled to the in-plane magnetization. Magneto-optical simulations suggest that this effect cannot be explained by a canted film magnetization. The experimental data indicate that a part of the magnetization originates from the interface region. Therefore, it would be interesting to find out more about the nature of this interface magnetism. E.g., there remains the question which particular states at the interface are responsible for this effect.

In this context, we should look back at chapters 4 and 5 where a quantitative analysis of the ideal Fe/*p*-GaAs{110} by means of cross-sectional scanning tunneling spectroscopy and density functional calculations have shown an additional positive charge inside the valence band due to a strong hybridization between Fe and As atoms at the interface. In section 4.3 it was shown that the energy range where this additional positive charge is found starts about ~0.35 eV below the valence band maximum (see also Figure 4.10). Interestingly, from literature it is well-known that about ~0.34 eV below the valence band maximum the maximum of the spin-orbit split-off band is located. This is illustrated by Figure 8.1 where the dependence of the energy on the wave vector in the energy range around the band gap of GaAs was obtained from nonlocal pseudopotential calculations [152, 153]. This immediately raises the question if the additional positive charge starting at ~0.35 eV below the valence band maximum is somehow connected to the split-off band and responsible for the unidirectional magnetic anisotropy observed by the MOKE experiment.

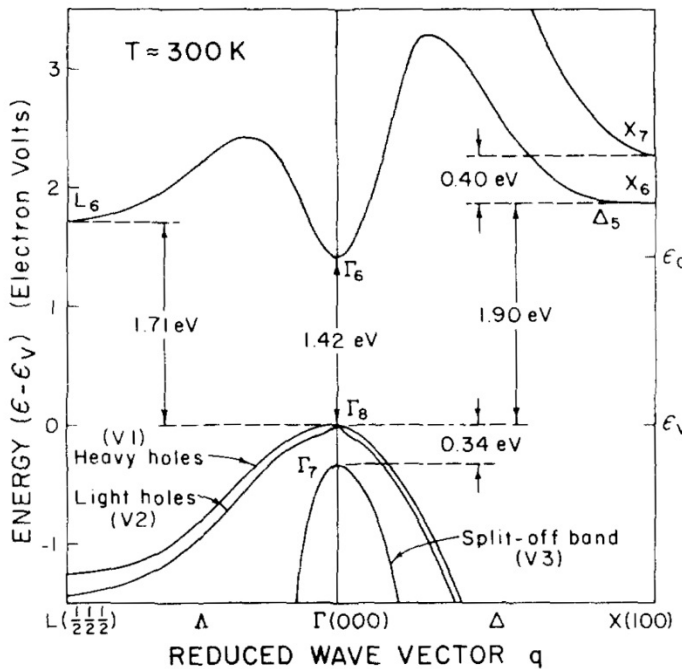


Figure 8.1: Dependence of the energy on the wave vector in the energy range around the band gap of GaAs obtained from nonlocal pseudopotential calculations [152]. The Figure is taken from [153].

One possibility to address this question could be photon energy-dependent MOKE measurements at different optical wavelengths. Here the idea is to choose different laser wavelengths corresponding to the energy range around the band gap of GaAs as illustrated in Figure 8.2 and to energetically probe if the split-off band needs to be addressed to observe the unidirectional magnetic anisotropy of the 2–3 ML thick Fe films on GaAs{110}. At the wavelengths of  $\lambda = 532$  nm (Nd:YAG laser with frequency doubler) and  $\lambda = 632.8$  nm (HeNe laser) states in the split-off band are addressed. At a wavelength of  $\lambda = 785$  nm (diode laser) states in the split-off band cannot be addressed anymore but this wavelength still corresponds to a larger energy than the energetic width of the band gap. A wavelength of  $\lambda = 1064$  nm (Nd:YAG laser) corresponds to a smaller energy than the energetic width of the band gap and is therefore above the absorption limit. For the experimental realization of the MOKE measurements at different wavelengths the MOKE setup remains the same as described in section 2.2.2. For the desired wavelength the corresponding laser has to be chosen. Furthermore, the linear polarizers and the  $\lambda/4$  waveplate have to be chosen in accordance with the wavelength of the laser and the photo-elastic modulator has to be adjusted to the correct wavelength.

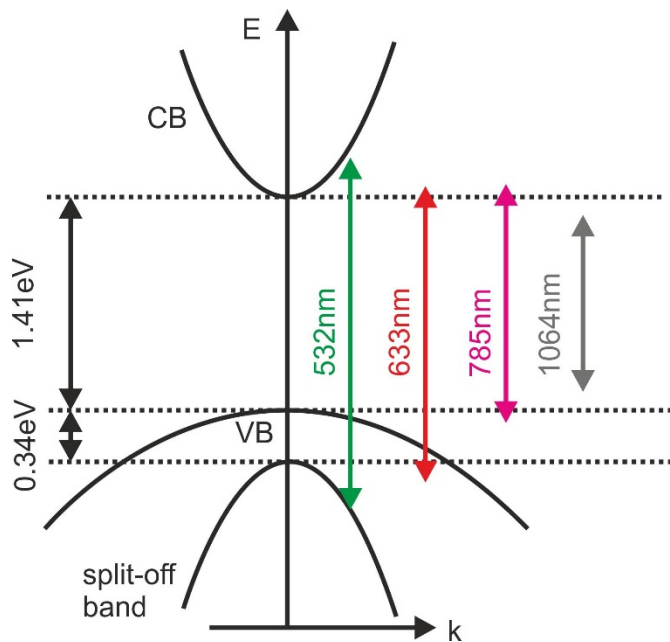


Figure 8.2: Energy band scheme of GaAs and corresponding optical wavelengths.

The same experiment as described in section 7.1 is conducted with a sample of 2.5 ML Fe grown at LT on a GaAs(1̄10) surface. The Kerr rotation of the sample is measured for  $\alpha = \vartheta = 0^\circ$  and  $\alpha = \vartheta = 180^\circ$ . The experimentally obtained Kerr rotations are depicted in Figure 8.3. Obviously, the reversal of the sense of the hysteresis curves is observed for all laser wavelengths. This means that the magnetic anisotropy with an out-of-plane component, which is coupled unidirectionally to the in-plane component along the  $<001>$  direction, can be detected for all applied photon energies. This yields us to the conclusion that the states from the spin-orbit split-off band alone cannot be responsible for the observed unidirectional magnetic anisotropy. The fact that the unidirectional magnetic anisotropy is also observed for a laser wavelength of  $\lambda = 1064$  nm suggests that this effect is dominated by either the metal-induced gap states or by states inside the metal film or by both.

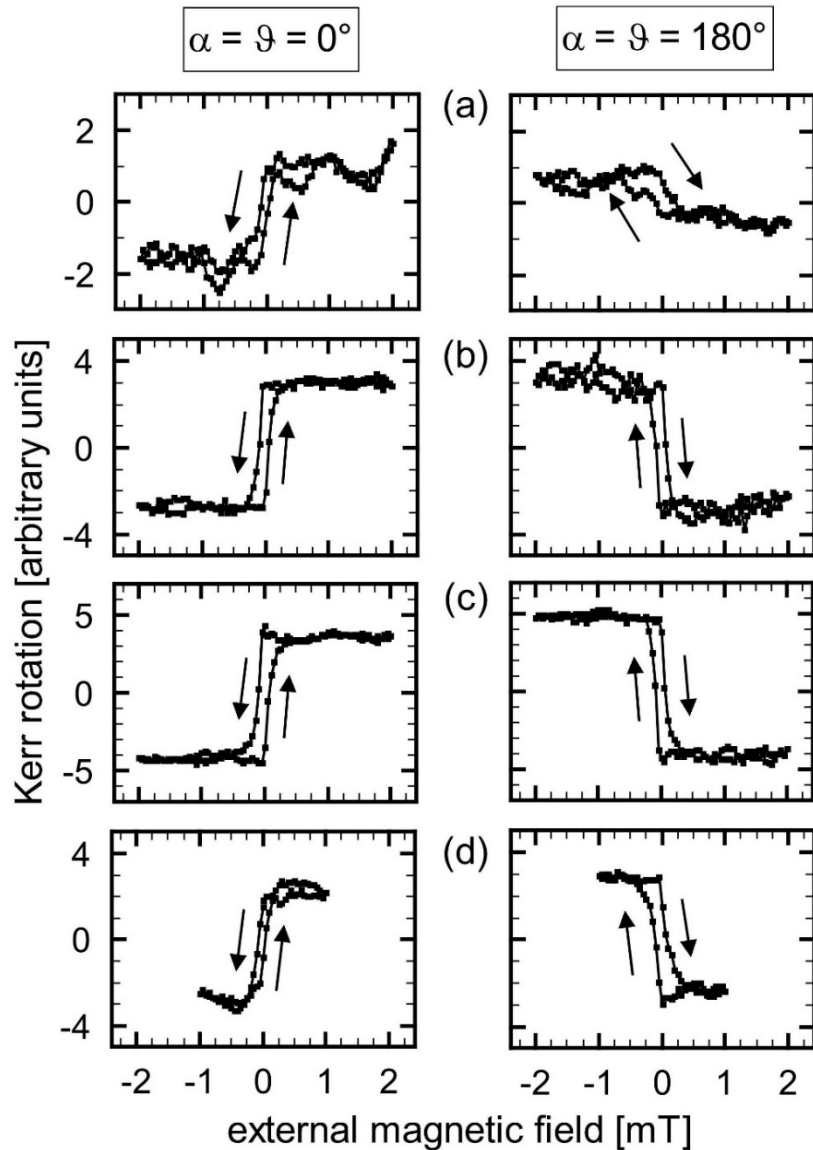


Figure 8.3: Experimentally obtained Kerr rotation at optical wavelengths of (a)  $\lambda = 532\text{ nm}$ , (b)  $\lambda = 632.8\text{ nm}$ , (c)  $\lambda = 785\text{ nm}$ , and (d)  $\lambda = 1064\text{ nm}$  for relative sample orientations in (left)  $[001]$  direction ( $\alpha = \vartheta = 0^\circ$ ) and (right)  $[00\bar{1}]$  direction ( $\alpha = \vartheta = 180^\circ$ ). The reversal of the sense of the hysteresis curves is observed for all wavelengths.

## 9 Summary

Goal of this thesis has been the investigation of the structural, electronic, and magnetic properties of Fe/GaAs{110} interfaces. In order to check the validity of theoretical models describing the microscopic process of Schottky barrier formation, the objective has been to study an ideal metal-semiconductor interface on the atomic scale. Based on work by Winking [47], in this thesis, the low-temperature grown Fe/GaAs{110} interface serves as an ideal model system that is studied by means of atomically resolved cross-sectional scanning tunneling microscopy (XSTM) and spectroscopy (XSTS). For the first time, this approach yields a spatial and energetic map of the local density of states that covers both the band gap and the valence and conduction bands at the interface. In combination with density functional calculations performed by Dr. Ali Al-Zubi and Prof. Stefan Blügel this allows a better understanding of the relevance of metal-induced gap states and bond polarization at the interface. Moreover, goal of this thesis has been a detailed investigation of the magnetic anisotropy of ultrathin (2—3 ML) low-temperature grown Fe films on the GaAs{110} surface by means of *in situ* magneto-optic Kerr effect measurements in longitudinal, polar, and transverse geometry. In the following, the main results of this thesis are summarized:

The technique of XSTM and XSTS has been successfully applied to study the structural and electronic properties of the ideal *p*-type Fe/GaAs(110) interface at low temperatures. The XSTM measurements of the low-temperature (LT) grown epitaxial *p*-type junction reveal an abrupt, nonintermixed, and defect-free interface and therefore confirm earlier work by Winking [47] who investigated the LT grown *n*-type Fe/GaAs( $\bar{1}10$ ) interface at room temperature and also found an ideal interface.

Highly resolved LT XSTS measurements show a downwards bending of the valence and conduction band towards the interface for the *p*-type junction and a continuum of states inside the band gap of the *p*-type semiconductor. These gap states cannot be attributed to surface states that could be possibly generated by the abrupt potential change or dangling bonds at the immediate interface. This is demonstrated by a control experiment across the *p*-type GaAs(110)-( $\bar{1}10$ ) edge without Fe film that does not exhibit any states inside the

band gap. Therefore, the gap states observed for the ideal Fe/*p*-GaAs(110) interface are induced by the metal and underline the relevance of the metal-induced gap states (MIGS) model.

By combining XSTS along the space charge region of the semiconductor with three-dimensional (3D) finite element method (FEM) simulations of the electrostatic potential inside the space charge region [47], the Schottky barrier (SB) height is extracted from the data: While the SB height for the ideal *n*-type interface of  $\Phi_{SB}^n = 0.94(3)$  eV as already found by Winking [47] is in very good agreement with the MIGS-and-electronegativity model, the SB height for the ideal *p*-type interface of  $\Phi_{SB}^p = 0.78(2)$  eV strongly deviates from the predictions of this model.

Furthermore, in this thesis, XSTS along the space charge region is combined with 3D FEM simulations to obtain information on the variation of the local density of states (LDOS) inside the valence band of the ideal *p*-type Fe/GaAs(110) interface. The LDOS variation map reveals a sharp drop of LDOS about 0.35 eV below the valence band maximum and is located in the first few GaAs layers at the interface. Density functional theory (DFT) calculations of the Fe/GaAs(110) interface performed by Dr. Ali Al-Zubi and Prof. Stefan Blügel are in very good agreement with the experimental data and yield a SB height of  $\Phi_{SB}^p = 0.69$  eV differing by only 12% from the experimentally obtained value.

The very good agreement between experimental data and DFT predictions demonstrates that the XSTS technique is an excellent approach to investigate the microscopic process of SB formation. The combined XSTS and DFT study also reveals the relevance of both MIGS and bond polarization models. While for the *n*-type junction the MIGS model can explain the experimental data [47], for the *p*-type junction the detailed atomic structure in the sense of the bond polarization (BP) model has to be considered to understand the experimental observations. For the *p*-type case, a combined MIGS-and-BP model qualitatively explains the experimentally observed large SB height by taking into consideration the additional positive charge inside the valence band due to Fe-As hybridization that partially compensates the negative charge of the MIGS.

Moreover, in this thesis, the influence of different growth conditions on the SB height and the charge distribution at *p*-type interfaces is investigated by XSTM and XSTS. XSTM topographies indicate that Fe submonolayer pre-growth at room temperature has a significant impact on the atomic structure of the interface and increases the degree of intermixing. XSTS measurements in combination with 3D FEM simulations show that this alters the electronic structure at the interface and has an influence on the SB height of the system. Furthermore, XSTS and 3D FEM data reveal that also the Fe film thickness has an influence on the electronic structure of the interface and consequently on the SB height of the system. These findings emphasize that the detailed atomic structure of the interface is of crucial importance for the microscopic process of SB formation.

Moreover, in this thesis, the magnetic properties of ultrathin (2–3 ML) Fe films on GaAs{110} are discussed. Based on the discovery of an out-of-plane magnetization component coupled to the relative orientation of the in-plane magnetization of the Fe film

---

along the <001> direction [52], additional *in situ* magneto-optic Kerr effect (MOKE) measurements with an in-plane and out-of-plane rotatable magnetic field are performed. These measurements confirm a unidirectional magnetic anisotropy of the Fe/GaAs{110} interface for Fe film thicknesses of 2—3 ML with the out-of-plane magnetization unidirectionally coupled to the in-plane magnetization component along the <001> direction and directly related to the inversion asymmetry of the GaAs{110} surface in the same direction.

Magneto-optic simulations show that this uniaxial magnetic anisotropy cannot be explained by a simple canted magnetization of the Fe film [52]. Also the fact that square-shaped hysteresis curves are found for all applied field directions indicates a magnetic structure other than a canted film magnetization and supports the notion of a single domain structure [52]. For partially intermixed interfaces no out-of-plane magnetization component is detected indicating an interface-induced magnetism [52]. Even a more elaborate model of a canted film magnetization extended by an additional magnetic interface layer cannot explain the experimental data. All findings taken together suggest a more complex spin structure for the system of 2—3 ML Fe on GaAs{110}.

Photon energy-dependent *in situ* MOKE measurements show the unidirectional magnetic anisotropy for all applied laser wavelengths in the range between 532—1064 nm. The fact that the unidirectional magnetic anisotropy is also observed for a laser wavelength of  $\lambda = 1064$  nm lying above the absorption limit of GaAs suggests that the unidirectional magnetic anisotropy is dominated by either the metal-induced gap states or by states inside the metal film or by both.



## A Appendix

### A.1 Topographic Analysis of the Space Charge Region

In this section the structural properties and the contribution from the different tunnel channels along the space charge region of the low temperature (LT) grown *p*-type Fe/GaAs(110) with an acceptor concentration of  $N_A = 2.75 \times 10^{18} \text{ cm}^{-3}$  from chapter 3 are investigated by means of multi-bias STM measurements.<sup>17</sup> The upper panels in Figure A.1(a) and Figure A.2(a) show constant current topographies of this interface at negative and positive sample bias voltage, respectively. An atomic corrugation is observed along the entire space charge region indicating an atomically flat GaAs(110) surface. For the negative sample bias voltage the anionic surface resonances A<sub>4</sub> and A<sub>5</sub> (see section 3.1.1) from the valence band dominate and show an atomic corrugation in [001] direction. At positive sample bias voltage (see Figure A.2) the topography exhibits an atomic corrugation in both the [001] and [110] directions indicating that also the cationic surface resonance C<sub>3</sub> inside the conduction band is addressed (compare section 3.1.1).

Two characteristic features in the topographies from Figure A.1(a) and Figure A.2(a) (bumps at negative voltage and dips at positive voltage) are observed at around  $x = -25 \text{ nm}$  and  $x = -7 \text{ nm}$  and can be identified as Zn acceptors [95, 154]. Taking the acceptor concentration of  $N_A = 2.75 \times 10^{18} \text{ cm}^{-3}$  into account, in average one would expect around 2 Zn atoms in a volume of  $V = 30 \times 12 \times 2 \text{ nm}^3$  as the one probed in Figure A.1(a) and Figure A.2(a). Aside from the two Zn acceptors no other defects (e.g., vacancies or adsorbates) are observed along the entire space charge region providing the ideal conditions to investigate the Fe/GaAs(110) interface on the Debye length scale.

---

<sup>17</sup> A similar investigation for a LT grown *n*-type Fe/GaAs(110) interface was presented by Winking [47].

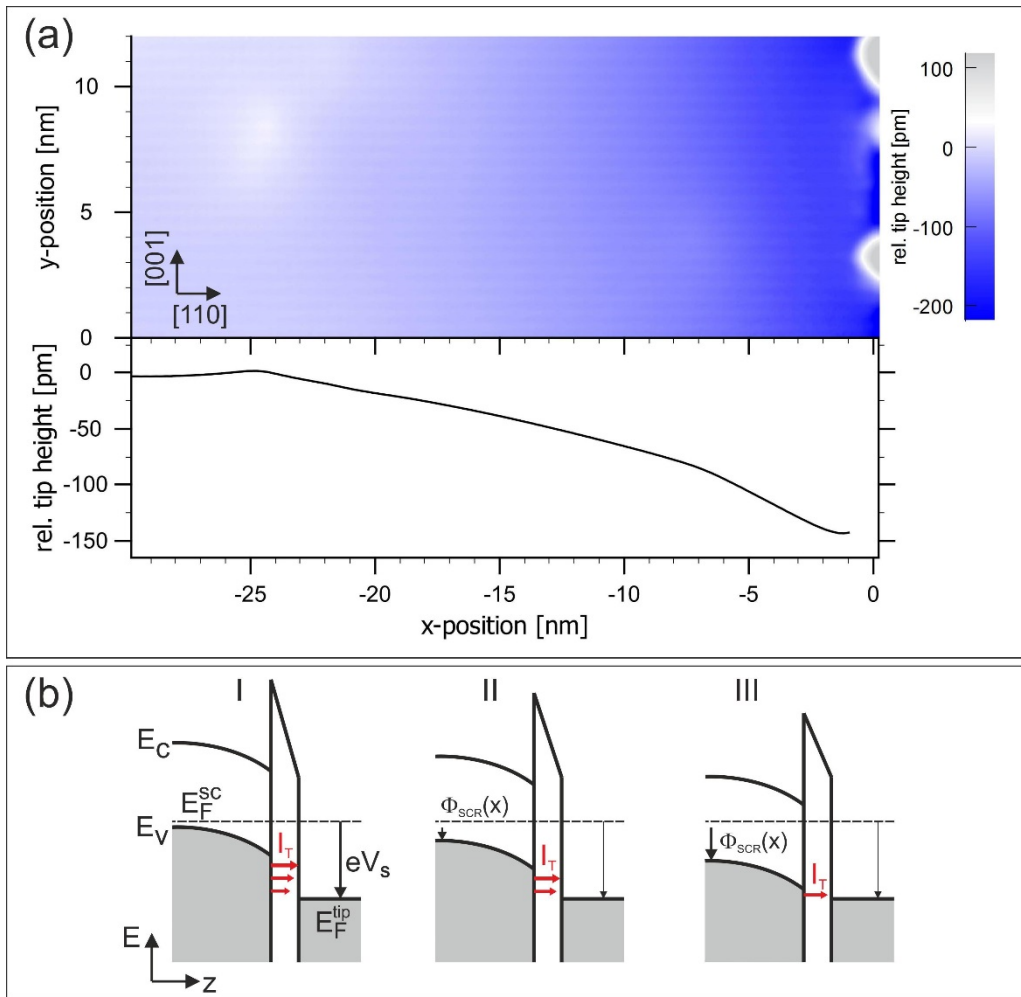


Figure A.1: (a)  $30 \times 12 \text{ nm}^2$  constant current topography of an Fe/p-GaAs(110) interface (7 ML Fe) at  $V_s = -1.5 \text{ V}$  and  $I_T = 60 \text{ pA}$  [125]. The relative tip height in the lower panel is averaged over the entire topography in  $y$  direction. The interface is located at  $x = 0 \text{ nm}$ . (b) Schematic of the qualitative dependency of the tunnel current on the distance to the interface and the band bending of the space charge region  $\Phi_{\text{SCR}}(x)$ .

The lower panel in Figure A.1(a) shows the relative tip height in dependence on the distance to the interface for a sample bias voltage of  $V_s = -1.5 \text{ V}$  and a constant tunnel current of  $I_T = 60 \text{ pA}$ . The relative tip height at each  $x$  position is averaged over the entire topography in  $y$  direction from the upper panel. Aside from small bumps in the profile due to the two Zn acceptors, the relative tip height monotonously decreases with decreasing distance to the interface.

The monotonous decrease of the relative tip height with decreasing tip-interface distance can be explained by means of the 1D energy band scheme model from Figure A.1(b). The left panel (case I) represents the situation far away from the interface on the free GaAs(110) surface. At negative bias voltages the valence and conduction band edges  $E_V$  and  $E_C$  at the surface are bent downwards with respect to the bulk (tip-induced band bending, TIBB) as described in section 3.2.1. However, for sufficiently high negative bias

---

voltages the valence band edge at the surface lies above the Fermi level of the tip and therefore allows electron tunneling from occupied states within a broad energy range inside the valence band of the semiconductor into unoccupied states of the metal tip.

As was already discussed in section 1.1 the energy bands of the semiconductor are also bent downwards (upwards) along the space charge region of the *p*-type (*n*-type) Fe/GaAs(110) Schottky contact. Hence, if the tip is located above the space charge region of the semiconductor the TIBB will be superimposed by the additional band bending of the space charge region  $\Phi_{SCR}(x)$ . Case II in Figure A.1(b) shows the additional downwards shift of the energy bands  $\Phi_{SCR}(x)$  with respect to the Fermi level if the relative tip height is kept constant with regard to case I. This decreases the energy range between the valence band edge  $E_V$  and the Fermi level of the tip reducing the number of available tunnel channels. To keep the tunnel current constant, the tunnel probability for the reduced number of available tunnel channels has to be increased which is achieved by decreasing the relative tip height.

The closer the tip approaches the interface, the stronger will be the additional downward band bending from the space charge region  $\Phi_{SCR}(x)$  which is shown in case III in Figure A.1(b). This even further decreases the number of available tunnel channels and the relative tip height has to be further decreased to keep the tunnel current constant.

For a positive sample bias voltage of  $V_s = +2.2$  V the relative tip height depends in a somewhat different way on the tip-interface distance as can be seen in the lower panel of Figure A.2(a). Starting at  $x \approx -25$  nm the relative tip height initially decreases with decreasing tip-interface distance and reaches a minimum at  $x \approx -15$  nm. After that the relative tip height rapidly increases with decreasing tip-interface distance. The 1D energy band scheme in Figure A.2(b) can explain this behavior. The situation for tunneling into the free GaAs(110) surface is shown in case I. Due to the positive sample bias voltage the energy bands inside the semiconductor are bent upwards. The bias voltage is high enough to shift the valence band edge  $E_V$  at the surface above the Fermi level. This creates an accumulation layer of holes inside the valence band at the surface and allows electrons to tunnel from the metal tip into the anionic surface resonances  $A_4$  and  $A_5$  inside the valence band of the semiconductor. Furthermore, the square-shaped corrugation pattern of the topography indicates that also the cationic surface resonance  $C_3$  inside the conduction band is addressed. However, the tunneling of electrons into the conduction band is hindered by the additional barrier of the upward bent band gap. Therefore, the tunnel current is dominated by the electron tunneling into the valence band.

If now the tip is moved further to the interface, the additional band bending of the space charge region has to be taken into consideration (see case II in Figure A.2(b)). Along the space charge region of the *p*-type junction the bands are shifted downwards by the potential  $\Phi_{SCR}(x)$ . This downward shift of the energy bands decreases the size of the accumulation layer and the number of available tunnel channels into the valence band. To keep the tunnel current constant the tip-sample distance (relative tip height) has to be decreased.

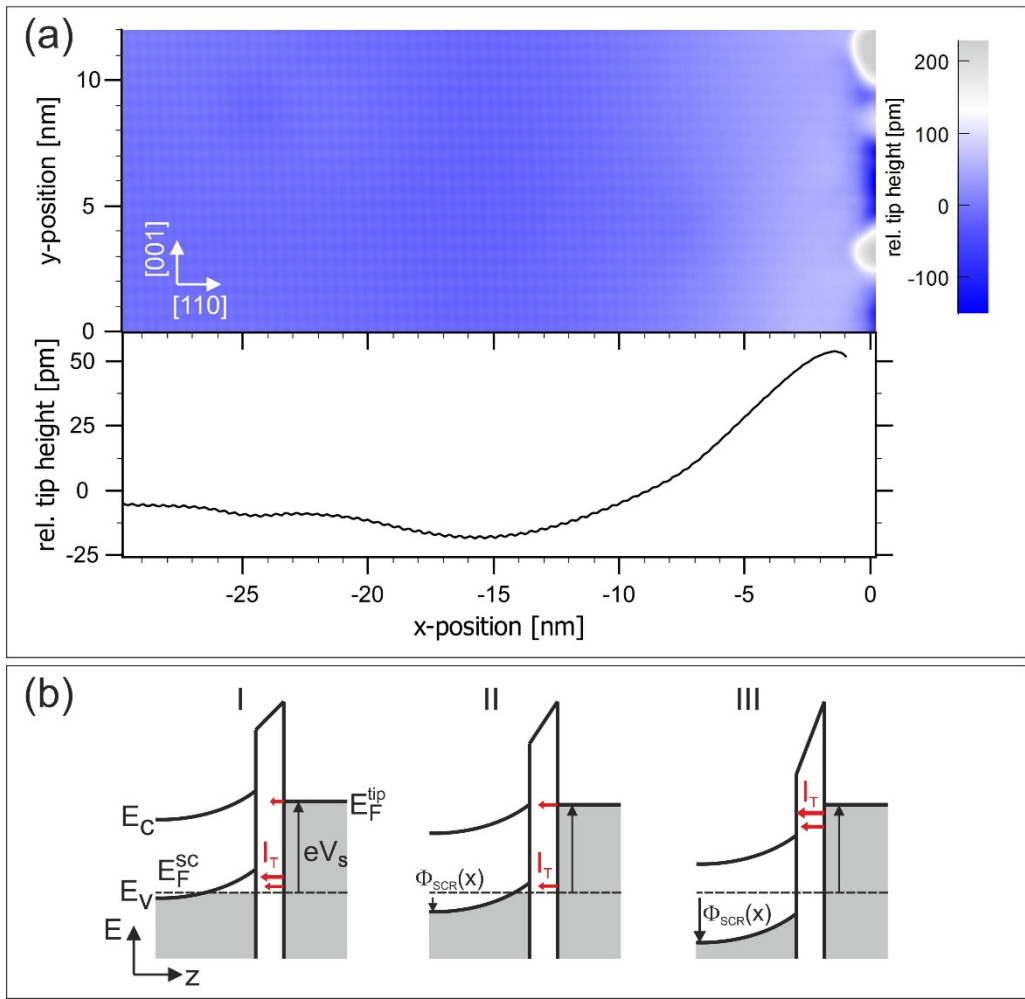


Figure A.2: (a)  $30 \times 12 \text{ nm}^2$  constant current topography of an Fe/p-GaAs(110) interface (7 ML Fe) at  $V_s = +2.2 \text{ V}$  and  $I_T = 10 \text{ pA}$  [125]. The relative tip height in the lower panel is averaged over the entire topography in  $y$  direction. The interface is located at  $x = 0 \text{ nm}$ . (b) Schematic of the qualitative dependency of the tunnel current on the distance to the interface and the band bending of the space charge region  $\Phi_{SCR}(x)$ .

Case III in Figure A.2(b) shows that a further approach of the tip to the interface increases the additional band shift  $\Phi_{SCR}(x)$ . This increases the number of additional tunnel channels into the anionic surface resonances inside the conduction band because the Fermi level of the tip surpasses the conduction band edge  $E_C$  at the GaAs(110) surface. Due to the much lower tunnel barrier for electrons tunneling from the tip into the conduction band the tunnel probability is significantly increased. To keep the tunnel current constant the tip-sample distance (relative tip height) has to be increased with decreasing tip-interface distance. If the tip is brought closer to the interface, the tunneling of electrons into the empty cationic surface resonance  $C_4$  inside the conduction band dominates. This also changes the corrugation pattern at the interface from a square-shape to a line-shape parallel to the [110] direction.

## Bibliography

- [1] G. E. Moore, “Cramming more components onto intergrated circuits,” *Electronics*, vol. 38, p. 114, 1965.
- [2] International Technology Roadmap for Semiconductors, <http://www.itrs.net/>, 2013.
- [3] B. T. Jonker, “Electrical Spin Injection and Transport in Semiconductors,” in *Handbook of Spin Transport and Magnetism*, E. Y. Tsymbal and I. Zutic, Eds. CRC Taylor & Francis, Boca Raton, 2012, ch. 17.
- [4] G. A. Prinz, “Magnetoelectronics,” *Science*, vol. 282, p. 1660, 1998.
- [5] S. A. Wolf, D. D. Awschalom, R. A. Buhrman, J. M. Daughton, S. von Molnar, M. L. Roukes, A. Y. Chtchelkanova, and D. M. Treger, “Spintronics: A Spin-Based Electronics Vision for the Future,” *Science*, vol. 294, p. 1488, 2001.
- [6] S. Datta and B. Das, “Electronic analog of the electro-optic modulator,” *Applied Physics Letters*, vol. 56 (7), pp. 665–667, 1990.
- [7] G. Schmidt, D. Ferrand, L. W. Molenkamp, A. T. Filip, and B. J. van Wees, “Fundamental obstacle for electrical spin injection from a ferromagnetic metal into a diffusive semiconductor,” *Physical Review B*, vol. 62, p. R4790, 2000.
- [8] E. I. Rashba, “Theory of electrical spin injection: Tunnel contacts as a solution of the conductivity mismatch problem,” *Physical Review B*, vol. 62, p. R16267, 2000.
- [9] H. J. Zhu, M. Ramsteiner, H. Kostial, M. Wassermeier, H.-P. Schönher, and K. H. Ploog, “Room-Temperature Spin Injection from Fe into GaAs,” *Physical Review Letters*, vol. 87, p. 016601, 2001.
- [10] A. T. Hanbicki, B. T. Jonker, G. Itskos, G. Kioseoglou, and A. Petrou, “Efficient electrical spin injection from a magnetic metal/tunnel barrier contact into a semiconductor,” *Applied Physics Letters*, vol. 80(7), pp. 1240–1242, 2002.
- [11] L. R. Fleet, K. Yoshida, H. Kobayashi, Y. Kaneko, S. Matsuzaka, Y. Ohno, H. Ohno, S. Honda, J. Inoue, and A. Hirohata, “Correlating the interface structure to spin injection in abrupt Fe/GaAs(001) films,” *Physical Review B*, vol. 87, pp. 024401–, 2013.

## Bibliography

---

- [12] F. Braun, “Ueber die Stromleitung durch Schwefelmetalle,” *Pogg. Ann. Physik*, vol. 153, p. 556, 1874.
- [13] W. Schottky, “Halbleitertheorie der Sperrsicht,” *Naturwissenschaften*, vol. 26, p. 843, 1938.
- [14] W. Schottky, “Abweichungen vom Ohmschen Gesetz in Halbleitern,” *Phys. Zeitschr.*, vol. 41, p. 570, 1940.
- [15] N. F. Mott, “Contact between metal and insulator or semiconductor,” *Proc. Camb. Phil. Soc.*, vol. 34, p. 568, 1938.
- [16] J. Bardeen, “Surface States and Rectification at a Metal Semi-Conductor Contact,” *Physical Review*, vol. 71, pp. 717–727, 1947.
- [17] V. Heine, “Theory of surface states,” *Physical Review*, vol. 138, pp. A1689–A1696, 1965.
- [18] W. Mönch, “Role of Virtual Gap States and Defects in Metal-Semiconductor Contacts,” *Physical Review Letters*, vol. 58, p. 1260, 1987.
- [19] J. Tersoff, “Schottky Barrier Heights and the Continuum of Gap States,” *Physical Review Letters*, vol. 52, pp. 465–468, 1984.
- [20] S. G. Louie, J. R. Chelikowsky, and M. L. Cohen, “Ionicity and the theory of Schottky barriers,” *Physical Review B*, vol. 15, pp. 2154–2162, 1977.
- [21] W. E. Spicer, I. L. L. Skeath, C. Y. Su, and P. Chye, “Unified Mechanism for Schottky-Barrier Formation and III-V Oxide Interface States,” *Physical Review Letters*, vol. 44, pp. 420–423, 1980.
- [22] W. E. Spicer, I. Lindau, P. Skeath, and C. Y. Su, “Unified defect model and beyond,” *J. Vac. Sci. Technol.*, vol. 17, p. 1019, 1980.
- [23] M. Mönch, “Chemisorption-Induced Defects at Interfaces on Compound Semiconductors,” *Surface Science*, vol. 132, p. 92, 1983.
- [24] W. E. Spicer, Z. Lilienthal-Weber, E. Weber, N. Newman, T. Kendelewicz, R. Cao, C. McCants, P. Mahowald, K. Miyano, and I. Lindau, “The advanced unified defect model for schottky barrier formation,” *Journal of Vacuum Science & Technology B*, vol. 6, pp. 1245–1251, 1988.
- [25] R. T. Tung, “Chemical Bonding and Fermi Level Pinning at Metal-Semiconductor Interfaces,” *Physical Review Letters*, vol. 84, pp. 6078–, 2000.
- [26] R. T. Tung, “Formation of an electric dipole at metal-semiconductor interfaces,” *Physical Review B*, vol. 64, pp. 205310–, 2001.
- [27] R. T. Tung, J. M. Gibson, and J. M. Poate, “Formation of Ultrathin Single-Crystal Silicide Films on Si: Surface and Interfacial Stabilization of Si-NiSi<sub>2</sub> Epitaxial Structures,” *Physical Review Letters*, vol. 50, pp. 429–432, 1983.
- [28] R. T. Tung, “Schottky-Barrier Formation at Single-Crystal Metal-Semiconductor Interfaces,” *Physical Review Letters*, vol. 52, pp. 461–464, 1984.
- [29] D. R. Heslinga, H. H. Weitering, D. P. van der Werf, T. M. Klapwijk, and T. Hibma, “Atomic-Structure-Dependent Schottky Barrier at Epitaxial Pb/Si(111) Interfaces,” *Physical Review Letters*, vol. 64, pp. 1589–1592, 1990.

- 
- [30] K. Yamane, K. Hamaya, Y. Ando, Y. Enomoto, K. Yamamoto, T. Sadoh, and M. Miyao, “Effect of atomically controlled interfaces on Fermi-level pinning at metal/Ge interfaces,” *Applied Physics Letters*, vol. 96, p. 162104, 2010.
  - [31] K. Kasahara, S. Yamada, K. Sawano, M. Miyao, and K. Hamaya, “Mechanism of Fermi level pinning at metal/germanium interfaces,” *Physical Review B*, vol. 84, pp. 205301–, 2011.
  - [32] W. J. Kaiser and L. D. Bell, “Direct investigation of subsurface interface electronic structure by ballistic electron emission microscopy,” *Physical Review Letters*, vol. 60, pp. 1406–1409, 1988.
  - [33] M. H. Hecht, L. D. Bell, W. J. Kaiser, and F. J. Grunthaner, “Ballistic-electron-emission microscopy investigation of Schottky barrier interface formation,” *Appl. Phys. Lett.*, vol. 55, p. 780, 1989.
  - [34] A. A. Talin, R. S. Williams, B. A. Morgan, K. M. Ring, and K. L. Kavanagh, “Nanometer-resolved spatial variations in the Schottky barrier height of a Au/n-type GaAs diode,” *Physical Review B*, vol. 49, pp. 16474–16479, 1994.
  - [35] H.-J. Im, Y. Ding, J. P. Pelz, and W. J. Choyke, “Nanometer-scale test of the Tung model of Schottky-barrier height inhomogeneity,” *Physical Review B*, vol. 64, pp. 075310–, 2001.
  - [36] A. Olbrich, J. Vancea, F. Kreupl, and H. Hoffmann, “Potential pinch-off effect in inhomogeneous Au/Co/GaAs<sub>67</sub>P<sub>33</sub>(100)-Schottky contacts,” *Appl. Phys. Lett.*, vol. 70, p. 2559, 1997.
  - [37] L. Stockmann and H. van Kempen, “Ballistic electron emission microscopy and spectroscopy of the Au/GaAs(110) interface,” *Surface Science*, vol. 408, p. 232, 1998.
  - [38] S. Forment, R. L. V. Meirhaeghe, A. D. Vrieze, K. Strubbe, and W. P. Gomes, “A comparative study of electrochemically formed and vacuum-deposited n-GaAs/Au Schottky barriers using ballistic electron emission microscopy (BEEM),” *Semiconductor Science and Technology*, vol. 16, p. 975, 2001.
  - [39] R. M. Feenstra, “Electronic States of Metal Atoms on the GaAs(110) Surface Studied by Scanning Tunneling Microscopy,” *Physical Review Letters*, vol. 63, p. 1412, 1989.
  - [40] R. M. Feenstra, “Scanning tunneling microscopy and spectroscopy of gold on the GaAs(110) surface,” *J. Vac. Sci. Technol. B*, vol. 7, p. 925, 1989.
  - [41] R. M. Feenstra and P. Martensson, “Fermi-level pinning at the Sb/GaAs(110) surface studied by scanning tunneling spectroscopy,” *Physical Review Letters*, vol. 61, pp. 447–450, 1988.
  - [42] P. N. First, J. A. Stroscio, R. A. Dragoset, D. T. Pierce, and R. J. Celotta, “Metallicity and Gap States in Tunneling to Fe Clusters on GaAs(110),” *Physical Review Letters*, vol. 63(13), pp. 1416–1419, 1989.
  - [43] T. C. G. Reusch, M. Wenderoth, L. Winking, N. Quaas, and R. G. Ulbrich, “Origin of Schottky Barriers in Gold Contacts on GaAs(110),” *Physical Review Letters*, vol. 93, pp. 206801–, 2004.

- [44] T. C. G. Reusch, M. Wenderoth, L. Winking, N. Quaas, and R. G. Ulbrich, “Nanoscale mapping of the space charge layer of Au/GaAs(110) contacts,” *Applied Physics Letters*, vol. 87, pp. 093103–, 2005.
- [45] T. Reusch, “Cross-sectional Scanning Tunneling Microscopy of Au contacts on GaAs(110),” Ph.D. dissertation, Georg-August-University Göttingen, 2003.
- [46] L. Winking, M. Wenderoth, J. Homoth, S. Siewers, and R. G. Ulbrich, “Fe films grown on GaAs(110) in a two-step process: Improved structural and magnetic properties,” *Applied Physics Letters*, vol. 92, p. 193102, 2008.
- [47] L. Winking, “Untersuchung der lokalen strukturellen und elektronischen Eigenchaften von Fe-GaAs Schottky-Kontakten mit atomar aufgelöster Raster-Tunnel-Mikroskopie in Querschnittsgeometrie,” Ph.D. dissertation, Georg-August-University Goettingen, Germany, 2009.
- [48] G. A. Prinz and J. J. Krebs, “Molecular beam epitaxial growth of single-crystal Fe films on GaAs,” *Applied Physics Letters*, vol. 39(5), pp. 397–399, 1981.
- [49] T. W. Kim and Y. S. Yoon, “Microstructural and atomic arrangement studies in Fe(110)/GaAs(110) heterostructures,” *Journal of Physics and Chemistry of Solids*, vol. 61, pp. 847–851, 2000.
- [50] T. J. Zega, A. T. Hanbicki, S. C. Erwin, I. Zutic, G. Kioseoglou, C. H. Li, B. T. Jonker, and R. M. Stroud, “Determination of interface atomic structure and its impact on spin transport using Z-contrast microscopy and density-functional theory,” *Physical Review Letters*, vol. 96, pp. 196101–1–4, 2006.
- [51] T. Taniyama, E. Wada, M. Itoh, and M. Yamaguchi, “Electrical and optical spin injection in ferromagnet/semiconductor heterostructures,” *NPG Asia Materials*, vol. 3, p. 65, 2011.
- [52] T. Iffländer, “Magnetic Properties and Proximity Effects of the Fe-GaAs{110} Interface,” Master’s thesis, Georg-August-University Göttingen, 2010.
- [53] W. Mönch, *Semiconductor Surfaces and Interfaces*, G. Ertl, R. Gomer, H. Lüth, and D. L. Mills, Eds. Springer Berlin Heidelberg, 2001.
- [54] L. J. Brillson, Ed., *Contacts to Semiconductors*. Noyes Publications, Park Ridge, New Jersey, U.S.A., 1993.
- [55] E. H. Rhoderick, *Metal-Semiconductor Contacts*, P. Hammond and D. Walsh, Eds. Clarendon Press Oxford, 1978.
- [56] R. T. Tung, “Recent advances in Schottky barrier concepts,” *Materials Science & Engineering*, vol. R 35, pp. 1– 138, 2001.
- [57] M. van Schilfgaarde and N. Newman, “Electronic Structure of Ideal Metal/GaAs Contacts,” *Physical Review Letters*, vol. 65, pp. 2728–2731, 1990.
- [58] J. Tersoff, “Calculation of Schottky barrier heights from semiconductor band structures,” *Surface Science*, vol. 168, pp. 275–284, 1986.
- [59] S. G. Louie and M. L. Cohen, “Electronic structure of a metal-semiconductor interface,” *Physical Review B*, vol. 13, p. 2461, 1976.

- 
- [60] R. G. Dandrea and C. B. Duke, “Interfacial atomic composition and Schottky barrier heights at the Al/GaAs(001) interface,” *Journal of Vacuum Science & Technology*, vol. B11, pp. 1553–1558, 1993.
  - [61] W. Mönch, “Chemical trends of barrier heights in metal-semiconductor contacts: on the theory of the slope parameter,” *Applied Surface Science*, vol. 92, p. 367, 1996.
  - [62] R. W. Grant, J. R. Waldrop, S. P. Kowalczyk, and E. A. Kraut, “Correlation of GaAs surface chemistry and interface Fermi-level position: A single defect model interpretation,” *J. Vac. Sci. Technol.*, vol. 19, p. 477, 1981.
  - [63] E. R. Weber, H. Ennen, U. Kaufmann, J. Windscheif, J. Schneider, and T. Wosinski, “Identification of As<sub>Ga</sub> antisites in plastically deformed GaAs,” *J. Appl. Phys.*, vol. 53, p. 6140, 1982.
  - [64] S. Adachi, *GaAs and Related Materials - Bulk Semiconductors and Superlattice Properties*. World Scientific, Singapore, 1994.
  - [65] R. Höllinger, M. Zölfel, R. Moosbühler, and G. Bayreuther, “In-plane spin reorientation transition in epitaxial Fe(110)/GaAs(110) films,” *Journal of Applied Physics*, vol. 89(11), pp. 7136–7138, 2001.
  - [66] Y. B. Xu, E. T. M. Kernohan, D. J. Freeland, A. Ercole, M. Tselepi, and J. A. C. Bland, “Evolution of the ferromagnetic phase of ultrathin Fe films grown on GaAs(100)-4×6,” *Physical Review B*, vol. 58(2), pp. 890–896, 1998.
  - [67] J. W. Freeland, I. Coulthard, J. W. J. Antel, and A. P. J. Stampfl, “Interface bonding for Fe thin films on GaAs surfaces of differing morphology,” *Physical Review B*, vol. 63, pp. 193301–1–4, 2001.
  - [68] M. W. Ruckman, J. J. Joyce, and J. H. Weaver, “Interdiffusion and reaction at the Fe/GaAs(110) interface,” *Physical Review B*, vol. 33(10), pp. 7029–7035, 1986.
  - [69] S. A. Chambers, F. Xu, H. W. Chen, I. M. Vitomirov, S. B. Anderson, and J. H. Weaver, “Simultaneous epitaxy and substrate out-diffusion at a metal-semiconductor interface: Fe/GaAs(001)-c(8x2),” *Physical Review B*, vol. 34(10), pp. 6605–6611, 1986.
  - [70] B. D. Schultz, H. H. Farrell, M. M. R. Evans, K. Lüdge, and C. J. Palmstrøm, “ErAs interlayers for limiting interfacial reactions in Fe/GaAs(100) heterostructures,” *J. Vac. Sci. Technol. B*, vol. 20, p. 1600, 2002.
  - [71] A. Filipe, A. Schuhl, and P. Galtier, “Structure and magnetism of the Fe/GaAs interface,” *Appl. Phys. Lett.*, vol. 70, p. 129, 1997.
  - [72] J. J. Krebs, B. T. Jonker, and G. A. Prinz, “Properties of Fe single-crystal films grown on (100)GaAs by molecular-beam epitaxy,” *J. Appl. Phys.*, vol. 61, p. 2596, 1987.
  - [73] F. A. Volkening, B. T. Jonker, G. A. Prinz, and N. C. Koon, “Mössbauer study of <sup>57</sup>Fe single-crystal films grown on (110) GaAs by MBE,” *Journal of Applies Physics*, vol. 67(9), pp. 5646–5648, 1990.
  - [74] B. Lépine, S. Ababou, A. Guivarc'h, G. Jézéquel, S. Députier, R. Guérin, A. Filipe, A. Schuhl, F. Abel, C. Cohen, A. Rocher, and J. Crestou, “Solid state interdiffusion of Fe and Ga in the Fe/GaAs(110) system,” *Journal of Applied Physics*, vol. 87(11), p. 113511, 2000.

## Bibliography

---

- sions in epitaxial Fe/GaAs(001) heterostructures during ultrahigh vacuum annealings up to 450°C,” *Journal of Applied Physics*, vol. 83(6), pp. 3077–3080, 1998.
- [75] J. A. C. Bland, A. Hirohata, Y.-B. Xu, C. M. Guertler, and S. N. Holmes, “Spin-Polarized Electron Transport Processes at the Ferromagnet/Semiconductor Interface,” *IEEE Transactions on Magnetics*, vol. 36(5), pp. 2827–2832, 2000.
- [76] J. M. LeBeau, Q. O. Hu, C. J. Palmstrom, and S. Stemmer, “Atomic structure of postgrowth annealed epitaxial Fe/(001)GaAs interfaces,” *Applied Physics Letters*, vol. 93, pp. 121909–121911, 2008.
- [77] C. H. Li, G. Kioseoglou, O. M. J. van ’t Erve, A. T. Hanbicki, B. T. Jonker, R. Mallory, M. Yasar, and A. Petrou, “Spin injection across (110) interfaces: Fe/GaAs(110) spin-light-emitting diodes,” *Applied Physics Letters*, vol. 85(9), pp. 1544–1546, 2004.
- [78] B. D. Schultz, N. Marom, D. Naveh, X. Lou, C. Adelmann, J. Strand, P. A. Crowell, L. Kronik, and C. J. Palmstrøm, “Spin injection across the Fe/GaAs interface: Role of interfacial ordering,” *Physical Review B*, vol. 80, p. 201309(R), 2009.
- [79] S. C. Erwin, S.-H. Lee, and M. Scheffler, “First-principles study of nucleation, growth, and interface structure of Fe/GaAs,” *Physical Review B*, vol. 65, p. 205422, 2002.
- [80] A. Grünebohm, H. C. Herper, and P. Entel, “Ab initio study of the interface properties of Fe/GaAs(110),” *Physical Review B*, vol. 80, p. 64417, 2009.
- [81] G. Binnig and H. Rohrer, “Scanning tunneling microscopy – from birth to adolescence,” *Rev. Mod. Phys.*, vol. 59, p. 615, 1987.
- [82] R. M. Feenstra and J. A. Stroscio, “Tunneling spectroscopy of the GaAs(110) surface,” *Journal of Vacuum Science & Technology B*, vol. 5, p. 923, 1987.
- [83] K. Teichmann, “Scanning tunneling spectroscopy of space charge regions in semiconductors: From single donor to heterostructure systems,” Ph.D. dissertation, Georg-August-University of Göttingen, 2012.
- [84] D. Bonnell, *Scanning Tunneling Microscopy and Spectroscopy. Theory, Techniques, and Applications*, D. Bonnell, Ed. VCH, New York, 2001.
- [85] J. Chen, *Introduction to Scanning Tunneling Microscopy*. Oxford University Press, 1993.
- [86] R. Wiesendanger, *Scanning Probe Microscopy and Spectroscopy*. Cambridge University Press, 1994.
- [87] J. Bardeen, “Tunneling from a many particle point of view,” *Physical Review Letters*, vol. 6 (2), pp. 57–59, 1961.
- [88] J. Tersoff and D. R. Hamann, “Theory and Application for the Scanning Tunneling Microscope,” *Physical Review Letters*, vol. 50, p. 1998, 1983.
- [89] J. Tersoff and D. R. Hamann, “Theory of the scanning tunneling microscope,” *Physical Review B*, vol. 31, p. 805, 1985.
- [90] R. J. Hamers and D. F. Padowitz, “Methods of tunneling spectroscopy with the STM,” in *Scanning Probe Microscopy and Spectroscopy*. Wiley, New York, 2001, ch. 4, pp. 59–112.

- 
- [91] K. Besocke, “An easily operable scanning tunneling microscope.” *Surface Science*, vol. 181, pp. 145–153, 1987.
  - [92] M. A. Rosentreter, “Rastertunnelmikroskopie auf der GaAs(110)-Oberfläche bei Temperaturen von 8 K – 300 K,” Ph.D. dissertation, Georg-August-University Göttingen, 1997.
  - [93] A. J. Heinrich, “Ordering in Ternary Compound Semiconductors on the Atomic Scale,” Ph.D. dissertation, Georg-August-University Göttingen, 1998.
  - [94] A. Weismann, “Scanning Tunnelling Spectroscopy of Subsurface Magnetic Atoms in Copper Electron Focusing and Kondo Effect,” Ph.D. dissertation, Georg-August-University Göttingen, 2008.
  - [95] S. Loth, “Atomic Scale Images of Acceptors in III-V Semiconductors: Band Bending, Tunneling Paths and Wave Functions,” Ph.D. dissertation, Georg-August-University Goettingen, Germany, 2007.
  - [96] K. Sauthoff, “Scanning Tunneling Spectroscopy on Single Donors and Donor Complexes near the GaAs(110)-Surface,” Ph.D. dissertation, Georg-August-University Göttingen, 2003.
  - [97] H. Schleiermacher, “Charakterisierung von Spitzen für die Rastertunnelmikroskopie,” Master’s thesis, Georg-August-University Göttingen, 2006.
  - [98] P. N. Argyres, “Theory of the Faraday and Kerr Effects in Ferromagnets,” *Physical Review*, vol. 97 (2), pp. 334–345, 1955.
  - [99] H. Bennett and E. Stern, “Faraday Effect in Solids,” *Physical Review*, vol. 137(2A), pp. A448–A461, 1965.
  - [100] P. Bruno, Y. Suzuki, and C. Chappert, “Magneto-optical Kerr effect in a paramagnetic overlayer on a ferromagnetic substrate: A spin-polarized quantum size effect,” *Physical Review B*, vol. 53, pp. 9214–9220, 1996.
  - [101] A. Hubert and R. Schäfer, *Magnetic Domains - The Analysis of Magnetic Microstructures*. Springer Berlin Heidelberg, 1998.
  - [102] E. Hecht, *Optics (4th ed.)*. Addison Wesley, San Francisco, 2002.
  - [103] K. Shinagawa, *Magneto-Optics - Springer Series in Solid-State Sciences*, S. Sugano and N. Kojima, Eds. Springer-Verlag, Berlin, 2000.
  - [104] R. Vollmer, “Linerare und nichlineare Magnetooptik an ultradünnen ferromagnetischen Schichten und Vielfachschichten,” in *Magnetische Schichtsysteme - 30. Ferienkurs des Instituts für Festkörperforschung 1999*. Forschungszentrum Jülich GmbH, 1999, ch. C 7.
  - [105] G. Meyer, “In situ Abbildung magnetischer Domänen in dünnen Filmen mit magnetooptischer Rasternahfeldmikroskopie,” Ph.D. dissertation, Freie Universität Berlin, 2003.
  - [106] R. M. A. Azzam and N. M. Bashra, *Ellipsometry and Polarized Light*. North-Holland Publishing Company, Amsterdam, 1977.
  - [107] R. C. Jones, “A new calculus for the treatment of optical systems, I. Description and Discussion of the Calculus,” *Journal of the Optical Society of America*, vol. 31(7), pp. 488–493, 1941.

## Bibliography

---

- [108] J. Schoenes, in *Materials Science and Technology, Vol. 3A Electronic and Magnetic Properties of Metals and Ceramics Part 1*. VCH Weinheim, 1991.
- [109] J. Zak, E. R. Moog, C. Liu, and S. D. Bader, “Universal approach to magneto-optics,” *Journal of Magnetism and Magnetic Materials*, vol. 89, pp. 107–123, 1990.
- [110] J. Zak, E. Moog, C. Liu, and S. D. Bader, “Fundamental magneto-optics,” *Journal of Applied Physics*, vol. 68(8), pp. 4203–4207, 1990.
- [111] J. Zak, E. Moog, C. Liu, and S. D. Bader, “Magneto-optics of multilayers with arbitrary magnetization directions,” *Physical Review B*, vol. 43 (8), pp. 6423–6429, 1991.
- [112] E. D. Palik, *Handbook of Optical Constants of Solids I*. Academic Press Orlando, 1985.
- [113] Z. Q. Qiu and S. D. Bader, “Surface magneto-optic Kerr effect,” *Review of Scientific Instruments*, vol. 71 (3), pp. 1243–1255, 2000.
- [114] A. Grimsel, Master’s thesis, Georg-August-University, 2010.
- [115] S. Weikert, *Bachelor’s Thesis: Untersuchung der magnetischen Eigenschaften von Fe-GaAs(110) mit Hilfe des magneto-optischen Kerr-Effektes*. Georg-August-University, Göttingen, Germany, 2012, supervised by Tim Iffländer.
- [116] M. Münzenberg, “Untersuchungen zur Zwischenschichtkopplung bei [La/Fe]-Vielfachschichten und am Reorientierungsübergang von [CeH<sub>2</sub>/Fe]-Vielfachschichten mir dem magnetooptischen Kerreffekt,” Master’s thesis, Georg-August-University, Goettingen, Germany, 1997.
- [117] S. N. Jasperson and S. E. Schnatterly, “An Improved Method for High Reflectivity Ellipsometry Based on a New Polarization Modulation Technique,” *The Review of Scientific Instruments*, vol. 40(6), pp. 761–767, 1969.
- [118] S. N. Jasperson, D. K. Burge, and R. C. O’Handley, “A modulated ellipsometer for studying thin film optical properties and surface dynamics,” *Surface Science*, vol. 37, pp. 548–558, 1973.
- [119] M. Abramowitz and I. A. Stegun, *Handbook of Mathematical Functions*. Dover, New York, 1965.
- [120] T. Iffländer, S. Rolf-Pissarczyk, L. Winking, R. G. Ulbrich, A. Al-Zubi, S. Blügel, and M. Wenderoth, “Local Density of States at Metal-Semiconductor Interfaces: An Atomic Scale Study,” *Supplemental Material of Physical Review Letters*, vol. 114, p. 146804, 2015.
- [121] T. Iffländer, S. Rolf-Pissarczyk, L. Winking, R. G. Ulbrich, A. Al-Zubi, S. Blügel, and M. Wenderoth, “Local Density of States at Metal-Semiconductor Interfaces: An Atomic Scale Study,” *Physical Review Letters*, vol. 114, p. 146804, 2015.
- [122] D. J. Chadi, “(110) surface atomic structures of covalent and ionic semiconductors,” *Physical Review B*, vol. 19, p. 2074, 1979.
- [123] J. R. Chelikowsky and M. L. Cohen, “Self-consistent pseudopotential calculation for the relaxed (110) surface of GaAs,” *Physical Review B*, vol. 20, p. 4150, 1979.

- 
- [124] P. Ebert, B. Engels, P. Richard, K. Schroeder, S. Blügel, C. Domke, M. Heinrich, and K. Urban, “Contribution of Surface Resonances to Scanning Tunneling Microscopy Images: (110) Surfaces of III-V Semiconductors,” *Physical Review Letters*, vol. 77, p. 2997, 1996.
  - [125] S. Rolf-Pissarczyk, *Master’s Thesis: Untersuchung der Fe-GaAs(110) Grenzfläche mit Rastertunnelspektroskopie in Querschnittsgeometrie*. Georg-August-University, Göttingen, Germany, 2013, supervised by Tim Iffländer.
  - [126] S. Mirbt, B. Sanyal, C. Isheden, and B. Johansson, “First-principles calculation of Fe on GaAs(100),” *Physical Review B*, vol. 67, pp. 155421–1 – 155421–9, 2003.
  - [127] S. Siewers, “Rastertunnelmikroskopie an der GaAs{110}-{110}-Spaltkante,” Master’s thesis, Georg-August-University, Goettingen, Germany, 2008.
  - [128] G. J. de Raad, D. M. Bruls, P. M. Koenraad, and J. H. Wolter, “Interplay between tip-induced band bending and voltage-dependent surface corrugation on GaAs(110) surfaces,” *Physical Review B*, vol. 66, p. 195306, 2002.
  - [129] R. M. Feenstra, “Electrostatic potential for a hyperbolic probe tip near a semiconductor,” *Journal of Vacuum Science & Technology B*, vol. 21, p. 2080, 2003.
  - [130] J. R. Waldrop, “Schottky-barrier height of ideal metal contacts to GaAs,” *Applied Physics Letters*, vol. 44, pp. 1002–1004, 1984.
  - [131] G. Myburg, F. D. Auret, W. E. Meyer, C. W. Louw, and M. J. Staden, “Summary of Schottky barrier height data on epitaxially grown n- and p-GaAs,” *Thin Solid Films*, vol. 325, pp. 181–186, 1998.
  - [132] J. K. Garleff, “Quasi-eindimensionale elektronische Zustände auf der Si(111)-2x1-Oberfläche,” Ph.D. dissertation, Georg-August-University Göttingen, 2005.
  - [133] E. F. Schubert, *Doping in III-V Semiconductors*. Cambridge University Press, Cambridge, 1993.
  - [134] R. C. Weast, Ed., *CRC Handbook of Chemistry and Physics 56th Edition*. CRC Press, Cleveland Ohio, 1975.
  - [135] K.-J. Friedland, R. Nötzel, H.-P. Schönher, A. Riedel, H. Kostial, and K. H. Ploog, “Spontaneous Hall effect in MBE grown Fe layers on GaAs(311) and GaAs(331) substrates,” *Physica E*, vol. 10, p. 442, 2001.
  - [136] S. M. Sze, *Physics of Semiconductor Devices*. Wiley, New York, 1969.
  - [137] W. Mönch, *Electronic Properties of Semiconductor Interfaces*, G. Ertl, H. Lüth, and D. L. Mills, Eds. Springer Berlin Heidelberg, 2004.
  - [138] G. Münnich, A. Donarini, M. Wenderoth, and J. Repp, “Fixing the Energy Scale in Scanning Tunneling Microscopy on Semiconductor Surfaces,” *Physical Review Letters*, vol. 111, p. 216802, 2013.
  - [139] The Jülich full-linearized augmented plane waves (FLAPW) code family: <http://www.flapw.de>.
  - [140] M. Grundmann, *The Physics of Semiconductors: An Introduction Including Nanophysics and Applications*. Springer Berlin Heidelberg, 2010.
  - [141] F. K. Schulte, “A theory of thin metal films: electron density, potentials and work function,” *Surface Science*, vol. 55, p. 427, 1976.

## Bibliography

---

- [142] J. Kim, S. Qin, W. Yao, Q. Niu, M. Y. Chou, and C.-K. Shih, “Quantum size effects on the work function of metallic thin film nanostructures,” *PNAS*, vol. 107, p. 12761, 2009.
- [143] B. Slomski, G. Landolt, G. Bihlmayer, J. Osterwalder, and J. H. Dil, “Tuning of the Rashba effect in Pb quantum well states via a variable Schottky barrier,” *Scientific Reports*, vol. 3, p. 1963, 2013.
- [144] H. F. Ding, S. Pütter, H. P. Oepen, and J. Kirschner, “Experimental method for separating longitudinal and polar Kerr signals,” *Journal of Magnetism and Magnetic Materials*, vol. 212, pp. L5–L11, 2000.
- [145] H. F. Ding, S. Pütter, H. P. Oepen, and J. Kirschner, “Spin-reorientation transition in thin films studied by the component-resolved Kerr effect,” *Physical Review B*, vol. 63, pp. 134425–1–6, 2001.
- [146] S. Rolf-Pissarczyk, *Bachelor’s Thesis: Untersuchung der magnetischen Eigenschaften der Fe-GaAs(110) und der Fe-InAs(110) Grenzfläche mit Hilfe des magneto-optischen Kerr-Effekts*. Georg-August-University, Göttingen, Germany, 2011, supervised by Tim Iffländer.
- [147] I. E. Dzyaloshinskii, *Sov. Phys. JETP*, vol. 5, no. 1259, 1957.
- [148] T. Moriya, “Anisotropic superexchange interaction and weak ferromagnetism,” *Physical Review*, vol. 120, no. 91, 1960.
- [149] S. D. Bader and J. L. Erskine, *Ultrathin Magnetic Structures II - Measurement Techniques and Novel Magnetic Properties*, B. Heinrich and J. A. C. Bland, Eds. Springer Berlin Heidelberg, 2005.
- [150] J.-M. Lee, J.-Y. Kim, S.-U. Yang, B.-G. Park, J.-H. Park, S.-J. Oh, and J.-S. Kim, “Magnetism of pristine Fe films on GaAs(100),” *Physical Review B*, vol. 76, pp. 052406–1–4, 2007.
- [151] from personal communication with Prof. Blügel from the Jülich research center.
- [152] J. R. Chelikowsky and M. L. Cohen, “Nonlocal pseudopotential calculations for the electronic structure of eleven diamond and zinc-blende semiconductors,” *Physical Review B*, vol. 14, p. 556, 1976.
- [153] J. S. Blakemore, “Semiconducting and other major properties of gallium arsenide,” *J. Appl. Phys.*, vol. 53, p. R123, 1982.
- [154] P. Ebert, “Nano-scale properties of defects in compound semiconductor surfaces,” *Surface Science Reports*, vol. 33, pp. 121–303, 1999.
- [155] D. J. Griffiths, *Introduction to Electrodynamics*, 3rd ed. Prentice Hall, Upper Saddle River, New Jersey, 1999.

## Darstellung der wissenschaftlichen Zusammenarbeit

Im Sinne guter wissenschaftlicher Praxis möchte ich hier darstellen, wie die Ergebnisse dieser Dissertation entstanden sind, den Eigenanteil an dieser Arbeit herausstellen und klären an welcher Stelle Teile dieser Dissertation bereits veröffentlicht wurden.

Gleich zu Beginn dieser Darstellung sei erwähnt, dass im Rahmen dieser Dissertation zahlreiche Gespräche stattgefunden haben, die den Erfolg dieser Arbeit maßgeblich mitbeeinflusst haben: So wurden z.B. grundlegende physikalische Fragestellungen im Zusammenhang dieser Arbeit intensiv mit Prof. Rainer G. Ulbrich erörtert. Bezuglich der experimentellen Umsetzung und der Interpretation der Messdaten fanden eingehende Diskussionen mit Dr. Martin Wenderoth statt. Ebenfalls wurde im Rahmen dieser Arbeit eine Kollaboration mit dem Peter-Grünberg-Institut und dem Institute for Advanced Simulation vom Forschungszentrum Jülich initiiert. Namentlich seien hier Prof. Stefan Blügel und Dr. Ali Al-Zubi erwähnt, die die Dichte-Funktional-Theorie (DFT) Rechnungen der Fe/GaAs(110)-Grenzfläche durchführten, und mit denen über die Interpretation der DFT-Daten ausgiebig diskutiert wurde.

Die Untersuchung der strukturellen und elektronischen Eigenschaften von bei tiefen Temperaturen gewachsenen „idealen“ Fe/GaAs(110)-Grenzflächen im Rahmen dieser Arbeit basiert auf Vorarbeiten von Lars Winking (Dissertation, Georg-August-Universität Göttingen, 2009), der einen „idealen“ n-dotierten Fe/GaAs(110) Schottky-Kontakt mit Hilfe von Rastertunnelmikroskopie und -spektroskopie in Querschnittsgeometrie (XSTM/XSTS) bei Raumtemperatur untersucht hat. In der hier vorliegenden Dissertation wurden hingegen sowohl „ideale“ als auch partiell „durchmischte“ p-dotierte Fe/GaAs(110)-Grenzflächen mit Hilfe von Tief temperatur-XSTM/XSTS untersucht.

Die Messungen an der „idealen“ p-dotierten Fe/GaAs(110)-Grenzfläche wurden gemeinsam mit dem von mir betreuten Masterstudenten Steffen Rolf-Pissarczyk durchgeführt. In seiner Masterarbeit hat Steffen Rolf-Pissarczyk zudem die ursprünglich von Lars Winking entwickelte dreidimensionale (3D) Finite-Elemente-Simulationen auf die neuen

experimentellen Bedingungen (Spitzengeometrie,  $p$ -Dotierung) angepasst, und konnte so die Schottky-Barrieren-Höhe für die „ideale“  $p$ -dotierte Grenzfläche aus den experimentellen Daten extrahieren. In dieser Dissertation wurde darüberhinausgehend und basierend auf den 3D Finite-Elemente-Simulationen ein Auswerte-Tool entwickelt, das es erstmals ermöglicht die Variation der lokalen Zustandsdichte in der Umgebung der Grenzfläche auch im Energiebereich von Leitungsband (für die  $n$ -dotierte Grenzfläche) und Valenzband (für die  $p$ -dotierte Grenzfläche) darzustellen. DFT-Rechnungen der Fe/GaAs(110)-Grenzfläche, die von Dr. Ali Al-Zubi und Prof. Stefan Blügel vom Forschungszentrum Jülich durchgeführt wurden, zeigen eine hohe Übereinstimmung mit den experimentellen Ergebnissen. Aufbauend auf den XSTS- und DFT-Ergebnissen wird in dieser Dissertation ein Modell entwickelt, das den Zusammenhang zwischen Schottky-Barrieren-Höhe und der elektronischen Ladungsverteilung an der  $p$ -dotierten Grenzfläche qualitativ beschreibt. Darüber hinausgehend wurde in dieser Arbeit ein Kontrollexperiment an der  $p$ -dotierten GaAs(110)-(110)-Kante ohne Eisenfilm durchgeführt.

Die Teile dieser Dissertation, die die kombinierten Ergebnisse der XSTM/XSTS-Messungen und der DFT-Rechnungen zu den elektronischen Eigenschaften der „idealen“  $n$ - und  $p$ -dotierten Fe/GaAs{110}-Grenzflächen diskutieren, wurden bereits in dem Artikel „Local Density of States at Metal-Semiconductor Interfaces: An Atomic Scale Study“ von T. Iffländer, S. Rolf-Pissarczyk, L. Winking, R. G. Ulrich, A. Al-Zubi, S. Blügel und M. Wenderoth in *Physical Review Letters* **114**, 146804 (2015) als „Editors’ suggestion“ und im zugehörigen *Supplemental Material* veröffentlicht. Dies trifft insbesondere auf die Kapitel 3.2, 4 und 5.1 dieser Dissertation zu, deren Abbildungen, Bildunterschriften und Fließtexte nahezu wortwörtlich – der größte Teil davon insbesondere in dem oben erwähnten *Supplemental Material* – veröffentlicht wurden. Die Abbildungen und der Text für diese Veröffentlichung wurden bis auf den DFT-Teil im *Supplemental Material* S8 komplett selbstständig von mir (Tim Iffländer) unter der Anleitung meines Betreuers Dr. Martin Wenderoth verfasst. Alle übrigen Koautoren haben den Text und die Abbildungen vor Veröffentlichung kommentiert und ihre Vorschläge wurden so gut es ging in die finale Fassung eingearbeitet. Die XSTM/XSTS-Daten der  $n$ -dotierten Grenzfächer in der Veröffentlichung stammen wie bereits weiter oben erwähnt von Lars Winking.

Neben der Erforschung der „idealen“ Fe/GaAs(110)-Grenzfläche wird in dieser Dissertation auch erstmals der Einfluss einer partiellen Grenzflächen-Durchmischung auf die strukturellen und elektronischen Eigenschaften der Fe/GaAs(110)-Grenzfläche mit Hilfe von XSTM/XSTS untersucht. Des Weiteren wird in dieser Arbeit auch erstmals der Einfluss der Dicke des Eisenfilms auf die elektronischen Eigenschaften der Grenzfläche untersucht.

Die Untersuchung der magnetischen Eigenschaften der „idealen“ Fe/GaAs(110)-Grenzfläche basiert auf Ergebnissen, die in meiner eigenen Diplomarbeit entstanden sind. Um die magnetische Anisotropie der ultradünnen Eisenfilme auf GaAs(110) gezielter untersuchen zu können, wurde in der Masterarbeit von Arne Grimsel die Ultrahochvakuumkammer für *in situ* Messungen des magneto-optischen Kerr-Effektes (MOKE) weiter-

---

entwickelt. Eine *in situ* 4-Magnet-Pol-Anordnung erlaubt nun neben der longitudinalen MOKE-Geometrie auch die transversale und polare Geometrie, und das angelegte Magnetfeld kann beliebig in alle Raumrichtungen gedreht werden. Die magnetische Anisotropie der ultradünnen Eisenfilme auf GaAs(110) wurde dann anschließend mit Hilfe des rotierbaren Magnetfeldes in den von mir betreuten Bachelorarbeiten von Steffen Rolf-Pissarczyk und Steffen Weikert untersucht. In dieser Dissertation wurden diese Messungen noch einmal mit einem Laser durchgeführt, der im Vergleich zu den beiden Bachelorarbeiten weitaus rausch- und driftärmere Kerr-Signale zuließ, sodass aus diesen Messungen weitere Informationen gewonnen werden konnten. Um dem Leser einen Gesamtüberblick über die magnetischen Eigenschaften dieser ultradünnen Eisenfilme auf GaAs(110) geben zu können und die darauffolgende im Vergleich zur Diplomarbeit erweiterte Diskussion nachvollziehen zu können, werden in dieser Arbeit neben den neuen Ergebnissen auch noch einmal alle wichtigen Ergebnisse aus meiner Diplomarbeit präsentiert. Darüber hinausgehend werden im Rahmen dieser Dissertation auch erstmals Lichtwellenlängen-abhängige *in situ* MOKE-Messungen an den ultradünnen Eisenfilmen auf GaAs(110) durchgeführt und diskutiert.

Das in dieser Dissertation vorgestellte Promotionsprojekt wurde über Drittmittel der Deutschen Forschungsgemeinschaft finanziert.



## Danksagung

Zum Schluss möchte ich noch all denjenigen danken, die zum Gelingen dieser Arbeit beigetragen haben.

An erster Stelle möchte ich mich bei Herrn Prof. Dr. R. G. Ulbrich dafür bedanken, dass er es mir ermöglicht hat an diesem spannenden Thema arbeiten zu können. Die Diskussionen mit ihm und seine Denkanstöße haben wesentlich zum Gelingen dieser Arbeit beigetragen.

Bei Herrn Prof. Dr. H. C. Hofsäss möchte ich mich für die Übernahme der Zweitkorrektur bedanken. Außerdem danke ich Herrn Prof. Dr. H.-U. Krebs, Herrn Prof. Dr. V. Moshnyaga, Herrn Prof. Dr. M. Seibt und Frau Prof. Dr. C. A. Volkert für ihr Mitwirken in der Prüfungskommission.

Ein besonderer Dank gebührt Dr. M. Wenderoth für die Betreuung dieser Arbeit. Nur durch seine fachliche Kompetenz und die zahlreichen gewinnbringenden Diskussionen mit ihm konnte diese Arbeit in dieser Form zustande kommen. Menschlich möchte ich ihm ebenfalls danken für die aufmunternden Worte während der Erstellung dieser Dissertation.

Ein besonderes Dankeschön richtet sich an Bernhard Spicher, der immer zur Stelle ist, wenn man ihn braucht. Ohne seine technische Expertise hätte wohl so manche UHV-Anlage ihren Dienst versagt. Außerdem hat er immer einen flotten Spruch parat: ob beim Mittagessen im Klinikum oder nach dem „x-ten Zwischenfall“ im Labor.

Für die erstklassige Zusammenarbeit und die schöne Zeit zusammen möchte ich außerdem allen aktuellen und ehemaligen Mitgliedern der Tunnelgruppe danken: Thomas Druga, Philipp Kloth, Karen Teichmann, Henning Prüser, Karolin Löser, Sergej Burbach, Thomas Kotzott, Philip Willke, Terence Thias, Philipp Ansorg, Anna Sinterhauf, Philipp Buchsteiner, Katharina Kaiser, Christian Werner, Thomas Spaeth, Till Hatje, Felix Lüpke als auch den am MOKE-Projekt beteiligten Arne Grimsel und Steffen Weikert.

Besonders hervorzuheben ist hier Steffen Rolf-Pissarczyk, den ich durch seine Bachelor- und Masterarbeit begleiten durfte. Die Zusammenarbeit mit ihm war stets bereichernd, sowohl bei unseren gemeinsamen Messungen nachts im STM-Labor als auch bei unseren Diskussionen über Physik.

## Danksagung

---

Außerdem möchte ich mich bei meinem Vorgänger Lars Winking dafür bedanken, dass er am Ende seiner Promotion noch die Zeit gefunden hat mir die ersten Schritte für MOKE- und STM-Messungen an Metall-Halbleiter-Grenzflächen zu vermitteln.

Herzlich danken möchte ich auch Herrn Prof. S. Blügel und Dr. A. Al-Zubi vom Forschungszentrum Jülich für die DFT-Rechnungen der idealen Fe/GaAs(110)-Grenzfläche. Die gemeinsamen Diskussionen haben wesentlich zum Verständnis der DFT-Daten beigetragen.

Vielen Dank auch an Christian Zube für die Hall-Messungen zur Bestimmung der Ladungsträgerdichte der *p*-dotierten GaAs-Proben.

Ebenfalls bedanken möchte ich mich bei den Mitarbeitern der Werkstätten des IV. Physikalischen Instituts. Rasit Köske war immer vor Ort, wenn es mal mit der Elektronik nicht so funktionierte, wie es sollte. Andreas Juretzko stand für Fragen rund um die Feinmechanik zur Verfügung. Außerdem möchte ich mich bei den Mitarbeitern der Zentralwerkstatt, namentlich Christof Schmidt, Alexander Gehrt und Kerstin Thöne, für die Anfertigung zahlreicher filigraner Teile für unsere Probenhalter bedanken.

Bei der Deutschen Forschungsgemeinschaft möchte ich mich für die finanzielle Unterstützung dieses Projektes in Form von Drittmitteln (SFB 602, SPP 1285) bedanken.

Bei all meinen Freunden aus Göttingen und aus der Ferne bedanke ich mich für die schöne Zeit während des Studiums und der Promotion.

Ein ganz besonderer Dank gilt meinen Eltern, die mich in jeder Situation liebevoll unterstützen und immer für mich da sind. Es tut gut einen so großen Rückhalt von Euch erfahren zu dürfen! Vielen Dank für Alles!

Mein größter Dank gilt meiner lieben Sandy, die ihren Physiker in den letzten Monaten vor Abgabe ertragen musste. Zeit mit Dir zu verbringen ist immer etwas Besonderes. Ob gemeinsam auf dem Campus in Göttingen, bei einem Halbmarathon in Wolfsburg, auf Reisen um die halbe Welt oder einfach nur zuhause beim gemütlichen Abendessen: wenn Du da bist, dann scheint immer die Sonne!

# Lebenslauf

## **Tim Iffländer**

geboren am 12.04.1983 in Wolfsburg

Staatsangehörigkeit: deutsch

12/2010	<b>Beginn der Promotion</b> als wissenschaftlicher Mitarbeiter am IV. Physikalischen Institut der Universität Göttingen
11/2010	<b>Diplom im Fach Physik</b>
05/2009	<b>Beginn der Diplomarbeit</b> am IV. Physikalischen Institut der Universität Göttingen
09/2006- 12/2006	<b>Auslandssemester über das Erasmus-Programm</b> an der University of Helsinki, Finland
07/2005	<b>Vordiplom im Fach Physik</b>
10/2003	<b>Beginn des Physikstudiums</b> an der Universität Göttingen
07/2002 - 03/2003	<b>Wehrpflicht</b>
06/2002	<b>Allgemeine Hochschulreife</b> an der gymnasialen Oberstufe der Heinrich-Nordhoff-Gesamt-Schule Wolfsburg

---

## **Publikationen:**

1. T. Iffländer, S. Rolf-Pissarczyk, L. Winking, R. G. Ulbrich, A. Al-Zubi, S. Blügel, and M. Wenderoth  
**Local Density of States at Metal-Semiconductor Interfaces: An Atomic Scale Study**  
*Physical Review Letters* **114**, 146804 (2015) selected as “Editors’ suggestion”

## **Präsentationen:**

2. T. Iffländer, S. Rolf-Pissarczyk, L. Winking, R. G. Ulbrich, and M. Wenderoth  
**Electronic properties of the ideal Fe/GaAs(110) interface**  
*Frühjahrstagung der DPG 2014 in Dresden*
3. T. Iffländer, M. Wenderoth, S. Rolf-Pissarczyk, S. Weikert, L. Winking, and R. G. Ulbrich  
**Magnetic Properties of the Fe/GaAs(110) Interface with ultrathin films investigated by In-Situ MOKE Measurements**  
*Frühjahrstagung der DPG 2013 in Regensburg*
4. T. Iffländer, M. Wenderoth, S. Rolf-Pissarczyk, L. Winking, and R. G. Ulbrich  
**Magnetic and Structural Properties of the Fe/GaAs(110) Interface Investigated by In-Situ MOKE, STM, and LEED Measurements**  
*21<sup>st</sup> International Colloquium on Magnetic Films and Surfaces (ICMFS) 2012 in Shanghai, People’s Republic of China*
5. T. Iffländer, M. Wenderoth, A. Grimsel, T. Druga, L. Winking, and R. G. Ulbrich  
**In-Situ STM, LEED, and MOKE Measurements of Ultrathin Epitaxially Flat Grown Fe Films on the GaAs(110) Surface**  
*28<sup>th</sup> European Conference on Surface Science (ECOSS) 2011 in Wroclaw, Poland*
6. T. Iffländer, M. Wenderoth, T. Druga, L. Winking, and R. G. Ulbrich  
**In-Situ STM, LEED, and MOKE Measurements of Ultrathin Epitaxially Flat Grown Fe Films on the GaAs(110) Surface**  
*Frühjahrstagung der DPG 2011 in Dresden*
7. T. Iffländer, M. Wenderoth, L. Winking, and R. G. Ulbrich  
**Magnetic properties of ultrathin epitaxially flat grown Fe films on the GaAs(110) surface**  
*International Conference on Nanoscience and Technology (ICN+T) 2010 in Beijing, People’s Republic of China*
8. T. Iffländer, M. Wenderoth, T. Druga, and R. G. Ulbrich  
**In-Situ STM, LEED, and MOKE Measurements of Ultrathin Epitaxially Flat Grown Fe Films on the GaAs(110) Surface**  
*Frühjahrstagung der DPG 2010 in Regensburg*
9. L. Winking, M. Wenderoth, T. Iffländer, T. Druga, and R. G. Ulbrich  
**Cross-Sectional Scanning Tunneling Microscopy Across a Metal-Semiconductor Interface – Structural and Electronic Properties on the Atomic Scale**  
*Frühjahrstagung der DPG 2009 in Dresden*